VIBRATION MONITORING OF RETROFITTED RC FRAMES USING GFRP

A thesis report Submitted in Fulfillment of requirement for the Award of the Degree of

DOCTOR OF PHILOSOPHY
IN
CIVIL ENGINEERING

Submitted By

Atiwat Vimuttasoongviriya
Roll No. 9050201

Under the supervision of

Dr. Maneek Kumar Kwatra
Professor & Head,
Civil Engineering Department,
Department,
Thapar University, Patiala

Dr. Naveen
Associate Professor,
Civil Engineering

Thapar University, Patiala

Department of Civil Engineering
Thapar University, Patiala,
Punjab-147004, INDIA
MAY-2011

CERTIFICATE

It is certified that the thesis report entitled "**Vibration Monitoring and Damage Assessment of Retrofitted RC Frames using GFRP**", which is being submitted herewith by **Atiwat Vimuttasoongviriya**, in partial fulfillment for the award of degree in **Doctoral of Civil Engineering (Structures)** at **Thapar University, Patiala** is an authentic record of student's own work carried out under my supervision and guidance. The matter presented in the thesis has reached the standards fulfilling the requirements of the regulation for the award of said degree.

Dr. Maneek Kumar

Professor,
Civil Engineering Department,
Thapar University, Patiala
(Supervisor)

Dr. Naveen Kwatra

Associate Professor,
Civil Engineering Department,
Thapar University, Patiala
(Supervisor)

Dr. Maneek Kumar

Head of Department
Civil Engineering Department,
Thapar University, Patiala

ACKNOWLEDGEMENT

"SUCCESS DEGINS WITH A SINGLE STEPS"

A dissertation cannot be completed without the help of many peoples who contribute directly or indirectly through there constructive criticism in the evolution and preparation of this work. It would not be fair on my part, if I don't say a word of thanks to all those whose sincere advice made this period a real educative, enlightening, pleasurable and memorable one.

First of all, a special debt of gratitude is owned to my thesis supervisor, Professor **Dr. Maneek Kumar** and Associate Professor **Dr. Naveen Kwatra** for their gracious efforts and keen pursuit, which has remained as a valuable asset for the successful instrument of my research proposal. His dynamism and diligent enthusiasm has been highly instrumental in keeping my spirit high. His flawless and forthright suggestions blended with an innate intelligent application have crowned my task a success.

My thanks are due to Professor Dr. Abhijit Mukherjee, Professor Dr. Somchai Choocheepsakun, Associate Professor Dr. Mongkol Jiravacharadet and Professor William Billgor for providing excellent suggestions and aid in preparation of the thesis.

My special thanks to Er. Jan Cervenka, Cervenka Consulting form Czech Republic for solving all the problems occurred in the software ATENA used in the thesis work.

I would also like to thank to my parents, sister, brother and my friends for their constant encouragement during the entire course of my thesis work.

I am also like to offer my sincere thanks to all faculty, teaching and non-teaching of Civil Engineering Department (CED), and staff of central library, Thapar University, Patiala for their assistance.

ATIWAT VIMUTTASOONGVIRIYA

Ph.D. Civil Structures

Roll No. 9050201

ABSTRACT

The need for structural damage identification is continuously growing to monitor the damage of existing civil structures. The information of damage identification is utilized to make decisions on maintenance of damaged structure. Detecting structural damage using the information contained in vibration signatures has become more widely accepted by many researchers. In high seismic region of north India, existing reinforced concrete buildings have been constructed at time when seismic zones were not recognized. Therefore, these buildings need to monitor the damage and improve their load carrying capacities for the purpose of seismic safety. The Fiber Reinforcement Polymer is one popular strengthening technique. This material with epoxy resin has received considerable attention due to its high strength, light weight, easy manageability on-site and high resistance against corrosion. This paper intends to investigate the effect of lateral loads on nonlinear behavior and the damage identification of retrofitted RC frame models. Vibration based damage identification namely modal plastic softening damage index, stiffness-mass ratio damage method, modal flexibility damage index and frequency response function based mode shape method were used. The three story reinforced concrete moment resisting frame model was constructed and tested under lateral quasi-static loads to simulate different damage states on the structure. The damaged frame was repaired by using Glass Fiber Reinforced Polymer (GFRP) sheets to increase load resistance capacities of structural elements and beam to column connections. Failure mechanism of the experimental frame model has been investigated. The effects of GFRP wrap have been reported. Subsequently, the damage indexes based on the change in dynamic characteristics were investigated using OROS software program with the help of impact hammer excitation test. Finite element (FE) models, nonlinear and dynamic analysis, were used to model experimental frames. Finally, the identification methods based on measured modal parameters, Modal Assurance Criterion (MAC) and Coordinate Modal Assurance Criterion (COMAC), were utilized and the efficiencies of these methods were investigated.

Results of this study show that the use of GFRP wrapped for structural retrofitting provides increased significant lateral load capacity and ductile behavior. The damage

indices of retrofitted frames reduce indicating better performance as compare to the control frame. Damage indices based on the change in frequency response function shows a much acceptable accuracy correlation with damage based on the change in natural frequency. For FE models, the nonlinear FE analytical results exhibit similar trends with those of the experimental frame model, but the FE model is slightly stiffer than the experimental model. Moreover, the comparisons between the results of dynamic FE model and the experimental results show reasonable accuracy of modal parameter identification. The results of FE model of vibrating frame specimens agree with the experimental results. The MAC is subjected to very small change by damage of retrofitting. This factor cannot determine the stiffness changes in each degree of freedom, but it can present information about overall stiffness change of the structure due to damage or retrofitting. It is concluded that COMAC factors may detect the changes in frame damage. This index is rather able to detect, locate or quantify damage and effectiveness of retrofitting.

TABLE OF CONTENTS

LIST OF TABLES

LIST OF FIGURES

LIST OF SYMBOL

DI_{DIP}	Dipasquale and Cakmak Damage Index
DI_{FRF_MS}	Frequency Response Function Damage Index
DI_k	Stiffness Damage Index
DI_{PARK}	Park and Ang Damage Index
Drift	Drift ratio
COMAC	Coordinate Modal Assurance Criterion
E	Elastic modulus
G_c	Initial concrete shear modulus
H	Story height
I	Section moment inertia
m	Structural mass
MAC	Modal Assurance Criterion
q	Shape parameter
r	Pearson correlation
$f_c^{'}$	Cylinder strength of concrete
k_i	Structural stiffness
r_c	Compressive reduction factor of concrete
r_{et}	Reduction factor of the tensile strength of concrete
r_g	Shear retention factor of concrete
w	Crack width
ζ	Damping coefficient
Δ_y	Yield displacement
Δ_u	Ultimate displacement
P_i	Apply force
$\delta_{\max}$	Maximum experienced deformation
δ_y	Structural yield deformation
δ_u	Ultimate deformation
β	Model constant parameter

ν_j	Stiffness ratio
μ	Displacement ductility factor
ω_n	Resonant frequency
ϕ	Phase angle
$H(\omega)$	Frequency response function
τ_d	Damped period
γ	Coherence function
$G_{yy}(f)$	Power spectrum
$H_{lj}(\omega)$	FRF magnitude of undamaged
$H^*_{lj}(\omega)$	FRF magnitude of damaged
σ_c^{ef}	Effective stress
ε^{eq}	Equivalent uniaxial strain
$\mathbf{M}$	Structural Mass matrix
$\mathbf{K}$	Structural Stiffness matrix
$\boldsymbol{\varphi}_r$	Structural mode shape matrix

CHAPTER 1
INTRODUCITON

1.1 GENERAL

As buildings age and specifically in North India, they may experience seismic activity or other potentially altering phenomena. Building codes change to incorporate structurally safer and stronger design. Also the use of a particular building can change requiring code change and possible building modification. The need to accurately assess a building's safety or, conversely, the nature and magnitude of accumulated damage is paramount in maintaining public safety. Correlation between typical hazard events and social-economic consequences is presented in Figure 1.1(Elnashai and Sarno, 2008).

Today there are many methods used in measuring structural damage, some better than others, but none is without its limitations. Park and Ang (1985) suggested a linear combination of maximum displacement response and total hysteretic energy dissipation under cyclic load. The relation between Park and Ang's damage index and various states is examined in Table 1.1. Powell and Allahabadi (1987) introduced a deformation-based damage index in terms of displacement or ductility. Kanwar et. al. (2007) proposed a measure based on stiffness change. However, crack propagation is not generally known under service loads. Vibration measuring is one solution to this issue.

The approach of vibration measurement for damage detection defines the baseline vibration signature of a piece of equipment before damage occurs. Many researchers found that if the new vibration signature obtained during a routine operation deviates from that of the baseline value, the building should be checked for possible local defects (Kanwar et al., 2006; Yao et al., 1992). Typical vibration identification assumes that the dynamic property of a structure is a sensitive indicator of its physical integrity. When any of the properties like mass, stiffness, or damping of the structure changes due to a structural defect, the vibration response of the structure will also change (Vimuttasoongviriya et al., 2009; Goyal, 2007; Dincal, 2005). These dynamic characteristics can be measured directly by vibrating a structure using digital signal processing equipment and Fast Fourier Transform (FFT) routines (Rao, 2000; Reddy et

al., 1994; Meirovitch, 1986). Damage detection by calculating the change in modal parameters, such as natural frequency, mode shape, and frequency response function (FRF), are also non-destructive techniques that are widely used.

Gheorghiu et al. (2005) and Jian et al. (2005) investigated the damage identification based on data analysis on general RC elements and steel elements respectively. A few researchers studied strengthened structures as well (Doebling et al., 1998; Goyal, 2007). Dipasquale and Cakmak (1990) presented a damage index based on the change of frequency ratios. This method considers fundamental structural frequencies before and after damage. Rodriguez and Barroso (2002) and Wang et al. (2005) proposed a stiffness-mass ratio using modal parameters to measure damage. Ko et al. (2002) developed the Modal Flexibility Damage Index. This index compares flexibility matrices from two sets of mode shapes. Maia et al. (2003) presented an FRF-based mode shape method that uses FRF data taken directly from structures without any intermediate steps.

Prevention of structural damage is a fundamental objective of external load resistances. The definition of structural damage may be expressed in terms of different response quantities at local or global system. Generally, structural collapse occurs if load-carrying elements fail in compression or if shear transfer is lost between structural elements. Damage of structures may also be caused by global instability. Brittle structures fail when the maximum applied loads exceed the strength of the systems. Ductile structures do not collapse under the condition of maximum strength. They sustain inelastic deformations and dissipate the input energy (Elnashai and Sarno, 2008; Said and Nehdi, 2004). They are safe as long as the required ductile capacity is available. In order to increase the lateral resistance and to improve the ductility, RC elements can be efficiently reinforced with longitudinal and transverse steel bars. Alternating actions may cause stiffness and strength deterioration, especially in RC members. The net effect is the erosion of the ductility and the energy dissipation capacity.

Strengthened buildings have uncertain load resistance capacity and ductility due to long duration ageing. Most of the structures continually accumulate damage during their service life. There are various methods suitable for strengthening these structural systems. The affected parts of the structures can be jacketed with steel plates or braced

frames can be added. Although time-consuming, these methods are cost-effective (Khalifa et al, 1998; Al-Sulaimani et al, 1994). However, they do add considerable mass to the structure.

Another solution involves the use of advanced materials like Fiber Reinforced Polymers (FRP). Lighter and easier to apply, they are widely used for strengthening RC components. It should be noted that after repair it is all the more important to monitor the health of the building as cracks tend to be covered by layers of strengthening material. The use of strengthening laminates for RC structural repair has been studied extensively (Chang et al., 2004; Triantafillou, 1998; Ye et al., 2002). The resistance behavior of FRP material when subjected to axial and lateral loads has been investigated by many authors (Ghobarah and Elmandoohglal, 2004; Jain et al., 2005; Wang and Restrepo, 2001). Glass Fiber Reinforced Polymers (GFRP) and Carbon Fiber Reinforced Polymers (CFRP) are rapidly becoming a superior alternative to traditional steel reinforcements for RC structures (Chih and Hsu, 2009; Mukherjee and Joshi, 2005; Mukherjee et al., 2004; Kachlakev and Mccury, 2000). They have a very high specific strength, high stiffness-to-weight ratio, and increased resistance to corrosion. Within current cultural and economic context, FRP materials have been proposed for a very wide variety of construction and repair applications, including bridges, power stations, parking facilities, offshore structures, and general buildings (Ludovico et al., 2005; Pavese et al., 2004; Khalifa et al., 1998).

Most of these studies on strengthened structural elements have reported only load-defection behavior vis-a-vis form of composite overlay bond failure. This research work investigated both nonlinear behavior and the change in dynamic characteristics of RC frame models with and without damage under lateral loads. GFRP was used as the strengthening material for retrofitting damaged frames, and vibration monitoring was carried out to study the effects of damage and damage repair. The dynamic characteristics studied included the natural frequency, damping coefficient, and FRF magnitude of the three-story RC frame model. Then the change in these characteristics was studied after subjecting the models to different levels of control damage. Some of the damage indices have been selected to indicate the damage for both nonlinear static and dynamic approach. The damaged RC frame models were strengthened with GFRP and the dynamic characteristics were investigated in the same manner as the control

frames. Subsequently, Finite Element (FE) software program was used for modeling, structural analysis, and results processing of the specimen. A three-dimensional FE model was developed to replicate the experimental RC frame before and after GFRP strengthening. The results from control frames and strengthened frames have been interpreted.

1.2 SYSTEM IDENTIFICATION AND VIBRATION MONITORING

It is known that dynamic properties of structure can change whenever damping, mass or stiffness is changed (Li et al., 1998). Generally, structural vibrations are damped forced vibrations. This means that the applied forcing disturbance will produce a magnified vibration according to the ratio between the forcing disturbance frequency and structural frequency (Satake et al., 2003; Ndambi et al., 2000). Damping is likely to be significant in structural vibrations. This is the energy dissipating effect of internal friction, fixation looseness, etc.

Structures of doubtful integrity may vibrate with excessive amplitudes. For such structures the change in stiffness, mass or damping would appear to be the dominant consequence of deterioration (Dowrick, 1988; Salane, 1981). Vibration monitoring involves the relationship between applied force and the resulting vibration. Techniques of vibration monitoring are well developed and for many structures the use of vibration monitoring techniques can be recommended without restriction (Buchholdt, 1997; Farrar and Cone, 1995). Vibration of a structural element, frequency ranges, and vibratory amplitudes depend on many factors such as material, supports, cross-section area, and structural system (Ibrahim and Mikulcik, 1977; Rao, 2000).

Defects like mechanical slackness, loose foundations, and ineffective load-bearing members can cause excessive vibration. When a structure suffers from excessive vibration, it is being subjected to undesirable excitations which can sometimes be measured (Key, 1988).

The excitation response in the dimension of time may be difficult to interpret and it can be random, deterministic or a combination of both. But if a Fourier transform is performed over a time window, then the spectrum of the transformed signal will operate along with some discrete periodic signals. If the Fourier transform operation is not stationary and repeated for several intervals, then each spectrum will change with

time. This analysis is difficult unless the change over each time interval is small. If the structure vibrates in one or more modes, then the combination of the response spectrum may be random for an array of similar structures (Newmark and Rosenblueth, 1971). Figure 1.2 shows possible effects of varying stiffness and mass. It shows that increasing stiffness can reduce response unless one moves the resonance to a peak of the excitation, and increasing the mass can do a similar thing. On the other hand, increasing damping reduces response near each resonance. But damping cannot reduce the effect of the discrete excitation spike unless the resonance frequency lies atop one of those spikes. Modifying the excitation to reduce the spikes is effective in reducing response amplitudes. Unlike the mass and stiffness of a structure, damping does not relate to a unique physical process but rather to a number of possible processes. Damping values depend on several factors; a few among these are vibration amplitude, material of construction, fundamental periods of vibration, mode shapes, and structural configurations.

1.2.1 Structural collapse prevention

In seismic region, failure modes observed in existing structures during past earthquakes worldwide were caused by a number of member, connection, and system deficiencies. In general, deficiencies in structures are classified as structural or non-structural. The former refers to sections, members, connections, diaphragms and foundations (Mo, 1994; Newmark and Rosenblueth, 1971). Common structural deficiencies in RC buildings include:

(i) Poor quality and inadequate detailing;

(ii) Excessive and unexpected member over-strength, especially for dissipative components;

(iii) Change of material and detailing at intermediate floors. In some cases, the bottom storey may be constructed from composite changing to RC at an upper level. Deformation demand may be concentrated at the floor, where the change occurs;

(iv) Reduction in column dimensions due to high over-strength if uniform sections are used at higher stories. An abrupt change in stiffness and

strength may lead to failure at the level of change, since the floor load above and below is similar;

(v) Inadequate storey shear caused by an insufficient number of columns and walls;

(vi) Irregularities of mass, stiffness, and strength distribution in plan and elevation. Torsion effects may be caused by non-coincidence on the floor plan of the centre of gravity and the centre of stiffness;

(vii) Low structural redundancy, insufficient number of lateral resisting systems;

(viii) Large openings in floor diaphragms due to the presence of stairwells and lifts;

(ix) Inadequate separation joints between adjacent buildings, especially for buildings with different heights and different materials of construction;

(x) Large differential displacements due to settlement of the foundation system.

Structural damage is generally assessed according to the type of construction material such as reinforced concrete, masonry, steel, and composite material. RC buildings can experience several types of failure under loading condition, which primarily include (Said and Nehdi, 2004);

(i) Brittle shear failure of columns or beams;

(ii) Bucking of longitudinal bars in beam-columns due to inadequate spacing or lack of transverse stirrups;

(iii) Shear failure of columns which were shortened by the supporting effect of non-structural elements;

(iv) Brittle failure in corner columns caused by torsion and biaxial bending effects;

(v) Shear cracking in beam-to-column connections in panel zones;

(vi) Bond failure, particularly in zones where there are high cyclic stresses in the concrete;

(vii) Brittle failure of single or coupled structural walls, particularly walls with openings;

(viii) Tearing of slabs at discontinuities and junctions with very stiff elements;

(ix) Excessive damage to infill-wall and other non-structural components;

(x) Concentration of damage at a given storey level;

(xi) Pounding between adjacent buildings;

(xii) Overturning and uplift.

Figure 1.3 displays the target hinging mechanism of a multi-storey frame along with different hinging mechanisms of the sub-assemblage, showing clearly that a joint failure results in a decrease in the redundancy in the structure by at least an order of 2, whereas hinging in the structural element decreases it by only an order of 1. Beam-to-column joint deficiencies combined with the weak-column and strong-beam glitches contradict failure hierarchy of the design concept. A failure in the beam is usually less critical than that in the column, and the latter is less critical than a failure in the joint. Hinging in the joint allows excessive rotation both in the beam and in the column in conjunction with a loss of load carrying capacity of the column. Such a dangerous failure mechanism is unacceptable and must be prevented in design.

1.2.2 Damage of beams

The ductile design of beams presupposes the formation of plastic hinges at their ends to comply with the requirements of capacity design philosophy. The dissipation of energy through stable hysteretic loops without significant degradation of stiffness and strength plays a significant role in the response.

Under cyclic loading, mechanisms of shear resistance in compression zone, aggregate interlock, dowel action, and truss action tend to deteriorate as inelasticity is increased. A very undesirable behavior known as “sliding shear” may occur. In members with high shear stress, open cracks in the tension and compression zone remain open. Shear behavior is governed by a vertical crack which does not intersect the hoops, however close they may be. In poor detailing and insufficient strength, the first damage pattern is flexural cracking in the middle zone of the beam span. Such cracks would have been preexisting due to gravity loads and may have opened further because of the effects of the vertical component of the earthquake. The overall safety of the building is not compromised. The second damage pattern is shear cracking which occur near supports. These diagonal cracks are attributed mainly to inadequate shear reinforcement. They are more hazardous than flexural cracks but in general are not critical regarding overall

safety of the building. The third pattern is flexural cracking in beam supports, which defines the extent and severity of the damage. The fourth damage pattern is cracking in beam span at locations of indirect support. These cracks are mainly due to the vertical component of the earthquake. They may be prevented if suspension reinforcement is installed (Penelis and Kappos, 1997; Panlay and Priestley, 1992; Mo, 1994).

The potential strength and ductility of many RC beams is often reduced because of the absence of proper detailing. For example, the lack of proper stirrup spacing and use of smooth longitudinal steel bars generate the formation of shear cracks. These cracks have, in turn, led to reductions in both flexural and shear strength. Shear mechanism is always avoided in RC members because it is associated with low energy dissipation and suddenly failure or brittle failure. Typical damage patterns in beams are shown in Figure 1.4.

1.2.3 Damage of columns

Columns play an important role in the stability of framed systems. To achieve ductile seismic response, plastic hinges should not form in columns with the exception of the base for ground storey columns and top storey columns. To prevent the possibility of plastic hinging in columns, beam over-strength factors are often utilized in seismic design (Bazant and Oh, 1983). However, these factors are generally either insufficient or unfeasible since the confinement reinforcement requirements in the ensuing heavily reinforced columns cannot be achieved. Hence, there is need for ductility in most columns of the structure.

Compressive axial loading influences the response under cyclic loading. The effects are either favorable or unfavorable. Tensile loads, as a result of high overturning moments, although not harmful from the ductility point of view, may cause significant degradation and risk of sliding shear. The mode of failure in columns depends on the shear-span ratio. The different failure modes of columns are a function of the reinforcement layout. The first type, which has conventional reinforcement of hoops and longitudinal bars with high axial load, results in cross-inclined shear cracks when subjected to cyclic loading (Memon and Sheikh, 2005). This behavior may be improved if cross-inclined reinforcement is utilized, and particularly, if multiple cross-inclined reinforcement is used.

In short columns, the members employ conventional steel reinforcement consisting of ribbed longitudinal bars and rectangular stirrups. The increased relative stiffness of these short columns attracts high lateral loads. In turn, shear demand in these structural members is extremely high; even adequate seismic detailing is usually ineffective to prevent the occurrence of shear failure (Ghobarah and Elmandoohgalal, 2004).

On the other hand, columns of medium and high slenderness are characterized by a flexural type of failure. This type of damage consists of spalling of the concrete cover and then crushing of the compression zone, bucking of longitudinal bars, and possible fracture of hoops due to the expansion of the core. Columns of low to medium slenderness and with insufficient shear reinforcement present a mixed type of failure. The critical parameter is the amount of transverse reinforcement.

1.2.4 Damage of beam-column joints

The design philosophy of RC beam-column joints first requires that the strength of the joint shall not be inferior to that of the weakest member framing into it. This is a fundamental requirement. It results from the need to avoid seismic energy dissipation through mechanisms characterized by strength and stiffness degradation under cyclic loading conditions. Secondly, the resistance capacity of a column should not be jeopardized by possible strength degradation of the joint core. During an earthquake of moderate intensity, it is preferable that beam-column joints remain in the elastic range, so that no repair is required. Under cyclic loads, shear transfer in joint cores takes place mainly through the application of strut and tie mechanisms (Mo, 1994). Contribution of aggregate interlock and dowel action is practicably negligible, since the shear deformation in the joint core is not large enough to activate these mechanisms. It is important to note that adjacent beams restrain joint core expansion and develop axial forces, which contribute to joint confinement. Floor slabs tend equally to increase both stiffness and strength of joints. However, slab reinforcement increases negative moment capacity of beams, and at exterior joints torsion induced by the slab causes cracking of transverse beams. In this case, slab reinforcement tends to be ineffective. (Elnashai and Sarno, 2008).

As far as interior joints are concerned, the worst type of failure corresponds to the onset of yield penetration at both sides of the joint. Bond conditions may be improved if the diameter of beam bars passing through the joint is limited to minimize slippage. In the case of exterior and corner joints, unfavorable bond conditions may also develop. Splitting cracks along the beam bars affect the efficiency of part of the anchorage before the hook. Moreover, column bars at the exterior face are in compression at one end and in tension at the other, while being affected by radial forces at hooks. This leads to large splitting cracks and extensive spalling at the exterior face. Inadequate number of stirrups at beam-column joints has caused extensive damage in previous earthquakes in exterior connections of framed structures.

Lateral damage patterns of beam-column and column-foundation joints are shown in Figure 1.5. Failure of beam-column joints has caused several collapses of multistory RC frames during earthquakes. Most damage occurred in insufficiently ductile members and connections. Shear compression failure of beam-column joints led to significant reductions of the capacity of the entire lateral resisting system. The formation of a soft storey was observed at the second floor of many of the building structures (Penelis and Kappos, 1997).

1.2.5 Primary sources of damping

Structural damping is a measure of energy dissipation in a vibrating system that results in bringing the structure back to a quiescent state. It is associated with absorption of vibration energy in structural components. It also accounts for material viscosity and friction at connections and supports. In structural components, the energy imparted by cyclic loads or earthquakes is dissipated mainly through hysteretic damping characterized by load-deformation loops. Such loops express load-deformation relationships of materials, sections, members, connections, or systems under alternating loads. For hysteretic damping, dissipation varies with level of displacement, but it is constant with velocity (Satake et al., 2003; Li et al., 1998; Beards, 1996). The amount and mechanism of material hysteretic damping vary significantly depending on whether the material is brittle or ductile. Whereas hysteretic damping is complex and cannot be expressed in simple forms, it is almost always represented in dynamic analysis as equivalent viscous damping, which is proportional to the velocity. This form of

damping conveniently allocates a parameter to the velocity in the dynamic equilibrium equations that matches the mass and stiffness terms associated with acceleration and displacement, respectively.

External energy transmitted to structures can be dissipated through different damping mechanisms (Glanville et al., 1996; Beards, 1996). Primary sources of damping are as mentioned below:

(i) Structural damping, due to energy dissipation in materials of construction, structural components and their connections;

(ii) Supplemental damping, due to energy dissipation of devices added to structural systems to increase their damping;

(iii) Foundation damping, due to the transfer of energy from the vibrating structure to the soil, through the foundations;

(iv) Radiation damping, due to radiation of seismic waves away from foundations.

Values of damping for common materials of construction are outlined in Table 1.2. These are expressed as ratios of the critical damping. It is observed that damping increases with the amplitude of action or deformation, and damping ratios increase in proportion to the natural frequency of vibration in structural systems (Bachmann et al., 1995).

1.2.6 Impedance and structural response

Applied forces and the resulting motions at different points in a structure are related by their mechanical impedance. Measurements of mechanical impedance can be used to:

(i) determine dynamic characteristics of structure such as natural frequencies, mode shapes and frequency response function (Hossdorb and Amerongen, 1974; Hearn and Testa, 1991),

(ii) measure specific material properties such as damping capacity (Ndambi et al., 2000),

(iii) provide the basis of an analytical model. From measurements of impedance of individual components or substructures it is possible to predict the behavior of combined systems (Piszczek and Niziol, 1986).

Both force and motion are vectors in space as well as in time. Thus, care should be taken to define directions of motion relative to the direction of force when this is not obvious from the measurement conditions or from the calculations. Point impedance relates to force and motion. Values are measured at the same point and in the same direction; the ratios are termed “driving point values”, or “point values” for short. Transfer impedance relates to force and motion measurements at different points or angularly at the same point.

1.3 AIM AND SCOPE OF THE PRESENT INVESTIGATION

There are many available and developed procedures for measuring damage. They are based on measuring change of frequencies, mode shapes, or other structural properties before and after the occurrence of natural hazards. The concept of structural health monitoring is rapidly growing to enable early identification of damage and provide warning for unsafe conditions. Current evaluation methods and the damage detection of structures vary according to the materials used in the construction of the building. Based on an extensive literature survey prior to starting the current investigation, gaps in research suggesting avenues of study were illuminated. Consequently, the objectives and scope of this work were refined and defined. The same are presented in the succeeding discussion. The detailed literature review is presented in chapter 2.

1.3.1 Gaps in research area

In the area of health monitoring and as regards to retrofitting with composite materials under diverse conditions, there is an abundance of experimental and analytical research from many countries. There has been some research using only analytical approaches (Samtani et al. 1994, Lagomarsino, 1993), but health monitoring of buildings is a problem transcending purely experimental or purely analytical approaches (Mazurek and DeWolf, 1990; Yao et al., 1992). Experiments without analysis can lead to results that are difficult to interpret or understand, and there is little point in performing analysis without testing since the accuracy of the analysis lacks verification. For these reasons, the experimental studies in the laboratory augmented by analytical approaches using nonlinear static analytical software modeling were proposed for the current research. The structural identification or health monitoring is defined as the

measurement of critical response of a structure under the operating and loading environments, to evaluate the symptoms of operational incidents, anomalies, and deterioration of damage indicators that may reveal compromises to structural health.

Many strategies are available for reducing the seismic risk inherent in an existing building. These include traditional approaches such as the addition of braced frames and shear walls and steel plate laminates. However, there are difficulties in using braced frames or shear walls to retrofit the existing building in some cases. To overcome this, other techniques like use of advanced materials like FRP are being widely used for strengthening of RC components subjected to axial and lateral loads. FRP material has very high tensile strength, shear resistance capacity, strength to weight ratio, and increased resistance to corrosion. Applying FRP material can eliminate the need for scaffolding and subsequently reduce labor costs. In the current research FRP was used for retrofitting the RC frames.

The use of advanced materials like FRP for reinforced concrete structural repair and strengthening applications has been studied extensively in previous researches (Shahowy et al., 1995; Norris and Saadatmanesh, 1994; Bhutta, 1993) . However, all such studies of strengthened structural elements have reported only load-defection behaviors and form-of-composite-overlay bond failure. But for retrofitted structures, the damage position and crack propagation is not generally known under service loads or natural hazards, as cracks remain covered by strengthening material layers. For the purpose of assuring safety, structural health monitoring is a necessary technique to define the damage effects on the materials or geometric properties of the retrofitted structures. Undetected damage may potentially lead to more seismic damage under future earthquakes and eventually to catastrophic failure. Vibration signature analysis is a well-known technique of damage detection of structures. Typical vibration diagnosis assumes that the dynamic property of a structure is a sensitive indicator of its physical integrity. This technique was proposed in order to detect the structural damage in the research conduces.

1.3.2 Aims of investigation

Considering the above gaps, the following specific objectives were laid down for the research work:

1. To study experimentally the dynamic characteristics of constructed model of three-story reinforced concrete frames subjected to different levels of control damage.

2. To study the dynamic characteristic of joint deficient RC frames having deficiency in reinforcement detailing.

3. To study the load deflection behavior and the dynamic characteristics of the retrofitted model of RC frames which are subjected to different damage levels after strengthening using GFRP.

4. To carry out nonlinear modeling of experimental RC frames (with and without damage) and of retrofitted frames using GFRP.

1.3.3 Scope of the work

The dynamic characteristics of three-story RC frames were proposed to be determined for both original and retrofitted frames. The following parameters were proposed to be measured:

(i) Nonlinear static load-deflection behavior.
(ii) Dynamic properties of structures such as natural frequency, mode shape, FRF magnitude, and damping at each damage stage of testing.
(iii) Damage indices and relevant relationships.
(iv) Type and degree of damage and location of damage.

Also studied was the effect on the above parameters due to use of the retrofitting materials like FRP for strengthening the experimental frames subjected to various damage levels.

1.4 ORGANIZATION OF THESIS

The thesis is presented in seven chapters as detailed below:

Chapter-1 introduces the concept, the need for system identification and vibration monitoring, and the objectives of the present work.

Chapter-2 literature review presents the work done by various researchers in the field of strengthening description of structures with FRP laminates, damage detection

and vibration monitoring, and finite element modeling of retrofitted structures.

Chapter-3 details the scheme of experimentation, materials used, model of structures, methodology of testing and strengthening scheme. The mechanical properties of concrete, steel reinforcements and GFRP laminate generated from the experimental program have also been presented in this chapter.

Chapter-4 presents definitions of the fundamental response parameters of structure under lateral load. This chapter also presents load-displacement behavior results, failure mechanism of experimental tests and discussion.

Chapter-5 presents vibration measurement technique and structural dynamic characteristic results of experimental tests, with discussion and correlation of damage indices based on the change in dynamic characteristics.

Chapter-6 deals with finite element model developed for analysis of the non-linear and dynamic behaviors of RC structures for both control and retrofitted frames using GFRP sheet. The comparative analysis between FE model and experimental results is presented in this chapter.

Chapter-7 gives the major conclusions of the study.

References and Appendices follow in succession.

The relevant Tables and Figures, in the same order, are placed at the end of each chapter.

Table 1.1 Relation between damage index and various states (Park and Ang, 1985).

Damage State	Damage Index, *DI*	State of Building
No Damage	0.0	No Damage
Slight Damage	0.0-0.1	No Damage
Minor Damage	0.1-0.25	Minor Damage
Moderate Damage	0.25-0.4	Repairable
Severe Damage	0.4-1.0	Beyond Repair
Collapse	> 1.0	Loss of Building

Table 1.2 Damping for different construction materials (Bachmann et al., 1995)

Material	Damping, (%)
Reinforced concrete	
- Small amplitudes (un-cracked)	0.7-1.0
- Medium amplitudes (fully cracked)	1.0-4.0
- High amplitudes (fully cracked) but no yielding of reinforcement	5.0-8.0
Pre-stressed concrete (un-cracked)	0.4-0.7
Partially stressed concrete (slightly cracked)	0.8-1.2
Composite	0.2-0.3
Steel	0.1-0.2

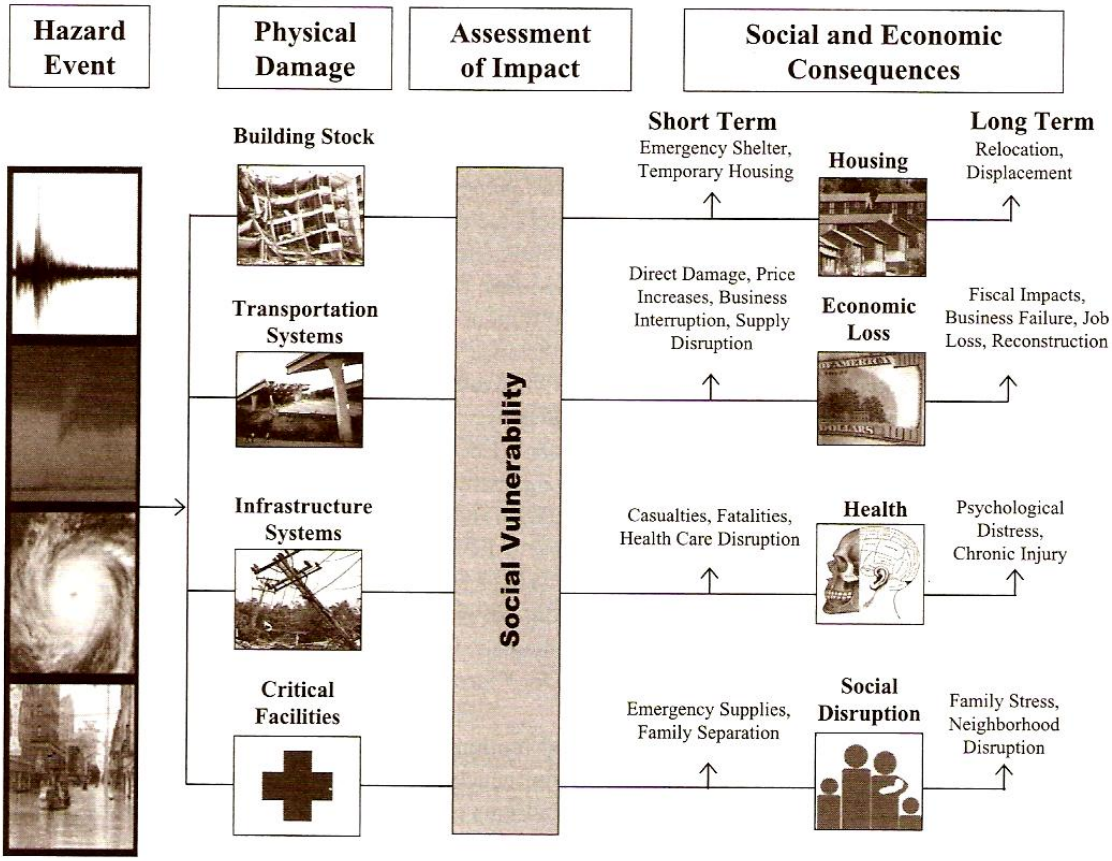

Figure 1.1 Correlation between typical hazard events and social and economic consequences (Elnashai and Sarno, 2008)

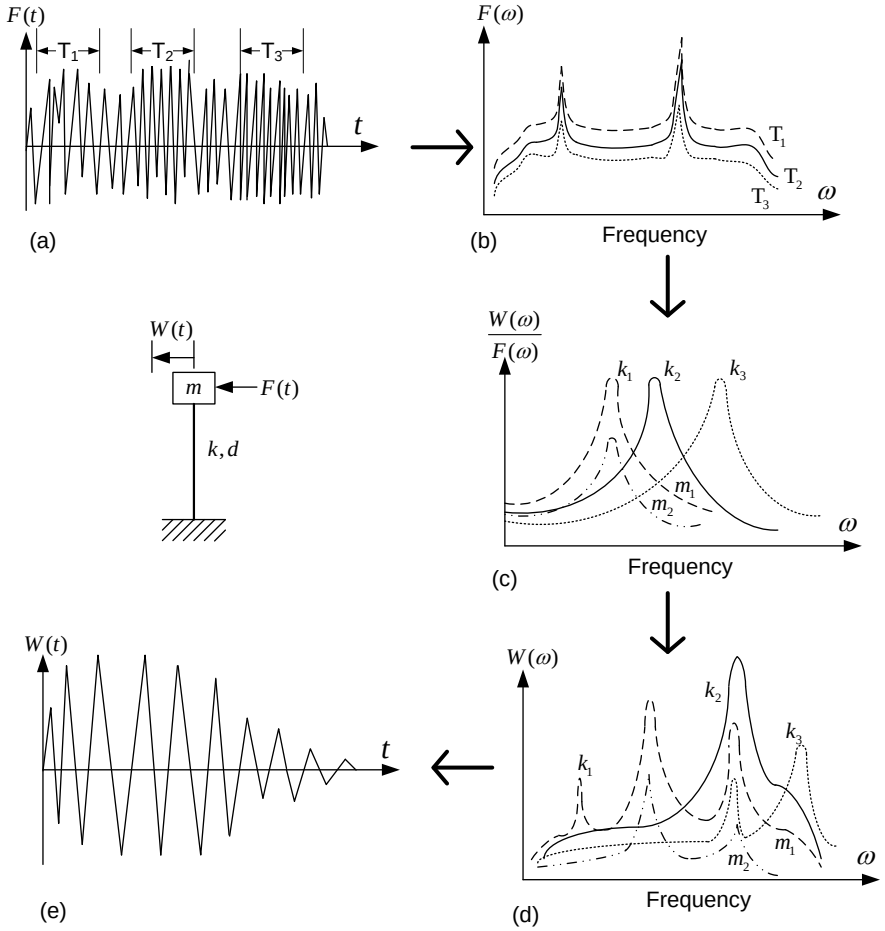

Figure 1.2 Random response behavior. (a) Excitation signal, (b) Spectrum of excitation, (c) Transfer function, (d) FRFs and (e) Response signal (Newmark and Rosenblueth, 1971).

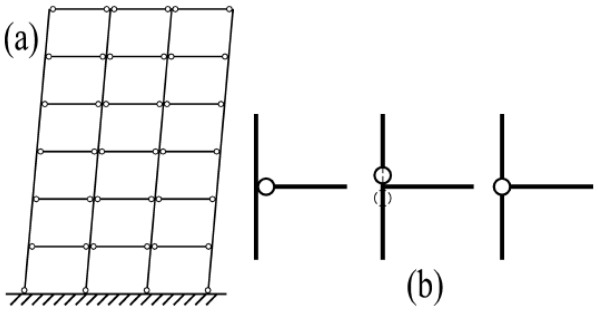

Figure 1.3 The target hinging mechanism of a multi-storey frame along with differenthinging mechanisms of the sub-assemblage. (Said and Nehdi, 2004)

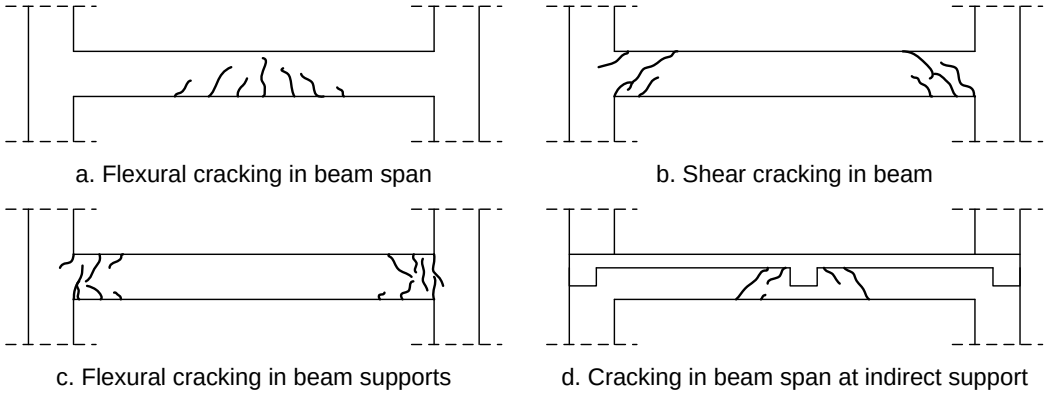

Figure 1.4 Typical damage patterns in beam elements (Penelis and Kappos, 1997)

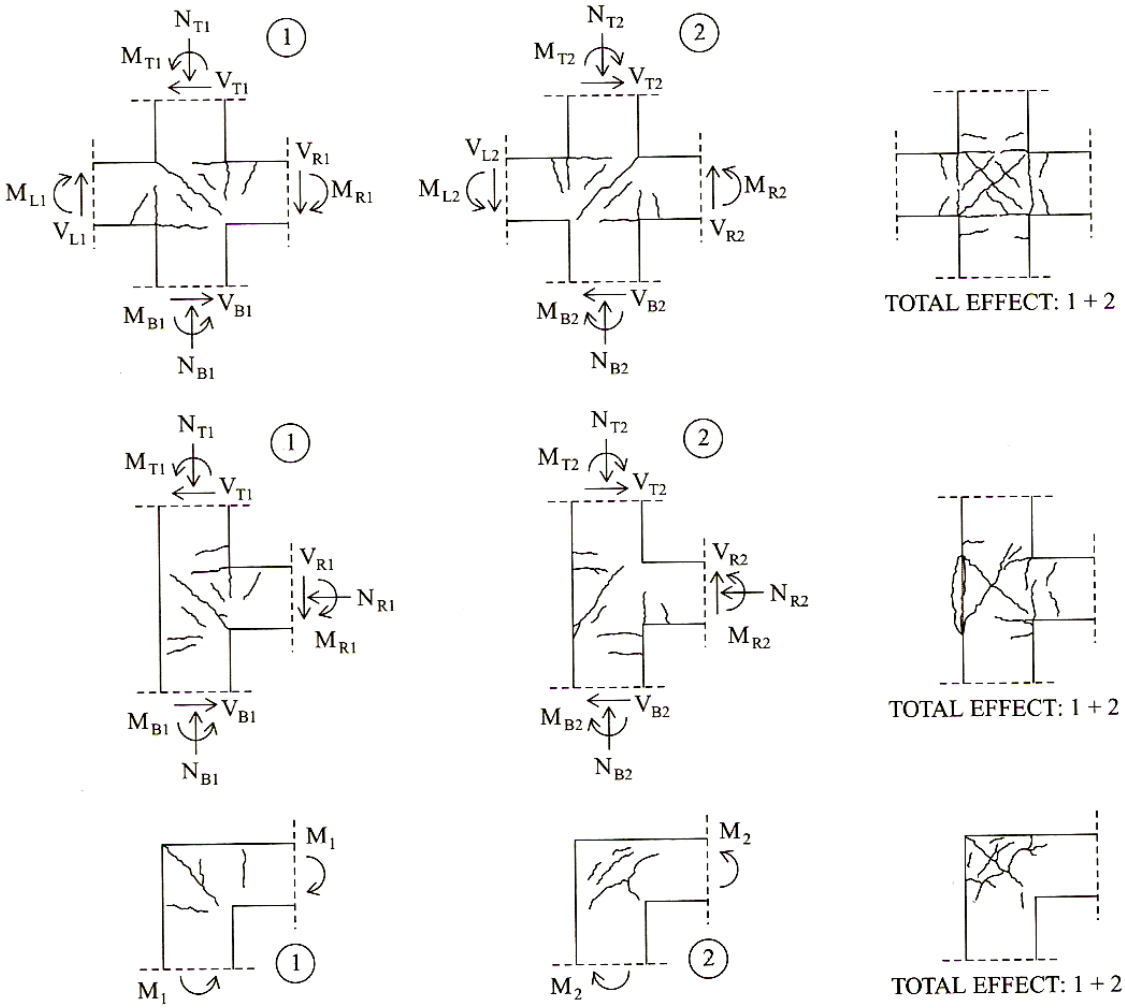

Figure 1.5 Lateral damage patterns of beam-to-column and column-to-foundation joints (Penelis and Kappos, 1997; Elnashai and Sarno, 2008).

CHAPTER 2
LITERATURE REVIEW

2.1 GENERAL

Although thousands of successful RC structures are annually constructed worldwide, there are large numbers of them that deteriorate, or become unsafe due to changes in loading, use, configuration, or due to natural hazards. A large number of existing buildings in North India as well as around the world were built when seismic zones were often not recognized, resulting thus in structural elements designed for gravity loads only (Kanwar et al., 2006). Existing RC buildings, although characterized by high flexural strength and stiffness, have uncertain resistance and displacement capacities. These RC buildings consist of beams and columns, and each such element in a frame contributes to its strength. During earthquakes or high velocity winds, these structures are subjected to increasing base shears (Paz, 1997; Mo, 1994; Newmark, 1991; Dowrick, 1988). These lateral loads may cause damage to the structural elements through the formation of different plastic hinge mechanisms.

The concept of structural health monitoring for maintenance of existing buildings is continually undergoing rapid advancement. The trend towards the development of new technology has accelerated after recent natural hazards that posed the problem of rapid damage assessment of existing structures (Dincall, 2005; Fang et al., 1998; Stubbs et al., 1992; Park and Ang 1985). Most building structures continuously accumulate damage during their service life. Damage to building structures may be due to long duration deterioration, called ageing. For the purpose of assuring seismic safety, it is necessary to monitor. Undetected damage may lead to more seismic damage from future earthquakes and eventually to catastrophic failure (Bracci et al., 1997). Hence, monitoring and rapid structural damage detection is essential.

Structural diagnosis by measuring and analyzing vibration signals is a well-known technique. This technique first defines the baseline vibration signature of a structural element before damage occurs. If the new vibration signature obtained during a routine operation deviates from that of the baseline value, the structure should be checked for possible local defects (Rao, 2000; Thomson, 1993). Typical vibration diagnosis assumes that the dynamic property of a structure is a sensitive indicator of its physical

integrity. When any one of the mass, stiffness, or damping properties of the structure changes due to a structural defect, the vibration response of the structure will also change. In modal structural testing, accelerometers have been widely used as sensors to obtain vibration signals because of their convenience of application and accuracy (Reddy et al., 1994). These dynamic characteristics may be determined from frequency response data, which can be measured directly from the vibrating structure using digital signal processing equipment and FFT routines. When compromise to the integrity of the structure is found, strengthening through retrofitting is necessary. Generally, brittle RC structures break easily. If the columns of brittle structures can be strengthened, this will inhibit the formation of story mechanisms and will also inhibit the formation of overall structural drifts.

There are various methods of strengthening the elements of a structural system. Traditionally, the affected parts of the structures have been jacked with steel plates or reinforced concrete added. Although this method may be cost effective, it is time consuming, dust prone, unreliable and difficult to implement. It also adds considerable mass to the structure. Fiber reinforced polymer alleviates all these difficulties. In addition, they have a very high specific strength (strength-to-weight ratio), specific stiffness (stiffness-to-weight ratio) and increased resistance to corrosion (Balaguru, 2003). FRP materials are rapidly becoming a superior alternative to traditional steel reinforcements for RC and masonry structures in North America, Western Europe, and Japan. Within this cultural and economic context, these materials have been proposed for a very wide variety of construction and repair applications, including bridges, buildings, power stations, parking facilities, and offshore structures (Kachlakev and Mccury, 2000; Triantafillou, 1998; Al-Sulaimani, 1994; Bhutta 1993). Significant literature is available with regards to both vibrations monitoring and retrofitting of stressed elements. A brief review of the same is presented below:

2.2 STRENGTHENING DESCRIPTION OF STRUCTURAL ELEMENTS WITH FRP

Today, most strengthening of RC elements is accomplished using FRP materials, as this type of reinforcement possesses excellent properties such as low weight and high

corrosion resistance, reasons why it is widely chosen for repairing and retrofitting. A brief review of the work done using FRP is presented below:

Jia et.al. (2005) studied the effects of different environmental conditions in conjunction with sustained load and the application of external FRP reinforcement including to degradation due to environmental conditioning. A procedure to quantify the degradation of FRP and concrete bond due to environmental conditions in the framework of nonlinear mechanics was formulated. The effect of application of load in one of four environments was studied: freeze-thaw, air-conditioned laboratory environment, real time outdoor, and elevated dry temperature. It was observed that the ultimate strength of the specimens did not change appreciably as a result of sustained loading; localized slip at the concrete-FRP interface underwent substantial changes, including a dramatic reduction in the amount of energy required to effect debonding of the sheet at any given location. Also it was expected that over a long term, the debonded length will increase and that the long term deflections will also increase substantially.

Memon and Sheikh (2005) studied the effectiveness of strengthening deficiently built columns as well as repairing damaged square columns with GFRP for seismic resistance. Eight specimen structures consisting of square columns cast integrally with a stub were studied. Cyclic loading was applied by pushing downward on the stub near the columns. It was found that at a low axial load level, the structures showed an almost elastic behavior for the first three cycles in all the tests. In the later cycles, the first sign of the deformation was the formation of the ridges or bumps in GFRP on the top and the bottom surfaces of the specimens in the test region. The ridges mostly initiated near the column-stub surface. In all, the high axial load tests, deterioration in the hinging zone was quite rapid. Also in most of the specimens, the formation of ridges started in the third cycle downward. The overall ductile performance depends on the extent of damage sustained by the specimens prior to being wrapped. It was also seen that more GFRP layers were needed for highly damaged columns to achieve a performance similar to that of undamaged retrofitted columns. A larger amount of GFRP is therefore required for columns subjected to higher axial load levels to realize similar

performance enhancements as those demonstrated by retrofitted columns under lower axial loads.

Mukherjee and Joshi (2005) and ***Chih and Hsu (2009)*** investigated the performance of RC beam-column joints under cyclic loading. Joints have been cast with adequate and deficient bond of reinforcements at the beam-column joint as shown in Figures 2.1 to 2.3. FRP sheets and strips have been applied on the joints in different configurations. The columns are subjected to an axial force while the beams are subjected to a cyclic load with controlled displacement. The amplitude of displacement is increased monotonically using a dynamic actuator. The hysteretic curves of the specimens have been plotted. The energy dissipation capacity of various FRP configurations has been compared. In addition, the control specimens have been reused after testing as damaged specimens that are candidates for rehabilitation. The rehabilitation has been carried out using FRP and their performance has been compared with that of the undamaged specimens.

Chang et.al. (2004) investigated, pseudo-dynamic testing of two bridge columns with a reduced scale of two is to five. The seismic performance of two damaged bridge columns was recovered after repairing with CFRP sheets. Three identical RC bridge columns were fabricated. One column was used to perform the reversed cyclic loading test in order to obtain the basic properties of these specimens, and the other two were tested pseudo-dynamically so that accurate seismic responses and reliable hysteretic loops of the RC bridge columns under near fault ground motions could be achieved. In addition to pseudo dynamic testing of the as built bridge columns, the damaged bridge columns were repaired with carbon fiber reinforced polymer and retested pseudo-dynamically. The repair of these specimens was focused in the plastic hinge zone. Three layers of the CFRP composite sheets were applied in the potential plastic hinge zone, which was about one-fourth of the column height. They found that the strength and ductility of the repaired bridge column may be largely restored after the CFRP composite sheets are engaged and external confinement is developed at larger lateral displacements. The displacement response of the same column before and after repair is very similar except that a slightly larger displacement response occurs during testing of the repaired specimen. Also there were no observable flexural cracks on the outside

CFRP layer along the fiber direction and no tension failure of the CFRP composite sheet was seen.

Ghobarah and Elmandoohgalal (2004) tested three rectangular short columns under cyclic lateral loads and constant axial load. One specimen was tested as control specimen, while two specimens were strengthened using three layers of CFRP. They found that several short RC columns failed in brittle shear, when subjected to lateral cyclic displacements. The strengthening of a short RC column that contains high percentage of transverse reinforcement using anchored CFRP sheets prevented its brittle shear failure and significantly improved the displacement ductility and energy dissipation capacity. Anchoring techniques used were effective in improving the column confinement and in reducing the concrete bulging at the column sides. Regarding the crack pattern several 45^{o} cracks were observed at first yield. The number of cracks increased and cracks from the push and pull loading crossed forming a diamond shaped pattern at the middle of the column and zigzag shapes near the edges.

Mukherjee et al. (2004) presented the mechanical response of concrete columns confined with FRP composites. Practical columns often deviate from axisymmetric conditions due to noncircular cross section, geometric imperfections, and loading eccentricities. This study discusses these complicating effects on the mechanical behavior of columns confined with FRP. Experiments have been carried out to examine the effects of geometric and loading imperfections on columns of various shapes. A model originally developed for axisymmetric situations has been extended to include the complicating effects. An analytical study for the corner radius that avoids concentration of stress is carried out. The theoretical models have been verified with the present and published experimental results.

Said and Nehdi (2004) studied the effect of beam-column joint rehabilitation techniques using FRP. They presented forces and stresses in interior beam-column joints as shown in Figure 2.4. A full-scale code-conforming beam-column joint was made and tested under reversed cyclic load to serve as a benchmark for this comparison. Enhancements imparted to substandard beam-column joints by FRP rehabilitation techniques in terms of strength, ductility and energy dissipation gains are

assessed. They found that FRP joints repair schemes generally enhanced the performance of substandard joints, but they often came short of satisfying current standard level performance, and that different rehabilitation strategies can be adopted depending on the type of joint deficiency and the purpose of the rehabilitation scheme.

El-Amoury and Ghobarah (2002) presented experimental results of tests carried out on plain RC and GFRP reinforced RC beam-column joints, the possibility to avoid the shear failure of the joint through the externally bonded composite reinforcement and forcing the plastic hinge to form by flexure at the beam end. In addition, they strengthened the bottom part of the beam end in such a way to integrate the existing non-adequately anchored steel reinforcement. The latter GFRP sheets reduced fixed-end rotation effects improving the sub-assemblage stiffness. In all the retrofitting schemes, steel plates and angles were used for avoiding the composite sheets debonding as shown in Figure 2.5 and 2.6.

In another study by ***Li et al. (2001)***, the RC beams were strengthened with externally bonded CFRP sheets. One beam is strengthened in flexure only, and four others are strengthened in flexure and in shear. The authors found that for the strengthened beam, the ultimate strength also significantly increased in comparison with the normal beam. The experimental results indicated that the beam strengthened in both flexure and shear had a slight advantage, in ultimate strength, in comparison with the beam strengthened in flexure.

The technique of strengthening of RC structures with externally bonded FRP was investigated by ***Kachlakev and Mccury (2000), Triantafillou (1998) and Al-Sulaimani et.al. (1994)***. The RC beams are strengthened with externally bonded FRP sheets both in flexure as well as shear zone. They studied the effect of the shear strengthening of RC beams on the stress distribution, initial cracks, crack propagation, and ultimate strength. It was observed that stiffness increases on increasing the FRP sheet area at the flank, and strengthening the entire lateral faces of the beam is not necessary. For the strengthened beam, the ultimate strength significantly increased in comparison to the normal beam. The experimental results indicated that the beam strengthened in both flexure and shear had a slight advantage, in ultimate strength, in comparison with the

beam strengthened in flexure only. The beams failed mainly as a result of diagonal tension cracking.

Khalifa et.al. (1998) and Carlin (1998) studied shear strengthening with FRP and proposed design algorithms to compute the contribution of FRP towards the shear capacity of RC flexural members as shown in Figure 2.7 and 2.8. They suggested two design approaches to calculate the contribution of external CFRP sheets towards the shear capacity of RC structures. The first design approach was based on the effective FRP stress as a function of stiffness and ultimate strain. This is suitable only if failure is controlled by FRP sheet rupture. The second design approach was based on the bond mechanism between the FRP sheet and the concrete. The effective width of the FRP sheet at delamination is considered. This design approach is valid only for FRP continuous sheets or strips.

The research by ***M'Bazaa et al. (1996)*** was based on optimizing the length and orientation of the CFRP to increase beam strength and ductility. Eight beams were minimally reinforced with steel and over- designed for shear to cause a flexural failure. One beam was used as a control while the others were bonded with three layers of CFRP. The sheets varied in length and orientation of the fibers. Four had unidirectional fibers with different lengths, and the other three had various fiber directions with regard to the longitudinal direction. The results of the experiment showed an increase in strength and stiffness and a decrease in deflection as compared to the control beam. All failures occurred at a load at least 57% higher than the control beam. The stiffness was similar until the cracking moment. At this point, less deflection was observed in the repaired beams. The load versus deflection plots exhibit three different section modulus; the start of the experiment to first crack, first crack to yielding of the steel began, and yielding of the steel to failure of the member. The use of small angle, off-axis laminates and different CFRP sheet lengths had no effect on strength or stiffness of the repaired beams. However, the off-axis CFRP provided improved warning of failure due to cracking sounds.

Naaman and Jeong (1995) developed a new definition for the measurement of the ductility index. The conventional definition, which is based on yielding of the

reinforcement, is inappropriate for evaluating concrete beams that are reinforced with FRP. This is due to the inability of most FRP materials to yield. The new definition is expressed with a ratio of the total energy of beam and the elastic energy released at failure. This index is applicable to concrete beams reinforced with steel tendons, FRP tendons, or a combination of both. To evaluate the proposed ductility index, a series of 24 prestressed concrete beams were studied. The results showed the FRP prestressed concrete beams have less ductility than that beams with steel strands. Also, the proposed ductility index accurately predicted the ductility of the beams.

Shahawy et al. (1995) assessed the effectiveness of external reinforcement in terms of the cracking moment, maximum moment, deflection, and crack patterns. Four beams were tested using minimum steel reinforcement and varying the layers of unidirectional CFRP. Also, nonlinear finite element computer model was used to compare to the results of the experiment. The cracking moment of the CFRP repaired beams was much larger than that of the control beam. For one, two, and three layers of GFRP, the cracking moment increased 12%, 61%, and 105%, respectively. The maximum moment also became larger and corresponded well to the theoretical data. A 13%, 66%, and 105% increase was observed for the three different layers. This showed the CFRP behaved similarly before and after cracking of the beam. The deflection and cracking patterns showed results similar to experiments previously discussed. The deflection decreased inversely with the number of CFRP layers on each beam. This, alternatively, caused the stiffness to increase. The cracking patterns between the control and the CFRP repaired beams exhibited different patterns. The control had wider cracks while the repaired beams showed smaller cracks at relatively close spacing. This shows an enhanced concrete refinement due to the CFRP.

Norris and Saadatmanesh (1994) cast thirteen RC beams for flexural tests to compare three different fiber-epoxy systems and several orientations of fiber. The beams contained close to the minimal amount of steel reinforcement and were over-designed against shear. Some beams were pre-cracked before the application of the CFRP to see if pre-cracking caused any substantial differences in behavior. Two types of fiber were tested with 0, 90 and 45 orientations, and the third fiber was used with

orientations of 0/90 and 45 with respect to the longitudinal axis. The same fiber weight was applied to every beam. The research showed little difference in the results between the fiber types or the behavior between pre-cracked and un-cracked beams, but the different fiber orientations provided amiable results. The unidirectional fibers yielded the largest strength and stiffness increase and deflection decrease with respect to the control beam. These beams failed very abruptly due to the peeling-off of the CFRP. The 0/90 fibers had a maximum strength which was 20% less than the unidirectional, but showed much more ductility and deflection. They also failed less explosively than the unidirectional fibers. A 45% decrease in strength and stiffness occurred with the 45 laminate compared to the 0 orientation. However, the 45 laminate experienced much more ductility than the other lay-ups. Failure of the beam applied with 45 laminate acted in such a slow, ductile manner that loading had to be stopped.

Norris et al. (1994) concluded that off-axis CFRP laminates need to be studied at length. Use of different orientations could increase the strength and stiffness of concrete beams without causing catastrophic, brittle failures associated with unidirectional laminates. Also, they may provide ductile yielding properties that are very important in the civil engineering field.

Moment, stiffness, and deflection models of reinforced concrete beams with applied FRP were developed by ***Bhutta (1993)***. Glass, carbon, and kelvar fiber reinforced plastics were utilized. Beams reinforced with kelvar showed the highest increase in moment capacity and stiffness, while the smallest was the beams reinforced with glass. The moment capacity of beams reinforced with carbon fell between these two composites.

Unidirectional and bi-directional GFRP sheets bonded to concrete beams using epoxy adhesive and a combination of epoxy and bolts were investigated by ***Dublois et al. (1992)***. A series of specimens reinforced with steel in the tension region and shear reinforcement consisted of one of the following lay- ups for the GFRP: (a) Bi-directional sheets with epoxy bonding, (b) Bi-directional sheets with combination epoxy and bolt bonding, (c) Unidirectional sheets with epoxy bonding, and (d) Combination of unidirectional and bi-directional sheets with epoxy and bolt bonding. The

unidirectional sheets increased the ultimate load by 58% over the control beam, while the bi-directional laminate resulted in a 32% increase. However, the maximum load was reached with a combination of the two sheets. The maximum load of this specimen was 77% larger than the control beam. The two bonds used with the bi-directional sheets caused very little difference in the ultimate load. The beam bonded with the inclusion of bolts only increased the ultimate load 2% as compared to the epoxy-bonded beam. Additionally, a larger specimen, strengthened using the combination of the two GFRP sheets, was tested. Similar to the previous results, the maximum load increased 66% over the control beam. Due to the GFRP sheet, the ductility of all the beams decreased along with the deflection at maximum load.

An et al. (1991) developed a model to predict the stresses and forces of a RC beam with externally applied GFRP. Their study was based on five assumptions: (a) linear strain distribution throughout the beam, (b) small deformations, (c) tensile strength of concrete was ignored, (d) shear deformation was ignored, and (e) perfect bond between concrete and GFRP. Using classical flexural theory and strain compatibility, affects of variables such as material strength, modulus of elasticity, and reinforcement ratios of the steel and GFRP were compared with experimental results of a previous test. The behaviors of the beams were predicted with reasonable accuracy using the model.

Ritchie et al. (1991) tested sixteen RC beams with minimum steel reinforcement to study the effects of external strengthening using three different types of FRP; glass, carbon, and aramid fibers. The beams were tested in flexure under four-point loading. Also, an analytical model was developed to predict the strength and stiffness of the FRP strengthened beams. The results showed an increase in stiffness from 17% to 99% and an increase in strength of 40% to 97% based on the type, amount, and orientation of FRP that was applied to the beam. Also, the predicted and actual behavior showed good agreement, except that the analytical model predicted a slightly stiffer response than was achieved during the tests. They also investigated anchorage methods for the FRP. Since the beams in the initial tests failed at the ends of the FRP plate instead of at the constant moment region, a series of anchorage types were developed in hopes to shift the failure to the constant moment region. The first consisted of anchoring the

ends of the plate with fiberglass angles. This led to a larger load capacity, but the failure was still located at the ends of the plate. The second method consisted of wrapping FRP plates around the beam at the ends. This type also raised the load capacity, but was unsuccessful in transferring the failure to the constant moment region. The final method consisted of extending the plates up to the supports. This method was very successful in both increasing the load capacity and shifting the failure to the constant moment region.

The static strength of RC beams strengthened by gluing GFRP plates to their tension flanges was experimentally investigated by ***Saadatmanesh and Ehsani (1991)***. Five rectangular beams cross-sections and one T-beam were tested to failure under four-point bending. The measured load versus strain in GFRP plate, steel rebar, extreme compression fiber of concrete, and the load versus deflection for the section at mid-span of the beams were plotted and compared to the predicted values. It was found that the flexural strength of RC beams can be significantly increased by gluing GFRP plates to the tension face. In addition, the epoxy bonded plates improved the cracking behavior of the beams by delaying the formation of visible cracks and reducing crack widths at higher load levels.

Triantafillou and Deskovic (1991) studied the short term mechanical behavior of a pre-stressing technique. The technique involved external bonding of pre-tensioned FRP composite sheets on the tension zones of structural elements. Analytical model was developed for describing the maximum achievable pre-stress level so that the FRP system does not fail near the anchorage zones. Both adhesive layer and beam material failures were considered. It was found that the method's efficiency is improved by increasing the thickness of the adhesive layer and/or increasing the area fraction of the composite material; efficiency being defined as the level of pre-stress at the bottom fiber of the member. Moderate to high pre-stress levels are achieved depending on whether failure of the system is controlled by the shear strength of the beam material or that of the adhesive layer. The technique is applicable to the rehabilitation of existing structures as well as the construction of new ones.

Triantifillou & Plevris (1991) used strain compatibility and fracture mechanics to

analyze RC beams applied with externally bonded CFRP. The same assumptions were used with the inclusion of a rectangular compression stress distribution in the concrete at failure. The applied moments that would cause each of the three failure modes were predicted. The failures were yielding of the steel reinforcement followed by CFRP rupture; yielding of the steel reinforcement followed by the crushing of the concrete compression zone; and concrete crushing before either tensile component fails. These models were compared with experimental studies and deemed creditable.

Barecchia (nd.) used FRP materials for the seismic upgrading of existing RC structures. His experimental setup and results are shown in Figure 2.9 and 2.10 respectively. He presented that the global behavior of framed structures equipped with composite materials under seismic loads has been successively examined. The comparison between the experimental and numerical results gave good results. The experimental data allowed confirming the numerical studies, showing an increase of global ductility and the capacity of FRP to increase both strength and stiffness.

2.3 DAMAGE DETECTION AND VIBRATION MONITORING OF STRUCTURES

Most damage indices available have been developed from research in the earthquake engineering community. During an earthquake, a structure is expected to experience inelastic response. Consequently, it is possible to measure factors such as ductility and dissipated energy. A measure of damage or a damage index is required to make a rehabilitation decision. This information helps interpret the stiffness changes the parameter estimation procedures identified. A damage index, often normalized to a fixed scale for structural integrity, is an essential criterion in the damage assessment process.

Baghiee et al. (2009) studied damage and CFRP strengthening of RC beams by vibration monitoring. They focused on the use of mode shapes and their derivatives. The Modal Assurance Criterion and Coordinate Modal Assurance Criterion factors were used to detect damage. These factors were derived from mode shapes and modal curvatures. They found that the modal assurance criterion was subjected to very small

change by damage or strengthening. The coordinate modal assurance criterion factors might detect the changes in beam stiffness at degree of freedom.

Brehm et al. (2009) presented a mode selection strategy that enhanced the pure mathematical modal assurance criterion by physical information in terms of modal strain energies of the numerically obtained mode shapes. They found that the energy based modal assurance criterion leaded to a more reliable mode assignment. The modal assurance criterion approach indicated a sensitivity of bearings, which disappeared when the energy based criterion was applied.

Failure mode control is significantly affected by material randomness, presence of non-structural components and quality control. Variations of mechanical properties depend on the construction material utilized. ***Kwon and Elnashai (2006)*** found that values of coefficients of variations for material properties are generally lower than 15-20% and are often negligible compared to the randomness of both seismic input and quality control. In the past it has been extremely difficult to develop equations to predict the level of damping in real-life structures, and so designers were generally only able to conduct a dynamic analysis once the structure had been built using non-destructive testing. Despite the wealth of damping research undertaken in a huge variety of research areas, there remains to be found: (a) a consensus regarding basic damping levels in reinforced and pre-stressed concrete beams; (b) clarification of the mechanisms that affect in- service damping; and (c) an accurate prediction methodology to estimate real-life damping levels in concrete beams at any stage of their service life. In this review, concrete damping research has been broadly classified into the three main categories of material, member and structure damping.

Dincal, S. (2005) investigates the performance of an existing structural damage detection method (SDIM) when only experimentally-obtained measurement information can be used to calculate the frequency response function used to detect damage as shown in Figure 2.11. The development of a SDIM that can accurately identify damage while processing measurements containing realistic noise levels and overcoming experimental modeling errors would provide a robust method for identifying damage in the larger, more complex structures found in practice. The

existing SDIM program uses an advanced genetic algorithm, along with a 2-D finite element model of the structure, to identify the location and the severity of damage using the linear vibration information contained in FRF as response signatures. Datagen is a Matlab program that simulates the 3-D dynamic response of the four-story, two-bay UBC test structure. The dynamic response of the structure can be obtained for a range of preset damage cases or for any user-defined damage case. Therefore, using the FRF measurements obtained from the UBC test structure allows for a more realistic evaluation of the performance of the SDIM provided by GaDamDet as the impact on performance of more realistic noise and model errors can be investigated. Previous studies evaluated the performance of the SDIM using only simulated FRF measurements obtained form a 2-D structural model. In addition, the disparity between the 2-D model used by the SDIM used to identify damage and the measurements obtained from the 3-D test structure is analyzed. The results indicate that the SDIM is able to accurately detect structural damage to individually damage members or to within a damaged floor, with little false damage identified. The SDIM provides an easy to use, visual, and accurate algorithm and its performance compares favorably to performance of the various damage detection algorithms.

An experiment on a three-story frame structure was conducted by ***Jian et.al. (2005)*** to obtain vibration test data in 36 damage cases. Using four steel columns and three slabs, a shear type frame structure was fabricated with bolted connections. The structural model had acceleration sensors installed for each slab and a strain gauge on the bottom of column near ground level. They simulated column damage on different levels. An impact force was applied on the slab of the third layer to excite structural vibration. Thirty-seven sets of dynamic vibration response data were acquired by a dynamic test system for undamaged structure and three damaged structures. The structural natural frequencies were obtained by Fourier Transform from the first three natural frequencies. It was found that the natural frequencies changed little because of structural damage. A neural network based multi-sensor information fusion was proposed to achieve identification of damage occurrence, damage localization and damage quantification, respectively.

A neural network based-approach for structural health monitoring was presented by ***Kao (2003)***. The proposed approach involved two steps. The first step, system identification, uses neural network to identify the undamaged and damaged states of a structural system. The second step, structural damage detection, uses neural networks to generate free vibration responses with the same initial condition or impulsive force. The inputs of the neural network are usually structural responses in time or frequency domain, or structural modal parameter (frequency, damping ratio, and mode shape), and the outputs are usually the damaged levels of members in the structure. He presented that change in structural properties (stiffness and damping) cause changes in periods and amplitudes of the free vibration of the structure system. Therefore, periods and amplitudes of the free vibration are useful indices to reflect changes of structural properties. The proposed approach makes it easy to accurately generate a free vibration response of an unknown structure system using neural networks.

Maia et al. (2002) present the subject of damage detection in structures. A series of numerical simulations on a simple beam are made in order to compare various damage detection methods based on mode shape changes. A generalization of these methods to the whole frequency ranges of measurement is proposed, i.e. methods based on mode shape changes become based on operational mode shapes. The objective of such a study is to ascertain the possibility of using various damage detection methods without the need for modal identification. He has developed some simple methods and tools based upon the use of FRF, which seem promising and have given good results in some practical applications. He also presented a new approach of FRF-based methods.

Burgueno et al. (2001) studied dynamic characterization of a full scale FRP composite bridge prototype of the Kings Storm Water Channel Bridge. Their research addressed the results of the modal vibration tests, and compared results as part of an assessment into its eventual use as a standardized non-destructive health monitoring. The test setup for the three girder deck and the results are show in Figure 2.16. They found that the modal vibration studies were a quick, effective, and relatively inexpensive, method for determining the dynamic structural properties. The modal vibration test data were successful in determining the changes in structural behavior due to changes in boundary conditions, as well as structural degradation or damage caused by loading.

Pagnini and Solari (2001) found that the availability of experimental data on the damping of steel poles and tubular towers is extremely rare. In response to this, full-scale testing was conducted, where it was found that damping, increased considerably with motion amplitude. From this overview of structural damping, it may be concluded that a wide range of different concrete structures have been studied by many different researchers. Most significantly the studies indicate that it is difficult to undertake a meaningful dynamic analysis without in-depth knowledge about the damping of the individual structural components.

Boroschek and Yáñez (2000) obtained strong earthquake motion and ambient vibration records of 22-storey high Chilean buildings. The data was used to determine damping ratios for the whole structure and to add to the database used for the dynamic modelling of a Chilean building's response to seismic actions.

Formenti, D. (2000) presented the sources of variations in FRF measurements on steel beam. An FFT spectrum analyzer was used to simultaneously measure two FRF measurements, the excitation point and direction was in different directions. The experimental test setup and results are presented in Figure 2.12 and 2.13. The results indicate that the test setup allowed for fairly repeatable measurements with the possible exception being the result for Mode 3 of the low force excitation. The peak amplitude of this mode had the largest variation of FRF. However, the rest of the results were very repeatable in terms of the two levels of excitation and the resulting peak FRF amplitude.

Ndambi et al. (2000) found from RC beam tests that damping increased with excitation amplitude, and that modal damping ratios were highly influenced by non-linear effects, and are, therefore, highly subjective and difficult to estimate.

Damping capacity experiments of small plain mortar beams were undertaken by ***Wen and Chung (2000)***. It was found that damping increased three-fold with the embedment of steel reinforcing bars into the mortar. Damping was also increased by at least two orders of magnitude with the addition of silica fume.

Using data collected from a 78-storey high-rise building in China***, Fang et al. (1998)***

developed an empirical equation to predict the value of damping at high amplitudes of vibration in RC buildings.

Bracci et.al. (1997), evaluated the seismic performance and retrofit of existing low-to-midrise RC buildings. The proposed technique was applied to a one-third scaled model of a three story RC frame building, which was subjected to repeated shaking table excitations. The same was later retrofitted on the interior columns using a pre-stressed concrete jacking with additional longitudinal and transverse reinforcement. The retrofitted model building was then experimentally tested on the shaking table for same excitations. The nonlinear static load-deflection behavior curve was typically established from a pushover analysis, and it was compared with the estimated site specific elastic response spectrum earthquake demands.

Most previous experiments have been done with dynamic excitations. Parameter estimations can be performed in either time or frequency domain to obtain structural parameters with identified or measured modal properties. Directly using dynamic testing data in the time domain prevents further contamination resulting from data processing. ***Ibrahim and Mikulcik (1997)*** developed the algorithm that uses free vibration response of a structure to determine its modal parameters.

Denoon and Kwok (1996) and ***Glanville et al. (1996)*** developed and installed equipment for the measurement of the dynamical response of an 84 m high RC control tower. The focus of the investigation was on the effects that different wind turbulence regimes, natural frequencies, mode shapes and structural damping, have on the code specified serviceability criteria for human comfort.

As a minimum input, structural parameter identifications require some structural response measurements to static or dynamic loads. ***Doebling et al. (1996)*** summarized current damage identification methods using measured vibration data. Figure 2.14 shows typical excitations and outputs of a parameter identification system. Structural responses to controlled or operating excitations are combined within the parameter identification system to produce either structural modal estimates or structural element parameter estimates. When controlled excitations are used, the excitation information can be added in the parameter identifications; however, a more practical approach is to

perform structural parameter identifications with unknown operating excitations. Figure 2.15 shows that structural parameter identification can be classified into problems with and without mathematical models. Then the mathematical models are subdivided into static and dynamic models. The static model is further divided into displacement and rotational measurements and strain measurements. The dynamic model is divided into time domain and frequency domain. Structural parameter identification with no mathematical models is subdivided into neural network, signal processing, pattern recognition, and expert systems.

Prion H.G.L. and Rezai M.K. (1996) have done model testing, using ambient and impact vibration methods. The comparison of vibration measurements before and after the cyclic tests revealed a significant shift in the fundamental frequencies and mode shapes of the frame in longitudinal and transverse direction for both the undamaged and damaged stages.

Sanayei et al. (1996) studied the effect of measurement noise on the parameter estimates, and the researchers proposed a heuristic best-in-worst-out method for the preselection of static forces and displacement measurements based on error sensitivity analysis.

Full-scale experimental data was collected by ***Suda et al. (1996)*** on the dynamic properties of 123 steel structure buildings and 66 RC buildings in Japan. It was found that the damping ratio is dependent, to varying degrees, on building height, foundation height, building usage, vibration amplitude and type of damping evaluation method. Despite the large amount of collected data, the authors were unable to develop any relationship between damping and these variables.

Aktan and Helmicki (1995) performed a study to explore the issues and advancement of knowledge in instrumented monitoring of a full-scale bridge. When impact testing may not be the appropriate method (such as for buildings, large bridges, large facilities with complex geometry, or structures subjected to lateral loads), forced-excitation modal testing using larger vibrators may be required.

Farrar and Cone (1995) determined that damage to a bridge superstructure must be significant before the global dynamic properties are affected. ***Stubbs et al. (1995)*** located the damage in the Rio Grande Bridge by successfully using the first few dynamic modes, a baseline structure, and pattern recognition.

Ghanem and Shinozuka (1995) evaluated four of the most popular methods for time domain parameter estimations with experimental data in a laboratory. Based on the expertise required for each method and the quality of the estimated results, the method of recursive least square with exponential memory was found to be the most promising.

Hjelmstad et al. (1995) developed a robust time-domain estimator using velocities and displacements derived from the measured accelerations. This method can accommodate structural responses sampled incompletely in time, state, and space, and it is applicable to complex structural systems.

Lutes and Sarkani (1995) assessed the effect that building foundations have on the damping characteristics of an entire structure in a parametric study. It was suggested that the two separate dynamic characteristics of both the structure and foundation should be merged to obtain a mathematical expression for the whole system.

Pierce and Dowding (1995) reported on a long-term monitoring method for RC bridge piers using Time Domain Reflectometry (TDR). This method focused on the determination of internal cracking and large local deformations caused by earthquakes. To use the method, coaxial TDR cables must be embedded in the concrete during construction or retrofitting. The cables were placed in critical areas such as the column/base connection. The cables were selected as either extension sensitive or shear sensitive. If localized extension or shear occurred along the length of any cable, it could be identified as a reflector using the TDR external electronics.

Salawu and Williams (1995) reported a study of the forced vibrations of a bridge before and after repair. The test results demonstrated the changes in natural frequency induced by the repair; however, the magnitude of the changes is quite small, on the order of 2 percent.

Brownjohn (1994) examined published suspension bridge damping databases in order to determine the primary factors contributing to the damping characteristics exhibited by suspension bridges. In practice, this is extremely difficult because a suspension bridge is comprised of friction and bearing joints, construction joints, hysteresis damping in wire hangers, aero-dynamic damping and foundation damping. Therefore, determining the overall damping cannot be defined by a small set of certain factors, such as material or dimensions alone.

Casas and Aparicio (1994) presented a methodology for the use of dynamic response as an inspection and surveillance tool for RC beams. Dynamic response was measured by acceleration transducers. The experimental verification clearly shows the effectiveness of the proposed method in the identification of location, extension, and amount of cracking when some important requirements concerning the dynamic data recorded are taken into account. The experimental tests were performed on four types of RC beams with simply supports. Cracking was simulated by means of formwork dispositions during concrete pouring at different positions. Vibration is measured using accelerometers or acceleration transducers located at mid-span and quarter-spans. The dynamic excitation is induced by means of an impact hammer at that quarter-point of the beam, where no accelerometer is located. Several modes are excited and after the transient response, the damped free vibrations of the beam were recorded. It was found that the measurement of only the fundamental frequency in not enough to distinguish the causes of modification in the original value of simple beam. Only one frequency can lead to erroneous conclusions with respect to location, extension, and amount of cracking.

Farrar et al. (1994) studied the I-40 Bridge over the Rio Grande River in Albuquerque, NM, with both FEM and experimental data. The researchers concluded that the analytical and measured resonant frequencies or modal shapes were not sensitive to the damage through the plate girder.

Finno and Prommer (1994) studied the impulse response method for inaccessible drilled shafts under pile caps. Several drilled shafts connected together with concrete grade beams were tested using the nondestructive IR method. Based on the field data, it

was found that shaft heads that were more rigid (because of larger or several grade-beam connections) exhibited greater signal attenuation, and become more difficult to evaluate.

Pandey and Biswas (1994) presented a damage detection and location method based on changes in the measured flexibility of the structure. The method was applied to several numerical examples and to an actual spliced beam where the damage was linear in nature. Results of the numerical and experimental investigation show that estimates of damage condition and location of the damage could be obtained from just two measured modes of the structure. ***Pandey et al. (1991)*** reported a component evaluation technique based on dynamic responses to a hammer impact on the component of interest. Results were confirmed with laboratory models, but field verification was limited and did not produce conclusive results.

Samtani et al. ***(1994)*** found that 2-D stress elastic-plastic finite element analysis underestimates the pier resistance to ship impact because it does not account for the wedging resistance in the plane strain analysis and the side friction on the out-of-plane sides of the caissons. They presented a methodology that helps extrapolate 2-D models to account for 3-D effects. Further research is needed in this area.

Woodward et al. (1994) conducted dynamic tests for a full-scale bridge subject to artificially induced fatigue cracking of vertical cuts in a main girder. Preliminary field test results showed that the changes in dynamic characteristics due to the damage were detected, but only when the maximum amount of damage was inflicted.

The most common full-scale experiments on damping in RC structures have been conducted on bridges and buildings. Generally, the intent is to develop damping databases that assist structural designers in assigning nominal damping values in a dynamic analysis. Assigning damping values is not easy to achieve because the fundamental knowledge about essential damping mechanisms of individual structural components is not yet fully understood. ***Lagomarsino (1993)*** found that the mechanisms which produce dissipation during oscillation in a building are varied in nature and include: (a) damping intrinsic to the structural material; (b) damping due to friction in the structural joints and between structural and non-structural elements; (c)

energy dissipated in the foundation soil; (d) aerodynamical damping; and (e) passive and active dissipation systems.

Warren and Malvar (1993) used a falling weight deflectometer to assess structural conditions of RC piers. By comparing the deflected shapes from the FEM and testing results, the local stiffness and soft areas of the piers were determined. The FEMs of the piers were generated from the design data and drawings using a commercial software package called Automatic Dynamic Incremental Nonlinear Analysis (ADINA). The differences between a rating of ideal and actual testing data were resolved by the systematic changes of the stiffness parameters based on matching dynamic responses of the FEMs to the measured data. This method was demonstrated on a real bridge with timber piles in New Jersey. Because the bridge geometry was well known, it was deemed sufficient to identify the effective stiffness of the piers and damaged areas.

Raghavendrachar and Aktan (1992) successfully conducted a multi-reference impact testing on a reinforced concrete slab bridge. This pilot study demonstrated that a multi-reference impact testing could serve as the main experimental component for comprehensive structural identification of large constructed facilities. If an accurate measure of flexibility (displacement divided by force as a function of frequency, that is, the inverse of stiffness) is to be obtained directly from the experimental data, demanding standards are required for modal testing designs.

Yao et.al. (1992) conducted experiments using strain mode shape for the purpose of structural diagnosis using a shaking table as source of input excitation. The test model was a one-bay, five story X-braced steel frame. Beams and columns were I-shaped steel members. The bottom of the column of the test structure was welded to the base plate, which was then bolted to the foundation. Six accelerometers were installed on the structure, one on every floor and one at the base, to measure the translational acceleration. They were aligned along the center of the beam span. Six damage configurations were intentionally created on the modal structure. These damage configurations consisted of two specimen groups, where in one group had loosened connection bolts and other group had damaged cross-section area of member. The time domain data acquired were processed by software to calculate FRF. The results

indicated no detectable natural frequency change for beam-column when connection bolts were loosened. But the natural frequency changed when cross section of member was damaged.

Lim (1991) determined that damage is most easily detected for the elements that are fully participating in load bearing and contain the most energy. Damage in such elements appears in the parameter estimation results. If there is a system wide change in the estimated parameters, individual element damage cannot be isolated.

Hajela and Soeiro (1990) proposed the idea of dominant displacements for both static and dynamic testing, indicating that certain forces and responses are more representative of the structural system. They also showed that errors are more prevalent when loading does not result in an equal stress distribution in each of the structural elements. In a related paper, they showed through the experimental results that a uniform stress loading produces excellent results.

The investigation by ***Mazurek and DeWolf (1990)*** involved laboratory model tests to evaluate the detect ability of aluminum highway bridge structural degradation through measured vibratory response. The dynamic characteristics were determined from FRF plots, which were measured directly from a vibrating structure using digital signal processing equipment and fast Fourier transform. Two accelerometers were used, one being the reference accelerometer and the other the field accelerometer. The reference accelerometer remained at one location during the course of testing, while the field accelerometer was moved from station to station as data was collected. After the measurement was completed, data was transferred to a computer for subsequent processing. It was found that the ambient vibration method provides nearly the same results as the conventional impact hammer approach for resonant frequency and mode shape determination, but clearly overestimates damping. The model permitted the examination of various failure modes, thereby providing an indication of how the dynamic properties are consequently affected. The types of structural deterioration considered included support failure and crack propagation.

Beck (1989) proposed a statistical system identification procedure that used averaged response measurements to estimate the structural model parameters. ***Gangadharan et***

al. (1991) proposed a probabilistic system-identification method to infer structural model parameters of flexible joints.

Uncertainty in modeling and algorithms is inevitable, and further study in performing successful parameter identifications is needed. ***Brown (1987)*** developed a parameter identification procedure to estimate structural model parameters using measured responses and expert judgment. Fuzzy updating was used to supply subjective information when numerical measurements were unavailable.

Bridge superstructure condition evaluation research programs generally have focused on two primary areas: ultimate load tests and dynamic tests. An excellent reference on dynamic testing for modal vibration measurement and analysis is given by ***Ewins (1985).*** For the ultimate load tests, the bridges that were slated for removal from service were tested to failure. These studies generally provided some insight on the ultimate load capacity and mechanisms of failure that could be used in the future. On the other hand, laboratory and field studies to evaluate dynamic properties of bridges and relate them to condition assessments have been reported extensively in past years.

Salane et al. (1981) reported dynamic tests of a bridge for detecting structural deterioration caused by girder fatigue cracks. A concrete deck on steel girders was loaded with an electro-hydraulic actuator system up to 465,000 load cycles. Accelerometers were used to determine damping ratios, frequency contents, and impedance at various stages during the loading. The testing results indicated increases in damping ratios with cycles of loading, presumably caused by cracking, and a decrease in amplitude at resonant frequencies, as well as a 20 percent to 40 percent change in computed stiffness coefficients.

Natke and Yao (1980) developed a damage-detection method based on multiple data sets where each set was obtained from different locations on a structure. ***Stubbs and Osegueda (1990a and 1990b)*** developed a theory using changes in modal properties in beams, plates, and shells to detect damage. The validity was demonstrated with cantilevered specimens with known damage.

Bertero and Bresler (1971), ***Park and Ang (1985)*** and ***DiPasquale et al***. ***(1990)*** have expanded their element damage indices to structural system damage indices with the use of weighting functions. To determine the integrity of a full structural system, the local damage indices for each element in the structural system can be combined with a Monte Carlo analysis to determine the probability of a structure's failure. Nondestructive bridge condition assessment is performed either by visual inspection or with controlled or operating excitation, and it requires elastic structural responses. In a bridge management system, engineers commonly conduct visual inspections to assign a damage index to a bridge. Similarly, structural identification results must be interpreted on a comparable scale in a bridge management system.

Researchers ***Newmark and Rosenblueth (1971), Yao and Munse (1962)*** and ***Chung et al***. ***(1988)*** developed damage indices based on ductility ratios, cumulative damage, and component damage. Because of the redundancy of engineered structures, the damage estimate obtained for a simple structural element does not necessarily correspond to the damage sustained by the structural system.

2.4 FINITE ELEMENT MODELING OF RETROFITTED STRUCTURES

Barbato et al. (2009) studied the efficient FE modeling of RC beams retrofitted with FRP. This study presents a new simple and efficient 2-D frame FE able to accurately estimate the load carrying capacity of RC beams flexural strengthened with externally bonded FRP strips and plates. The proposed strengthened beam considers distributed plasticity with layer-discretization of the cross sections in the contest of a force based formulation. The FRP beam element is able to model collapse due to concrete crushing, reinforcing steel yielding, FRP rupture and FRP debonding. The strengthened beam is used to predict the load carrying capacity and the applied load mid span deflection response of RC beams subjected to three and four point bending loading. Numerical simulations and experimental measurements are compared based on numerous tests available in the literature and published by different authors. The numerically simulated responses agree remarkably well with the corresponding experimental results. The major features of this frame FE are its simplicity, computational efficiency and weak

requirements in terms of FE mesh refinement. These useful features are obtained together with accuracy in the response simulation comparable to more complex, advanced and computationally expensive FE. Thus, the strengthened beam is suitable for efficient and accurate modeling and analysis of flexural strengthening of RC frame structures with externally bonded FRP sheets and for practical use in design oriented parametric studies.

Camata et al. (2007) investigated experimental and analytical RC members strengthened in flexure by FRP plates. Both mid span and plate end failure modes are studied. In the experimental work, four RC members were cast, two slabs and two beams. Out of these four members, one slab and one beam were tested as a original members and the other one slab and one beam were tested as a strengthened member. Same work can be done analytically. These RC were modeled and analyze through the FE method. The FE analyses are based on nonlinear fracture mechanics. The FE model considers the actual crack pattern observed in the testes. The FE model uses both discrete and smeared crack discretization, because only a combination of the two crack model accurately traces the stiffness degradation of the strengthened members. The smeared crack mode was used for the beam concrete; the discrete crack model was used for the interfaces where delamination can be expected. The FE investigations were carried out using a 2-D plane tress representation of the actual test specimens. The specimen was discretized using three-node triangular elements for the concrete matrix, the FRP and the resin, Line-to-line four-node interface elements were used for the interfaces and two-node truss elements for the steel reinforcement. The concrete continuum was modeled using a smeared crack model. This approach describes the crack evolution using a stress-strain law. The smeared crack model implemented in the program is based on a rotating crack concept, which allows the crack to align with the principal strain directions. The principles of the smeared crack model are that cracking occurs when the principal stress exceeds the tensile strength. Cracking is normal to the direction of the principal stress and the material softens in the post-peak regime. The strengthening of the RC beams was done with both CFRP and GFRP and notice the difference between these two materials. This paper shows how concrete cracking, adhesive behavior, plate length, width and stiffness affect the failure mechanisms. The numerical and experimental work gave several results show that debonding and

concrete cover splitting failure modes occur always by crack propagation inside the concrete. For short FRP plates, failure starts at the plates end, while the longer FRP plates, failure starts at mid span. A comparison between CFRP and GFRP strengthening with the dame axial stiffness but different contact area shoed that increasing the plate width increases greatly the peak load and the deformation level of the strengthened beam. The FRP reinforcement width to RC member width ratio is important to determine whether the strengthened member fails due to either debonding or concrete cover splitting. The lower this ratio, the lower the probability of concrete covers splitting. The analyses also indicated that an important parameter is the distance between flexural and shear cracks.

Ferracuti and Savoia (2006) studied the numerical modeling for FRP concrete delamination. A nonlinear bond-slip model is presented for the study of delamination phenomenon. This research showed that FRP retrofit could be very useful to improve the behavior of the RC structure under both short term and long term service loadings. A nonlinear interface law is adopted; the bonding between FRP plate and concrete is modeled by a nonlinear interface law. A nonlinear system of equations is then obtained via finite different method. Newton-Raphson algorithm, different control parameters can be adopted in the various phases of delamination process (alternatively, force or displacements variables). Some numerical simulations are presented, concerning different delamination test setups and bond lengths. The numerical results of this study agree well with experimental data reported in the literature. A nonlinear shear stress-slip law is adopted for the method is used to solve the nonlinear system of governing equations. It is also shown that, adopting classical delamination test setup, snap-back behavior in the load-displacement curve occurs for bonded plate lengths greater than the minimum anchorage length.

Perera and Recuero (2004) studied the adherence analysis of FRP strengthened RC beams and discussed the effect of bonding between RC and CFRP when epoxy adhesive is used. They compared the analytical and experimental results which came out from the works can be done in this paper. A test had been designed to characterize the behavior of the adhesive connection between FRP and concrete; the test was based on the beam test, similar to the adherence test for steel reinforcement of concrete. In the same way, a

numerical model based on finite elements has been developed to simulate the behavior of RC members strengthened with FRP plates. The nonlinear response of the strengthened members is determined through the development of numerical material nonlinear constitutive models capable of simulating what happens experimentally. The results came out from this study was in the experimental tests, a local failure occurred mainly determined by high shear bond stresses transmitted to the concrete from the plates via adhesive. Debonding started at the mid span at the concrete blocks ends and propagated from there to the intermediate areas of the blocks. Therefore, it can be concluded that the shear bond stresses play a fundamental role in strengthening of RC beams with FRP plates. While in the analytical work, the model consider the position and increased of concrete cracks which has a very important influence on the overall response of the strengthened beam; it also affects the distribution of the stresses in the various locations of the member and the failure mechanism. In general, the model performs reasonably well in predicting the behavior of the FRP strengthened beam.

Supaviriyakit et al. (2004) performed analytically the nonlinear FE analysis of RC beam strengthened with externally bonded FRP plates. The FE modeling of FRP strengthened beams is demonstrated in this paper. The key for success of the analysis is the correct material models of concrete, steel and FRP. The concrete and reinforcing steel are modeled together by 8-nodes 2-D isoparametric plane stress RC element. The RC element considers the effect of cracks and reinforcing steel as being smeared over the entire element as shown in Figure 2.17. Concrete cracks and steel bars are treated in a smeared manner. The FRP plate is modeled by 2-D elastic element. The epoxy layer can also be modeled by 2-D elastic elements. Stress-strain properties of cracked concrete consist of tensile stress model normal to crack, compressive stress model parallel to crack and shear stress model tangential to crack. Stress-strain property of reinforcement is assumed to be elastic-hardening to account for the bond between concrete and steel bars. FRP is modeled as elastic-brittle material. The objective of the test was to investigate the effect of the bonded length on peeling mode of FRP. The results obtained from his analytical work that the finite element analysis can accurately predict the load deformation, load capacity and failure mode of the beam. It can also capture cracking process for the shear-flexural peeling and end peeling failures, similar to the experimental as shown in Figure 2.18.

Yang et al. (2003) conducted an experiment on FE modeling of concrete cover separation failure in FRP plated RC beams on the tension side of the RC beam. This paper deals with a fracture mechanics based finite element analysis of debonding failures. This study investigates the behavior of an FRP plated RC beam using a discrete crack model based on FEA. Linear elastic fracture mechanics was used in this study and on-going research is being undertaken to extend this to use non-linear fracture mechanism. In this research, only half of the beam was modeled accounting for its symmetry. Four node quadrilateral isoparametric elements and three node constant strain elements were used to model the concrete, adhesive and CFRP plate. The internal steel reinforcements were modeled using two-node truss elements. The concrete was modeled by near square elements to simplify the remeshing process. The concrete cover on the tension face was modeled using four layers of elements. Both the adhesive and the CFRP plate were modeled using one layer of elements. The results obtained from this study, in a preliminary study was successfully simulated the concrete cover separation failure mode in FRP strengthened RC beams. Initial numerical results confirmed that the bonding of a plate leads to smaller and more closely spaced cracks spaced cracks than the un-strengthened beam. For plated beam, the cracking can have a significant effect on the stress distribution in the FRP plates. The stress distribution is uniform in the constant bending moment span only before major cracks are developed or close to the ultimate state. The length of the plate has a significant effect on the failure mode. The numerical example showed that if all other parameters remain unchanged, a beam strengthened with a short plate is more likely to fail due to concrete cover separation and in a more brittle manner.

Lord and Ventura (2002) obtained the modal parameters of a high rise building of a 48 storey building in Vancouver using ambient vibration. The experimental results and the analytical results from FE model were studied. ETABS was used to develop a detailed FE model of the building for modal updating purpose. The modal assurance criterion was used to correlate the results obtained from experimental results and FE results, and showed with confidence that the mode shapes found were the actual structural mode shapes of the structure. A good correlation was achieved between the ambient vibration data and the FE model.

Kachlakev et al. (2001) investigated the structural behavior of Horsetail Creek Bridge, with and without FRP laminates; and established a methodology for applying computer modeling to RC beams and bridges strengthened with FRP laminates. Figure 2.19 shows loading and support locations. They found that the general behavior of the FE models represented by the load-deflection plots at mid-span show good agreement with the test data from the full-scale beam tests. However, the FE models show slightly more stiffness than the test data in both the linear and nonlinear ranges. The effects of bond slip and micro-cracks occurring in the actual beams were excluded in the FE models, contributing to the higher stiffness of the FE models. Figure 2.20 and 2.21 show FE model of beam and FE evolution of crack patterns. The final loads from the FE analyses are lower than the ultimate loads from the experimental results by 5% - 24%. This is probably due in part to neglecting the inclined portions of the steel reinforcement; ignoring the effects of concrete toughening mechanisms; and using assumed materials properties values instead of measured values. The crack patterns at the final loads from the finite element models correspond well with the observed failure modes of the experimental beams, and the crack pattern predicted by the FE analysis for the flexural strengthened beam agrees with hand calculations showing that the beam fails in flexure.

Ramsey (1983) discussed two popular parts of structural dynamics technology; the experimental portion and the analytical portion, which is referred to as FE analysis. He presented a comparison between test data acquired from the modal test of some hardware using FFT analyzer and numerical FE modeling results. The FRF measurement was used to identify structural resonances as shown in Figure 2.22. The effects of damping and stiffness to the dynamic response of a structure are shown in Figure 2.23 to 2.25 respectively. He found that structural dynamics modification method accurately represented the change in measurement frequencies when stiffness of structure increases. The FE model correctly predicted the changes in mode shape and frequency but underestimated the results. Finally, FE results of first mode were close in frequency to the test structure.

2.5 CLOSURE

As per the work done by earlier researchers, there are many available developed procedures which are based on measuring change of nonlinear behavior, dynamic characteristics, or other structural properties before and after the occurrence of natural hazards. The concept of structural health monitoring is rapidly growing to enable early identification of damage and provide warning for unsafe conditions. Current evaluation methods and the damage detection of structures vary according to the materials used in the construction of the building.

The traditional approaches to retrofit by addition of braced frames and shear walls operate on existing building stiffness and strength. A wide range of strategies are available for reducing the seismic risk inherent in an existing building. In some cases there are difficulties in using braced frames or shear walls to retrofit an existing building. Another solution involves the use of advanced materials like FRP, which are popular for strengthening of RC components. Since FRP have very high tensile strength, shear resistance capacity, strength to weight ratio, and increased resistance to corrosion, they eliminate the need for scaffolding, which can reduce labor costs. This research is concerned with retrofitting the RC structures using FRP material. It should be noted that the use of advanced materials like FRP for RC structural repair and strengthening applications has been studied extensively in previous research. However, most of the studies of strengthened structural elements have reported only load-defection behaviors and bond failures in composite overlay. But for retrofitted structures, the damage position and crack propagation is not generally known under service loads or natural hazards because cracks are covered by layers of strengthening material. Thus, for the purpose of assuring safety, structural health monitoring using dynamic characteristics is necessary to define the damage changes in material or geometric properties of the retrofitted structures. The purpose of this research is to study this type of monitoring, including non-linear behavior of the structures involved.

a)

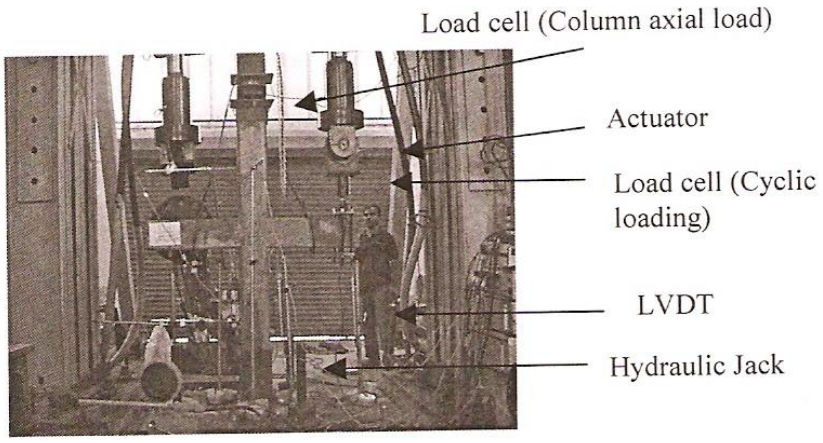

b)

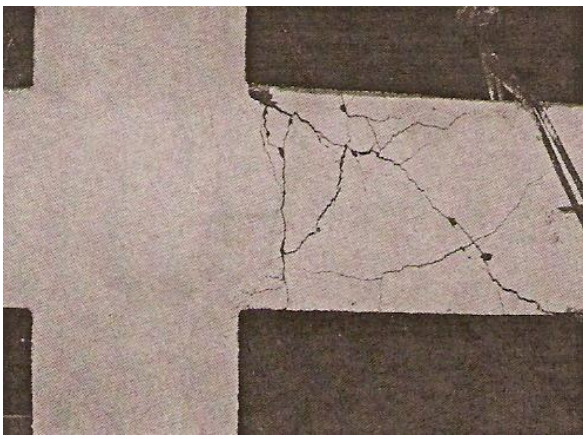

c)

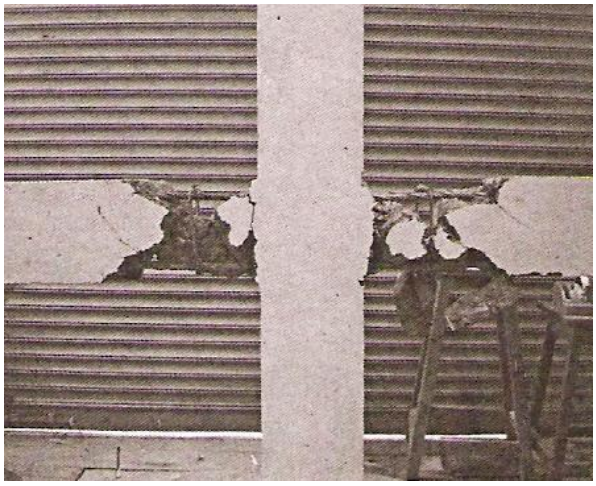

Figure 2.1 a) Experimental test setup, b) and c) crack patterns of beam-column joints (Mukherjee and Joshi, 2005)

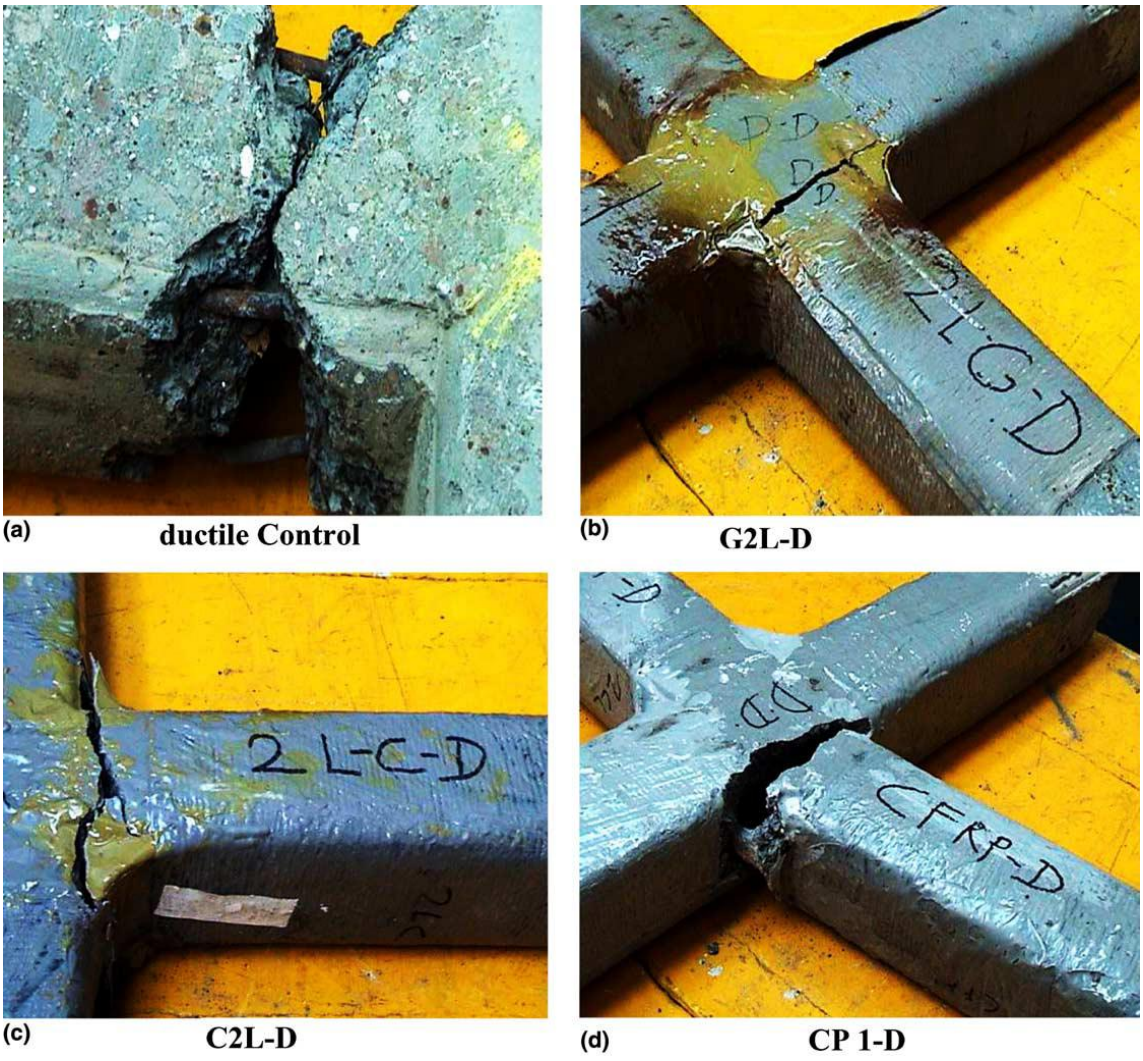

Figure 2.2 Crack patterns of retrofitted beam-column joints (Mukherjee and Joshi, 2005)

a)

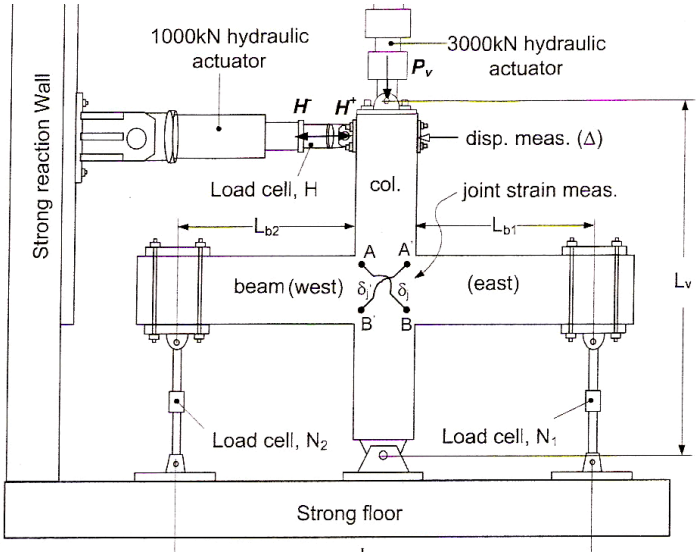

b)

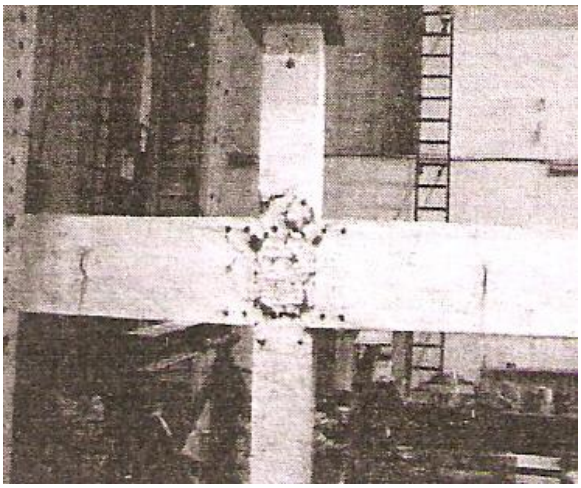

c)

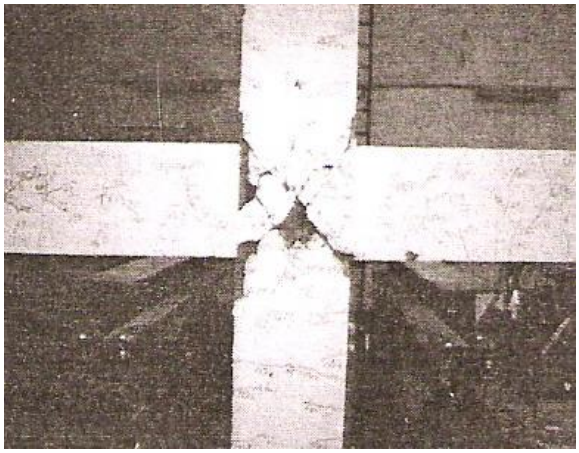

Figure 2.3 a) Experimental test setup, b) and c) crack patterns of beam-column joints (Chih and Hsu, 2009)

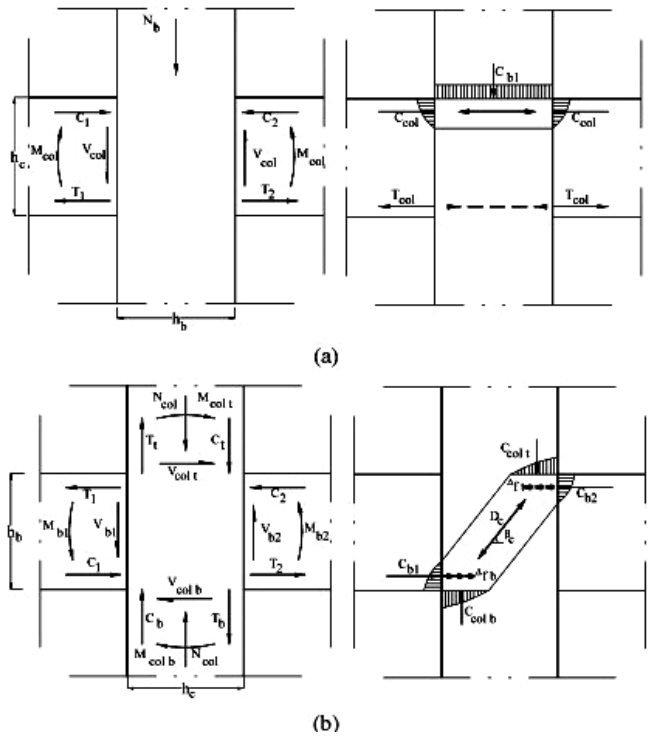

Figure 2.4 Forces and stresses in interior beam-column joints (Said and Nehdi, 2004)

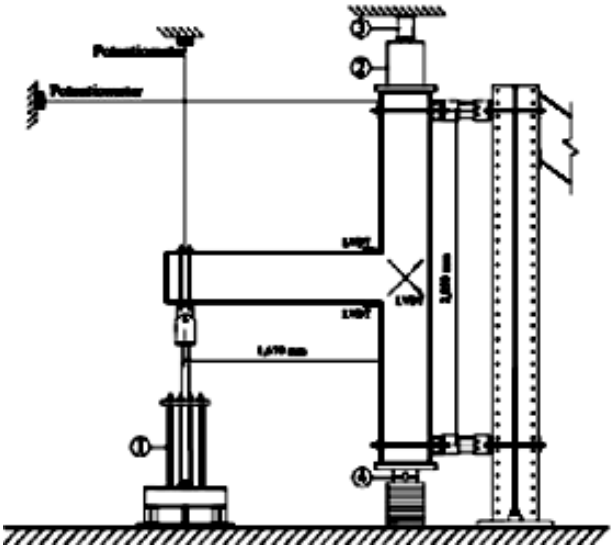

Figure 2.5 Test set up carried out by El-Amounry and Gobarah (2002)

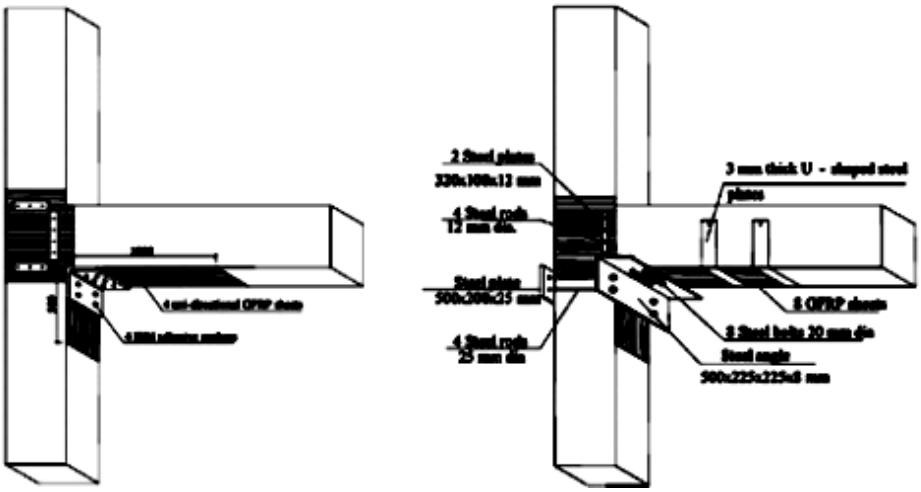

Figure 2.6 The retrofitting schemes carried out by El-Amounry and Gobarah (2002)

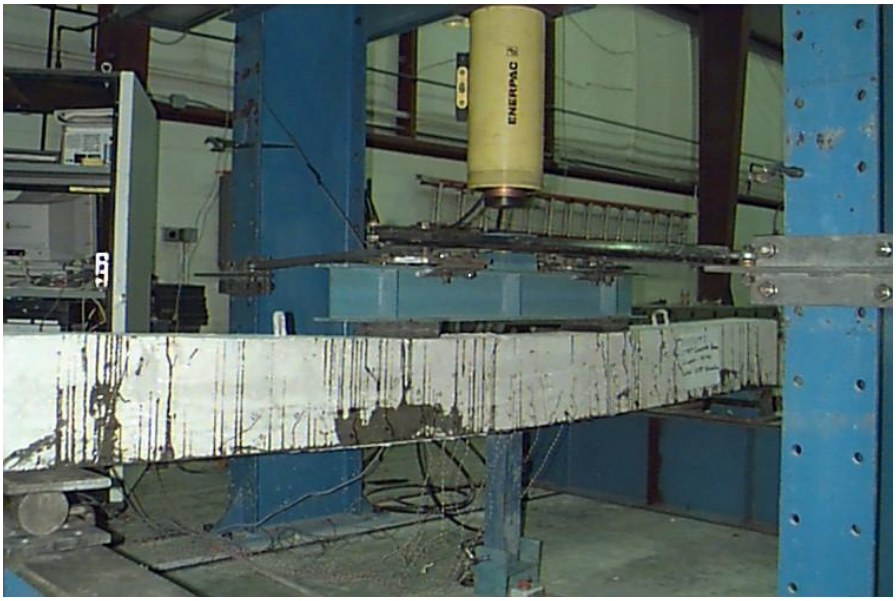

Figure 2.7 Hydraulic Load Frame (Carlin, B. P., 1998)

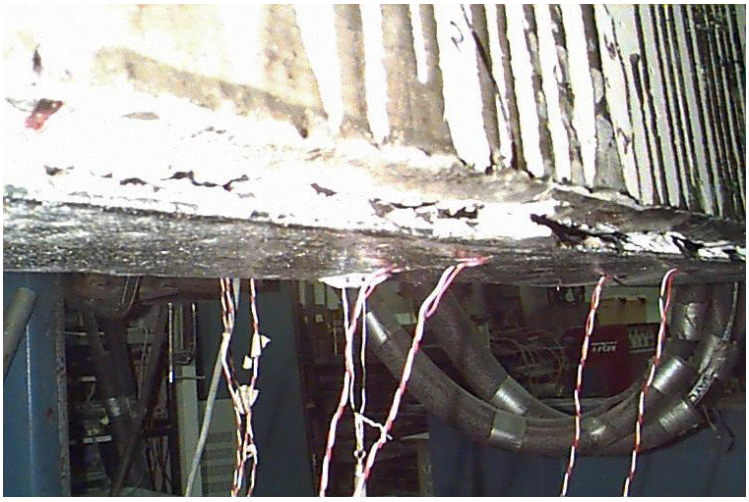

Figure 2.8 Debonding of the CFRP (Carlin, B. P., 1998)

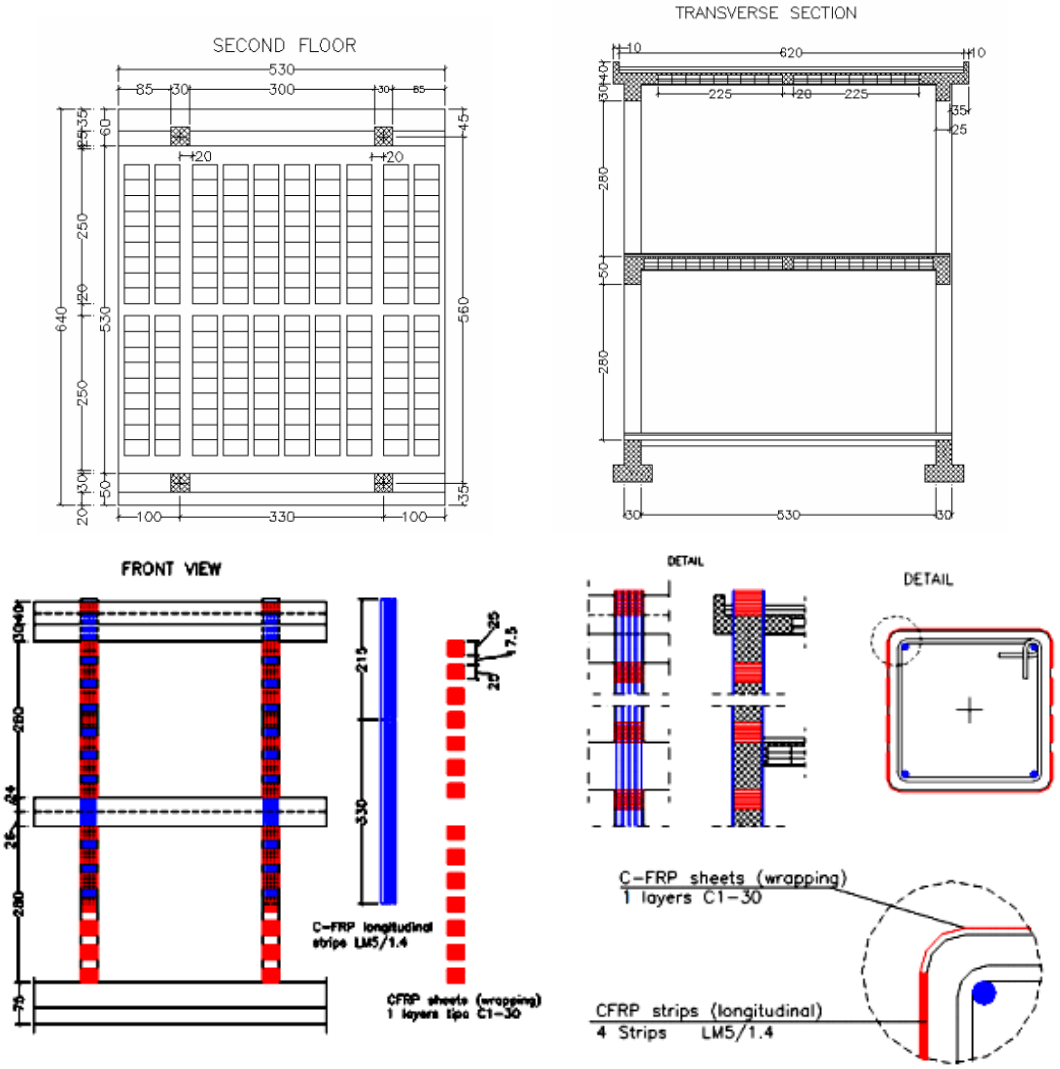

Figure 2.9 Geometry of the structure under investigation (Barecchia., nd.)

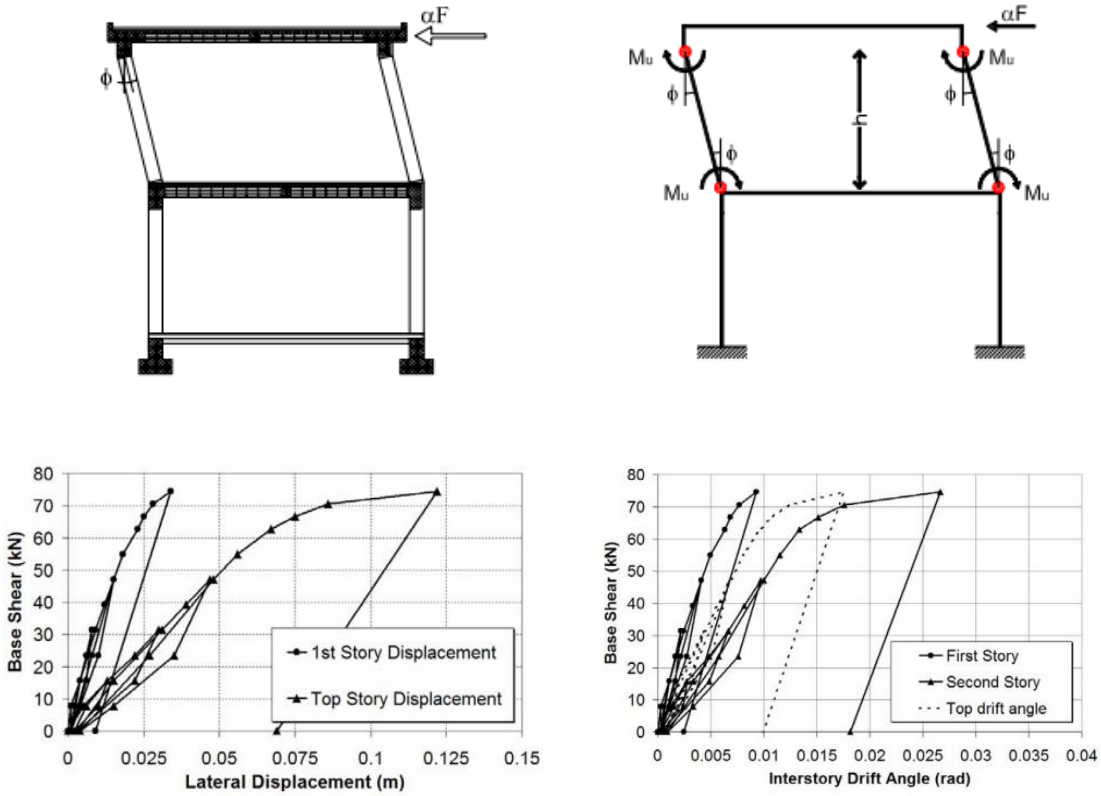

Figure 2.10 Results of the pushover test. (Barecchia., nd.)

a)

b)

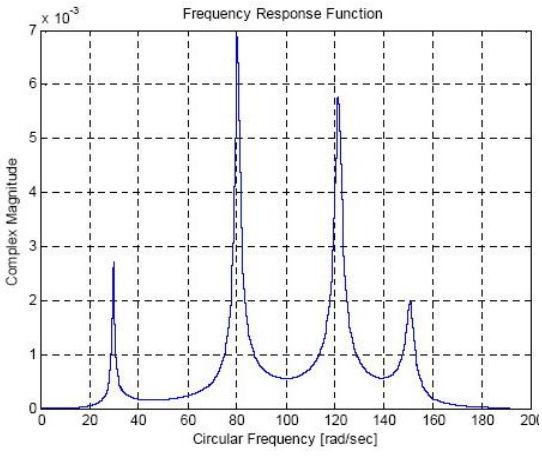

Figure 2.11 a) Experimental setup and b) frequency response function between force input and acceleration output (Dincal, S., 2005)

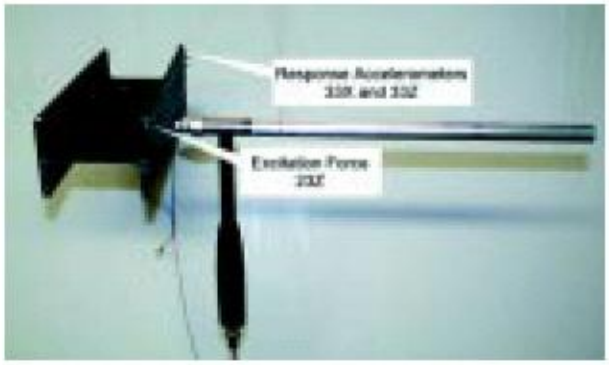

Figure 2.12 Experimental setup (Formenti, D., 2000)

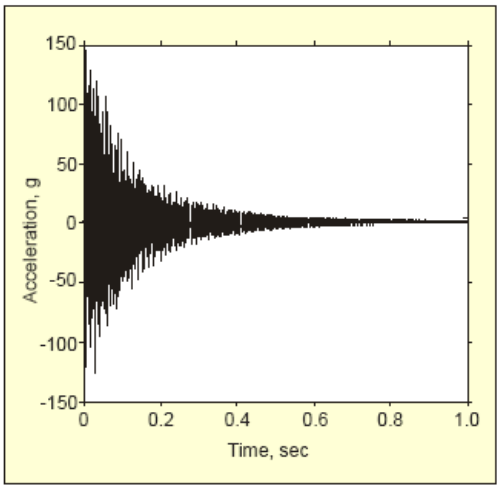

a)

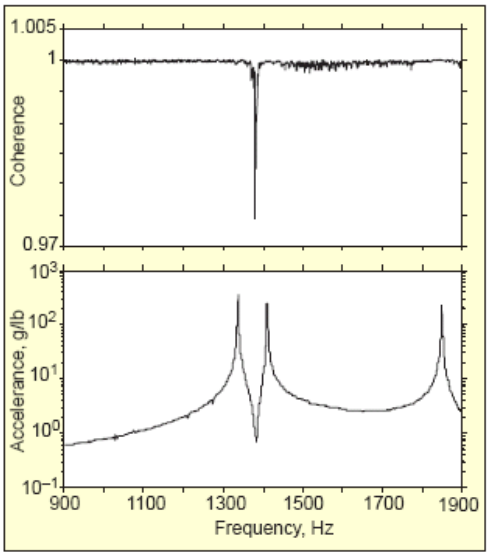

b)

Figure 2.13 Impulse response of damped structure and Typical Coherence Function and corresponding FRF (Formenti, D., 2000)

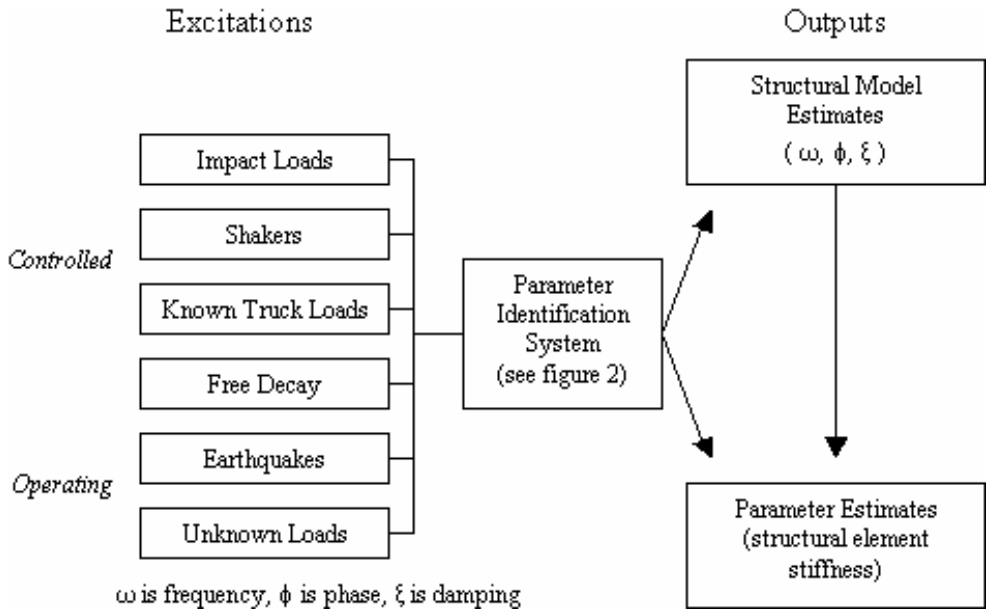

Figure 2.14 Parameter identification system excitation and output options.

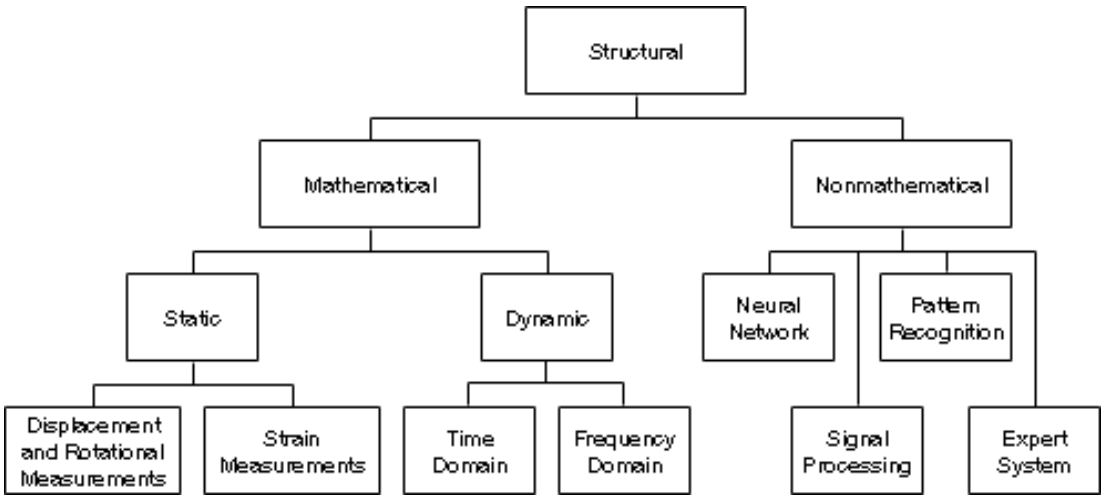

Figure 2.15 Diagram. Structural parameter-identification system tree.

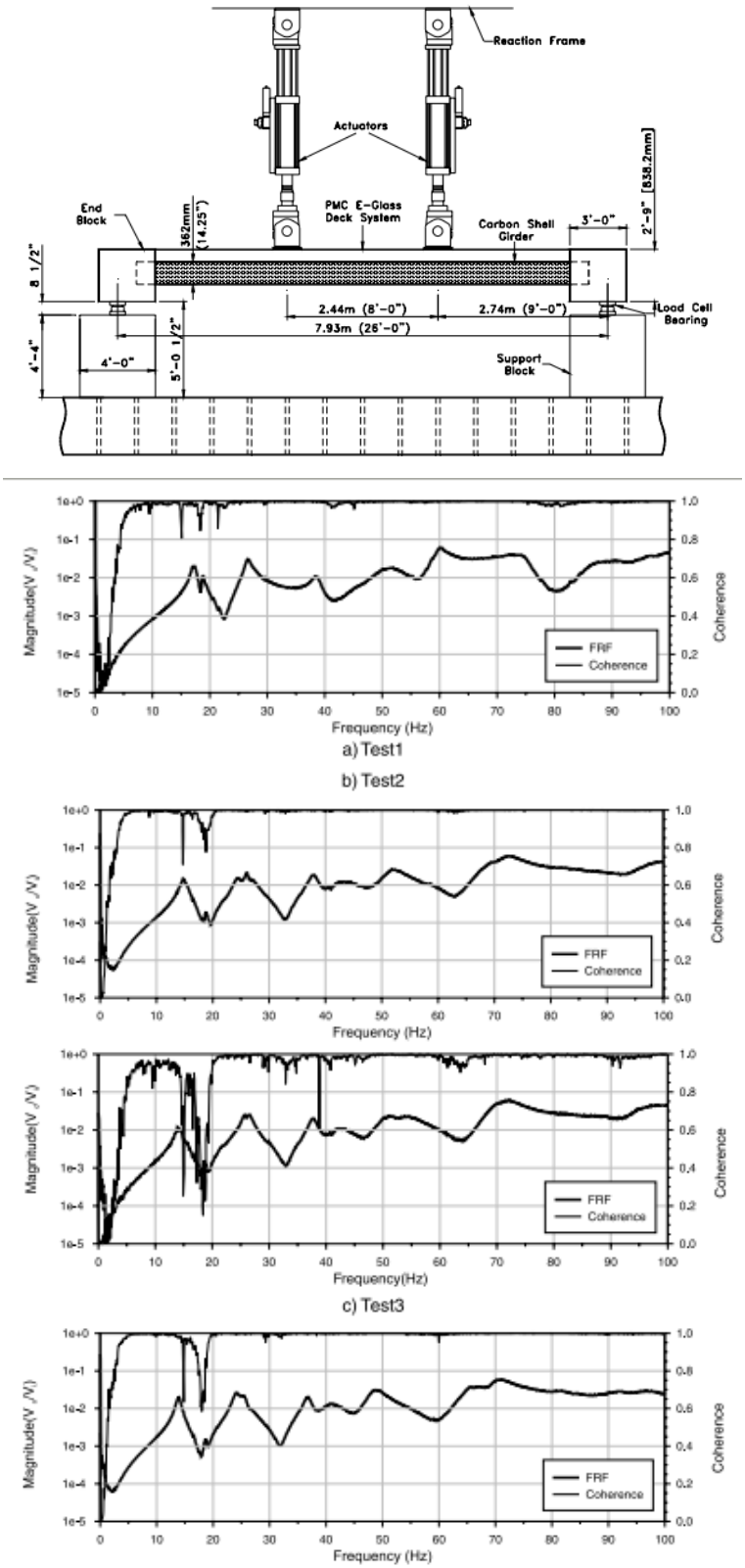

Figure 2.16 Test setup for the three-girder-deck assembly and the results of FRF and coherence. (Burgueno et al., 2001)

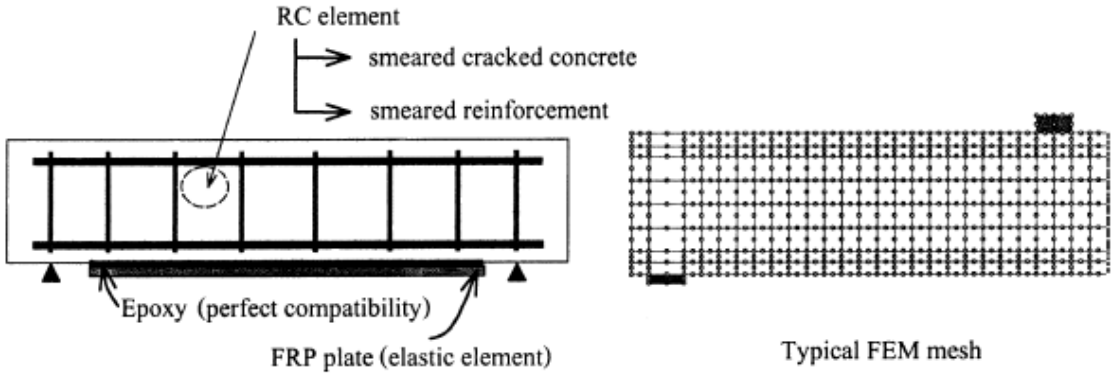

Figure 2.17 FE modeling and typical FE mesh (Supaviriyakit et al. 2004)

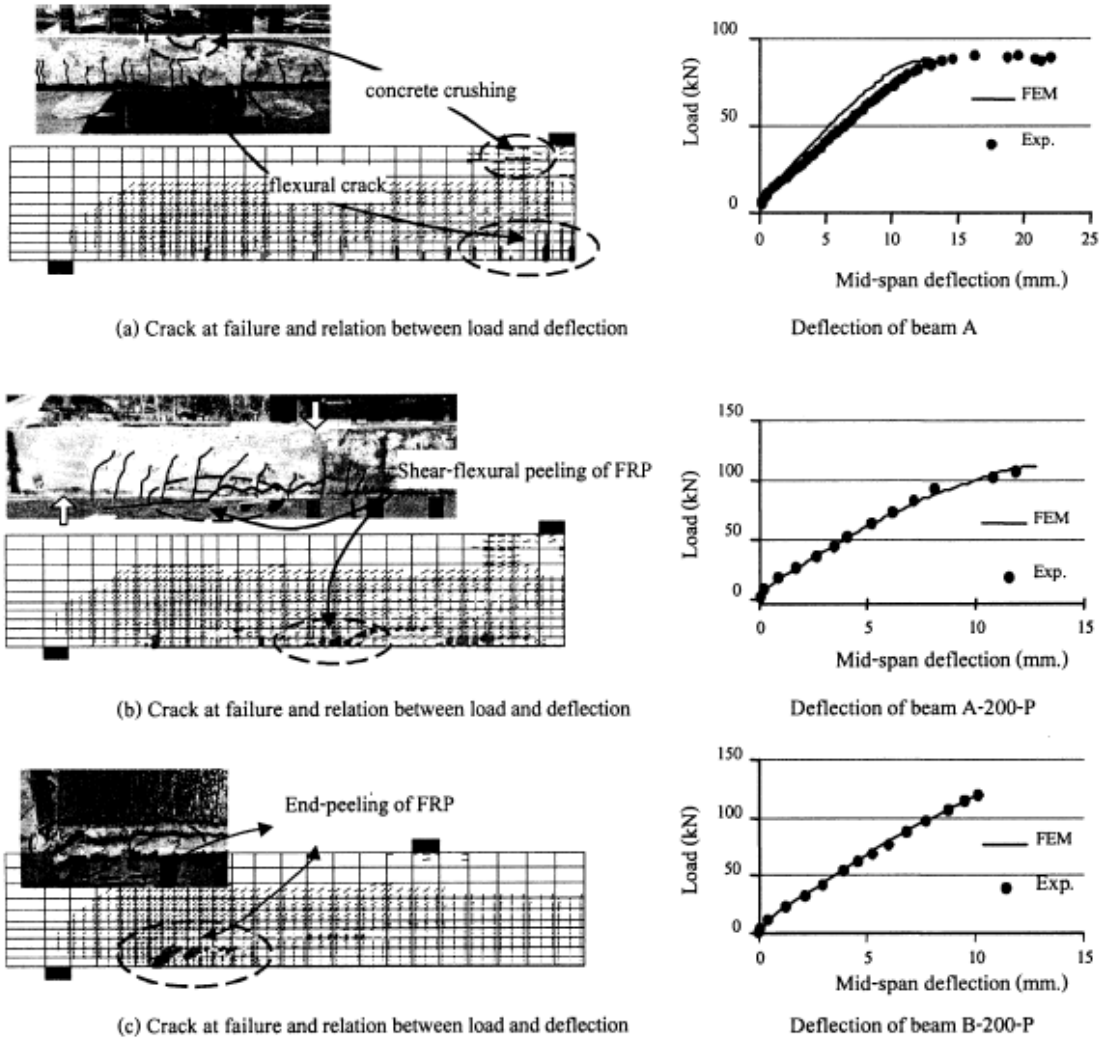

Figure 2.18 FE nonlinear analytical results of tested beams (Supaviriyakit et al. 2004)

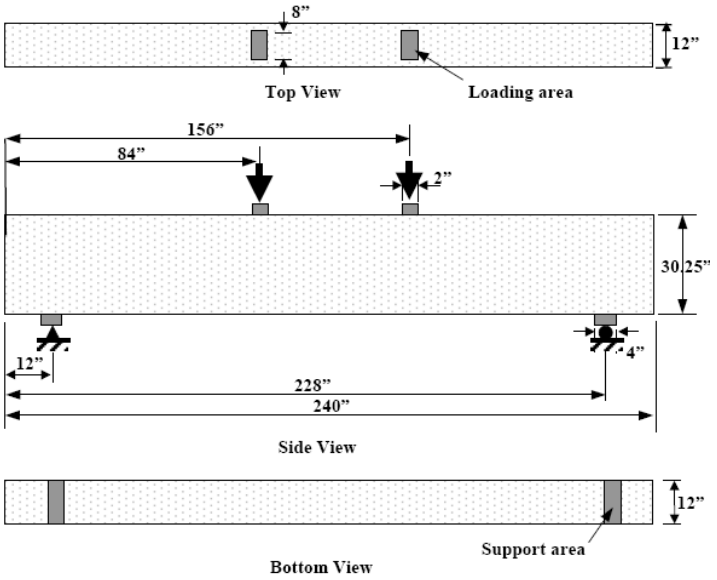

Figure 2.19 Loading and support locations (Kachlakev et al., 2001)

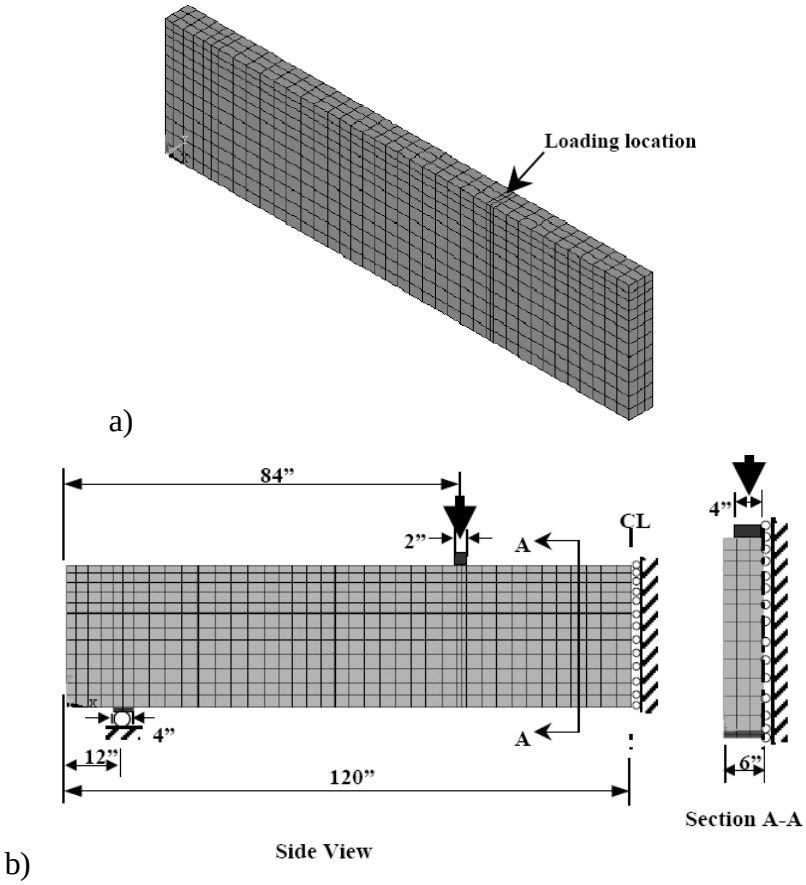

Figure 2.20 a) FE discretization for a quarter of beam and b) steel plate with line support of FE model (Kachlakev et al., 2001)

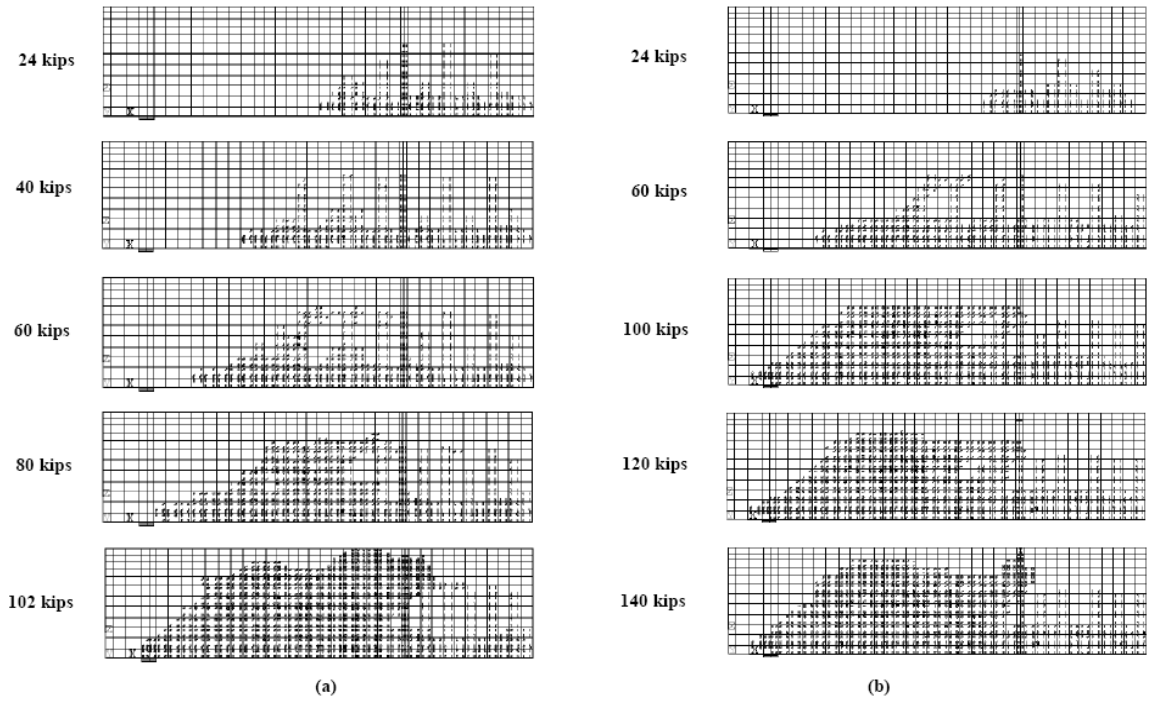

Figure 2.21 FE evolution of crack patterns of beams (Kachlakev et al., 2001)

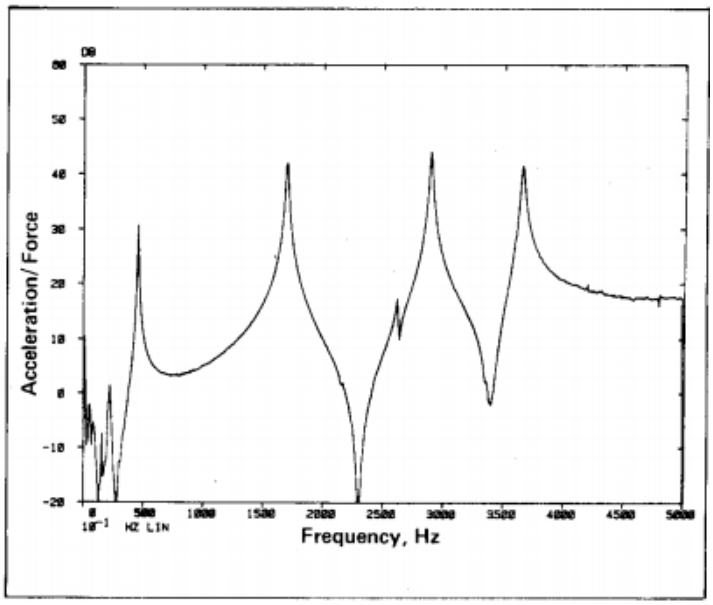

Figure 2.22 FRF measurement to identify structural resonances (Ramsey, 1983)

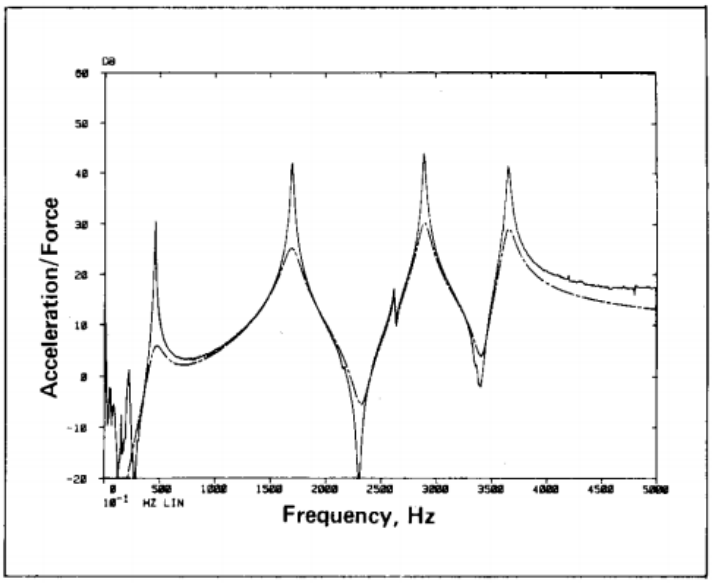

Figure 2.23 The effects of adding damping to reduce FRF of a structure at resonance (Ramsey, 1983)

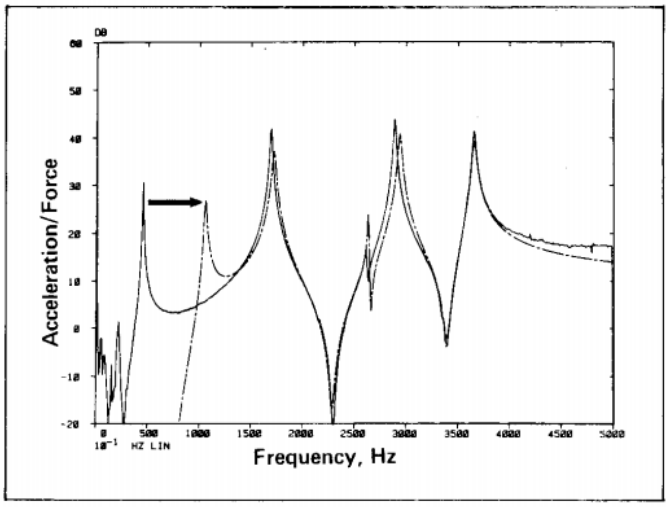

Figure 2.24 The effects of adding stiffness to reduce of FRF by shifting to higher frequency (Ramsey, 1983)

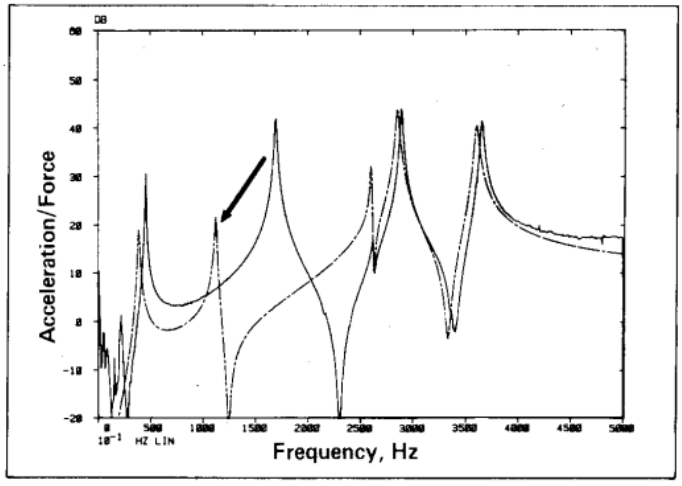

Figure 2.25 The effects of stiffness reduction to reduce of FRF by shifting to lower frequency (Ramsey, 1983)

CHAPTER 3
EXPERIMANTAL PROGRAM

3.1 GENRAL

Due to changes in building codes and ageing of existing structures, strengthening of RC structure has become a major focus of attention for structural engineers. There are various methods of repair or strengthening the damaged or below strength elements. The use of steel plate jackets and ferro-cement jackets to strengthen the structural elements has been reported earlier (Bansal et al., nd.). The application of such strengthening techniques is disruptive to the operation of the facility, labor intensive, and time consuming. One such popular technique is using FRP as wrapping material (Ghobarah and Elmandoohglal, 2004; Jain et al., 2005; Wang and Restrepo, 2001). FRP sheets with epoxy resin have received considerable attention due to their high strength, light weight, easy manageability onsite, and high resistance against corrosion. FRP material has been used successfully by many earlier researchers to increase bending and shear capacities of RC elements such as beam, column, and beam-column joints (Goyal, 2007; Memon and Sheikh, 2005; Mukherjee and Joshi, 2005). The strengthening of RC columns, which contains high percentage of transverse reinforcement, uses FRP sheets to prevent its brittle shear failure and significantly improve the displacement ductility and energy dissipation capacity (Kim, 1995).

Vibration monitoring and damage assessment of RC structures are intended to establish that sufficient strength remains to withstand the loads envisaged. Attention is mainly focused on the structural elements or connections which resist high stresses (Estekanchi and Arjomandi, 2007; Mo, 1994). In general, structural health monitoring using vibration response measurement involves positioning a set of accelerometers on the damaged elements. The vibrations induced may be monitored by comparing the frequency of the structure at different time intervals (Mazurek and DeWolf, 1990). The vibration data is generated in time as well as frequency domain. Vibration energy is distributed over a range of frequencies consisting of the fundamental frequency and combinations of the harmonics. With this technique, the defective component is identified by resolving the vibration signal into its constituent frequencies and relating

these to the known discrete frequency of the component. In this way the component's signature or thumbprint is established (Rao, 2000; Reddy et al., 1994).

Many experimental RC elements have been studied extensively under different conditions in different countries. Some researchers have investigated using only analytical approaches. But health monitoring of buildings is a problem which is neither purely experimental nor purely analytical approach. Experiments without analysis can lead to results that are difficult to interpret or understand, and there is little point in performing analysis without testing since the accuracy of the analysis cannot be verified. In the present work, considering these reasons, whole scaled RC frame models were constructed in the laboratory and tested under controlled conditions to assess their damage state.

The experimental program has been devised so as to assess the change in vibration behavior and study the load-displacement behavior for both control and strengthened frames. At level of increasing damage, vibration responses due to impact excitation were measured. Three RC frame models have been constructed in the laboratory. Frame 1 and 2 are non-ductile structures, built without transverse reinforcement bars in beam-column joints. Frame 3 is a ductile RC structure detailed as per IS: 13920, the ductile detailing code. The material system, specimen detail and testing procedure are presented as follows.

3.2 Material Properties

All the RC frames considered in the present study have been cast with the same set of materials. The materials consist of concrete, steel reinforcements, and GFRP sheets. Relevant tests in accordance with the Indian Standard (IS) codes of practice were conducted to determine the physical properties of the materials used in the study (IS-8112, 1989; IS-1489, 1976; IS-383, 1970). The details of the materials along with their properties have been presented in the subsequent sections.

3.2.1 Cement

Cement is very often the most important because it is usually the most delicate link in the chain. The function of cement, of all the materials, is to bind the sand and stone together, and also to fill up the void in between sand and stone particles to form a

compact mass. The cement used in this study is Ordinary Portland Cement (OPC) as per IS: 8112-1989, with a specific gravity 3.142 and fineness of 5 percent (percentage retained on 90 micron sieve). Specific gravity and compressive strength test of cement is shown in Figure 3.1 and 3.2, respectively. The physical properties of cement used in the study are given in Table 3.1.

3.2.2 Aggregates

Aggregate is the matrix or principal structure consisting of relatively inert, coarse particles. The coarse aggregate is used primarily to provide bulk to the workable, uniform concrete mix. The fine aggregate also assists the cement paste in holding the coarse aggregate particles in suspension (IS-383, 1970). This action promotes plasticity in the concrete mix and prevents segregation of the paste and coarse aggregate during its transport. The properties of these particles in aggregate greatly affect the performance of concrete.

a) Fine aggregate

IS: 383-1970 defines the fine aggregate, as the one passing 4.75 mm IS sieve. The fine aggregate is often termed as a sand size aggregate. Locally available riverbed sand is used in the present study and refined of any silt. The fine aggregate used is dried sand with a fineness modulus of 2.22 and specific gravity of 2.56.

b) Coarse aggregate

The coarse aggregate is defined, as that retained on 4.75 mm IS sieve. To increase the density of the resulting concrete mix, the coarse aggregate is frequently composed of two or more sizes. Two types of aggregate with different sizes have been used in the present study. Their details are as follows:

10 mm size: Aggregate passing 10 mm sieve and retained on 4.75 mm sieve.

4.75 mm size: Aggregate passing 4.75 mm sieve and retained on 2.36 mm sieve.

The coarse aggregates used were dried and removed of any silt.

The properties of fine and coarse aggregate have been listed in Table 3.1.

3.2.3 Concrete

The M20 concrete mix has been designed as per the Indian Standard Recommended Guideline for Concrete Mix Design (IS 1489, 1982). The average 28 days compressive strength of concrete of Frame 1 is 22.46 MPa; Frame 2 is 20.48 MPa; and Frame 3 is 23.56 MPa. The concrete compressive strengths have been listed in Table 3.1.

3.2.4 Casting of specimens

Three frames, two specimens of brittle RC frames and one specimen of ductile RC frame were cast for each steel reinforcement detail. During the casting of each frame specimen, three cubes (150 mm size) were cast for each story and every frame specimen. The cubes were tested at 28 days of curing period. On the specific day of testing, after curing for the period, these cubes were tested under compression to determine the average concrete compressive strength.

3.2.5 Curing of specimens

The cubes were cured in a curing tank designed for the purpose. The tank used had heating elements and thermostats. Pumps for circulation of water were installed to keep the temperature of the water at $27 \pm 2^{\circ}C$. The curing tank is shown in Figure 3.3. The temperature of water in the tank was kept within the prescribed range for the entire period of curing. The frames were continually kept moist with wet sacking. The compressive strength test of the concrete cubes of each specimen was carried out using a universal testing machine. The testing for compressive strength of concrete cubes is shown in Figure 3.4 and 3.5.

3.2.6 Reinforcement

The longitudinal internal steel reinforcements were made of deformed bars of 8 mm and 10 mm in diameter and round bars of 6 mm diameter were used as stirrups. These reinforcement bars met the minimum steel quantity required by the Indian Standard (IS: 456-2000) for RC structure. The steel bars exhibited a minimum yield strength of 415 MPa and a Young's modulus of 200 GPa (Fe 415 grade). Table 3.1 presents the test results for reinforcing steel used. Universal testing machine and tensile strength testing of reinforced steel bars are shown in Figure 3.6 to 3.8, respectively.

3.2.7 Fiber Reinforced Polymer Sheet

Glass fiber is the most commonly used additive in reinforced polymer sheets, commonly called GFRP. It lowers warpage and reduces creep, particularly at higher temperatures. Glass fibers can vary in length and have a general diameter of 10 to 15 microns with white colour as shown in Figure 3.9. GFRP used were model Mbrace Fibre G-Sheet EU 900. This material is enveloped in MBrace Saturant resin to yield a range of high performance features. MBrace Fibre reinforcement systems include bi-directional Glass fibers as shown in Figure 3.10. G-Sheet EU 900 has a tensile strength of 3.4 GPa, modulus of 73 GPa, and density of 2.6 g/cm^3. The thickness of the GFRP was 0.34 mm. The mechanical strength of the resin was ignored. Table 3.1 presents the details of this strengthening material.

3.2.8 Composite (FRP) strengthening systems and application

The MBrace Composite Strengthening Resin System consists of the following components:

a) MBrace Primer

MBrace Primer is the adhesive used for bonding concrete with the MBrace Composite Strengthening System. It is a 100% solids and low viscosity. Epoxy resin able to cure in the presence of moisture at temperatures as low as 2°C. This strengthening system has two parts: resin and hardener. Both parts are shown in Figure 3.11. When applied to sound concrete, MBrace Primer gives high tensile bond strength to the MBrace composite strengthening system. To make it effective the work site must be thoroughly ventilated. The MBrace Primer should not be applied if the ambient temperature is less than 5°C. Only the amount of primer as can be applied within its pot life should be mixed. Mixed primer should be applied with a roller brush. If necessary a second coat can be applied when the surface is very porous. MBrace Primer must be allowed to cure until tack free.

b) MBrace Putty

MBrace Putty is one type of epoxy as shown in Figures 3.12 and 3.13. This epoxy is the concrete smoothing material used in the MBrace Composite Strengthening System. It is 100% solid, non-sag paste epoxy resin material. Its

recommended usage include sealing surfaces prior to epoxy injection, bonding of rigid materials, and leveling uneven surfaces prior to the application of the MBrace Composite Strengthening System. This composite system consists of three parts: resin, hardener, and aggregate. Only mix as much putty as can be applied within its pot life. Apply the MBrace Putty Adhesive to the substrate using a steel trowel or other suitable implement in order to eliminate surface imperfections. Application thickness and coverage rates are highly dependent on the condition and profile of the concrete substrate. Primed and smoothed surfaces should be top coated within two days to ensure proper adhesion of the MBrace Fibre Reinforcement System to the substrate.

c) MBrace Saturant

MBrace Saturant resin is shown in Figure 3.14. This composite system is the easy-to-apply, 100% solids material that permits adhesion of a lightweight sheet within the MBrace Composite Strengthening System. When cured with the top sheet, MBrace Saturant resin produces a high performance composite system for use in external structural repair or upgrade applications. The MBrace Fibre Reinforcement must be cut into prescribed sizes using scissors or cutters before the application of MBrace Saturant. The number of sheets cut shall be limited to those that can be used within a day. Apply fully mixed MBrace Saturant resin first coat to the MBrace Fiber Reinforcement surface with a roller brush. Resin saturated MBrace Reinforcement should be placed fiber side down onto the concrete surface onto which the MBrace Primer has been applied. The Fiber Reinforcement should be strongly squeezed in the longitudinal direction of the fibers two or three times using a deforming roller and rubber spatula in order to impregnate the resin into the fibers and to deform the resin coat. For joining strips of fiber sheet, a 15cm overlap length is required in the horizontal direction and 2cm overlap length in the vertical direction. Additional resin must be applied at the overlap location on top of the outer layer of fiber sheet to be overlapped. The adhered Fiber Reinforcement System should be allowed to stand for at least 30 minutes. Any lifting or dislocation that occurs during this period must be corrected using the roller and spatula. The second or overcoat of mixed MBrace Saturant should then be applied onto the surface of the fiber sheet. The coated surface should be strongly squeezed in the fiber longitudinal direction two or three times with the roller and spatula in order to impregnate the fiber sheet in the same manner

as above.

Concrete shot blasting or abrasive blasting to remove laitance and surface contamination. Surface defects in concrete made good using MBrace Putty. Depressions in the concrete surface such as a concrete joint are filled with MBrace Putty. Sharp corners need to be rounded with a radius of at least 10mm; internal concrete angles rounded using MBrace Putty. Adhesive epoxy, Dr.Fixit model of Pidicrete MRB, has been used for grouting concrete cracks in this study. Figure 3.15 shows the tensile strength testing of the GFRP specimen and Figure 3.16 shows epoxy resin grouting.

3.3 DETAILS OF TEST STRUCTURES

Two groups of test specimens including two brittle RC frames and one ductile RC frame were tested. These specimens are designed and manufactured. Each specimen consisted of one-third scale of three story RC frames. Each frame was identical in most of the geometrical and mechanical aspects and cast integrally with three slabs 2000 mm x 2000 mm x 50 mm. Each column was equally sized with rectangular of the cross section 100 mm x 100 mm with a height of 950 mm floor-to-floor. All the beams were equally sized having rectangular cross sections of 100 mm x 150 mm with a length of 2000 mm. Overall dimensions of the building model were 2000 mm x 2000 mm x 3050 mm tall (Kanwar et al., 2006).

3.3.1 First group of specimen

The first group of brittle specimens (Control Frame 1 and 2) were designed to resist vertical load according to the requirements of Indian Standard, IS 456:2000. Each column was equally sized with a square cross section 100 mm x 100 mm (having four 8 mm diameter longitudinal bars with 6 mm diameter transverse ties spaced at 100 mm as the reinforcement). All the beams were rectangular of the cross section 100 mm x 150 mm (having two 10 mm longitudinal bars at the tension and compression face with 6 mm diameter transverse ties spaced at 100 mm as the reinforcement). The schematic drawing of the model structure and steel reinforcement detail of frame 1 and 2 are presented in Figure 3.17 to 3.19, respectively.

3.3.2 Second group of specimen

The second group of ductile specimens (Control Frame 3) was designed to resist both vertical and lateral load according to the requirements of Indian Standard and the ductile detailing code (IS 13920, 1993). Dimension of this specimen was similar to the first group. Each column was equally sized with a square cross section of 100 mm x 100 mm (having four 8 mm diameter longitudinal bars with 6 mm diameter transverse ties spaced 25 mm at $H/4$ as the reinforcement). All the beams were rectangular in cross section having 100 mm x 150 mm dimension (with two 10 mm longitudinal bars at the tension and compression face with 6 mm diameter transverse ties spaced 38 mm at $L/4$ as the reinforcement). Here, H is the height of the column and L is length of beam, respectively. The schematic drawing of the structural model and steel reinforcement detail of Control Frame 3 are presented in Figure 3.20.

3.3.3 Supports

All columns and beams were provided with 6 mm diameter stirrups at 100 mm centre-to-centre. Each column was cast integrally with 150 mm x 200 mm x 400 mm stub foundation. The stub foundation details are shown in Figure 3.21. To avoid support movement, the stub was in turn bolted firmly using a total of four bolts of high tensile strength on steel plate which rest on strong floor (Memon and Sheikh, 2005; Ye et al., 2002). The curing of experimental RC frame is shown in Figure 3.22. Figure 3.23 show the whole frame model of 3-story building in laboratory.

3.3.4 Strengthening scheme

The damaged frame was retrofitted using GFRP sheets. The applications of GFRP on damaged elements were done using the following steps (Mukherjee and Joshi, 2005):

(1) The damaged frame was moved back to initial state.
(2) Loose concrete was removed and the surfaces were cleaned of dirt.
(3) All the corners of damaged elements were beveled and rounded to a radius of 10 mm.
(4) In Retrofitted Frame 1 and 2, the cracks of damaged frame are filled with the composite resin of MBrace Primer and surface is smoothened using MBrace Putty.

(5) In Retrofitted Frame 3, the cracks of damaged frame are filled with epoxy grouting and concrete surface is covered with adhesive layer of MBrace Primer. Then MBrace Putty is applied for smoothening of the surface.

(6) After surface smoothening, the GFRP sheets are wrapped with MBrace Saturant.

Application of GFRP wrap on the damaged element is shown in Figure 3.24. The strengthening positions and application of each epoxy resin system are shown in Figure 3.25 to 3.29, respectively. The GFRP sheets have been applied in various steps:

(1) One layer of GFRP sheet has been used on the tension and compression direction zone of the columns and beams to increase flexural strength capacity.

(2) Columns and beams were confined at each edge zones by being wrapped with one layer of transverse directional GFRP sheet.

(3) The connection joints were wrapped by two layers of GFRP. First layer was along the column direction and other layer was perpendicular column direction.

3.4 TEST EQUIPMENT

The equipment used for carrying out various tests on the materials as well as on the frames included the following:

3.4.1 Universal testing machine

Automatic compression testing machine of 3000 kN capacity was used to test concrete cubes of each frame model. The universal testing machine was used to determine the tensile strength of reinforced steel bars. Both these machines are shown in Figure 3.4 and 3.6, respectively.

3.4.2 Loading frame

Lateral quasi-static load was applied by a hydraulic jack of 200 kN capacity that was fixed on a rigid steel frame. Foundations of loading frame are fixed on the strong RC floor to resist both vertical and horizontal forces. The hydraulic jack was setup at a height of 3150 mm above ground floor to apply lateral load on top floor of frame models (Goyal, 2007; Kanwar et al., 2006). Load versus displacement test setup is shown in Figure 3.30.

3.4.3 Accelerometer

Accelerations were measured at each floor of the specimen using DYTRON model 11103, 11197 and 11305 with a sensitivity of 1.055 V/g. The accelerometer is shown in Figure 3.31. The data signal for each accelerometer was recorded at several sensitivity levels to allow reasonable resolution at all times over the exponentially decaying vibration signal (Kanwar et al., 2006). High strength cement plaster wax was used for mounting the accelerometer to the surface of the test structure.

3.4.4 Impact hammer

The vibration response was measured by performing impact testing on the structure. The impact excitation was applied 150 mm away from the mid span: an impact hammer having a hard rubber impact tip was swung from a horizontal distance of approximately 50 mm from the specimen (Goyal, 2007; Kanwar et al., 2006). The hammer was model PCB 20135 with a sensitivity of 0.00225V/N, made by OROS instruments. A typical impact-force hammer like the one used is illustrated in Figures 3.32 and 3.33.

The impact consisted of a nearly constant force over a broad frequency range and was capable of exciting all resonances in that range. The hammer size, length and material at impact determined the amplitude and frequency content of the force impulse. The impact tip materiel generally determined the frequency content. The hammer mass and velocity at impact determined energy content. A set of impact tips made from different materials and interchangeable mass could be selected to extend the frequency ranges and force levels for testing different machines and structures. The types and sensitivities of the force hammer and accelerometer could be selected and entered in the measurement setup menu of the recording instrument.

3.4.5 Eight channel FFT analyzer

Spectrum analysis is defined as the transformation of a signal from a time-domain representation into a frequency-domain representation. There are four forms of the Fourier Transform, explained as follows:

a) Fourier Series: Transforms an infinite periodic time signal into an infinite discrete frequency spectrum.

b) Fourier Integral Transform: Transforms a continuous time signal into a continuous frequency spectrum.

c) Discrete Fourier Transform (DFT): Transforms a discrete periodic time signal into a discrete periodic frequency spectrum

d) Fast Fourier Transform (FFT): A computer algorithm for calculating the DFT

In order to adapt the Discrete Fourier Transform for use with digital computers, the so-called Fast Fourier Transform was developed. The FFT is simply an algorithm for calculating the DFT in a fast and efficient manner (Formenti, 2000; Finno and Prommer, 1994). Cooley and Tukey discovered the FFT in 1967, but it existed much earlier as well, although without the digital computers it was difficult to use. The FFT algorithm places certain limitations on the signal and the resulting spectrum. For instance, the sampled signal to be transformed must consist of a number of samples equal to a power of two. The frequency range covered by FFT analysis depends on the number of samples collected and on the sampling rate (Raghavendrachar and Aktan, 1992). For the experimental modal analysis the setup was modified by having the accelerometer and charge amplifier connected to a laptop computer with data recording software. The eight channels FFT analyzer from OROS Instruments, shown in Figure 3.34, was used in this research.

3.5 METHODOLOGY OF TESTING

The testing methodology involved testing both control and retrofitted RC frames. The testing was done to find out the lateral load resistance behavior and vibration characteristics of both sets of frames. The vibration response of the structures was measured by using an impact hammer, accelerometers, and an FFT analyzer. The equipment setup for vibration testing is shown in Figure 3.35. Lateral load resistance behavior involves determination of the load-deformation relationship in a model of an RC frame, wherein load is applied at the top storey and corresponding displacement is measured. From the load deformation curves generated, both displacement ductility index and energy dissipation capacity was calculated. Subsequently, nonlinear modeling of the experimental frame was also performed for data verification. This procedure is explained in the subsequent subsection.

3.5.1 Damage loading

To simulate a change in the structural stiffness, a hydraulic jack was horizontally installed along the desired direction at the top floor. Each floor of the frame was equipped with one displacement dial gauge in the horizontal direction. The relation between loads and displacement at each floor was measured, and then the jack was removed to measure the stiffness damage index at different damage states. Applied load histories for both control frames and retrofitted frames are shown in Figure 3.36. The loading applied to the three different frames is explained as follows:

Frame 1: Load was applied at uniform pace rate on the original frame, from initial state to ultimate damage state (full failure). The damaged frame was then strengthened by GFRP and load was applied again until the ultimate damage state was again reached.

Frame 2: Load was applied at the same rate as for frame 1, from initial state to 70% of ultimate load of frame 1. The damaged frame was then strengthened by GFRP and load was applied again until full damage state.

Frame 3: Load was applied at uniform pace rate to original frame (the frame cast using ductile detailing), from initial state to ultimate damage state (full failure). The damaged frame was then strengthened by GFRP and load was applied again until ultimate damage state.

3.5.2 Vibration test

Vibration test is used to detect the health of an RC structure for original as well as retrofitted specimens. An instrumented force hammer was connected to the force input channel, channel 1, of an FFT analyzer. Generally, the hammer is connected to the force channel directly because FFT analyzer provides power to an integrated circuit piezoelectric (ICP) type force hammer. The response signal was measured by an accelerometer. Each accelerometer was connected to the vibration input channel of the FFT analyzer. Vibration response data was recorded on a computer laptop. Initially, the vibration test involved testing of the control frame for both aspects. The characteristics were again studied after retrofitting the same frames using GFRP. A similar procedure was also adopted for frames damped up to a predicated level.

3.5.3 Data recording

Structural dynamic characteristics data such as acceleration response, resonant frequency, mode shape, damping, frequency response function, and coherence function were measured by simultaneously sampling both impact force and system response signals. The captured time-waveforms of both impact force and system response contain amplitude and relative phase information. The dynamic characteristics of structure could be computed from the Fourier transforms of both impact and response signals by using FFT analyzer.

Table 3.1 The details of the materials

Frame 1		
Structural elements	Compressive cube strength (MPa)	Standard deviation
First floor	24.09	0.63
Second floor	23.42	2.89
Third floor	22.36	1.01
Average	22.46	1.60
Frame 2		
Structural elements	Compressive cube strength (MPa)	Standard deviation
First floor	20.04	1.38
Second floor	20.84	1.89
Third floor	20.55	1.91
Average	20.48	1.57
Frame 3		
Structural elements	Compressive cube strength (MPa)	Standard deviation
First floor	23.47	2.44
Second floor	24.20	1.48
Third floor	23.01	1.87
Average	23.56	1.78
Cement and aggregates		
Specific gravity of cement		3.142
Compressive strength of cement		
(a) at 7 days		33.5-35.0 MPa
(b) at 28 days		44.0-47.0 MPa
Coarse aggregate	Specific gravity on dry basis	2.61
(10 mm)	Percentage of water absorption	1.45
Coarse aggregate	Specific gravity on dry basis	2.62
(4.75 mm)	Percentage of water absorption	1.15
Fine aggregate	Specific gravity on dry basis	2.44
	Percentage of water absorption	2.99

Table 3.1 The details of the materials (continue)

Steel reinforcement bars		
Steel size	Yield strength (MPa)	Tensile strength (MPa)
Longitudinal bar (10 mm-diameter)	475.68	586.60
Longitudinal bar (8 mm-diameter)	516.65	628.91
Transverse bar (6 mm-diameter)	523.23	636.36
Mechanical properties of GFRP laminate		
Fiber	Glass fiber sheet	
Thickness	0.34 mm	
Density	2.6 g/cm^3	
Tensile strength	1.59 GPa	
Elastic modulus	63 GPa	

Figure 3.1 Specific gravity test of ordinary Portland cement

Figure 3.2 Compressive strength test of ordinary Portland cement

Figure 3.3 Concrete cute specimens in curing tank with temperature control

Figure 3.4 Automatic compression testing machine (3000 kN capacity)

Figure 3.5 Compressive strength test of concrete cube specimens

Figure 3.6 Universal Testing Machines

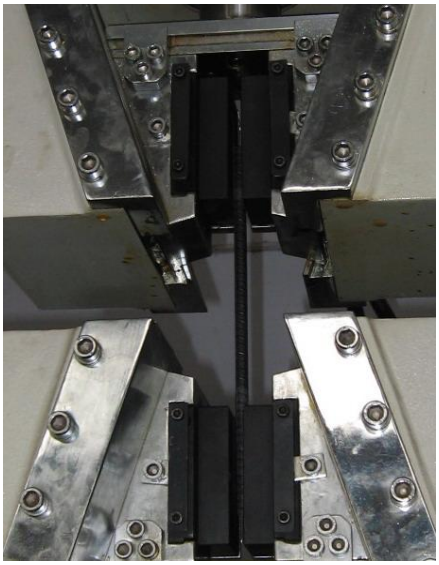

Figure 3.7 Tensile strength test of reinforced steel bars

Figure 3.8 Failed reinforced steel bar samples

Figure 3.9 Glass fiber material.

Figure 3.10 MBrace Fiber: glass fiber sheet (G sheet EU 900)

Figure 3.11 MBrace Primer: resin part A and hardener part B

Figure 3.12 MBrace Putty: resin part A and hardener part B

Figure 3.13 MBrace Putty: aggregate part C

Figure 3.14 MBrace Saturant: resin part A and hardener part B

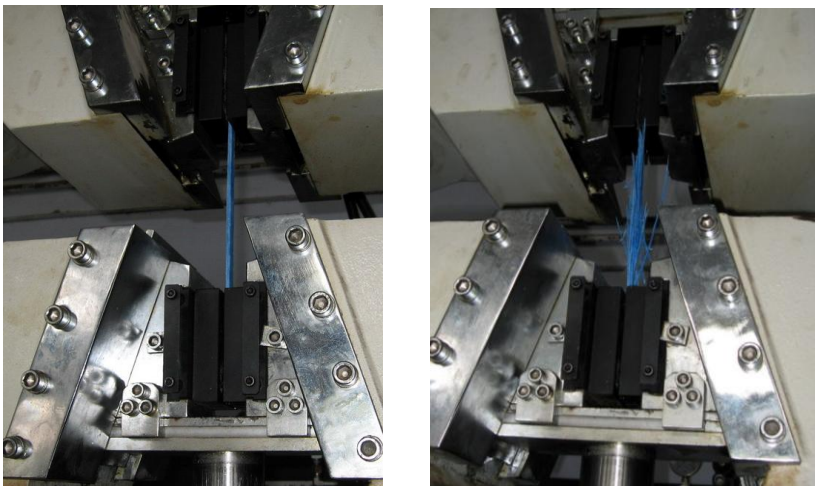

Figure 3.15 Tensile strength test of GFRP specimen with epoxy

Figure 3.16 Adhesive epoxy for concrete crack grouting

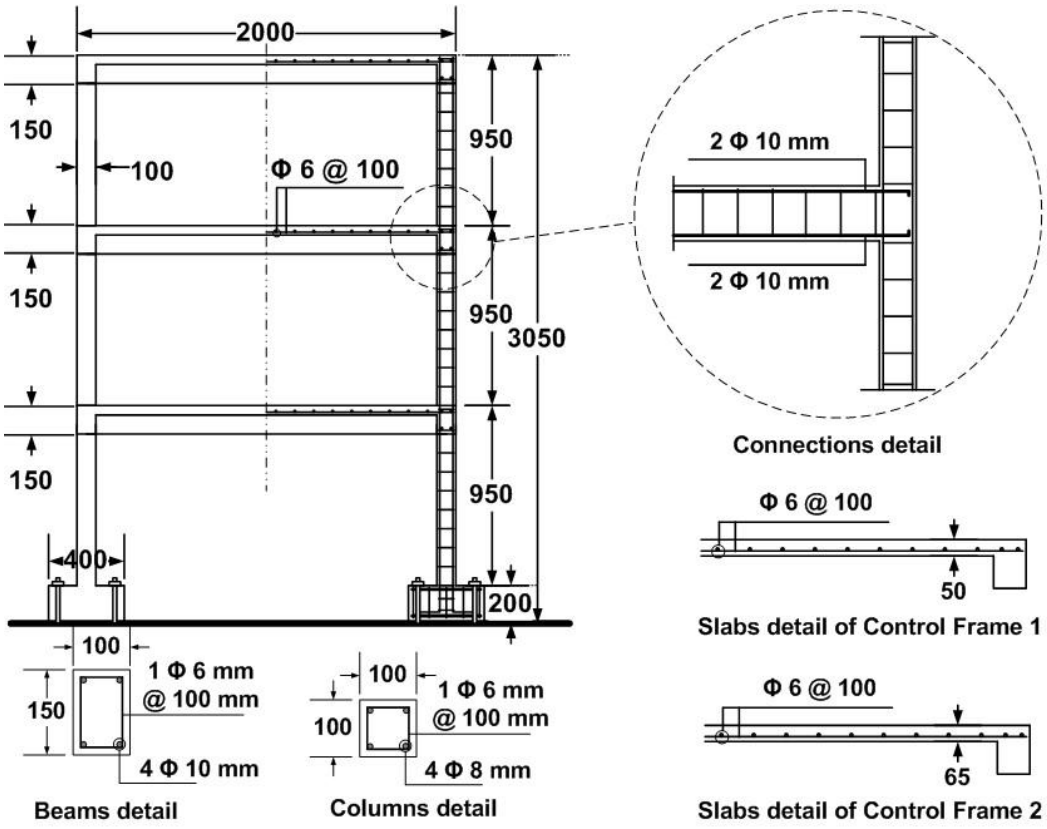

Figure 3.17 Schematic drawings of Control Frame 1 and 2. All dimensions in millimeters.

Figure 3.18 Beam detail of frame 1 and 2

Figure 3.19 Column detail with stub of frame 1 and 2

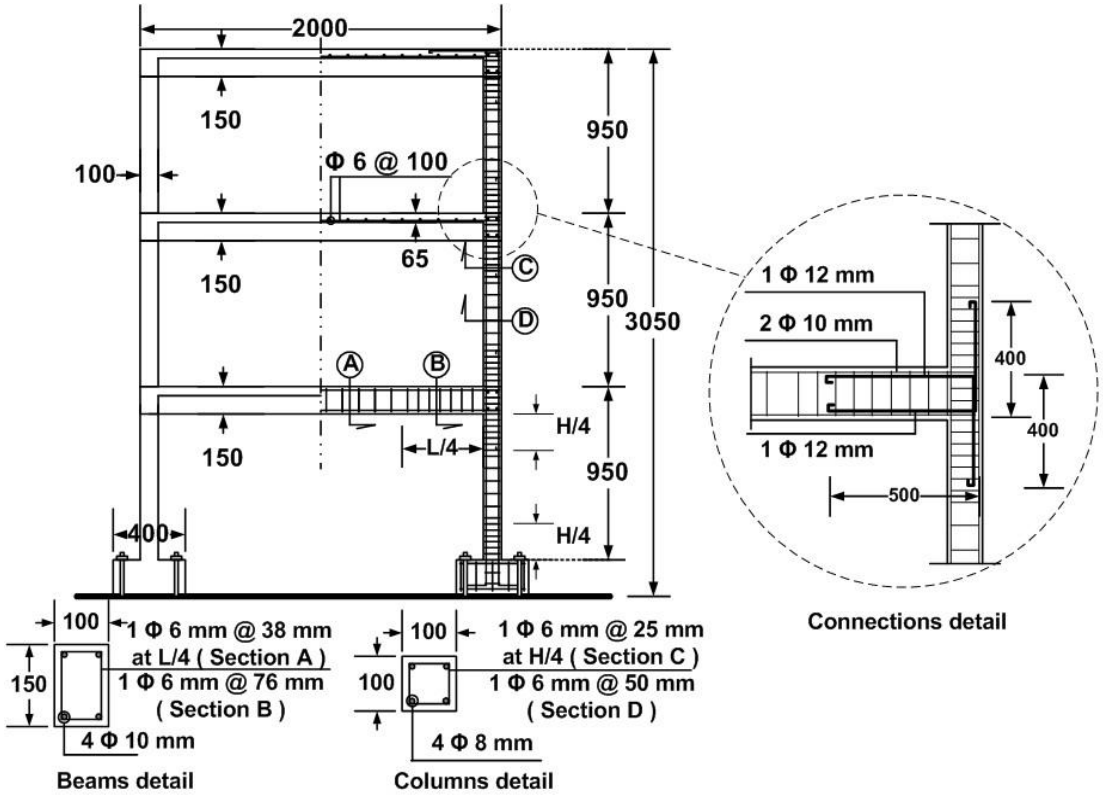

Figure 3.20 Schematic drawing of Control Frame 3. All dimensions in millimeters.

Figure 3.21 Foundation detail: column with stub

Figure 3.22 Curing specimens with wet sacks

Figure 3.23 Experimental control frame model of 3-story RC building.

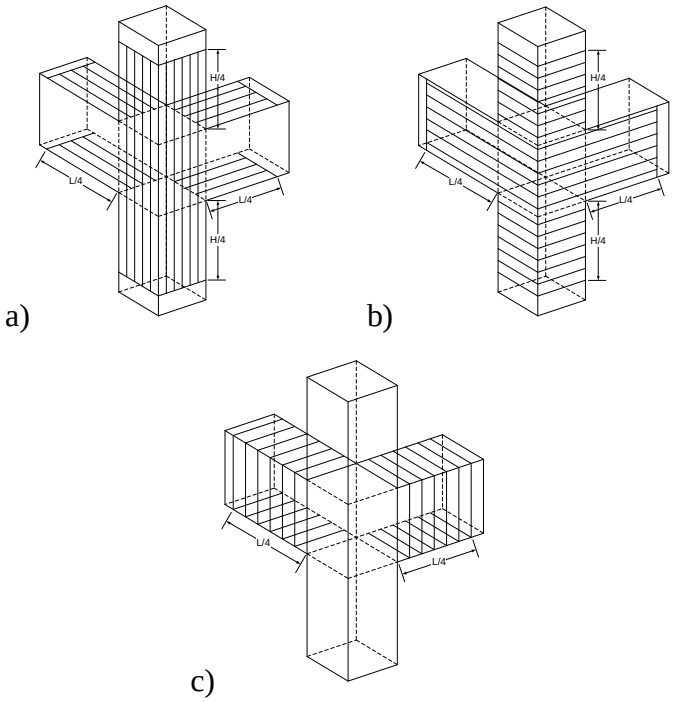

Figure 3.24. Application of FRP sheets: a) first step b) second step and c) final step.

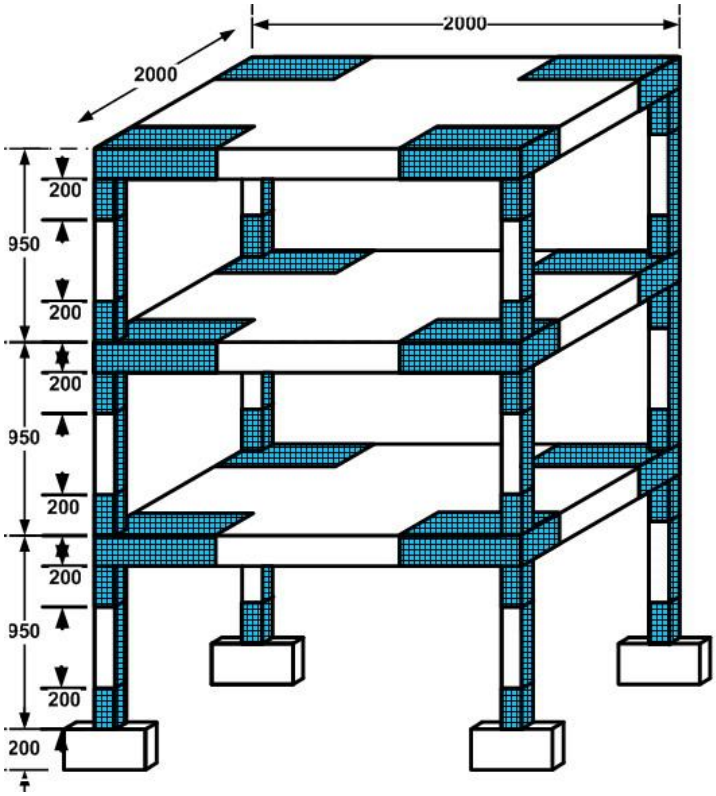

Figure 3.25. Schematic drawing of the strengthening frame. All dimensions in millimeters.

Figure 3.26 Applied MBrace Primer

Figure 3.27 Applied MBrace Putty

Figure 3.28 Applied MBrace Saturant with GFRP wrap

Figure 3. eets

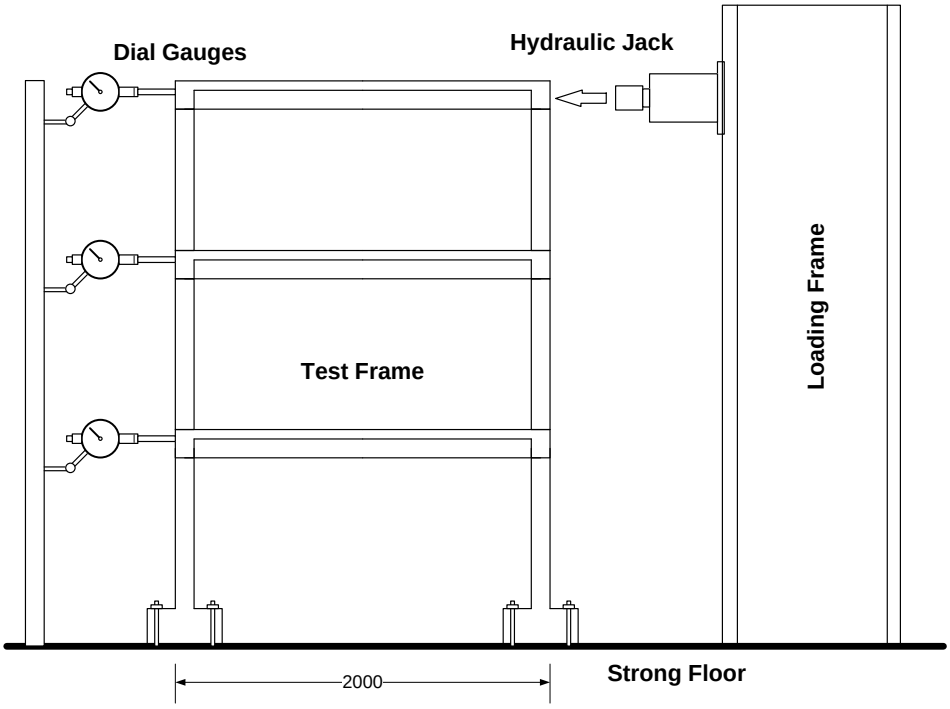

Figure 3.30 Lateral load resistant test of frame models

Figure 3.31 Accelerometers

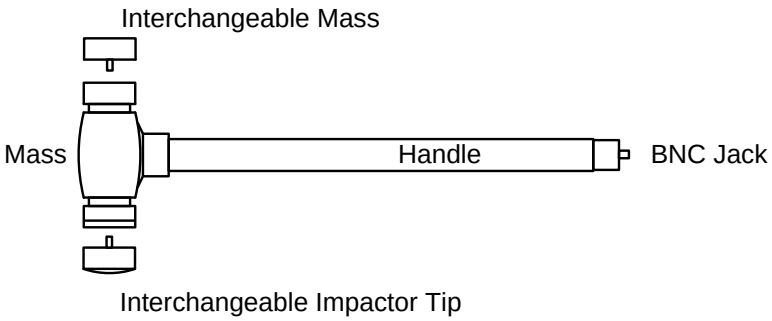

Figure 3.32 Typical impulse-force hammer.

Figure 3.33 Impact hammer instrument with impactor tips

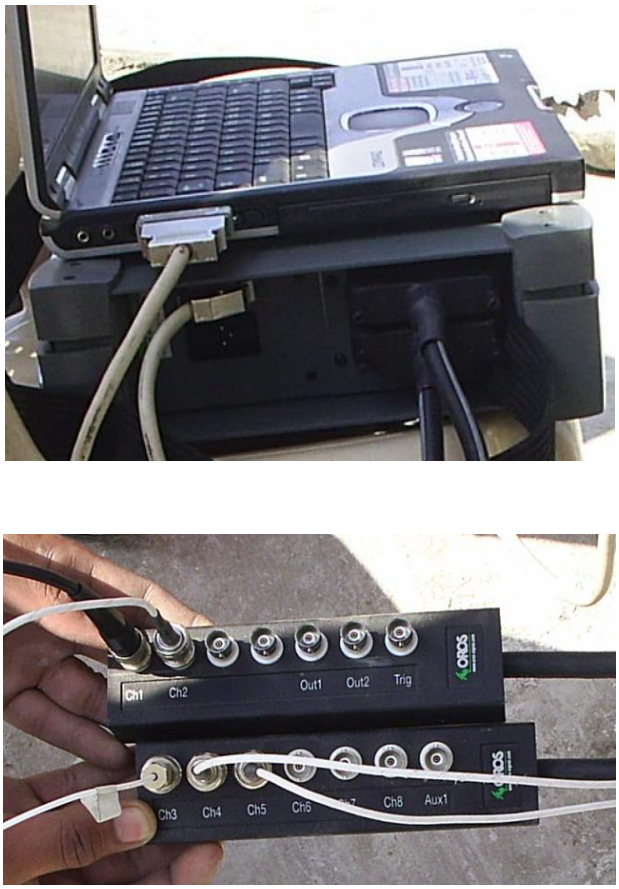

Figure 3.34 Computer laptop with eight channels FFT Analyzer

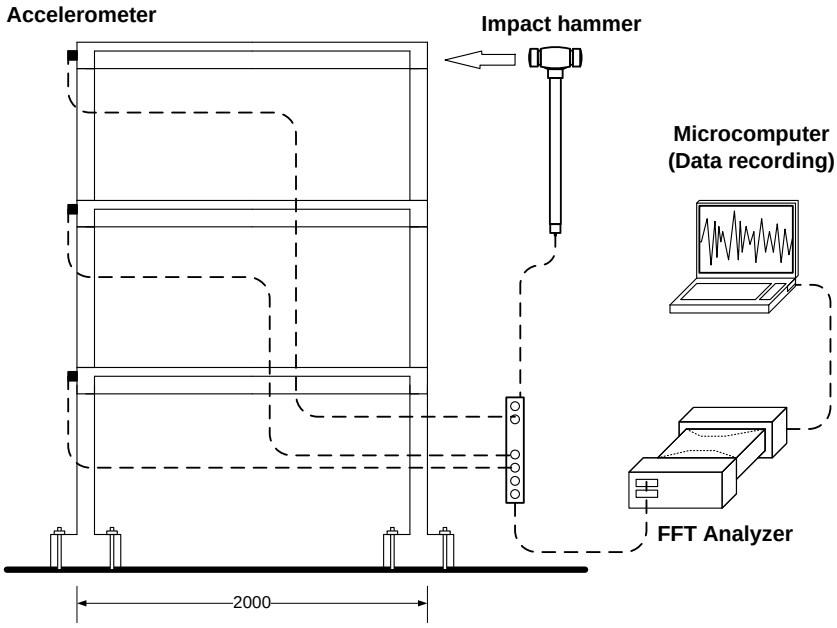

Figure 3.35 Vibration test setup

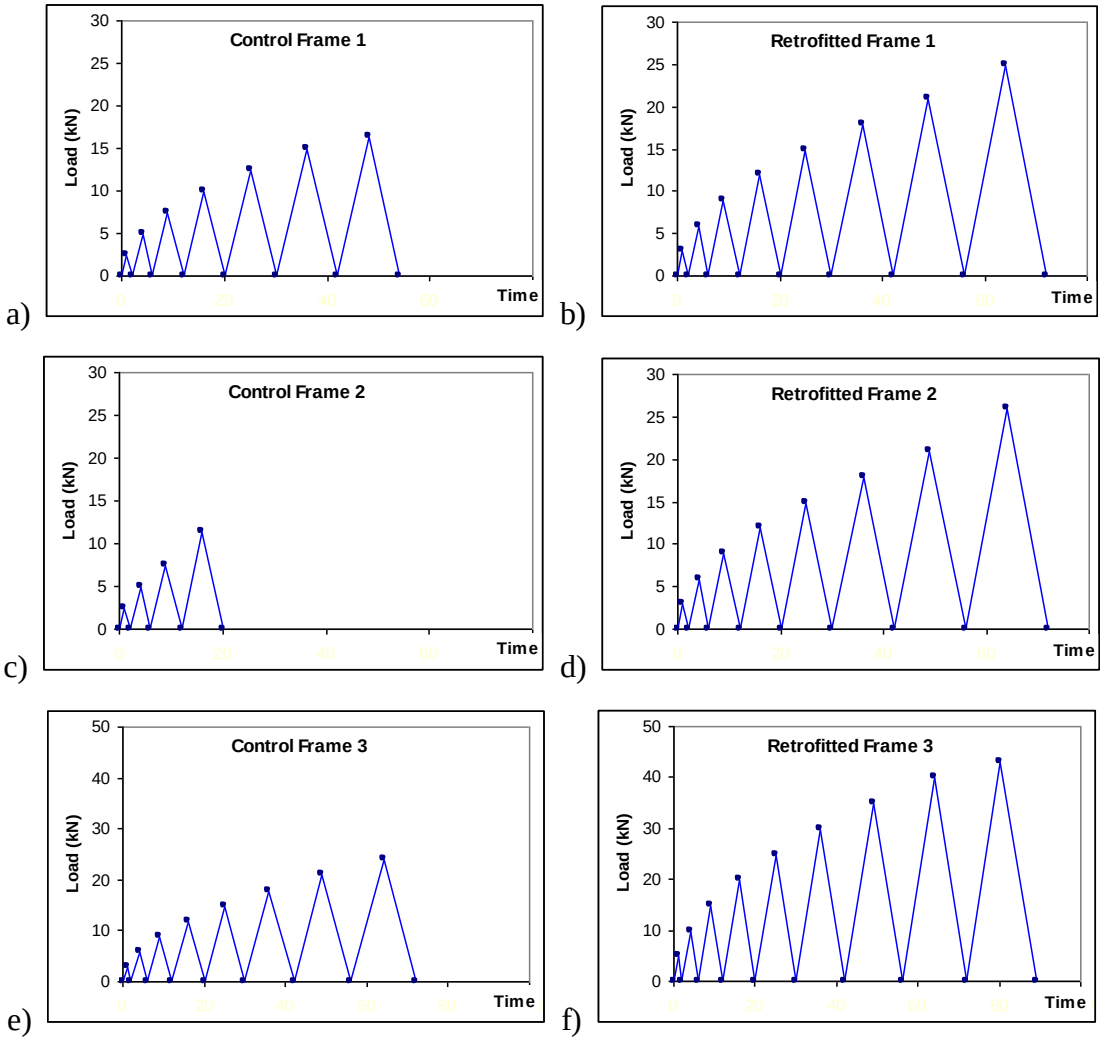

Figure 3.36 Applied quasi-static load histories: a) Control Frame 1, b) Retrofitted Frame 1, c) Control Frame 2, d) Retrofitted Frame 2, e) Control Frame 3 and f) Retrofitted Frame 3.

CHAPTER 4

STRUCTURAL RESPONSE PARAMETERS AND NONLINEAR BEHAVIOR RESULTS

4.1 GENERAL

The objectives of this chapter are to address and unify definitions of the fundamental response parameters. In general, the principal parameters controlling the load response of structures are stiffness, strength, and ductility (McGuire et al., 2000; Paulay and Priestley, 1992). Stiffness of structure is the most pertinent parameter in responding to the requirements of serviceability. In an analogous manner, strength is utilized to control the level of inelasticity under external loads. Finally, collapse prevention is most affected by ductility (Carlin, 1998; Naaman And Joeng, 1995). This chapter also presents the load-displacement behavior as well as a discussion about the failure mechanism in the RC frames under lateral loads.

4.2 STRUCTURAL RESPONSE PARAMETERS

The focus of the most important parameters that describe the behavior of structures when subjected to lateral loads is placed on the three response characteristics of stiffness, strength, and ductility. While defining these three quantities, it is instructive to discuss load and deformation.

4.2.1 Stiffness

Stiffness is the ability of a component or an assembly of components to resist deformations when subjected to load. It is expressed as the ratio between load and deformation at a given level of either of the two quantities and the corresponding value of the other. Therefore, stiffness is not a constant value. In Figure 4.1, K_i is the stiffness at a required deformation Δ_i and corresponds to force resistance P_i. If increments or first derivatives of loads and deformations are used, the ensuing stiffness is the tangent value. If total loads and deformations are used, the ensuing stiffness is the secant value (Taranath, 1998; Durkin, 1985; Mileti and Nigg, 1984). Stiffness defines the relationship between actions and deformations of a structure and its components, whereas member stiffness is a function of the lateral resisting mechanisms utilized.

Relationships between geometry, mechanical properties, actions, and deformations can be established from principles of mechanics. Their complexity depends on the construction material used. Cracking of concrete, yielding of reinforcement bars, and other sources of inelasticity in RC structures pose problems in defining a fixed value of stiffness (Bazant and Oh, 1983). For RC and masonry structures, the stiffness can be taken as the secant to the yield point or to any other selected point on the response curve. Slippage at connections, local bucking and yielding in steel structures are the counterparts to the above discussion on RC structures.

Figure 4.1 shows a plot of the structural response of a system subjected to lateral loads; the response curve is represented by lateral load P versus top horizontal displacement Δ. The initial slope K_o is the elastic stiffness of the structure, while the secant stiffness is the slope K_s of the line corresponding to a given level of load. The initial stiffness K_o is higher than the secant stiffness K_s for conventional materials of construction. For the latter, values of (Δ,P) pairs are generally utilized to define the secant stiffness. Variations in stiffness in the inelastic range are often expressed by the tangent stiffness K_i, which is the slope of the tangent to the response curve for a given (Δ,P) pair (Elnashai and Sarno, 2008; McGuire el al., 2000). A decrease in the values of K_i indicates that softening of the structure is taking place. In analysis of inelastic structures, use is often made of secant stiffness to avoid dealing with negative tangent stiffness beyond the peak action resistance.

Several types of stiffness may be defined, depending on the nature of applied loads. Structures designed for vertical loads generally possess sufficient vertical stiffness. Earthquake load or wind load generates inertial forces due to vibration of masses. Horizontal components of these inertial forces are often dominant; hence lateral stiffness is of primary importance for structural engineers. The definition of the lateral stiffness depends significantly on the region of interest in the response domain. The stiffness of a system is associated primarily with satisfaction of the functionality of the structure under lateral loads (Penelis and Kappos, 1997; Paulay and Priestley, 1992).

4.2.2 Strength

Strength is the capacity of a component or an assembly of components for load resistance at a given response. It is also not a constant value. The term "capacity" is

preferred to the term "strength" in representing both action resistance and the ability to endure deformation. In the Figure 4.1, P_y referred to as the yield strength, corresponding to the yield displacement, Δ_y, which is required for proportional ductility calculations.

Strength defines the capacity of a member or an assembly of members to resist actions. This capacity is usually defined as a function of the type of applied force. Axial, bending and shear resistance are utilized to quantify the capacity of structures and their components. In the response curve of structural system, the total base shear capacity of the system is defined with respect to either the base shear at yield or at maximum strength (Motos and Dodds, 2002; Bruneau et al., 1998; Paulay and Priestley, 1992). Alternately, the shear capacity can be expressed at any intermediate point between yield and maximum strength. Similarly, bending and axial resistances are evaluated through moment-rotation relationships and axial load-axial displacements.

The definition of strength is often more straightforward than that of stiffness. Relationships between geometry, mechanical properties, and strength can be derived from principles of engineering mechanics. These relationships depend on the type of construction materials employed. Uncertainties in the evaluation of structural capacities are attributed to

(i) the randomness in material properties, especially strength parameters,

(ii) geometric properties, e.g. section and member size, and

(iii) construction quality.

Attainment of shear, flexural, and axial capacities in a structural system can cause damage to structural components. Damage negatively impacts the safety of a system but it does not necessarily lead to structural collapse. Collapse prevention is the behavior limit state controlled by ductility.

4.2.3 Ductility

Ductility is the ability of a component or an assembly of components to deform beyond the elastic limit and is expressed as the ratio between the maximum value of a deformation quantity and the same quantity at the yield limit state. In the Figure 4.2,

the displacement ductility is the ratio between the maximum or ultimate displacement Δ_u and the yield displacement Δ_y.

In other words, ductility is the ability of a material, component, connection, or structural system to undergo inelastic deformations with acceptable stiffness and strength reduction. In force-displacement relationships for systems, brittle systems fail after reaching their strength at very low inelastic deformations. The collapse of brittle systems occurs suddenly beyond the maximum resistance because of lack of ductility. Conversely, the ultimate deformations corresponding to ultimate lateral forces are higher in ductile systems compared to brittle systems (Elnashai and Sarno, 2008 and Carlin, 1998; Naaman And Joeng, 1995). Figure 4.2 presents definition of structural ductility between a brittle and a ductile system.

The response amplitudes of earthquake-induced vibrations are dependent on the level of energy dissipation of structures, which is a function of the structure's ability to absorb and dissipate energy by ductile deformations. For low energy dissipation, structural systems may develop stresses that correspond to relatively large lateral loads. Structural ductility or displacement ductility is a global measure of the inelastic performance of structural sub-assemblages or systems subjected to horizontal loads. Several factors may lead to reduction of available ductility. These include primarily strain rate effects causing an increase in yield strength, reduction of energy absorption due to plastic deformations under alternating action, over-strength leading to a structure's not yielding when it was designed to yield, and the tendency of some materials to exhibit gribble fracture. These factors may affect both local and global ductility.

4.3 Factors Influencing Strength, Stiffness and Ductility

The following are the main factors influencing strength, stiffness and ductility of RC structures.

4.3.1 Material properties

Material properties that influence the structural stiffness are the elastic Young's modulus and the elastic shear modulus. In the inelastic range, the lateral stiffness still depends on the moduli of Young and shear, not on initial, but rater tangent values. The

material stiffness is often evaluated through the ratio of the elastic modulus to the weight.

In Figure 4.3, the efficient of material strength is quantified by the specific elasticity. Reinforced concrete, steel and fiber composites are suitable for structural engineering applications. For RC structures, a loss of both strength and stiffness takes place in concrete as the strain increases. This is referred to as strain softening or strength and stiffness degradation. Strain softening can be reduced in RC systems by providing transverse confinement of concrete by spirals or composite material wrap. The loss of bond between concrete and steel in RC structures under large alternating loads reduces strength and stiffness. Fiber composites and circular hoops are more efficient than those with rectangular shapes because they uniformly confine the core concrete.

Fu et al. (1991) found that the material strength of structural members increases with the increase in strain rate under cyclic loads. The increase of the stiffness in concrete is lower than that in compressive strength. Nevertheless, strain rates may be favorable for the stiffness degradation of concrete. In RC beams, where the forced response is controlled by steel reinforcement bars, strain rates have minor effects. Consequently, for RC structures, strain rates are likely to influence the response of members in which the behavior is dominated by concrete failure.

The ductility of structural systems significantly depends on the material response. Inelastic deformations at the global level require that the material possesses high ductility. Concrete is brittle material. It exhibits sharp reductions of strength and stiffness after reaching the maximum resistance in compression. This material possesses low tensile resistance, which is followed by abrupt loss of strength and stiffness. The material ductility can be expressed as the ratio of the ultimate strain and the strain at yield. Consequently, the ductility of concrete in tension is equal to unity, while the ductility is about 1.5 to 2.0 in compression. Steel reinforcement can be utilized in plain concrete to enhance their ductility. Stirrup steel or composite strengthening material confined concrete exhibits inelastic deformations 5 to 15 times higher than plain concrete. Unconfined concrete exhibits very limited ductility in compression. Confinement limits the post-peak strength reduction, this increasing the residual resistance. Ductility of concrete is significantly enhanced by confinement provided by transverse steel reinforcement (Mukherjee and Joshi, 2005). Confined

concrete is subjected to multi-axial stress states, which is beneficial for both strength and ductility.

4.3.2 Section properties

Section properties that affect the structural stiffness are the cross-sectional area and the flexural moment of inertia. Section area and flexural inertia primarily influence the axial, bending and shear stiffness of the system, for metal structures area and moment of inertia do not change with types and levels of applied loads. Conversely, for masonry and RC, the above properties are a function of the loading and boundary conditions. For the definition of the area of RC cross sections, it is generally assumed that only the steel reinforcement bars are effective because of the low tensile strength of concrete.

Strength of structural systems is influenced by section properties. Cross section area affects both axial and shear capacity, while flexural moments of inertia influence flexural capacity. For RC sections, the strength increases with the amount of steel longitudinal reinforcement. Cross section area and flexural moment of inertia vary with the type and value of applied loads. The tensile strength of these materials is much lower than their compression strength. The tensile strength is often less than 10-15% of the value of compression strength. Shear-axial and shear-flexure interactions affect the seismic response of beams and columns in framed systems. The effects of these interactions considerably reduce the capacity of RC sections. Lee and Elnashai (2002) presented that failure in RC beams is often caused by the interactions between flexure and shear actions. Similarly, in columns the response is influenced by both shear-axial and shear-flexure interactions.

The ductile response of cross sections of structural members subjected to bending moments is generally measured by the curvature ductility, which can be expressed by the ratio of the ultimate and yield curvatures, respectively. In RC structures, the curvature ductility significantly depends on the ultimate concrete compressive strain, the compressive concrete strength, the yield strength of the steel reinforcement bars, the stress ratio of reinforcement steel, the ratio of compression-to-tension steel, and the level of axial load. By increasing the ultimate concrete strains the curvature ductility is enhanced. Thus confined concrete behaves in a ductile manner. The use of high

strength steels increases yield curvature, while values of ultimate curvature do not change. The net effect is that these types of steel reduce the curvature ductility. Conversely, increases in the stress ratio of reinforcement steel increase the curvature ductility (Mukherjee and Joshi, 2005; Mo, 1994). Adding reinforcement steel bars in compression is beneficial to the ductile response of RC cross sections. The presence of axial compression loads increases the depth of the neutral axis, both at yield and ultimate limit states. The yield curvature increases while the ultimate curvature deceases. Consequently, the ductility is lowered.

Curvature ductility in RC members can also be affected by the presence of shear forces. Transverse confinement, which is used to confine plain concrete, increases the shear strength of structural components. Consequently, flexural inelastic response is not fully developed prior to shear distress. In steel structures, shear-flexure interaction does not generally affect the section ductility. On the other hand, the presence of axial loads considerably reduces the curvature ductility in both steel and composite cross section.

4.3.3 Member properties

The lateral stiffness also depends on the type of structural members utilized to withstand lateral loads. Geometrical properties of structural components, such as section dimensions, height and aspect ratio, influence significantly their horizontal shear and flexural stiffness values. Flexural deformations are normally higher than shear deformations for relatively slender structural components (Paulay and Priestley, 1992). System strength is affected by the properties of structural components. RC elements generally possess lower flexural and shear strengths than retrofitted elements. FRP composites are frequently used to increase stiffness and strength in low to medium rise frames.

An adequate metric for ductile behavior of structural members is the rotation ductility factor which is the ratio of the ultimate and yield rotations, respectively. The rotations are indeed computed by integrating the curvature distributions along the member length. Inelasticity is concentrated in flexural plastic hinges at the ends of beams and columns. It is often assumed that curvatures within plastic hinges are constant, thus allowing plastic rotation to be expressed by the multiple between plastic curvature and the length of the plastic hinge. The ductility of a frame member depends on the

spreading of inelasticity, which takes place in the region corresponding to the plastic hinge of length. To ensure adequate rotational ductility in flexural plastic hinges, it is necessary to carefully detail critical regions. In RC members, it is essential to provide closely spaced stirrups, which effectively confine the concrete and use sufficient lap splices and anchorage lengths.

4.3.4 Connection properties

Under lateral loads, high shear reversals are generated in beam-column and column-base connections. Both are critical components of framed systems. Stress concentrations in joints may be caused by their complex geometric layout and congestion, e.g. in RC structures several longitudinal steel bars from elements framing into them intersect. The loss of stiffness and strength of structural joints leads to the deterioration of stiffness and strength of the frame. Weak connections between foundations and structures may cause sliding shear or overturning (Terro et al., 2007; Mukherjee and Joshi, 2005).

The behavior of connections in moment resisting frames significantly affects the global ductile response of structures. In RC frames, the ductile behavior of joints is a function of several design parameters, which among others include:

(i) Joint dimension.
(ii) Amount of steel reinforcement.
(iii) Bond resistance.
(iv) Level of column axial loads.
(v) Presence of slab and transverse beams framing into the connection.

All other parameters being equal, increasing joint dimensions generates lower shear stresses. The advantage of increasing column depths is twofold. Joint shear stresses are considerably reduced and bond demands on longitudinal steel reinforcements of beam bars passing through the joint are minimized. Both effects prevent brittle failure modes in RC beam-column joints, i.e. loss of bond resistance along the joint boundary, inability to resist high stresses caused by perimeter bond actions, and inability to sustain diagonal compression strut in the joint core. Brittle failure due to low shear capacity can be prevented by adequately confining the joint by hoops. Shear strength

and bond resistance are enhanced. Similarly, the presence of slabs may erode the ductility of beam-column connections because of the additional shear demand caused by the raised beam moment (Elnashai and Sarno, 2008). Effects of column axial loads reduce the total lateral drift at yield, which benefits the ductile response. Nevertheless, as the vertical stresses increase in the joint, the contribution of the diagonal compression strut to the shear resistance is lowered. The net effect is that by increasing the column axial loads, the joint ductility is impaired. Transverse beams enhance joint shear resistance and provide concrete confinement, which in turn improves the ductility.

The global ductility of composite structures also depends on the response characteristics of the connections, especially beam-column and column-foundation connections. The ductility of beam-column connections is controlled by yield mechanisms and failure modes. Multiple yield mechanisms may contribute to plastic rotations if their resistances are all lower than the strength of the connection. On the other hand, failure modes cause fracture, rearing or deterioration of deterioration of connection capacity. Similar to yield mechanisms, all connections have a number of likely failure modes. The critical failure mode is that with the lowest resistance of all possible modes for the given connection. The ductility and the inelastic performance of a connection are controlled by the proximity of the critical failure mode resistance to the controlling yield mechanism resistance. Connections with a controlling yield mechanism resistance significantly lower than the critical failure mode resistance develop considerable inelastic deformations and therefore exhibit high plastic rotations capacity.

4.3.5 System properties

The lateral stiffness of a structure depends on the type of system utilized to withstand horizontal, the distribution of the member stiffness and the type of horizontal diaphragms connecting vertical members. Moment resisting frames are generally more flexible than braced frames. Frames with rigid connections exhibit higher stiffness than those with semi-rigid connections.

The lateral resistance of a system is not the sum of the resistance of its components and the connections between them. Beam, columns, and connections interact in a complex

manner. Their structural response is not amenable to simple parallel or series system representations. Moment resistance frames as lateral resistant systems possess relatively high lateral strength, although their stiffness and ductility vary significantly (Al Chaar et al., 2002; Fardis and Panagiotakos, 1997). Cyclic loading may cause loss of resistance in structural components and the connections between them.

The most convenient parameter to quantify the global ductility of structural systems under lateral loads is the displacement ductility. Displacement ductility factors should be expressed as storey drift ductility rather than roof lateral displacement. Storey translational ductility is a measure of the ductility distribution along the height in multi-storey frames and can be utilized to detect localized inelastic demands in irregular structures. Two frames may possess the same values of roof translational ductility although the distribution of the storey drift ductility is different along the height.

The evaluation of the deformation quantities from load-deformation relationships is not always straightforward. Yield points are often ill defined because of nonlinear properties and formation of plastic hinges in beams, columns, and joints. Response curves of RC structures frequently do not present well defined yield points because of cracking of concrete and sequential yielding of reinforcement bars. The global ductility of structural systems significantly depends on available local ductility. Large inelastic deformations and large amounts of energy dissipation require high values of local ductility.

In multi-storey framed buildings, plastic lateral displacements are frequently higher than those estimated for simple cantilever systems. The displacements include contributions from different sources of deformations, such as flexibility of the foundation system. Global mechanisms with plastic hinges at column bases and within beams are preferred due to the higher energy dissipation capacity. Consequently, to ensure adequate energy dissipation and prevent dynamic instability of the system as a whole, plastic hinges at the base should possess high rotational ductility. Members with large slenderness ratios should be avoided, and the level of axial loads should not exceed 25-30% of the plastic resistance in the columns (Elnashai and Sarno, 2008). High axial compressive actions endanger the inelastic deformation capacity of structural members. Furthermore, variations of axial loads in columns due to

overturning moments and vertical vibration modes increase the likelihood of local and global instability (Saneinejad and Hobbs, 1995).

Global ductility of structures is also correlated to the capacity of lateral resisting systems. It suffices to state here that in general, with a given earthquake ground motion and a significant vibration period, the global ductility increases as the yield level of the structural system decreases.

4.4 EFFECTS ON ACTION AND DEFORMATION DISTRIBUTION

Lateral forces are distributed among lateral resisting systems in the elastic range as a function of their relative stiffness and ductility. Stiffer elements and structural systems will reach their capacity earlier than their flexible counterparts. Significant reductions of the initial stiffness may occur in construction materials, structural members, and connections when they are subjected to increasing loads. Repeated loading also reduces effective stiffness in terms of stiffness degradation. The lateral deformability of structural systems is measured through horizontal drift. In buildings, storey drifts are the absolute displacements of any floor relative to the base, while inter-storey drifts define the relative lateral displacements between two consecutive floors. The storey drift is generally expressed as a ratio of displacement at the top floor to the total height of the building (Ambrose and Vergun, 1999). Drifts of the roof are also used to quantify the lateral stiffness of structural systems.

Inter-storey drifts are caused by flexural, shear, and axial deformations of structural elements, e.g. beams, columns, and connections. Axial deformations due to shortening or elongation of members are generally negligible. Flexural and shear deformations are the primary cause of non-structural damage. The overall lateral deformation is affected by the structural system utilized. In moment resisting frames, axial deformations of both beams and columns are not significant. Conversely, axial deformations influence the lateral response of braced frames (Andreason and Rose, 1994; Baker et al., 1989).

In addition to the importance of absolute stiffness, the relative stiffness of members within a structural system is significant, especially in lateral force assessment, because it influences the distribution of actions and deformations. For example, deep beams provide effective restraint for columns in frames structures. If the flexural stiffness of beams is much higher than that of columns, the structure exhibits shear-frame response.

However, in single-span frames, beam-floor systems with very low flexural stiffness do not restrain the rotation of the columns connected to them.

4.5 STRUCTURAL DAMAGE CONTROL

Strength is generally associated with the control of structural damage. Strength failure may be caused by accumulated stresses beyond the capacity of materials, members, and connections in the structure. The relationship between local and global structural response is shown in Figure 4.3. The occurrence of damage in structural components can also be associated with the onset of target values of strains in materials, curvatures in sections, rotations in connections, inter-storey in subsystem and global drift of structural systems (Elnashai and Sarno, 2008). Damage control can be achieved at sites of both local and global damage. It is recommended that limit states at all levels are defined and continuously assessed since no one single quantity is suited to controlling all levels of damage. In general, damage increases as allow for the occurrence of a limited amount of controlled structural damage. In RC structures, repairable damage includes spalling of concrete cover and formation of flexural cracks. Fractures and buckling of reinforcement bars are not readily repairable.

Under lateral loads, stress concentrations may occur in critical regions of sections with maximum bending and shear forces. The concentrations are also typically observed where abrupt changes in the structural layout are present. Large reversing actions may lead to stiffness and strength deteriorations. Stiffness and strength degradation accelerate the occurrence of failure.

Limiting damage in beam-column and column-foundation connections is essential to achieve adequate performance of the structural system. Excessive cracking and bound deterioration should be prevented, especially in RC joints. Reductions in joint shear capacities are detrimental to the seismic performance of framed systems. Damage in beam-column joints significantly increases the inter-storey drifts and may endanger the stability of the structure as a whole. In frame systems with no structural walls, strength and stiffness often increase proportionally, especially in RC and composite structures. Seismic retrofitting generally includes wrapping with fiber reinforced polymers.

Overturning of moments is caused by horizontal seismic loads, which tip the structure with or without its foundation. This mechanism is referred to as uplift. Strong

foundations are often more effective in resisting overturning moments than weak foundations. Overturning can also generate net tension and excessive compression in columns.

4.6 DAMAGE DETECTION METHODS BASED ON NONLINEAR BEHAVIOR OF STRUCTURE

In structural damage detection, a damage index (*DI*) is used to monitor the damage status of structure. This value is equal to zero when there is no damage and is equal to one when total collapse occurs. Damage indices can be classified in different ways. The local damage index indicates damage of the structural elements or a part of the structure while the global index considers damage of the whole structure. There are various parameters of physical responses to formulate the damage index of a structure. These parameters can be classified as deformation, change in stiffness, energy dissipation, and changes in dynamical parameters (Estekanchi and Arjomandi, 2007). A damage index can involve a combination of one or more damage variables in its calculation. Some of more significant damage indices are studied and presented in this work.

4.6.1 Park and Ang Damage Index

Park and Ang (1985) have formulated a well known damage index to estimate the level of damage in structures. This damage index contains the damage caused by the maximum deformation and the damage due to dissipated energy under cyclic loading. Both components of damage are linearly combined:

$$DI_{Park} = \frac{\delta_{\max}}{\delta_u} + \frac{\beta}{\delta_u P_y} \int dE_h \qquad (4\text{-}1)$$

where $\delta_{\max}$ is the maximum experienced deformation; δ_u and P_y are the ultimate deformation under monotonic loading and yield strength of the structure respectively, which can be calculated using nonlinear finite element analysis; $\int dE_h$ is the hysteretic energy absorbed by the structural element during the response history; and β is a model constant parameter.

4.6.2 Stiffness Damage Index

Kanwar et al. (2007) proposed the stiffness damage index DI_k, which uses an indicator based on the relationship between the material stiffness properties of the undamaged element and the damaged element of the structure. According to this method severity of damage is expressed as the fractional change in stiffness of an element:

$$DI_k = \frac{k_j - k_j^*}{k_j} = 1 - \frac{1}{\nu_j} \tag{4-2}$$

where ν_j is stiffness ratio, k_j is initial stiffness of undamaged element and k_j^* is the initial stiffness of the damaged element of the j^{th} member. The asterisk (*) denotes the damage state.

4.6.3 Displacement ductility and drift ratio

At service level, damage is also interpreted as the level of nonstructural damage that results from excessive building deformations. Considering the common concept of damage, displacement ductility factor, and drift ratio can be used to predict the damage state of a structure.

4.6.3.1 Displacement ductility

The structural displacement ductility factor, μ is defined as follows

$$\mu = \frac{\delta_u}{\delta_y} \tag{4-3}$$

where δ_y is the structural yield displacement and δ_u is the structural displacement at ultimate damage state.

4.6.3.2 Drift ratio

The drift ratio is defined as follows:

$$Drift = \frac{\delta_m}{H} \tag{4-4}$$

The structural drift is defined as the ratio between the displacement of structure δ_m at the target position *m*, and the story height *H*.

4.7 CORRELATION COEFFICIENT

In general statistical usage, correlation can refer to any departure of two or more random variables. There are several correlation coefficients. The most common of these is the Pearson correlation coefficient, which is sensitive only to a linear relationship between two variables. It is obtained by dividing the covariance of the two variables by the product of their standard deviations (Higgins, 2005 and Nelson, 2004). There is positive correlation if the variables tend to increase or decrease together, and negative correlation if one variable tends to increase as the other decreased.

However, the term is often restricted to describing the extent to which the variables have a linear relationship. If corresponding pairs of values are plotted as points on a graph to give a scatter diagram, the correlation between the variables is indicated by how close the points are to lying in a straight line. If the points are close to some line, the variables are said to be highly correlated.

If the variables are a series of *n* paired of *X* and *Y* written as x_i and y_i where $i = 1, 2, \ldots, n$, then the correlation coefficient can be used to estimate the Pearson correlation *r* between *X* and *Y*. The correlation coefficient is written

$$r = \frac{n\sum_i x_i y_i - \sum_i x_i \sum_i y_i}{\sqrt{\left(n\sum_i x_i^2 - \left(\sum_i x_i\right)^2\right)\left(n\sum_i y_i^2 - \left(\sum_i y_i\right)^2\right)}} \qquad (4\text{-}5)$$

Correlation between two variables is a number between -1 and +1. The value is close to +1 if the variables are highly positively correlated. High correlation need not imply a direct causal relationship.

4.8 NONLINEAR BEHAVIOR RESULTS AND DAMAGE INDICES

In order to assess the damage of experimental frames subjected to lateral loads, it is necessary to evaluate nonlinear behavior, which leads to the deterioration of strength,

stiffness, and energy dissipation capacity. According to these results, it is convenient to use the stiffness damage index and the Park and Ang damage index to calculate the probability of failure of a structure, because the stiffness damage index is based on the ratio between the changes in structural stiffness only. As is well known from the Park and Ang damage index, the causes of failure of RC elements are mainly inelastic deformations and energy dissipation. In this section, the nonlinear behavior and these indices are presented. Control Frame is the term for the experimental frame, undamaged or damaged, before retrofitting. Retrofitted Frame is the term for the experimental frame after damage and subsequent retrofitting.

4.8.1 Control Frame 1

The experimental frame model of Control Frame 1 was constructed as a brittle structure and the frame was loaded in a lateral direction on the top floor. The quasi-static load was applied uniformly in small incremental steps by a hydraulic jack as shown in Figure 4.4. Damage indexes can be calculated from the equations laid out in the previous section. Structural stiffness degradation can be observed from the load-displacement plot of each load step as shown in Figure 4.5. The summary of load and displacement behavior of the system is presented in Table 4.1. The experimental results show that the initial diagonal cracks appeared in the beam-column joints of the top floor at a load of 10 kN corresponding to a drift of 0.63%, indicating that structural elements of the top floor were the most stressed. The system damage indices of DI_{Park} and DI_k were 0.32 and 0.25 respectively, a moderate damage state. Large cracks started to open and small cracks occurred in the second and first floor connection at a load of 12.5 kN at displacement of 31 mm (1.09% drift), DI_{Park} of 0.49, DI_k of 0.47. The load-displacement plot at the top floor of Control Frame 1 is shown in Figure 4.2 and presented in Table 3.2. The crack pattern of this experimental frame is shown in Figure 4.6. After load removal, the frame model moved back to a new position 10 mm from initial state, indicating that the yield point was visible at a load 12.5 kN which was a severe damage state. The ultimate damage state of the frame was achieved at the load, P_{max}, of 16.5 kN with a displacement of 69 mm (2.42% drift), leading to DI_{Park} of 0.95 and DI_k of 0.69, respectively. The ductility index was 2.22, and the cumulative energy dissipation was observed to be 568 kN-mm.

Figure 4.8 presents the normalized plot of the correlation ratio between applied load P with ultimate load P_{max}, and DI_{Park}. Figure 4.9 presents the normalized plot of P with P_{max} and the relative change of DI_k. The correlation coefficient of 0.954 shows that DI_k of the control frame seems to increase in linearly due to a increase in load, while DI_{Park} with correlation of 0.936 exhibits two different trends. The general trend of DI_{Park} is slightly changed because the cumulative effects of deformation and energy dissipation are low when the damage is less than moderate. In a higher deformation trend, DI_{Park} changes shape when the structure starts to lose its load carrying capacity after huge cracks occurred in the structure. At final state, the crack pattern is diagonally shaped in joints. It indicates that shear resistance capacity of this specimen is low. The energy of the heavily damaged elements was absorbed in connections at the top floor. The first plastic hinges were formed in the top floor by shear failure.

4.8.2 Retrofitted Frame 1

The test for the Retrofitted Frame 1 was performed in the same manner as with Control Frame 1. The load-displacement plot is shown in Figure 4.5 along with the behavior of the Control Frame 1. After the last test on Control Frame 1 was concluded, the cracks of the damaged control frame were grouted with the MBrace Primer and made surface smooth with MBrace Putty, then covered with GFRP sheets as per the procedure explained in Section 3.3.4.

There were slipping sounds of GFRP sheets when a load of 6 kN was applied, indicating that MBrace Primer could not repair huge cracks in the damaged Control Frame 1. The results also show that the yield state was obtained at a load of 18 kN with a displacement of 24.8 mm corresponding to a drift of 0.87%. The system damage indices of DI_{Park} and DI_k were 0.24 and 0.50, respectively. The sound of fiber slip has been observed again with a flexural load of 18 kN at beam-column joints. The relationship between load and displacement can be roughly considered to be linear when the load is less than or equal to yield point. The ultimate state was achieved with a load of 25 kN and displacement of 83 mm from initial state (2.91% drift). At this state, the ductility index was 3.34; cumulative energy dissipation was 1,040 kN-mm; DI_{Park} was 0.88 and DI_k was 0.66, while there were breaking sounds of fiber and epoxy layers before fail.

The summary of load and displacement behavior of the system of Retrofitted Frame 1 is presented in Table 4.1 along with the results of Control Frame 1. Crack pattern of Retrofitted Frame 1 is shown in Figure 4.7. This figure shows that no significant flexural cracks were observed on the outside fiber layers. Failure mode of this retrofitted frame was governed by fiber layers slip. Moreover, flexural failures appeared inside connection joints of columns and beams at each floor. According to the correlation between applied loads and damage indices, it clearly shows that DI_k with correlation of 0.989 has more linear relationship with applied loads than DI_{Park} with correlation of 0.823.

Results of Retrofitted Frame 1 show that the use of GFRP wrap for structural strengthening provided significant lateral load capacity, increasing to 152% as compared to Control Frame 1. The FRP sheets wrapped around the structural elements in this manner are intended to provide external confinement and crushing of the concrete cover at larger displacements. According to the change of structural displacements, the ductile behavior and the cumulative energy dissipation of the retrofitted frame is largely restored after the GFRP sheets are engaged in general. The change in damage index is shown in Figure 4.8 and 4.9. Moreover, the health of these RC frames, both original and retrofitted, is compromised when DI_{Park} and DI_k increases to more than 0.5 or structural stiffness is reduced by more than 50% of the initial state.

4.8.3 Control Frame 2

The Control Frame 2 was constructed in same detail as Control Frame 1. This frame was loaded to 11.5 kN (70% of maximum load of Control Frame 1) in steps to simulate moderate damage. The change of displacement with the increase of applied loads is given in Figure 4.10; the crack pattern of Control Frame 2 is shown in Figure 4.11; and damage indices are shown in Figures 4.13 and 4.14. Stiffness degradation can be seen in the load-displacement plot. There was no cracking at a load less than 7.5 kN with displacement 9.47 mm, 0.31% drift, DI_{Park} 0.18, and DI_k 0.40. The initial diagonal cracks were observed in the beam-column joints of the top floor at a load of 10 kN. At final state of 11.5 kN, displacement was 22.05 mm, drift is 0.72%, and energy dissipation was 56 kN-mm. The system damage indices for DI_{Park} and DI_k were 0.61 and 0.56, a moderate damage state. At final state, cracking size at the top floor were

larger than at the second or first floor. It supports the conclusion that structural elements of top floor were the most stressed. At the corresponding load of final state, small diagonal cracks of shear failure mode were observed at the second floor. There was no plastic hinge on this frame. The summary of load versus displacement behavior of Control Frame 2 is presented in Table 4.2 and the correlation coefficients between applied load and damage indices are presented in Table 4.7.

4.8.4 Retrofitted Frame 2

At the conclusion of the final stage of the preceding test the cracks of the damaged Control Frame 2 were grouted in the same process as Retrofitted Frame 1. There was no slipping sound of GFRP sheet when a small load was applied. It seems that MBrace Primer properly repaired small cracks inside damaged Control Frame 2. The results of Retrofitted Frame 2 show a yield state of 18 kN, displacement of 22.4 mm, and corresponding drift of 0.73%. The system damage indices DI_{Park} and DI_k were 0.24 and 0.49, respectively. The slipping sound of GFRP sheet was observed from the load of 18 kN at beam-column joints. The ultimate state was achieved at the load of 26 kN with the breaking sounds of GFRP sheets, displacement 75.1 mm from initial state, 2.46% drift, ductility index 3.35, cumulative energy dissipation 918 kN-mm, DI_{Park} 0.87, and DI_k 0.71. Crack pattern of Retrofitted Frame 2 is shown in Figure 4.12. At the end of this test, no observable flexural cracks on the outside GFRP layer was seen. Delamination between GFRP and concrete caused the failure of Retrofitted Frame 2. After removing FRP layers, it was observed that old cracks were enlarged and new flexural cracks appeared at beam-column joints and structural elements. The summary of load versus displacement behavior of Retrofitted Frame 2 is presented in Table 4.2 and the correlation coefficients between applied load and damage indices are presented in Table 4.8. From Table 4.8, the non-monotonic behavior of DI_{Park} is due to the fact that this index is sensitive to cracks in RC structure after yield.

Results also show that GFRP sheets wrapped around moderately damaged elements in this manner increased load carrying capacity to 104% and 158% of Retrofitted Frame 1 and Control Frame 1 respectively. It also shows that energy dissipation of Retrofitted Frame 2 deceased nearly 12% as compare to Retrofitted Frame 1. The change in damage indices of Retrofitted Frame 2 is shown in Figure 4.13 and 4.14 along with the

behavior of Control Frame 2. The experimental results also support that the health of Retrofitted Frame 2 seem to become unsafe when DI_{Park} and DI_k increases to more than 0.5. Debonding of GFRP sheets at beam to column connections produced failure modes of Retrofitted Frame 2.

4.8.5 Control Frame 3

The Control Frame 3 was a ductile RC structure constructed to resist lateral load following Indian standard: IS-13920. The change of displacement with the increase of applied loads is shown in Figure 4.15, crack pattern of Control Frame 3 is shown in Figure 4.16. The onset of diagonal cracks occurred in beam-column joints of the top floor at a load of 15 kN, drift of 0.74%, DI_{Park} of 0.28, and DI_k of 0.49. Yield point was observed at a load 18 kN, displacement of 28 mm (0.98% drift), DI_{Park} of 0.37, and DI_k of 0.55, a severe damage state. Small diagonal cracks were observed in the second and first floor connections when the load was increased to more than 18 kN. The ultimate damage state has been achieved at the load of 24 kN, a displacement of 76 mm (2.67% drift), leading to DI_{Park} of 0.76 and DI_k of 0.68. At final state, wide diagonal cracks developed in beam-column joints and flexural cracks occurred in the hinge areas of columns. It indicates that mode of failure of Control Frame 3 was a combination of shear and flexural modes. The ductility index was 2.71 and cumulative energy dissipation was observed to be 748 kN-mm. The summary of load-versus-displacement behavior of Control Frame 3 is presented in Table 4.3. The correlation coefficient of Control Frame 3 between applied loads and DI_{Park} was 0.894 and correlation coefficient of DI_k was 0.990 as presented in Table 4.9.

It can be seen in Figures 4.18 and 4.19 that Park and Ang damage indices are higher compared to the stiffness damage index at the end of the test, indicating that Park and Ang index is a more reliable method, correlating with the change in stiffness index in this study. According to the results of the tested frame models as shown in Figure 2.20, the displacement ductility index of Control Frame 3 is approximately 22% higher than in the Frame 1, the load carrying capacity increases 45% and cumulative energy dissipation increases 32%. In other words, the ductile RC moment-resisting frame (Control Frame 3) provides significant lateral load capacity, ductility behavior and energy dissipation capacity as compared to the brittle frame (Control Frame 1).

Generally, the contribution of damage of each structural RC element to total displacement is associated with its internal confinement effect of transverse reinforcement bars and longitudinal anchorage of beam bars in external joints.

4.8.6 Retrofitted Frame 3

Wide cracks of the damaged Control Frame 3 were grouted using a high strength adhesive epoxy injection and fine cracks, with MBrace primer. Then this frame was retrofitted using MBrace Putty and GFRP with epoxy resin as per the procedure explained in Section 3.3.4. Experimental results of Retrofitted Frame 3 show that no initial moving sound of fiber layers was observed when a small load was applied. It seems that the use of high strength adhesive epoxy injection was successful in repairing wide cracks in the damaged elements. The relationship between load versus displacement plot and crack pattern of Retrofitted Frame 3 are shown in Figure 4.15 and 4.17. On the basis of these figures, the load displacement relation can be considered to be roughly linear when the load is smaller than or equal to 30 kN. Beyond that, the relation changes shape. It indicates that yield state of the Retrofitted Frame 3 occurred at a load 30 kN, displacement of 38 mm (1.33% drift), DI_{Park} of 0.30 and DI_k of 0.44. Under this load the sound of the GFRP layer slip was observed. The ultimate damage state of Frame 3 was achieved at the load of 43 kN at displacement of 123mm from initial state (4.32% drift) leading to the displacement ductility factor of 3.75, energy dissipation of 2414 kN-mm, DI_{Park} of 0.84, and DI_k of 0.57. There were breaking sounds of fiber layer in tension zones of beam-column joints and horizontal cracks occurred in columns near stub foundations at the final state. In addition to old cracks which reopened, new flexural cracks also appeared in structural elements. Summary of the experimental nonlinear behaviors is presented in Table 4.4.

The normalized plots of the correlation ratio between applied loads and damage indices of Retrofitted Frame 3 are presented in Table 4.10 and shown in Figure 4.18 and 4.19. These figures show that DI_k with correlation of 0.993 increases linearly from the initial state to the final state and the curve of DI_{Park} with correlation of 0.901 suddenly changes shape when the load increases beyond yield point. In the case of strengthening the ductile RC structure, although DI_{Park} and DI_k of Retrofitted Frame 3 reduce at the final stage of the test, they are still close to those of Control Frame 3. The load-

displacement plots at the top floor of all control frames are shown in Figure 4.20, as retrofitted frames are shown in Figures 4.21. These figures show that the use of GFRP wraps for Retrofitted Frame 3 provides significant lateral load capacity increases of approximately 79% and 72% vis-a-vis Control Frames 3 and Retrofitted Frame 1, respectively. Failure modes of Retrofitted Frame 3 were debonding of GFRP sheets at beam-column joints and flexural failure mode in columns near the stub foundation.

4.9 FAILURE MECHANISM

4.9.1 Failure Mechanism of Control Frames

The experimental crack patterns at final state of control frame models are shown in Figures 4.6, 4.11 and 4.16. These figures show that in the yield damage state first diagonal cracks were observed at beam-column joints of the top floor. These opening cracks increased with the increase of load. The second and third diagonal cracks occurred at beam-column joints of the second and first floors respectively. It indicates that first plastic hinges initiated at the top floor and the other hinges followed at second and first floors sequentially. The failure modes of Control Frame 1 and 2 show that the lateral load carrying capacity was rendered insufficient due to non-ductile reinforcement detailing, which included no beam-column joint transverse reinforcement. Therefore, the top and bottom bars move in opposite directions under the combined force. These forces are balanced by bond stress developed between concrete and steel bars. In such circumstances, plastic hinges were formed by debonded bars, and beam-column joints lost their capacity to carry loads. The load-displacement plots of Control Frame 1, 2 and 3 are shown in Figure 4.20. The load carrying capacity of Control Frame 3 (a ductile RC structure) was influenced by the internal confinement of steel stirrups and the bond strength of longitudinal anchorage beam bars. The sufficient detail of steel stirrups and anchorage steel bars increased its load resistance capacity and delayed both moment and shear force effects in external connections. The structure suddenly lost its load carrying capacity when cracks crossed from tension surfaces to compression surfaces of structural cross section elements. In the final state, both diagonal and flexural cracks occur in structural elements of each floor, indicating that the failure mode of control frames was a combination of shear mode and flexural

mode failure. Relatively few and only small flexural cracks were observed at columns near the stub foundation.

4.9.2 Failure Mechanism of Retrofitted Frames

The experimental results of retrofitted frames show that after the structure reaches yield load, the bond of flexural GFRP layers delaminate along the interface between the concrete and GFRP. It is observed that the delamination was always achieved at the corner of beam-column joints in tension zones. The cracks with sounds of fiber layer slip were initiated at connection of top floor and other cracks were subsequently formed at second and then first floors. Figure 4.7, 4.12 and 4.17 show that after the GFRP sheet debonded, the retrofitted structures lost their load carrying capacity. The GFRP confinement layers suddenly delaminated at ultimate load with breaking sounds. Cracks occurred at the edge of GFRP layers at final state and huge cracks occurred inside the existing RC elements behind strengthening layers. However, there was a wide horizontal crack inside each retrofitted column near the stub foundation, which was preferable overloading of the footing. At this position, there was a gap of around 5 mm between the edge of GFRP jacket and the adjacent stub foundation, which results in the existing columns' carrying a load without the help of strengthening material. Again, the primary failure mechanism of retrofitted frames was debonding of the FRP sheets. It occurred at the base of the huge cracks in tension zones of the damaged RC elements.

Table 4.1 Relationship between load and displacement at top floor of Frame 1

Control Frame 1				Retrofitted Frame 1			
P (kN)	Displacement (mm)	P (kN)	Displacement (mm)	P (kN)	Displacement (mm)	P (kN)	Displacement (mm)
0.0	0.0	2.5	13.56	0.0	0.0	9.2	12.64
1.00	0.46	4.0	16.34	1.5	0.62	12.3	16.60
2.5	**1.94**	8.0	22.74	**3.0**	**2.15**	15.0	20.10
0.0	0.30	10.0	26.52	0.0	0.35	16.5	22.13
1.5	1.04	12.0	28.31	0.8	0.70	**18.0**	**24.81**
2.7	2.35	14.0	32.58	2.5	1.82	0.0	3.92
4.0	3.80	**15.0**	**43.57**	4.0	3.55	3.0	6.86
5.0	**4.88**	0.0	21.06	**6.0**	**5.88**	6.0	10.76
0.0	0.80	1.1	22.71	0.0	0.50	9.0	14.72
1.5	1.62	2.2	24.22	1.9	1.45	15.2	23.23
2.7	2.97	4.0	27.93	3.0	2.92	18.0	26.99
4.5	4.57	5.5	30.42	5.0	5.36	19.5	29.40
6.0	6.90	6.8	33.02	6.0	6.41	**21.0**	**33.04**
7.5	**9.14**	9.0	34.99	8.0	8.66	0.0	6.42
0.00	2.45	11.5	39.85	**9.0**	**9.97**	3.2	10.36
2.5	4.76	13.5	43.83	0.0	1.00	7.0	15.15
5.0	7.45	15.0	51.87	2.0	2.17	10.0	19.41
7.5	9.97	16.5	54.90	4.0	4.41	15.0	27.11
9.0	12.33	**16.5**	**69.00**	6.0	6.57	18.0	31.18
10.0	**14.80**	0.0	35.62	8.1	8.98	21.0	39.50
0.0	5.13			10.0	11.21	23.2	47.32
1.7	6.57			**12.0**	**13.78**	24.0	50.95
2.5	8.03			0.0	1.92	25.0	64.06
4.5	10.45			2.0	3.32	**25.0**	**82.90**
5.5	12.68			4.6	6.27	0.0	42.92
7.0	14.48			7.4	9.59		
8.0	16.39			10.2	12.56		
10.0	19.00			12.3	15.10		
12.0	23.75			**15.0**	**18.75**		
12.5	**31.00**			0.0	2.92		
0.0	10.15			3.0	5.42		
1.0	11.37			6.0	9.04		

Table 4.2 Relationship between load and displacement at top floor of Frame 2

Control Frame 2		**Retrofitted Frame 2**			
P (kN)	Displacement (mm)	P (kN)	Displacement (mm)	P (kN)	Displacement (mm)
0.0	0.0	0.0	0.0	15.0	18.82
1.0	0.62	1.0	0.26	**18.0**	**22.36**
2.0	1.48	2.0	0.88	0.0	4.75
2.5	**2.10**	**3.0**	**1.53**	3.0	7.24
0.0	0.20	0.0	0.23	6.0	10.99
1.5	1.38	2.0	1.10	9.0	14.74
3.0	3.40	3.0	2.00	12.0	17.71
4.0	4.30	4.5	3.20	13.8	19.19
5.0	**5.66**	**6.0**	**4.45**	15.0	21.55
0.0	1.10	0.0	0.86	18.0	24.86
1.5	2.65	2.0	1.78	**21.0**	**30.79**
3.0	4.69	4.5	3.71	0.0	10.63
4.5	5.96	6.4	5.45	2.8	13.64
6.0	7.06	7.5	6.90	6.0	17.11
7.5	**9.47**	**9.0**	**8.17**	9.0	20.88
0.0	2.32	0.0	1.40	11.0	23.13
2.0	5.13	2.0	2.37	15.0	28.92
4.5	8.36	4.0	4.38	18.0	33.83
6.5	11.47	6.0	6.50	20.7	38.05
8.5	15.15	9.0	9.19	23.0	43.40
11.5	**22.05**	**12.0**	**11.94**	25.0	49.14
0.0	7.67	0.0	2.35	26.0	59.50
		3.0	3.98	**26.0**	**75.05**
		6.0	7.52	0.0	38.29
		9.5	11.36		
		12.0	14.03		
		15.0	**17.30**		
		0.0	3.28		
		2.5	4.92		
		6.0	8.57		
		9.0	11.86		
		12.0	15.83		

Table 4.3 Relationship between load and displacement at top floor of Frame 3

Control Frame 3				Retrofitted Frame 3			
P (kN)	Displacement (mm)	P (kN)	Displacement (mm)	P (kN)	Displacement (mm)	P (kN)	Displacement (mm)
0.0	0.0	6.0	13.26	0.0	0.0	20.0	25.50
0.7	0.34	9.0	16.41	2.5	1.04	25.0	31.30
1.5	0.96	12.0	19.79	**5.0**	**3.15**	**30.0**	**37.50**
3.0	**1.95**	15.0	23.54	0.0	0.50	0.0	9.52
0.0	0.20	**18.0**	**28.04**	2.5	1.59	2.0	11.02
1.0	0.76	0.0	10.38	5.0	3.42	6.0	15.32
2.0	1.50	1.5	12.04	7.5	5.22	10.0	19.57
4.0	2.90	3.0	13.07	**10.0**	**7.75**	15.0	25.52
6.0	**4.55**	6.0	16.41	0.0	0.91	25.0	36.57
0.0	0.74	9.0	19.41	3.0	2.34	30.0	43.37
1.0	1.41	12.0	23.16	6.0	4.34	**35.0**	**52.29**
2.0	2.21	15.0	26.54	9.0	6.62	0.0	15.32
4.0	3.60	18.0	31.41	12.0	9.66	3.0	17.72
6.0	5.58	**21.0**	**36.70**	**15.0**	**12.51**	6.0	21.66
7.5	7.11	0.0	14.88	0.0	2.72	15.0	32.02
9.0	**8.73**	1.5	16.70	2.0	3.78	20.0	38.42
0.0	2.70	3.0	18.34	6.0	6.62	25.0	44.02
1.5	3.85	6.0	22.34	9.0	8.66	35.0	58.82
3.0	5.20	9.0	26.43	15.0	12.64	38.0	66.02
6.0	7.74	12.0	31.11	**20.0**	**17.82**	**40.0**	**71.62**
9.0	10.89	15.0	36.57	0.0	4.72	0.0	30.52
12.0	**14.05**	18.0	43.41	2.0	5.89	5.0	35.02
0.0	5.38	21.0	50.73	6.0	8.48	10.0	40.52
1.5	6.75	23.0	60.35	10.0	11.92	15.0	47.28
3.0	8.37	24.0	65.36	15.0	16.06	20.0	53.57
6.0	11.64	**24.0**	**76.14**	20.0	20.54	25.0	61.64
9.0	14.43	0.0	34.88	**25.0**	**25.90**	30.0	72.27
12.0	17.31			0.0	6.75	35.0	80.00
15.0	**20.91**			2.0	8.04	40.0	92.24
0.0	7.38			6.0	12.51	43.0	114.34
1.5	8.89			10.0	15.49	**43.0**	**123.69**
3.0	10.45			15.0	20.50	0.0	62.02

Table 4.4 Performance of RC frame specimens

Specimens	Yield point		Ultimate point		Ductility Index	Energy Dissipation (kN-M)
	Load (kN)	Displacement (mm)	Load (kN)	Displacement (mm)		
Frame 1						
Control frame	12.5	31.0	16.5	69.0	2.22	567.57
Retrofitted frame	18.0	24.8	25.0	83.0	3.34	1039.68
Frame 2						
Control frame	11.5	22.0	16.5	-	-	56.12
Retrofitted frame	18.0	22.4	26.0	75.0	3.35	918.21
Frame 3						
Control frame	18.0	28.0	24.0	76.0	2.71	748.37
Retrofitted frame	30.0	38.0	43.0	123.0	3.75	2413.90

Table 4.5 Damage indices and appearance of Control Frame 1.

P,kN	P/P_{max}	DI_k	DI_{Park}	Appearance
0	0	0	0	Un-deformed
5.0	0.30	0.07	0.09	Un-cracked
7.5	0.45	0.15	0.18	Un-cracked
10.0	0.61	0.25	0.32	Minor cracking
12.5	0.76	0.47	0.49	Severe cracking
16.5	1	0.69	0.95	Loss of shear capacity
Correlation		0.954	0.936	

Table 4.6 Damage indices and appearance of Retrofitted Frame 1.

P,kN	P/P_{max}	DI_k	DI_{Park}	Appearance
0	0	0	0	Un-deformed
6.0	0.24	0.06	0.06	Un-cracked
12.0	0.48	0.29	0.14	Un-cracked
15.0	0.60	0.41	0.18	Un-cracked
18.0	0.72	0.50	0.24	Sound of fiber slip
21.0	0.84	0.58	0.32	Sound of breaking fiber
25.0	1	0.66	0.88	Loss of shear capacity
Correlation		0.989	0.823	

Table 4.7 Damage indices and appearance of Control Frame 2.

P,kN	P/P_{max}	DI_k	DI_{Park}	Appearance
0	0	0	0	Un-deformed
5.0	0.30	0.21	0.11	Un-cracked
7.5	0.45	0.40	0.18	Un-cracked
11.5	0.61	0.56	0.42	Minor cracking
16.5	1	-	-	-
Correlation		0.992	0.930	

Table 4.8 Damage indices and appearance of Retrofitted Frame 2.

P,kN	P/P_{max}	DI_k	DI_{Park}	Appearance
0	0	0	0	Un-deformed
6.0	0.23	0.14	0.05	Un-cracked
9.0	0.35	0.22	0.09	Un-cracked
15.0	0.58	0.43	0.19	Un-cracked
18.0	0.69	0.49	0.24	Sound of fiber slip
21.0	0.81	0.58	0.35	Sound of breaking fiber
26.0	1	0.71	0.87	Loss of shear capacity
Correlation		0.998	0.865	

Table 4.9 Damage indices and appearance of Control Frame 3.

P,kN	P/P_{max}	DI_k	DI_{Park}	Appearance
0	0	0	0	Un-deformed
6	0.25	0.18	0.07	Un-cracked
9	0.38	0.32	0.13	Un-cracked
12	0.50	0.40	0.21	Un-cracked
15	0.63	0.49	0.28	Minor cracking
18	0.75	0.55	0.37	Severe cracking
21	0.88	0.58	0.49	Spalling of concrete cover
24	1.00	0.68	0.96	Loss of shear capacity
Correlation		0.990	0.894	

Table 4.10 Damage indices and appearance of Retrofitted Frame 3.

P,kN	P/P_{max}	DI_k	DI_{Park}	Appearance
0	0	0	0	Un-deformed
10	0.23	0.18	0.07	Un-cracked
20	0.47	0.33	0.15	Un-cracked
25	0.58	0.38	0.21	Un-cracked
30	0.70	0.44	0.30	Sound of fiber slip
35	0.81	0.51	0.37	Severe damage
40	0.93	0.55	0.55	Sound of breaking fiber
43	1.00	0.57	0.84	Loss of shear capacity
Correlation		0.993	0.901	

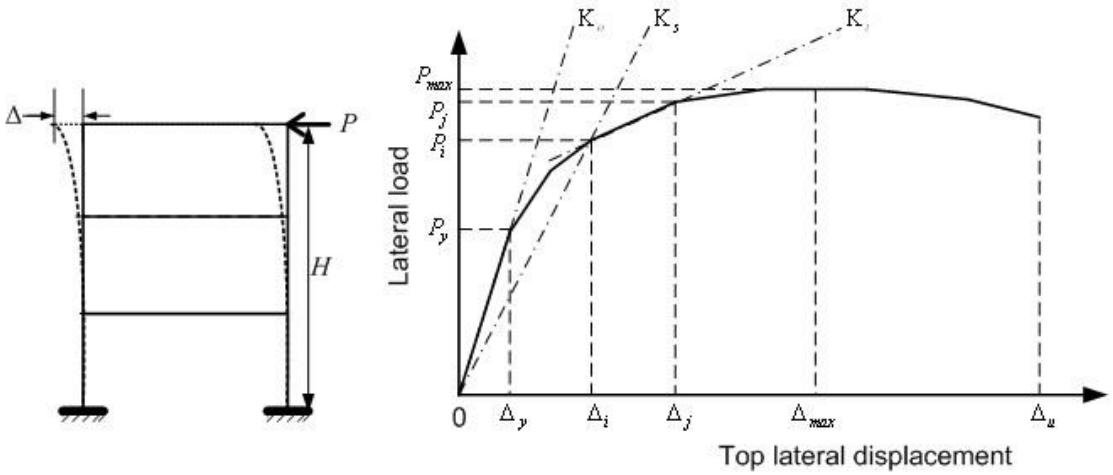

Figure 4.1 Definition of initial, secant and tangent stiffness of structure (Elnashai and Sarno, 2008)

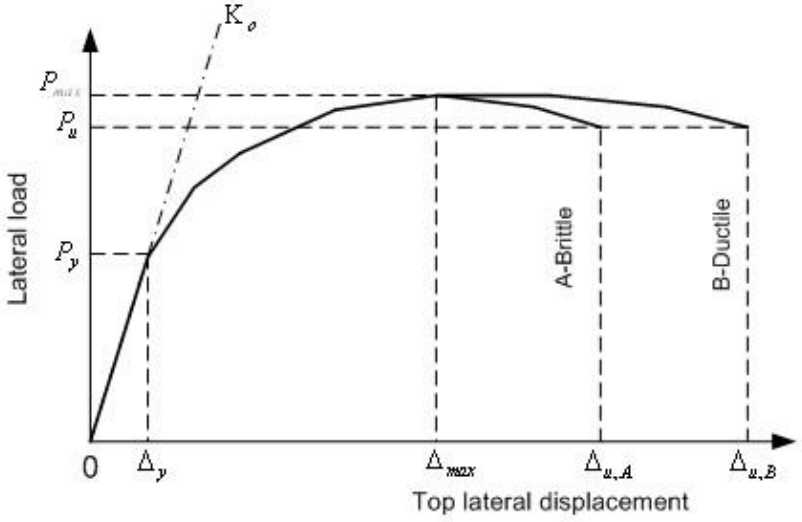

Figure 4.2 Definition of structural ductility (Elnashai and Sarno, 2008)

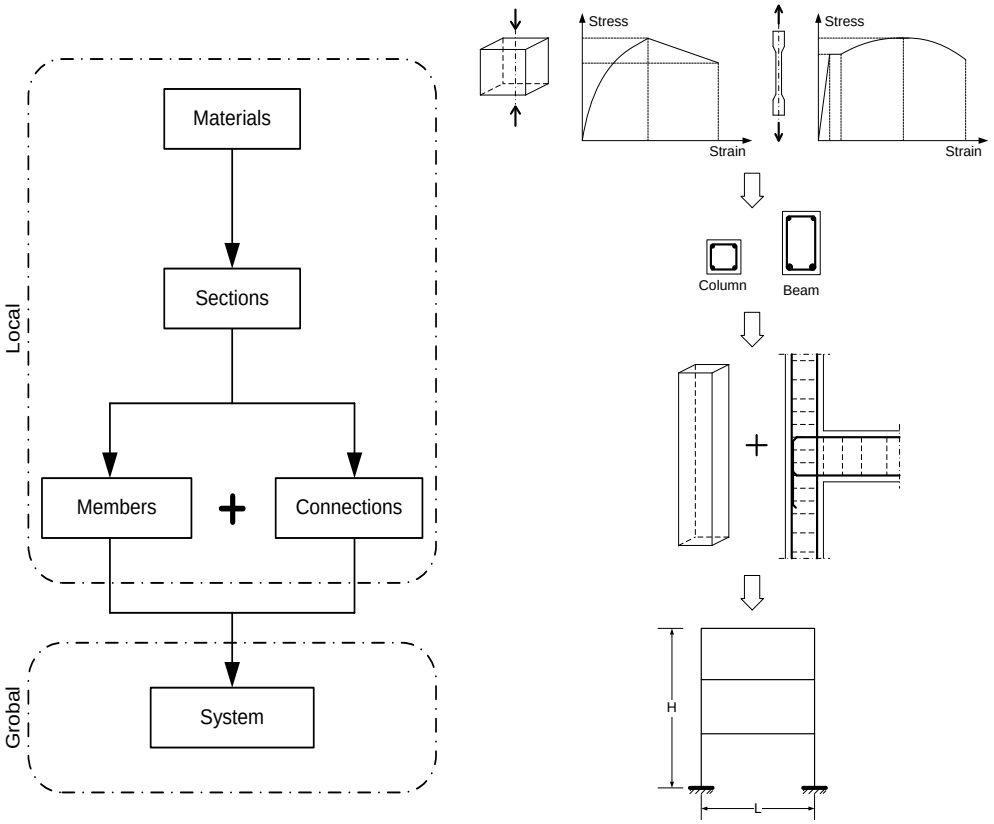

Figure 4.3 Relationship between local and global structural response (Elnashai and Sarno, 2008)

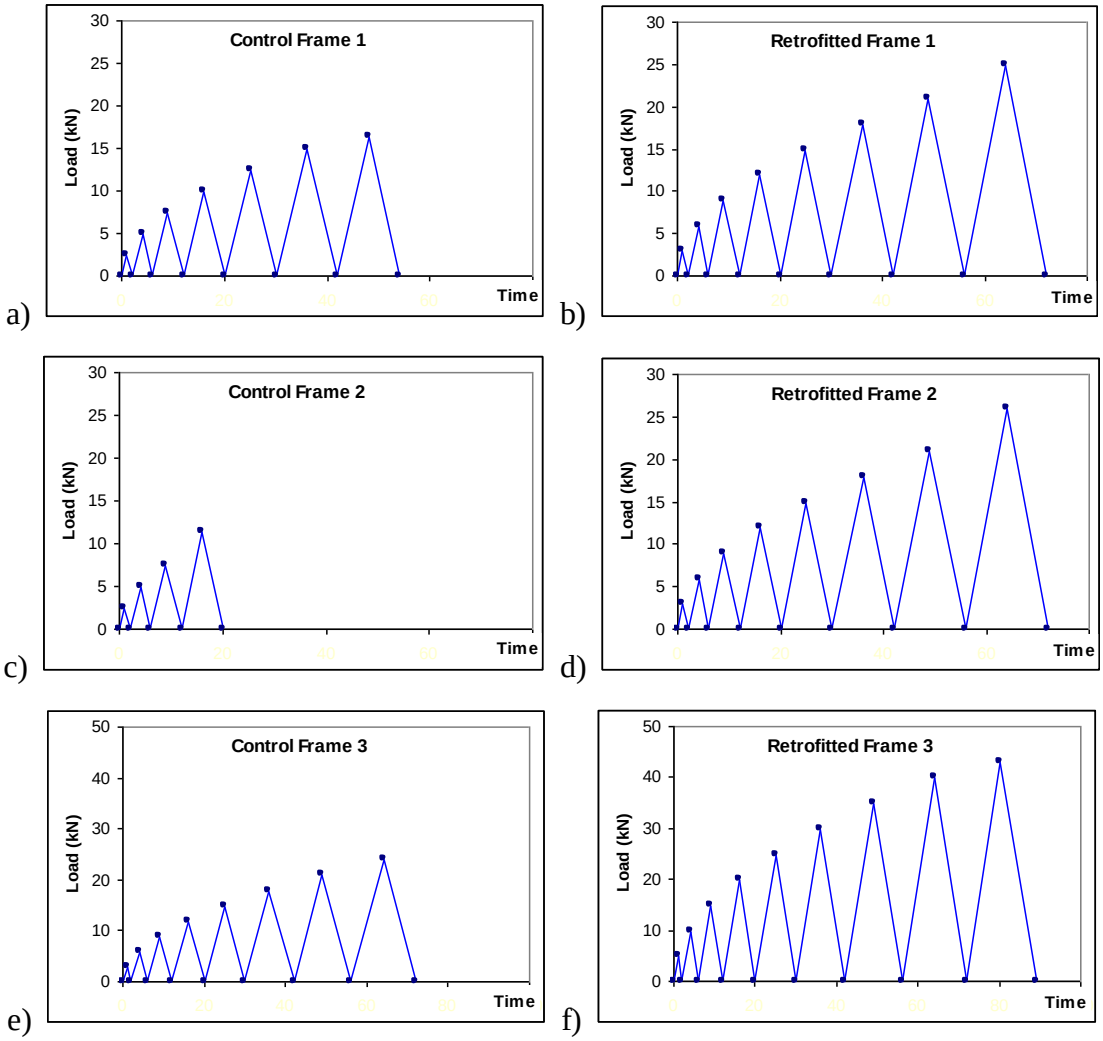

Figure 4.4 Applied quasi-static load histories: a) Control Frame 1, b) Retrofitted Frame 1, c) Control Frame 2, d) Retrofitted Frame 2, e) Control Frame 3 and f) Retrofitted Frame 3.

a)

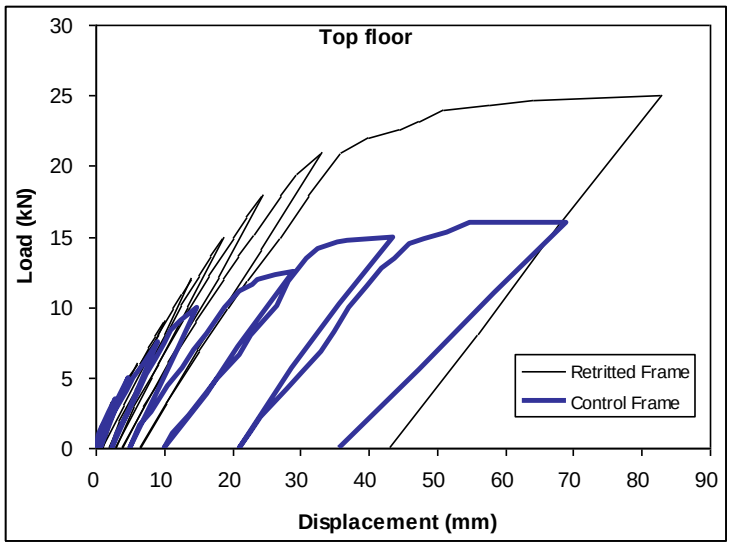

b)

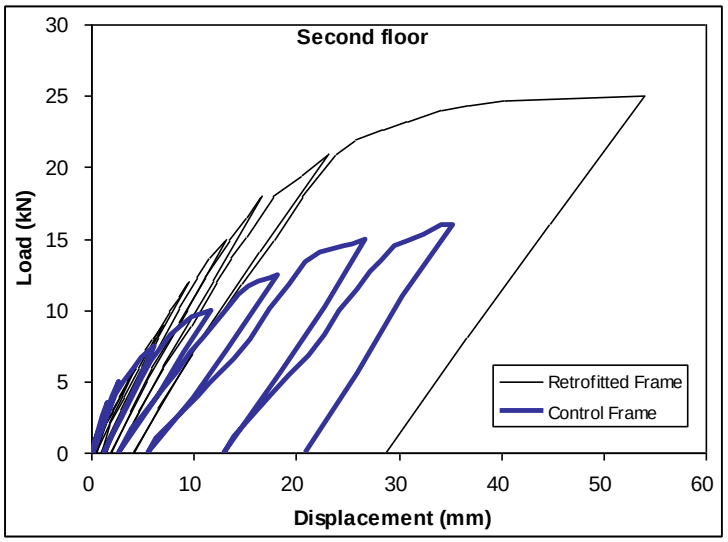

c)

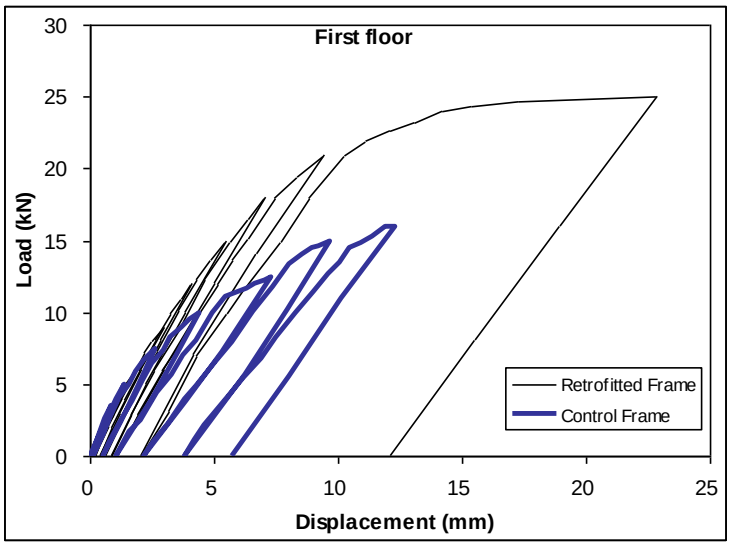

Figure 4.5 Load-displacement behaviors of Frame 1

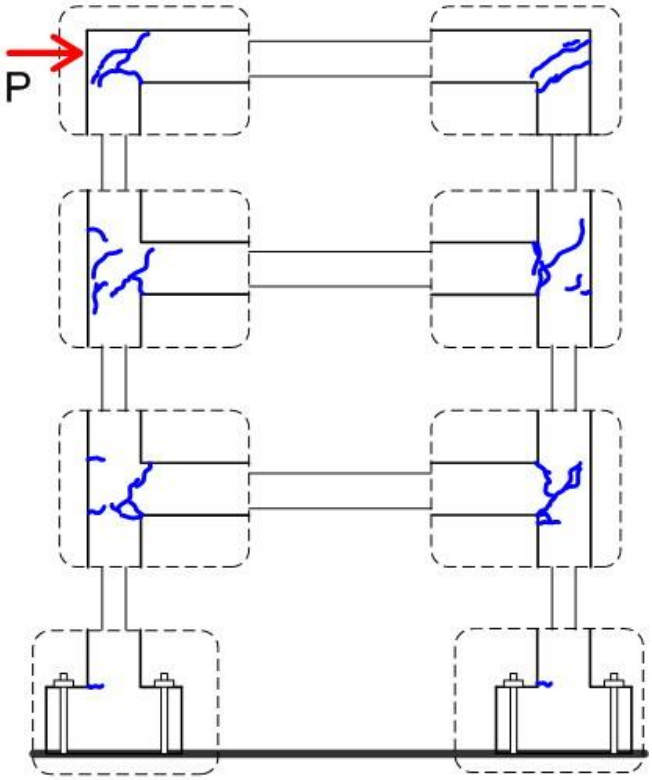

Figure 4.6 Crack pattern of Control Frame 1

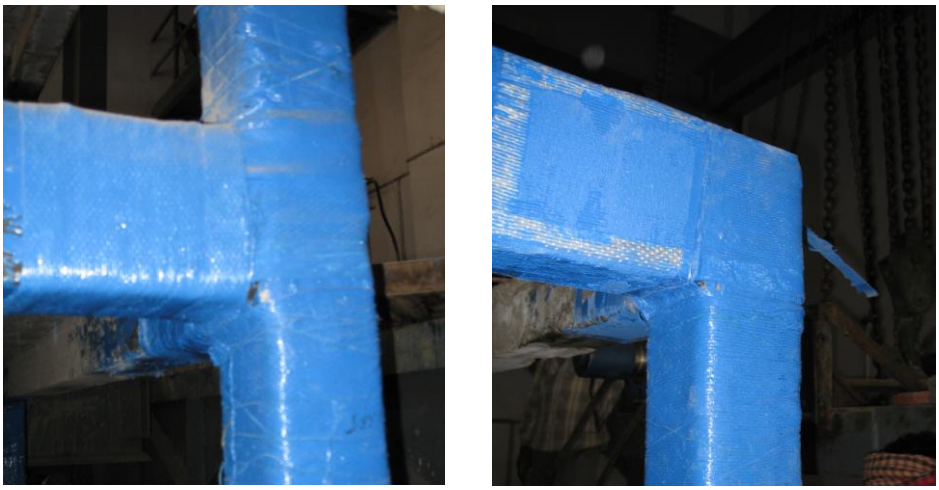

Figure 4.7 Failure pattern of Retrofitted Frame 1

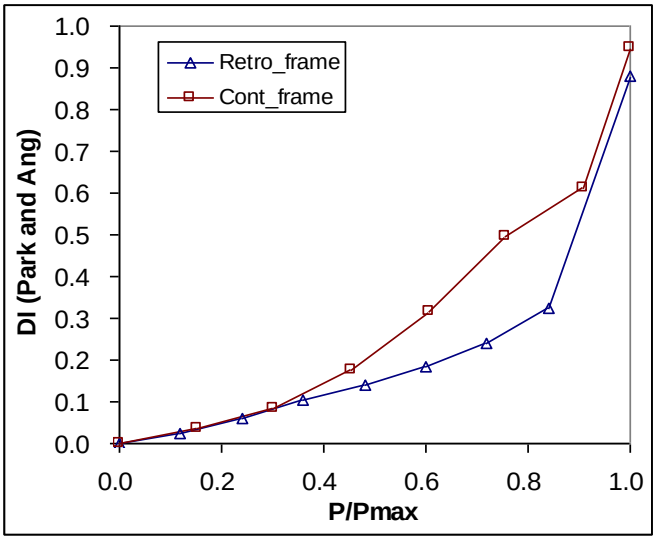

Figure 4.8 Park and Ang damage indices of Frame 1.

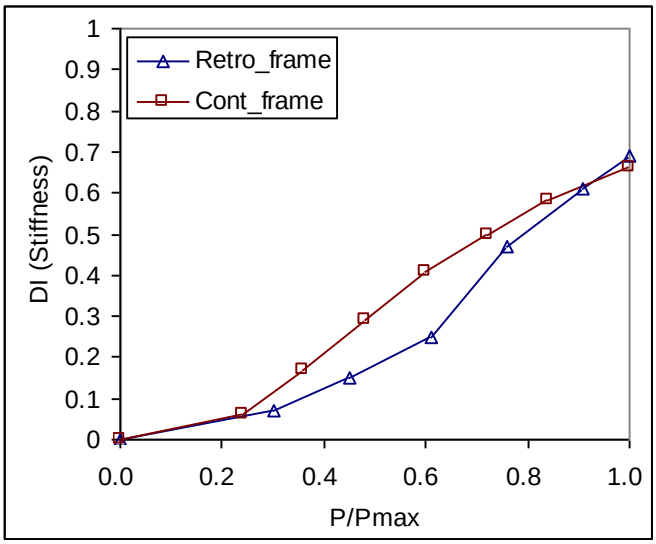

Figure 4.9 Stiffness damage indices of Frame 1.

a)

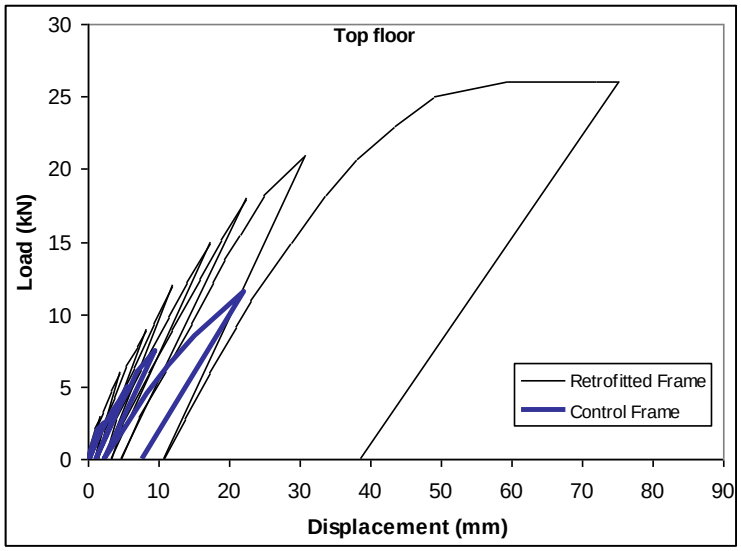

b)

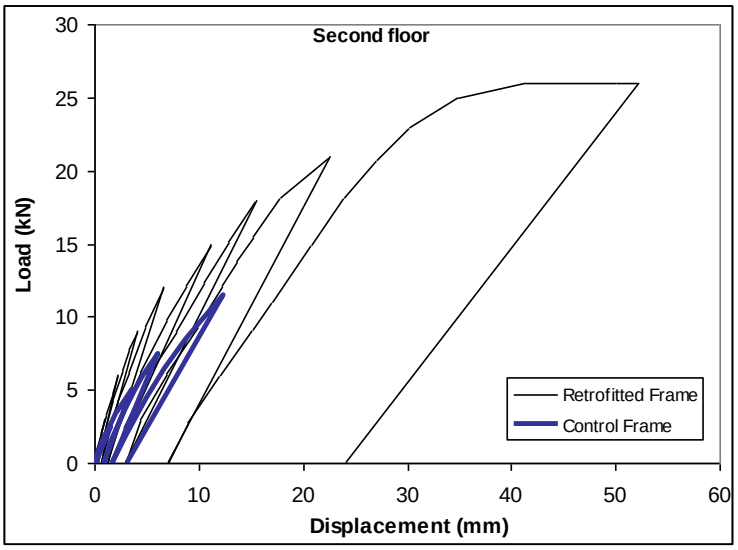

c)

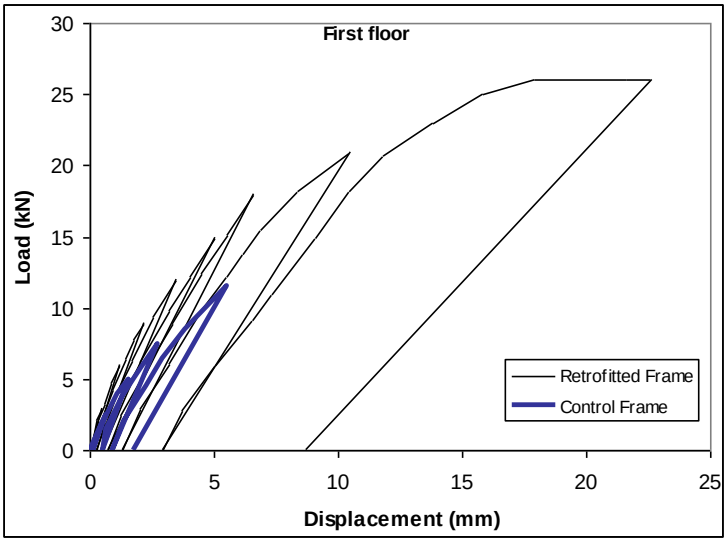

Figure 4.10 Load-displacement behaviors of Frame 2

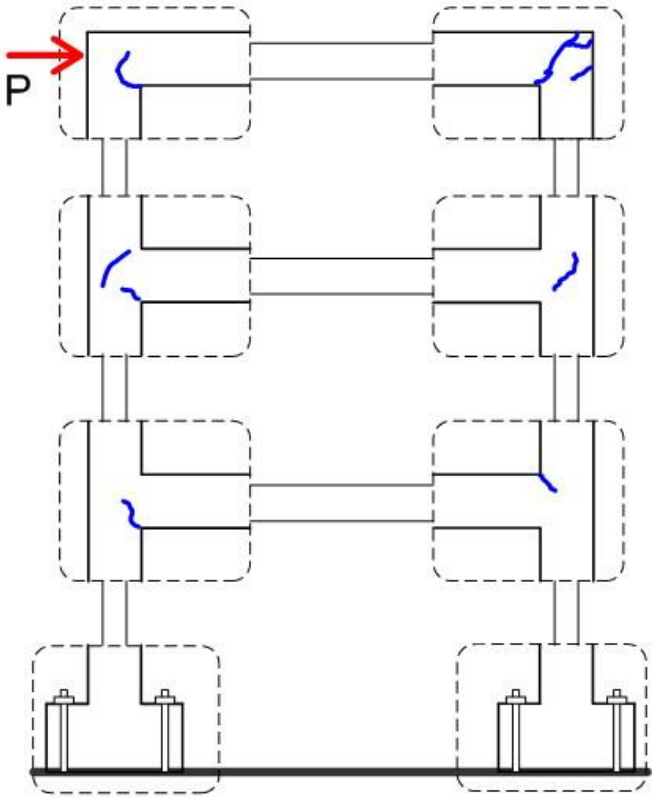

Figure 4.11 Crack pattern of Control Frame 2

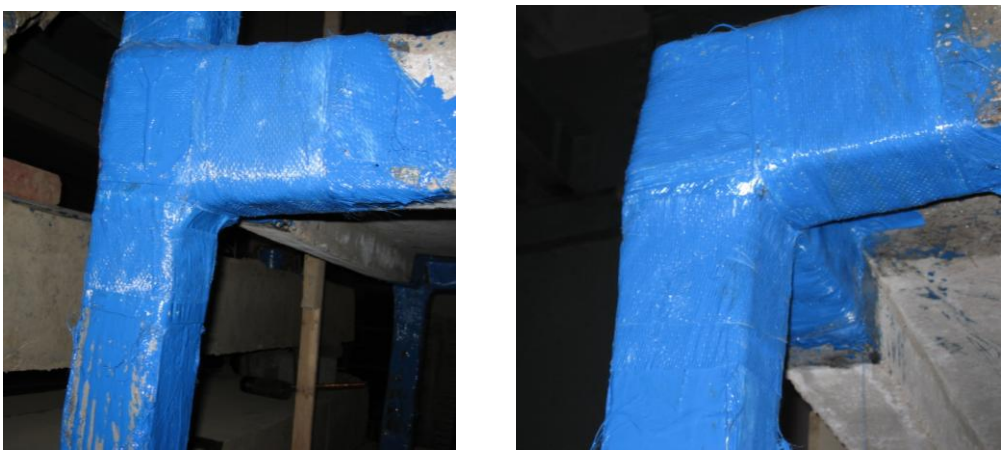

Figure 4.12 Failure pattern of Retrofitted Frame 2

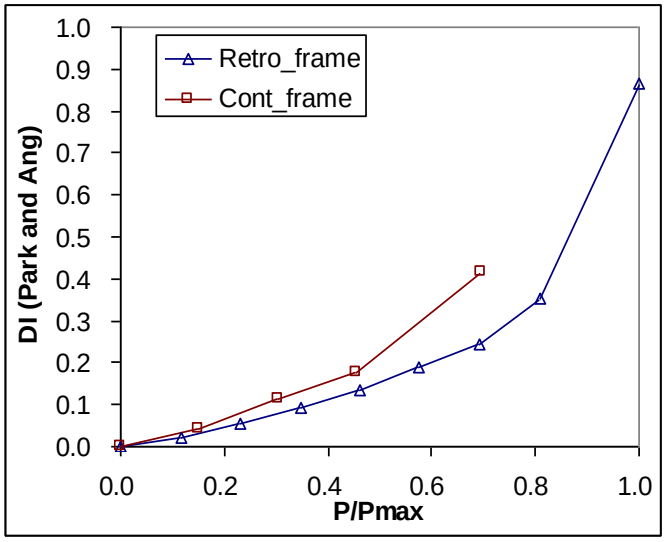

Figure 4.13 Park and Ang damage indices of Frame 2.

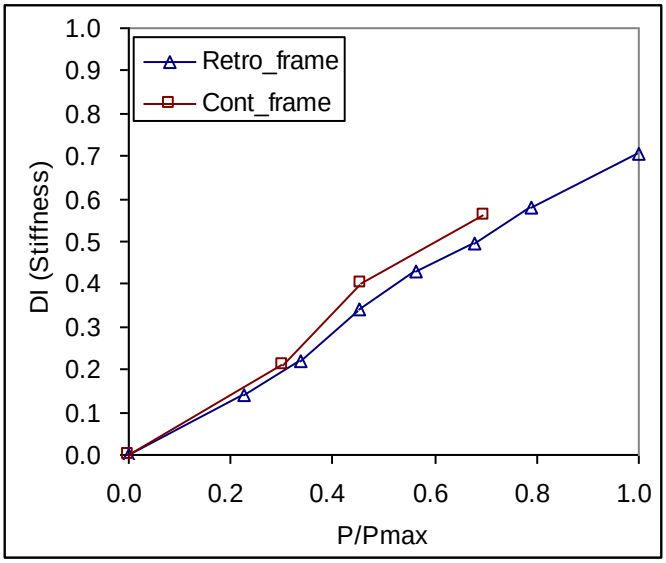

Figure 4.14 Stiffness damage indices of Frame 2.

a)

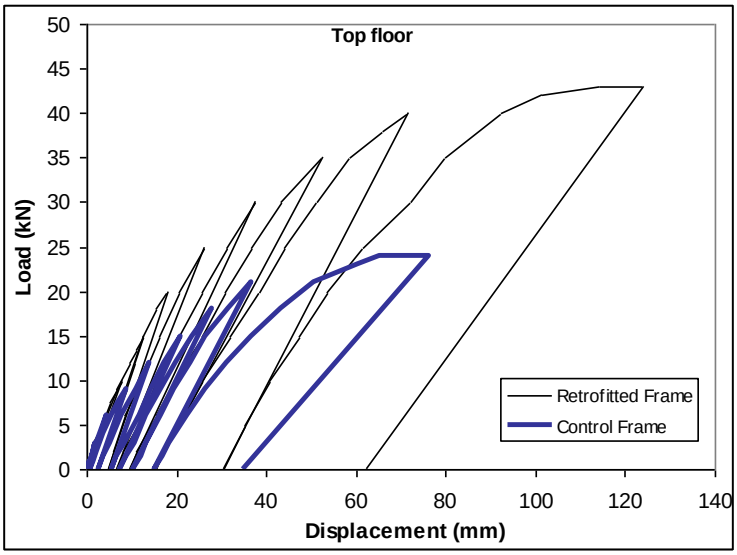

b)

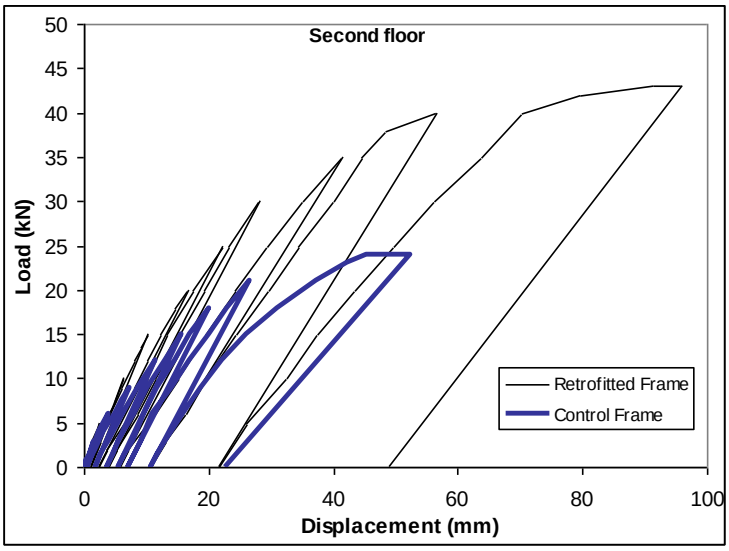

c)

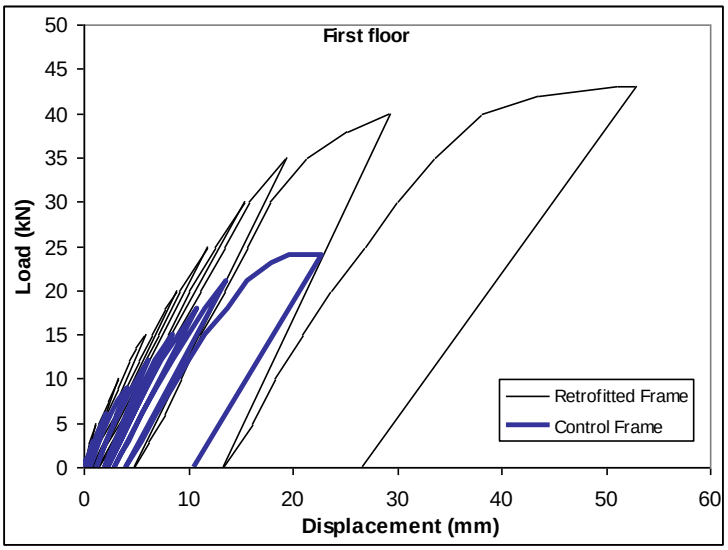

Figure 4.15 Load-displacement behaviors of Frame 3

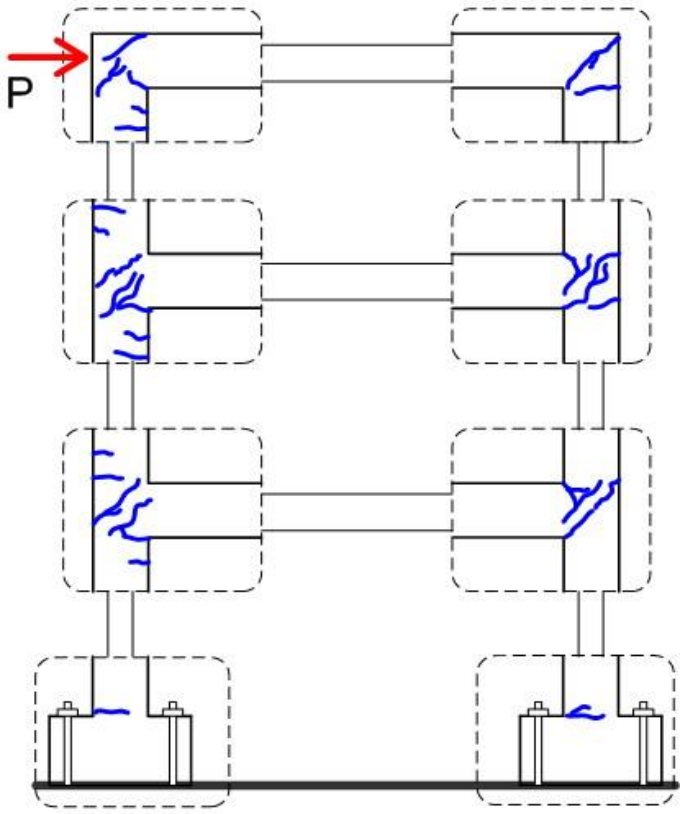

Figure 4.16 Crack pattern of Control Frame 3

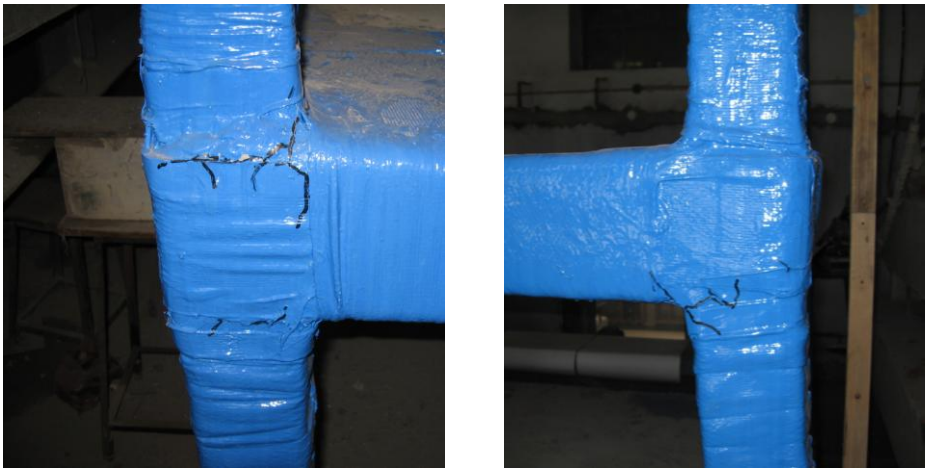

Figure 4.17 Failure pattern of Retrofitted Frame 3

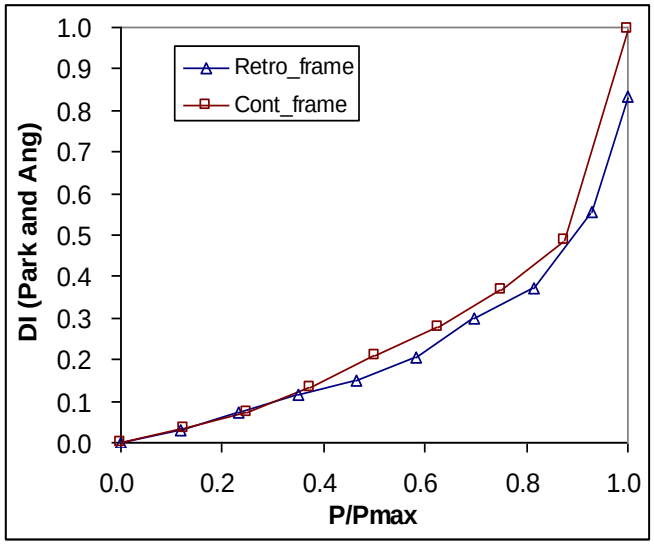

Figure 4.18 Park and Ang damage indices of Frame 3.

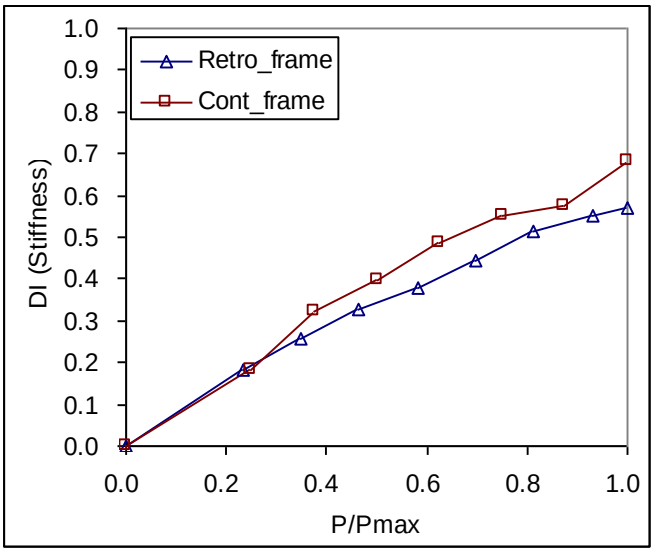

Figure 4.19 Stiffness damage indices of Frame 3.

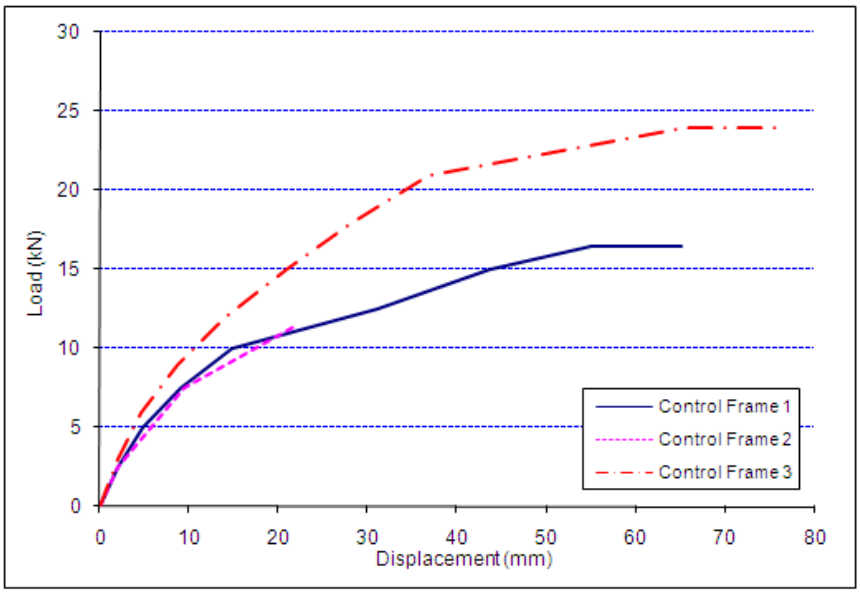

Figure 4.20 Load-displacement plots at top floor of Control Frames.

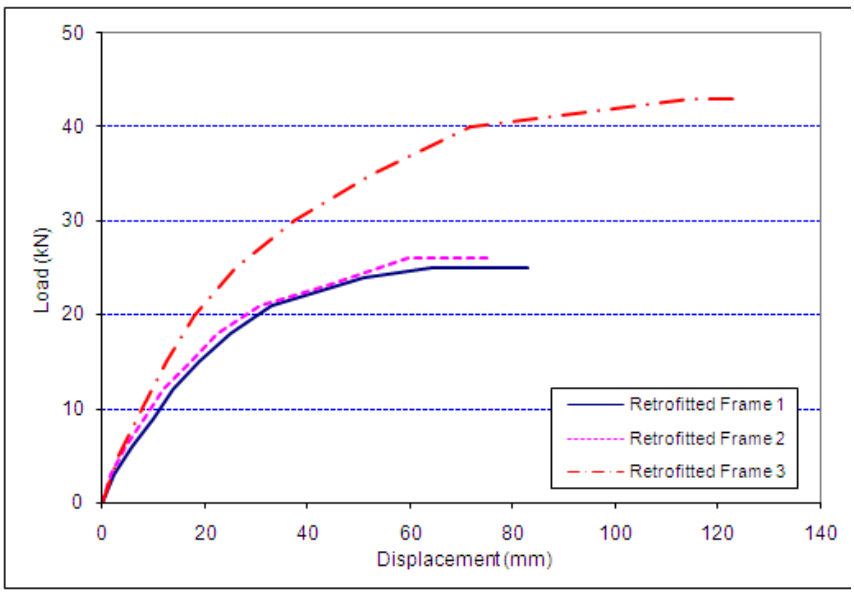

Figure 4.21 Load-displacement plots at top floor of Retrofitted Frames.

CHAPTER 5

VIBRATION MONITORING, DYNAMIC CHARACTERISTIC RESULTS AND CORRELATION OF DAMAGE INDICES

5.1 GENERAL

Experimental vibration analysis is a system identification endeavor. The structure is a 'black box' that needs to be deciphered. The traditional approach is to provide the 'black box' with a know input, measure the output and proceed with the identification (He and Fu, 2001). Real structures are made up of components possessing finite levels of rigidity, mass, and non-perfect energy transfer characteristics. It can be characterized by physical properties of structure such as the Young's modulus, shear modulus, bulk modulus and mass distribution. If an external force is applied at an arbitrary point on structural element, it will generate response. The magnitude of response will be proportional to the magnitude of force for a linear system, but the direction of response will depend on the physical properties of the structure and components of force (Burgueno et al., 2001; Ramsey, 1983). In the case of multiple inputs, the principle of superposition applies for linear systems set that responses from two or more inputs may be added vectorially. As a result the imposition of external or internal loads, during operation of the structure, will lead to nonzero responses at all times and will under certain conditions lead to very high amplitude vibrations at specific frequencies, or to instabilities of the static or dynamic responses. It is important in structural health monitoring to be able to accurately predict these responses, instabilities, or high amplitude vibrations. The usual aim of vibration measurement is to predict response to given force or moment in different damage states (Baghiee et al., 2009; Burgueno et al., 2001). For stationary structures, the specific frequencies at which resonant amplitudes occur are called the natural frequencies of the structure, and these frequencies and the corresponding distribution of amplitude are global properties. The amplitude distributions at the natural frequencies and modes of vibration are known as the natural modes of vibration.

This chapter describes the fundamentals of the theory and prediction of vibration response. A necessary prerequisite to the response of the vibrations of a structural system is an understanding of the detailed dynamic behavior of the system under

excitation by external forces. Many approaches toward this task have been taken, including direct measurement of the required information, mathematical modeling, and exact solution of the resulting partial differential equation of motion, discrete finite element modeling, etc. All these approaches have advantages but no method is always best. The approach should be tailored to the resources, time available, and the experience and skills of the individuals facing each specific task (Formenti, 2000). Dynamic behavior is no area for blind trust in anything, whether it is the infallibility of humans, of machines, or of structures. Vibration response in structures is partly art and partly science. This is because, though one can in principle obtain from analysis or experiment the data needed to develop and optimize the appropriate control measures, in practice one is constrained by factors of time, equipment, and economics and is often obliged to make decisions concerning the control measures without having complete information. This means that guesses must be made, past experience must be drawn on, and less than optimum measures must be sought.

The structural parameter purpose is to use measured data to determine the best-guess values of selected unknown parameters. Uncertainty in structural parameters such as inherent errors, measured data, and modeling errors inherently estimate a biased parameter. It is economical to use as few inputs (applied forces and measured responses) as necessary, but each set of inputs has its own input-output error relationship and some sets of measurements are more sensitive to errors than others. Therefore, designing a practical parameter requires a careful selection of sensor locations to produce meaningful results at minimum cost. Because sensor location selection has a large effect on input-output errors, the most promising subset of measurements must be selected.

5.2 VIBRATION MEASUREMENT TECHNIQUE

Vibration responses of structures are related to structural weaknesses associated with resonance behavior, e.g., natural frequencies being excited by operational forces. It can be shown that the complete dynamic behavior of a structure in a given frequency range can be viewed as a set of individual modes of vibration (He and Fu, 2001; Ramsey, 1983). Each result has a characteristic natural frequency, damping, and mode shape. By using these so-called modal parameters to model the structure, problems such as

specific resonances can be examined and subsequently solved. The first stage in modeling the dynamic behavior of a structure is to determine the modal parameters as introduced above:

(iv) The resonant frequency or natural frequency

(v) The structural damping

(vi) Frequency response functions

(vii) The mode shape

The modal parameters can be determined from a set of frequency response measurements between a reference point and a number of measurement points. Such a measurement point is usually called a degree of freedom (DOF). The modal frequencies and damping can be found from all frequency response measurements on the structure, except those for which the excitation or response measurement is in a position where the displacement is zero. These two parameters are therefore called "Global Parameters" (Formenti, 2000).

These types of frequency response measurements are made easy by using a Dual Channel Signal Fast Fourier Analyzer such as the standard configuration of PULSE for the Multi-analyzer System. The excitation forced (from either an impact hammer or a vibration exciter provided with a random or pseudorandom noise signal) is measured by a force transducer, and the resulting signal is supplied to one of the inputs. If a vibration exciter is used, a generator module should be installed in the analyzer. In order to measure the vibration of structure, the response is measured by an accelerometer and the resulting signal is supplied to another input. Consequently, the frequency response represents the structure's acceleration since the measured quantity is the complex ratio of the acceleration to force, in the frequency domain, FRF. There are two types to measure the vibration response. First, for impact hammer excitation, the accelerometer response position is fixed and used as the reference position. The hammer is used to excite the structure at the position corresponding to a DOF in the model. Second, for vibration exciter excitation, the excitation point is fixed and is used as the reference position, while the response accelerometer is moved around on the structure. For structures defined with a large number of DOF, extra response channels can be added to allow for easier and faster mobility measurements.

5.2.1 Determination of the Modal Frequencies

In a single degree of freedom (SDOF) system, all cases the equation of motion is a second order ordinary differential equation. The resonance or natural frequency of system, ω_n is defined by

$$\omega_n = \sqrt{\frac{k}{m}} \tag{5-1}$$

where *k* is stiffness of structure and *m* is mass of structure, respectively. In multi degree of freedom system, the values of each resonance frequency are evaluated by Eigen solution (Paz, 1997; Newmark and Rosenblueth, 1971).

In the laboratory test, the frequency at which it occurs is found using the analyzer's software program. A resonant frequency is identified at a peak in the vibration response of the structure such as in the FRF plot, displacement plot, velocity plot, or acceleration plot. The frequency resolution determines the accuracy of the frequency measurement. Greater accuracy can be attained by reducing the frequency range of the based band measurement or making a zoom measurement around the frequency of interest.

5.2.2 Determination of the Modal Damping

There are two well known classical methods of determining the viscous damping at a resonance, Half-Power Method and Logarithmic Decrement Method. This work employed the latter method because it is simpler and easier to use.

Logarithmic Decrement Method

Logarithmic Decrement is a measure of the rate of decay of free vibration. It is probably the simplest and most frequently used experimental damping technique. The original idea of utilizing the free vibration decay of a viscously damped system was to determine frequency information from musical tones. The equation that describes the damped free vibrating system represented by the response in Figure 5.1 is:

$$y(t) = Ae^{-\zeta \omega t} \sin\left(\omega_d t + \phi\right) \tag{5-2}$$

This equation represents pseudo-harmonic motion with and exponentially decaying amplitude $Ae^{-\zeta \omega t}$ and a phase angle ϕ (Paz, 1997; Key, 1988; Newmark and

Rosenblueth, 1971). Clearly the vibrations of damped structures will normally die away with time at a rate that may be used as a measure of the amount of damping. In the logarithmic decrement method, the amplitude of motion A_1 at the beginning of a cycle and the amplitude A_2 at the end of the cycle are measured based on the damped period, τ_d. Hence, from Euler's formula of the under-damped case comes expression

$$\frac{A_1}{A_2} = e^{\zeta \omega_i \tau_d} \tag{5-3}$$

For small damping ($\zeta < 0.2$) the damping ratio to be obtained from the equation

$$\zeta = \frac{1}{2\pi} \ln \frac{A_1}{A_2} \tag{5-4}$$

A major advantage of the traditional logarithmic decrement technique is that equipment and instrumentation requirements are minimal, free vibrations can be initiated by many convenient and appropriate methods, i.e. simple vibration hammer or from ambient excitations.

5.2.3 Determination of the Mode Shape

Mode shape is a vibration property of a multi-degree of freedom (MDOF) system. Natural mode of undamped systems relate to modal frequency. An example of a 3-DOF system is shown in Figure 5.2. Before considering properties of frequencies and modes, it is useful to consider some the properties of the stiffness and mass matrices encountered in structural dynamics (Clough and Penzien, 1975). Stiffness matrix **K** and mass matrix **M** were related to strain energy and kinetic energy, respectively. Both of **K** and **M** were seen to be symmetric, that is $\mathbf{K} = \mathbf{K}^{\mathrm{T}}$ and $\mathbf{M} = \mathbf{M}^{\mathrm{T}}$.

The free vibration equation of an undamped MDOF system, written in symbolic matrix form is

$$\mathbf{M}\ddot{\mathbf{x}} + \mathbf{K}\mathbf{x} = 0 \tag{5-5}$$

where **M** and **K** are $N \times N$ matrices and $x(t)$ is the corresponding $N \times 1$ vector of physical or generalized displacement coordinates.

The N^{th} order algebraic Eigen-value problem is

$$\left[\mathbf{K} - \omega^2 \mathbf{M}\right]\mathbf{X} = \mathbf{0} \tag{5-6}$$

For there to be a non trivial solution, it is necessary that

$$\det\left(\mathbf{K} - \omega^2 \mathbf{M}\right) = 0 \tag{5-7}$$

This is called the characteristic equation. When the determinant is expanded, there results a polynomial equation of degree N in ω^2 , whose roots are the Eigen-values, or squared natural frequencies, ω_r^2 . Corresponding to each Eigen-value ω_r^2 there will be an eigenvector, or natural mode, Φ_r, where

$$\Phi_r = \begin{Bmatrix} X_1 \\ X_2 \\ \vdots \\ X_N \end{Bmatrix}_r \quad \text{where} \quad r = 1, 2, ..., N \tag{5-8}$$

The modes are determined only to within a constant multiplier. Thus, modes may be scaled in any convenient manner.

5.3 DYNAMIC EQUATION OF MOTION

In vibration monitoring technique, the dynamic behaviors of structure are the target of testing. Dynamic properties including natural frequency, mode shape, and viscous damping are products of the mass, stiffness, strength of materials, connections, structural geometry, and damage state of structure. The difficult task is to monitor the damaged status of structures. Damage of a structure can change mechanical properties such as stiffness and the modal parameters. The magnitude of alterations depends on both the severity and the location of the deterioration (Paz, 1997; Clough and Penzien, 1975). A single damage event will affect each vibration mode differently. This effect on various modes, since it can be predicted, is the basis for the identification of

damaged members. If damage is expressed as a reduction in cross-section properties, then quantitative relations between damage and the resulting changes in modal parameters can be developed from a perturbation of the equation of motion. The equation of motion for a SDOF intact system is

$$m\ddot{x}+c\dot{x}+k\,x=p(t) \tag{5-9}$$

where m is the mass, c is the damping coefficient, k is the stiffness coefficient and $p(t)$ is external force, and $\ddot{x}$, $\dot{x}$ and x are acceleration, velocity, and deflection of system, respectively. In case of flexural element, the stiffness force can be obtain as

$$k\,x=EI\frac{\partial^4 x}{\partial y^4} \tag{5-10}$$

where E and I are elastic modulus and section moment inertia of intact element, and x is the flexural deflection along the distance y. In RC structures, cracks may often reduce stiffness without loss of mass. Lee and Shin (2001) suggested an approach to determine damaged status of structural element. This approach uses damage index to represent the damage induced change in stiffness by the degradation of elastic modulus as follows

$$E_d=E\left(1-DI\right) \tag{5-11}$$

where E_d is the effective elastic modulus in the damaged state and DI is the damage index which may characterize the state of damage. Damage index equal to zero indicates the intact state, while damage index equal to one indicates the complete rupture of material due to damage. Assume that the damages in an element are uniform through the thickness of element. Then, the dynamic equation of motion for the flexural element in the damaged state as follows

$$m\ddot{x}+c_d\,\dot{x}+\left(1-DI\right)k\,x=p(t) \tag{5-12}$$

where c_d is the damage damping coefficient. Damping brings the system to rest in finite time.

5.3.1 Impulse Excitation Response

The excitation force is important to conducting accurate vibration testing. The excitation force can be random, sinusoidal, periodic or impact ones. The decision on excitation is based on the optimum method for accurate measurement data that suit test objectives and the structure. The time domain force signal for impact excitation is a pulse with uncontrollable frequency contents. Impact excitation is convenient to use and very portable for field and laboratory test (He and Fu, 2001). It because no physical connection between the excitation and the structure. Impact test avoids the problem of interaction between them. Impulse excitation frequently encounters a force of very large magnitude that acts for a very short time but with a time integral that is finite (Craig and Kurdila, 2006). Impulsive force by the notation *P* is given by

$$P = \int p(t)\,dt \tag{5-13}$$

An impulsive force of magnitude P/t_d with a time duration of t_d is shown in Figure 5.3. Under free vibration, it can be found that the undamped of SDOF system with initial conditions $x(0)$ and $\dot{x}(0)$ behaved according to the equation

$$x(t) = \frac{\dot{x}(0)}{\omega_n}\sin\omega_n t + x(0)\cos\omega_n t \tag{5-14}$$

Hence, the response of this system initially at rest and excited by an impulse $\hat{F}$ is

$$x(t) = \frac{P}{m\,\omega_n}\sin\omega_n t \tag{5-15}$$

When damping is present, it can be started with the free vibration equation with initial conditions $x(0)$ and $\dot{x}(0)$ behaved according to the equation. The response of this system will be

$$x(t) = e^{-\zeta\omega_n t}\left(\frac{\dot{x}(0)+\zeta\omega_n x(0)}{\omega_n\sqrt{1-\zeta^2}}\sin\sqrt{1-\zeta^2}\,\omega_n t + x(0)\sin\sqrt{1-\zeta^2}\,\omega_n t\right) \tag{5-16}$$

Hence, the responses of this system initially at rest, $x(0)=0$ and $\dot{x}(0)=0$ and excited by an impulse P for $t>0$ are

$$\ddot{x}(t)=\frac{P}{m\omega_d}e^{-\zeta\omega_n t}\left\{\left[\left(\zeta^2\omega_n^2-\omega_d^2\right)\sin\omega_d t\right]-\left[2\zeta\omega_n\omega_d\cos\omega_d t\right]\right\} \tag{5-17}$$

where $\omega_d=\frac{2\pi}{\tau_d}=\omega_n\sqrt{1-\zeta^2}$ (5-18)

5.3.2 Relationship between Time Domain and Frequency Domain

The theoretical foundation employs FFT to analyze transient response, specifically the Fourier transform. The Fourier transform converts a function $y(t)$ defined over $-\infty<t<\infty$ into a function $Y(\omega)$, where ω is a frequency parameter (Craig and Kurdila, 2006). The definition is

$$Y(\omega)=\int_{-\infty}^{\infty}y(t)e^{-i\omega t}\,dt \tag{5-19}$$

If the transform $Y(\omega)$ is know, the corresponding time function may be found by applying the inverse Fourier transform,

$$y(t)=\frac{1}{2\pi}\int_{-\infty}^{\infty}Y(\omega)e^{i\omega t}\,d\omega \tag{5-20}$$

The basic properties of a Dirac delta function circumvent this difficulty. Given that the integral extend the limits of integration. The transform is proportional to a Dirac delta function. Let's take the argument of this function to be $\omega\pm\Omega$ because the finite value occurs at $\omega\pm\Omega$. The inverse transform of $\delta(\omega\pm\Omega)$ is

$$p(t)=\frac{1}{2\pi}\int_{-\infty}^{\infty}P(\omega)e^{i\omega t}\,d\omega=\frac{1}{2\pi}\int_{-\infty}^{\infty}\delta(\omega\pm\Omega)e^{i\omega t}\,d\omega=\frac{1}{2\pi}e^{\pm i\Omega t} \tag{5-21}$$

This establishes the transform $e^{\pm i\Omega t}$ pair as $2\pi\delta(\omega\pm\Omega)$. Another important transform pair is the one for an impulse in the time domain. The integration property of a Dirac delta function yields

$$P(\omega) = \int_{-\infty}^{\infty} p(t) e^{-i\omega t}\, dt = \int_{-\infty}^{\infty} \delta(t-\xi) e^{-i\omega t}\, dt = e^{i\omega\xi} \qquad (5\text{-}22)$$

The conjugation transform of a Dirac delta function, $\delta(t-\xi)$ is $e^{i\omega\xi}$. This solution concludes that an impulse excites all frequencies with equal magnitude, with all transformed values being real if the impulse occurs at $\xi = 0$.

5.3.3 Frequency Response Functions

The measurement for experimental modal analysis is to acquire frequency response function data from a test structure. For some time-domain analysis it is to obtain either the free decaying impulse response or the response due to ambient excitations. While, there are a variety of methods available to carry out measurement. As a result, the data contains a group of FRF that can be used for modal analysis of the structure (Maia et al., 2003; Ramsey, 1983). There are different types of excitation force on structure. Theoretically, the type of force does not matter as the FRF is defined as the ratio between the responses and force (He and Fu, 2001).

For a typical single input and single output system, the time waveform of an excitation force to the system is *f(t)* and the time waveform of the system response is *x(t)*. The Fourier spectra for input, *f(t)*, and output, *v(t)*, are $F(\omega)$ and $X(\omega)$, respectively. The frequency response function, $H(\omega)$, is defined as the ratio of the Fourier transforms of the system output $X(\omega)$ to the system input $F(\omega)$ and given by:

$$H(\omega) = \frac{Output}{Input} = \frac{X(\omega)}{F(\omega)} \qquad (5\text{-}23)$$

It is required for FRF that the input signal $F(\omega)$ is nonzero at all frequencies of interest (Craig and Kurdila, 2006). Depending upon he selected parameters for the system input and output, the representations of FRF are as follows:

(i) Accelerance (g/lbf or g/N) = Acceleration / Force

(ii) Mobility (in./lbf sec or m/N sec) = Velocity / Force

(iii) Dynamic Compliance (in./lbf or m/N) = Displacement / Force

where g is acceleration due to gravity, and g is equal to 386 in./sec^2 or 9.81 m/sec^2. If the system output is given by acceleration g and input is given by force N.

In MODF system under harmonic excitation, the mode superposition for the steady state response $\mathbf{x}(t)$, based on the modes $\boldsymbol{\varphi}_r$ of the undamped system, is given by

$$\mathbf{x}(t)=\sum_{r=1}^{N}\frac{\boldsymbol{\varphi}_r\,\boldsymbol{\varphi}_r^{\mathrm{T}}\,\mathbf{P}}{\mathbf{K}_r}\,\frac{1}{\left[1-\left(\omega/\omega_r\right)^2\right]+i\left(2\zeta_r\,\omega/\omega_r\right)}e^{i\omega t} \tag{5-24}$$

where ω is the forcing frequency in rad/s, which is varied over the frequency range of interest in the modal test. The steady state displacement response at coordinate *j* due to harmonic excitation of unit magnitude only at coordinate *k* is called the frequency response function for the response at *j* due to excitation at *k* (Craig and Kurdila, 2006). When the FRF deals with displacement per unit force, it is called a receptance. The receptance has the form

$$H_{jk}(\omega)=H_{x_j/p_k}(\omega)=\sum_{r=1}^{N}\frac{\phi_{jr}\,\phi_{kr}}{K_r}\,\frac{1}{\left[1-\left(\omega/\omega_r\right)^2\right]+i\left(2\zeta_r\,\omega/\omega_r\right)} \tag{5-25}$$

The mobility (i.e., velocity output at *j* per unit force input at *k*) for MDOF systems with modal damping is given by

$$H_{v_j/p_k}(\omega)=i\,\omega\sum_{r=1}^{N}\frac{\phi_{jr}\,\phi_{kr}}{K_r}\,\frac{1}{\left[1-\left(\omega/\omega_r\right)^2\right]+i\left(2\zeta_r\,\omega/\omega_r\right)} \tag{5-26}$$

The accelerance (acceleration output at *j* per unit force input at *k*) is given by

$$H_{a_j/p_k}(\omega)=-\omega^2\sum_{r=1}^{N}\frac{\phi_{jr}\,\phi_{kr}}{K_r}\,\frac{1}{\left[1-\left(\omega/\omega_r\right)^2\right]+i\left(2\zeta_r\,\omega/\omega_r\right)} \tag{5-27}$$

and the phase (lag) angle $\alpha(\omega)$ is given by

$$\tan\alpha_r(\omega)=\frac{2\zeta_r\left(\omega/\omega_r\right)}{1-\left(\omega/\omega_r\right)^2} \tag{5-28}$$

In modal testing, accelerance can measure the response in a wide frequency range by using accelerometer. Therefore, in structural health monitoring, the accelerance is more

convenient than mobility and dynamic compliance (Maia et al. 2002; Ramsey, 1983). Accelerance is the FRF used most commonly and the forcing frequency is usually given as f hertz = $\omega/2\pi$. Obviously, FRF contain information about natural frequencies, ω_r, damping ratios, ζ_r and mode shapes, ϕ_r.

FRF is measured by simultaneously sampling both excitation force and response signals, as shown in Figure 5.4. The captured time wave forms of excitation force and system response contain amplitude and relative phase information. An excitation force instrument was connected to the force input channel of an FFT spectrum analyzer. Generally, the excitation force instrument was connected to the force channel directly because FFT analyzer provides power to an integrated piezoelectric circuit. The response signal was measured by an accelerometer, which was connected to the response input channel of the FFT analyzer. The block diagram of signal process is shown in Figure 5.5 and 5.6. The spectrum analysis is defined as the transformation by using Fourier Transform of a signal from a time-domain representation into a frequency-domain representation. In order to transforms a discrete periodic time signal into a discrete periodic frequency spectrum for use with digital computer, the FFT was developed. Modal testing is the procedure that is employed to measure FRFs, and from them to estimate these physical properties of the structure being tested. There are three major types of modal test: single input-multiple output, multiple input-single output, and multiple input and multiple output. Figure 5.7 depicts a single input-multiple output test of 3-DOF frame. The single input is an impact hammer at DOF1 and there are three output locations on the frame namely $H_{11}(\omega)$, $H_{21}(\omega)$ and $H_{31}(\omega)$, respectively.

5.3.4 Coherence Function

The coherence function can be interpreted to determine measurement problems associated with linearity and noise. The coherence function gives a measure of the linear dependence between two signals as a function of frequency (Baghiee et al., 2009; Craig and Kurdila, 2006). This function is of particular importance and usefulness when making FRF measurements. The FFT spectrum analyzer provides the computation and display of the coherence function in conjunction with the output power spectrum to allow an efficient comparison between the coherence function and

the related output spectra components. The coherence function calculation is defined by the following equation:

$$\gamma^2(f) = \frac{|G_{xy}(f)|^2}{G_{xx}(f)G_{yy}(f)} \tag{5-29}$$

where $G_{xy}(f)$ is cross spectrum between the excitation and response signal, $G_{xx}(f)$ is power spectrum of the excitation signal, $G_{yy}(f)$ is power spectrum of the response signal and f is frequency. Its value can change depending on the frequency where it is evaluated. The coherence function result has been expanded about the value of 1.0 to better show its detail. The coherence function is not perfect unity although it is very near the value of 1.0. If the biggest dip in the coherence function occurs at the very deep valley (zero) it indicates that this dip is because of the relative large amount of noise present with respect to the low level of the response of the system at this frequency. In other words, we can say that the signal to noise ratio in this frequency range is low. This causes the measurement to have a lower coherence function value because of noise. This is a common occurrence in measurements where the response of the structure is very small at particular frequencies.

Rattles cause another common measurement problem in the system. When a system has loose joints, parts or components, rattles can be excited from the input excitation. These rattles cause additional force inputs to the system that are not being measured. However the system responds to these inputs, which then gets measured by the response accelerometer. These rattles add noise to the system that will dramatically affect the quality of the coherence function and vibration measurement.

5.4 MEASUREMENT CONSIDERATIONS OF IMPACT HAMMER TEST AND VIBRATION SENSOR SELECTION

To measure vibration response in this research, the first step is to set up an appropriate impulse-force hammer, transducer, and FFT analyzer. The mass and tip hardness of the hammer can be selected to give the desired magnitude and duration of the force pulse. Hammers can be constructed with weights ranging from a few grams up to several kilograms. They can cover a wide range of frequencies. In general, heavier hammers

are more effective at lower frequencies. However, if the hammer is too heavy and the structure is too week, the hammer may overload the structure or rebound to cause a double hit (Formenti, D., 2000). On the other hand, if the hammer is too light, there will not be enough energy imparted to the structure under test.

The hammer tip also affects the impact. A steel tip will provide a short duration force with large amplitude. A rubber tip will provide a long duration force with small amplitude. A plastic tip falls somewhere between steel and rubber (Dincal, 2005; Barecchia., nd.). In the frequency domain, a rubber tip will provide a narrow frequency response range, a steel tip will provide a wide frequency response range and a plastic tip again falls somewhere between the two. The testing object is also a consideration in tip selection because one does not want to permanently damage the structure under test. Impact hammers are supplied with calibration values for each hammer/tip combination. The proper tip can be selected based upon the desired frequency range and the mass of the structure under test.

The strongest influence on selection of the appropriated parameter is the frequency at which measurement is important. As a general rule, displacement measurements record large signals at low frequencies, while acceleration measurements are effective at high frequencies. A suitable vibration sensor or transducer involves:

(i) Displacement sensed by a proximity transducer with an output signal proportional to displacement

(ii) Velocity sensed by a seismic-type transducer

(iii) Acceleration sensed by an accelerometer

Accelerometers are widely used transducers for dynamical property testing. The weight of a selected accelerometer is important because it may alter the dynamic characteristics of the structure under test. Dynamic mass loading is the change in physical properties of the structure caused by adding the mass of the accelerometer. In this test, accelerometers of several weights were used to minimize the effect of dynamic mass loading. As explained earlier in Chapter 3.4, the positions of accelerations are measured at the modal of each floor of the frame. The detail of accelerations is DYTRON with a sensitivity of 1.055 V/g (model 11103, 11197 and 11305, respectively) (Goyal, 2007; Kanvar et al, 2006).

There are various means of mounting the accelerometer to the surface of the test structure, such as stud mounting, magnet mounting, or using a thin layer of wax (Formenti, D., 2000). In order to minimize the loss of high frequency signals in the transmission path, the contact surface should be flat, smooth, clean, and free of rust and paint. Stud mounting is the most reliable method and it allows better transmission of high frequency signals. Epoxy wax is also a convenient, temporary mounting method. Test results show that a frequency response equivalent to stud mounting can be achieved with a thin coating of wax on clean flat surfaces. As the thickness of wax at the interface of the accelerometer and test object increases, the first resonance of he system decreases, which limits the frequency response of the Fix-Turing. To obtain the best frequency response on flat surfaces, one should use as little wax as possible at the interface and press the accelerometer firmly against the test structure using a circular motion to secure the mounting.

FRF measurement parameters can be set before taking measurement data, such as frequency range, number of signal lines, unit type, and so on. In addition, the suitable parameters for the force channel and response channel can also be selected. The FRF is complex and three quantities are involved, namely frequency, magnitude, and phase. This is equivalent in frequency to the real part and imaginary part. The interpretation of impact testing data can be greatly enhanced by the use of a suitable graphic display. Typical display formats include time waveforms and frequency spectra of impact force and system response, magnitude, phase, real part, and imaginary part of FRFs and the coherence function. The example of input and output data are shown in Figures 5.8 to 5.11. Either a linear or a logarithmic display for FRFs may be selected to display data. However, only a linear amplitude display is used for time waveform, phase and coherence functions.

5.5 FORCE WINDOW AND CHECK MEASUREMENT DATA

5.5.1 Force window

In general, it is desirable to have a forcing function that is short in time duration to provide the FRF for the structural system. This short duration signal in the time domain corresponds to broadband frequency content in the frequency domain. Since the impact force signal represents a very small portion of the digital record analyzed, even very

low level noise may produce significant errors in the auto-spectrum of the force signal and FRF estimation (Formenti, D., 2000; Sek, nd.). This is especially true if the duration of the force signal is short relative to the total sample time. Such noise is not reduced by averaging with the usual FRF estimate because the noise is additive in the force auto-spectrum. Random noise can be greatly reduced by multiplying a force window by the force signal.

The force window has unity gain for the portion of the record which includes the force signal, and sets the remaining samples in the record to zero prior to Fourier processing. This procedure introduces no distortion as long as none of the force data are attenuated and the background noise is broadband in nature.

The captured time waveforms of both impact force and system response contain amplitude and relative phase information. The FRF and coherence function can be computed from the Fourier transforms of both impact and response signals.

5.5.2 Check bad impacts

Three types of bad impacts are common problems in impact testing, namely: overload, underload, and more than one impact (also referred to as double hit) (Formenti, D., 2000). Overloading is the most difficult problem to overcome in impact tests. When an overload occurs, the impact force signal is clipped, causing distortion in the measurement. In some cause, an anti-aliasing filter may smooth a clipped signal to make a distorted measurement look good. To detect overload problems, the unfiltered force signal should be checked before it passes through the anti-aliasing filter. In the FRF measurement, the overload force level can be set in unit of lb or Newton based on the experience of testing.

The opposite problem is underload due to low impact force level or improper gain setting. If the impact force is not adequate, the measured FRF does not represent the dynamic characteristics of the measured system. Therefore, underload needs to be checked before signal processing. The underload force level can be specified as a percentage of the overload limit. It is important to avoid more than one impact or impactor rebounds as shown in Figure 5.12. If more than one impact occurs within the data record, the Fourier transforms of the pulses tend to cancel at certain frequencies, creating sharp notches in the force spectrum. This can cause significant errors in the

FRF measurement at these frequencies due to a low signal to noise ratio in the force spectrum. Furthermore, the force window should not be used to eliminate secondary impacts from the force record prior to Fourier processing. In this case, the response will still include the effects of multiple impacts, thus resulting in an erroneous estimate of the FRF. The problem of a double hit can be detected by checking any secondary peak(s) within a data record. It is important to avoid impact hammer rebounds. If more than a single impact occurs within the data record, the Fourier transforms of the pulses tend to cancel at certain frequencies, due to a low signal to noise ratio in the force spectrum. Furthermore, the force window should not be used to eliminate secondary impacts from the force record prior to Fourier processing. In this case, the response will still include the effects of multiple impacts, thus resulting in an erroneous estimate of the frequency response function. Bad input signal is shown in Figure 5.13.

5.5.3 Check data quality

To determine the quality of time wave form of response data and the FRF estimation, it is not sufficient to know only the relationship between input and output. The question is whether the system output is caused by the system input or by other factors. For example, noise and nonlinear effects can cause large outputs at various frequencies, inducing errors in estimating the FRF (Baghiee et al., 2009; Ooi et al., 2004; Formenti, D., 2000). The influence non-linearity and the degree of noise contamination in the FRF is measured by calculating the coherence function. Figure 5.14 shows bad response data of time response record and FRF plot, respectively.

The coherence function can be calculated from the averaged auto-spectrum and cross spectrum of the impact force and the system response. The coherence function is dimensionless and its value is always between 0 and 1. If the coherence is equal to 1 at any specific frequency, the system is said to have perfect causality at that frequency. In other words, the measured response power is caused totally by the measured input power and the system is linear. If the value of coherence function is equal to 0, the two signals are totally uncorrelated. A coherence value less than 1 at a given frequency indicates that contamination exists in the two signals in terms of noise and nonlinear effects. Generally, the measured data are good or acceptable if the coherence value is greater than or equal to 0.75. In applications, low coherence at anti-resonance

frequencies is not generally a cause for concern about data quality. At such frequencies the machine or structural response is very small and may be near the noise floor of the instrumentation. Thus, the low coherence merely indicates a reduced signal-to-noise ratio. On the other hand, one should be aware that the coherence would always be unity for single impact estimation.

5.6 DAMAGE DETECTION METHODS BASED ON THE CHANGE IN DYNAMIC CHARACTERISTICS

The change in dynamic characteristics of structure such as resonance frequency, mode shape, and FRF is widely used to calculate the damage to structures because damage always accompanies the reduction of stiffness as well as modal frequency. This approach is called modal parameters damage method. This method has been widely applied in damage to of highway bridges (Samali et al., 2007). Damage in different locations and components actually leads to different frequency changes in various modes. The damage index definitions of change in dynamic characteristics are as follows:

5.6.1 Dipasquale and Cakmak Damage Index

Dipasquale and Cakmak (1990) defined the modal plastic softening index for the one-dimensional case, where the fundamental Eigen-frequency is considered. This damage index is given by

$$DI_{Dip} = 1 - \frac{\omega^{*2}}{\omega^2} \tag{5-30}$$

where ω and ω^* are the fundamental Eigen-frequency and damage frequency parameter, respectively. In this paper natural frequencies of structure are measured from experimental test in form of frequency response function plot. This plot gives FRF magnitude corresponding to resonance frequency of each mode.

5.6.2 FRF Based Mode Shape Method

Maia et al. (2003) studied damage index based on the assumption that the damage is located at the point where the change of an operational mode shape function is the

greatest for the entire frequency range. This is called FRF based mode shape method, (FRF_MS). This method can be expressed as

$$\Delta H_{lj}(\omega) = \left| H_{lj}(\omega) - H^{*}_{lj}(\omega) \right| \tag{5-31}$$

If more than one frequency and force are considered, the value of FRF_MS is the sum of each frequency and force:

$$FRF\_MS_{l} = \sum_{\omega} \sum_{j} \Delta H_{lj}(\omega) \tag{5-32}$$

Therefore, the damage index based on FRF_MS method can be defined as

$$DI_{FRF\_MS_{l}} = \frac{\sum_{\omega} \sum_{j} \Delta H_{lj}(\omega)}{\sum_{\omega} \sum_{j} H_{lj}(\omega)} = \frac{\sum_{\omega} \sum_{j} \left| H_{lj}(\omega) - H^{*}_{lj}(\omega) \right|}{\sum_{\omega} \sum_{j} H_{lj}(\omega)} \tag{5-33}$$

where $H_{lj}(\omega)$ and $H^{*}_{lj}(\omega)$ are the value of FRF magnitude of undamaged and damaged structure at j^{th} excitation point and l^{th} measurement point.

5.7 DYNAMIC CHARACTERISTIC RESULTS AND DAMAGE INDICES

Structural damage detection using information contained in vibration signatures is a useful technique to monitor health of structure without destroying it (Kanwar et al., 2006; Burgueno et al., 2001; Formenti, 2000). In this study, changes in structural dynamic characteristics of damaged frame model were investigated using the OROS software program with the help of impact hammer excitation test. One accelerometer was installed on each floor to measure the transient response. The program was set up to make a free zoom measurement with a frequency range of 0 to 50 Hz. This frequency range included the three majority sway-modes of all frame models. After applying each load step, the dynamic characteristics rendered records in OROS based on a linear analysis setup. These records included trigger hammer plot, time history

plot, and frequency response function plot, which gave the amplitude of vibration along with frequency.

In damage identification based mode shape method, FRF is a useful tool (Baghiee et al., 2009; Dincal, 2005; Ramsey, 1983) because it relates to three major structural parameters: mass, damping, and stiffness. Although, it is difficult task to calculate FRF by using classical method but modal analysis always obtain structural mode shape from measured FRF (He and Fu, 2001). To avoid this complicating effect, many concerned researchers mention only the fundamental measured FRF because FRF in higher mode are sensitive (Cakar and Sanliturk, 2003 and Kanwar et al., 2006). Therefore, this section present and discuss about the fundamental measured FRF magnitude. All dynamic records of experimental frames are presented in Appendix A. Based on the change in dynamic characteristics, the modal plastic softening damage index, DI_{Dip} and FRF damage index, DI_{FRF_MS} were utilized to monitor the damage of experimental frame models.

5.7.1 Control Frame 1

At initial state, the natural frequency of first, second, and third modes has been found to be 6.6 Hz, 19.5 Hz, and 31.8 Hz, respectively. The structural damping based on logarithmic decrement method has been observed to be 3.0. FRF magnitude of the top floor was 4.8×10^{-3} g/N, second floor was 3.6×10^{-3} g/N, and first floor was 2.0×10^{-3} g/N. At the initial cracking corresponding to the load of 10 kN, DI_{Dip} was 0.12 and DI_{FRF_MS} was 0.43. The frequencies in the ultimate damage state of first, second, and third mode are 5.2 Hz, 15.5 Hz, and 25.9 Hz respectively. FRF magnitude of top floor was 1.0×10^{-3} g/N, second floor was 0.6×10^{-3} g/N, and first floor was 0.3×10^{-3} g/N. At final state, damping was 5.21, DI_{Dip} was 0.34, and DI_{FRF_MS} was 0.57. The summary of natural frequency, FRF, and structural damping is presented in Table 5.1, while the summary of damage indices and appearances are presented in Table 5.2. From Figure 5.15, the average natural frequency decreases approximately 19% from initial state. The correlations between applied loads and natural frequencies as well as correlations of FRF are also shown in Table 5.1. In the correlation of natural frequencies, the linear relationship seems to be perfectly negative for all modes. The correlations of FRF seem to be distributed normally. The correlations between applied loads and damage indices

are presented in Table 5.2. The correlation of DI_{Dip} was 0.928 and the correlation of DI_{FRF_MS} was 0.978, indicating both damage indices are distributed normally. The change of structural damping is shown in Figure 5.16 and FRF magnitudes are shown in Figures 5.17 and 5.19, leading to the average change in damping to increase approximately 74% and average change of FRF magnitude to decrease approximately 400% compared to initial state. Compared to the FRF of top and second floors, the FRF magnitude of first floor decreased. This demonstrates the influence of increased mass of a storey on the FRF of the storey lying immediately below it in a multistory building. The normalized plot of the correlation ratio between applied load P with ultimate load P_{max}, and damage indices based on the change in dynamic characteristics of Control Frame 1 are shown in Figures 5.21 and 5.22. In order to estimate the dynamic properties of the frame model under different damage states, the measurement data subsequent to loading are extracted to represent the behavior of the structure. In general, the effects of the damaged structure on changes in natural frequencies are found to be negligible (Doebling et al., 1998). The FRF damage index of Control Frame 1 increases slowly with the increase in load and it change shape after cracks form inside structural element. The health of control frames is of great concern when DI_{FRF_MS} increases to larger than 0.4.

5.7.2 Retrofitted Frame 1

The summary of dynamic characteristics of Retrofitted Frame 1 and corresponding damage indices are presented in Tables 5.3 and 5.4 respectively. At initial state, the natural frequencies of the first, second, and third modes were 6.7 Hz, 20.7 Hz, and 34.3 Hz respectively; the damping was 3.07. FRF magnitude of top floor was 8.4×10^{-3} g/N, second floor was 6.5×10^{-3} g/N and first floor was 3.0×10^{-3} g/N. At a load of 18 kN, DI_{Dip} was 0.14 and DI_{FRF_MS} was 0.42, and there is the sound of the GFRP slip. At the final damage state, the damping of structure was 6.09, and the frequencies of first, second and third modes are 5.5 Hz, 17.2 Hz and 29.0 Hz, respectively. From Figure 5.15, the average natural frequency decreases approximately 17% from the initial state. The change of damping is shown in Figure 5.16, leading to the average increase in damping of approximately 98%. FRF magnitudes are shown in Figures 5.18 and 5.20. FRF magnitude of top floor was 1.5×10^{-3} g/N, second floor was 1.2×10^{-3} g/N and first

floor was $0.5x10^{-3}$ g/N. It shows that FRF magnitude decreases by 467% from initial state. The damage index DI_{Dip} was 0.30, and DI_{FRF_MS} was 0.50. The relationship between applied loads and damage indices of Retrofitted Frame 1 are shown in Figures 5.21 and 5.22 along with the results of Control Frame 1. The correlations between applied loads and natural frequencies as well as correlations of FRF are also shown in Table 5.3. The correlation between applied load and damage indices are presented in Table 5.4. The correlation of DI_{Dip} was 0.943 and the correlation of DI_{FRF_MS} was 0.986, indicating both damage indices are distributed normally.

According to the change of dynamic characteristics between final state of Control Frame 1and initial state of Retrofitted Frame 1, the average change of damping decreases by 67%, the average change of FRF magnitude increases by 567%, and corresponding resonance frequency increases by approximately 9%. Although GFRP sheets were not able to bridge the cracks of damaged structure fully, still GFRP wrap increased the dynamic properties of the structure.

5.7.3 Control Frame 2

The dynamic characteristics of the damaged structure have been measured in the same manner as those of Control Frame 1. The summary of dynamic characteristics of Control Frame 2 is presented in Table 5.5, and the damage indices are presented in Table 5.6. In the undamaged state, damping was 3.25. The natural frequencies of first, second and third modes are 5.3 Hz, 15.1 Hz and 26.0 Hz, respectively. FRF magnitude at the top floor was $4.0x10^{-3}$ g/N. At a load of 7.5 kN, DI_{Dip} was 0.14 and DI_{FRF_MS} was 0.37. At a load of 11.5 kN, DI_{Dip} was 0.20, DI_{FRF_MS} was 0.44, damping was 4.94, FRF magnitude of top floor was $1.7x10^{-3}$ g/N. The frequencies of first, second, and third modes are 4.8 Hz, 13.5 Hz and 23.5 Hz respectively. The change of natural frequency is shown in Figure 5.23, leading to the average decrease of corresponding frequency of approximately 11%. From Table 5.6, the correlation of DI_{Dip} was 0.999 and the correlation of DI_{FRF_MS} was 0.993, while the obvious relationship between the two variables can be observed, it is linear. The summary of damping is shown in Figure 5.24 and FRF magnitudes are shown in Figures 5.25 and 5.27, leading to a structural damping increase of approximately 52%. The average FRF magnitude decreased approximately 55% compared to initial state. It demonstrates that damping of the

damaged structure increases when structural stiffness decreases. Compared to initial frequencies and FRF of the Control Frame 1, the average change of frequency of Control Frame 2 decreased by nearly 25% and FRF decreased by 16% when dead load of each story of Frame 2 (slab thickness of 65 mm) was larger than Control Frame 1 (slab thickness of 50 mm). This sufficiently demonstrates that the increase in terms of storey mass exercises influence on natural frequency and FRF. The normalized plot of the correlation ratio between applied load P with ultimate load P_{max}, and damage indices based on the change in dynamic characteristics are presented in Figures 5.29 and 5.30.

5.7.4 Retrofitted Frame 2

The summary of dynamic characteristics of Retrofitted Frame 2 is presented in Table 5.7. The natural frequency plot is shown in Figure 5.23. In the initial state the damping was observed to be 3.37 as shown in Figure 5.24. The FRF magnitude at top floor was 10.2×10^{-3} g/N and the natural frequencies of first, second, and third modes are 6.4 Hz, 18.6 Hz, and 33.6 Hz, respectively. At yield state of 18 kN, DI_{Dip} was 0.20 and DI_{FRF_MS} was 0.45, and there was the sound of the GFRP layers slip. In the final damage state, the damping was observed to be 6.81, FRF magnitude at top floor was 3.7×10^{-3} g/N and the frequencies of first, second, and third modes were 5.2 Hz, 15.8 Hz, and 29.4 Hz respectively. The damage index of DI_{Dip} was 0.29 and DI_{FRF_MS} was 0.54. The FRF plots of Retrofitted Frame 2 are shown in Figures 5.26 and 5.28. The results shows that the average change of damping increased by 102%, the average change of FRF magnitude decreased by 226%, and corresponding resonance frequency decreased by approximately 17% from the initial state. The summary of damage index and appearance are presented in Table 5.8 and Figures 5.29 and 5.30. According to a comparison of dynamic characteristics at final state between Retrofitted Frame 1 and Retrofitted Frame 2, the average change of damping decreased by 30% from Frame 1 to Frame 2, the average change of FRF magnitude correspondingly increased by 29% and corresponding resonance frequency decreased by approximately 6%. The correlation between applied load and damage indices are presented in Table 5.8. The correlation of DI_{Dip} was 0.999 and the correlation of DI_{FRF_MS} was 0.980.

Based on the change in natural frequency, it can be claimed that the increase in term of story mass exercises influence on natural frequency. However, the value of FRF magnitude of Retrofitted Frame 2 is larger than Retrofitted Frame 1. It indicates that strengthening the moderate damaged structure is more likely to increase the load carrying capacity than severe damaged structure.

5.7.5 Control Frame 3

The change of natural frequency and damping are shown in Figures 5.31 and 5.32. In the initial state damping has been observed to be 2.34, the FRF magnitude at top floor was $5.0x10^{-3}$ g/N, the resonance frequencies at first, second and third modes were 5.6 Hz, 16.8 Hz, and 28.30 Hz, respectively. The comparison of FRF plot of Control Frame 3 is shown in Figures 5.33 and 5.35. Cracks started to open at a load of 18 kN, first frequency of 4.8 Hz, second frequency of 14.8 Hz, third frequency of 24.9 Hz, with DI_{Dip} of 0.27 and DI_{FRF_MS} of 0.50. At ultimate state of 24 kN, the damping was 5.21, FRF magnitude at top floor was $2.0x10^{-3}$ g/N, the frequencies of first, second and third modes were 4.4 Hz, 13.8 Hz, and 23.5 Hz respectively. The system damage index of DI_{Dip} was 0. 38 and DI_{FRF_MS} was 0.59. The correlations of Control Frame 3 are shown in Table 5.9. The correlation results of all frames supports that the linear relationship seems to be perfectly negative between applied loads and natural frequencies. And the correlation of FRFs seems to be distributed normally. The correlation between applied load and damage indices are presented in Table 5.10. The correlation of DI_{Dip} was 0.998 and the correlation of DI_{FRF_MS} was 0.963. The change of damping increased by 123%, the average change of FRF magnitude decreased by 198%, and the average change of resonance frequency decreased by approximately 19% compared to the initial state. The summary of dynamic characteristic results is presented in Table 5.9. Compared to the initial frequency of Control Frame 1, the average change of natural frequency of Control Frame 3 decreased by nearly 13% when the dead load of each storey of Frame 3 (slab thickness of 65 mm) was larger than Frame 1 (slab thickness of 50 mm) as shown in Figure 5.39. This sufficiently demonstrates that, although the confinement effect on the compressive strength of concrete with internal transverse steel bars increases structural stiffness, the increase in terms of storey mass exercises greater influence on natural frequency. Moreover, compared to the initial frequencies of

the Control Frame 2, the average change of natural frequency of Control Frame 3 increased by nearly 9% when dead load of each story of Frame 3 is equal to Frame 2. It indicates that the confinement effect with internal transverse steel bars increases structural stiffness leading to an increase in natural frequency.

The change in damage indices of Control Frame 3 are shown in Figures 5.37 and 5.38. The summary of damage indices and appearances is presented in Table 5.10. It demonstrates that the value of DI_{FRF_MS} is greater than DI_{Dip}, indicating that damage indices based on the change in FRFs show a much acceptable accuracy correlation with damage indices based on the change in natural frequency in general. However, it can be seen that DI_{Dip} is small which agrees with the fact that no visible damage is reported at loads less than yield point. Meanwhile, some damage index values around 0.2 were obtained. The health of control frames is said to be of great concern when DI_{FRF_MS} increases to larger than 0.4. On the other hand, the damaged structure seems to be unsafe when DI_{Dip} increases to more than 0.20 or the structure experiences severe damage.

5.7.6 Retrofitted Frame 3

The change of natural frequency and damping of Retrofitted Frame 3 are shown in Figures 5.31 and 5.32, respectively. In the initial state the structural damping has been observed to be 2.89, the FRF magnitude at top floor was 16.0×10^{-3} g/N and the resonance frequency at first, second and third modes was 6.2 Hz, 18.5 Hz, and 33.8 Hz, respectively. The comparison of FRF plot of Control Frame 3 is shown in Figures 5.34 and 5.36. At yield state of 30 kN, DI_{Dip} was 0.18 and DI_{FRF_MS} was 0.46. In the ultimate damage state of 43 kN, DI_{Dip} was 0.33 and DI_{FRF_MS} was 0.56, as the structure lost its load carrying capacity. At final state, the damping was 7.43, the FRF magnitude was 3.6×10^{-3} g/N and the resonance frequencies at first, second and third modes are 5.1 Hz, 16.1 Hz and 30.2 Hz, respectively. The comparison of natural frequencies between Retrofitted Frame 1, 2 and 3 are shown in Figure 5.40. The correlation between applied load and damage indices are presented in Table 5.12. The average change of damping increased 157%, the average change of FRF magnitude was 356%, and the average change of corresponding resonance frequency of Retrofitted Frame 3 increased by nearly 12% as compared to Control Frame 3 as shown in Figure 5.41 and 5.42. The

results of all Retrofitted Frames indicate that natural frequency and FRF increase when damaged elements are repaired by GFRP wrap with epoxy layers. The summary of dynamic characteristic results is presented in Table 5.11.

The summary of damage indices and appearance of Retrofitted Frame 3 is presented in Table 5.12. The damage indices based on the change in dynamic characteristics of Retrofitted Frames decreased at final state indicating better performance as compared to the Control Frames. However, damage indices based on deformation and change in stiffness show a more acceptable accuracy correlation with the change in dynamic characteristics based damage indices in general (Estekanchi and Arjomandi, 2007). These damage indices also show that damage assessment based on change in dynamic characteristics works well when damage reaches the severe stage (Dincal, 2005; Hwang and Kim, 2004). Nevertheless, this method with the help of the impact hammer test is a useful technique to monitor the health of structures without destroying them when damage is hidden within the structure behind strengthening material layers (He and Fu, 2001, Ramsey, 1983).

Table 5.1 Natural frequencies, FRFs and damping of Control Frame 1.

P,kN	P/P_{max}	Natural frequency of each mode, Hz			FRF magnitude of each floor, 10^{-3} g/N			Damping
		ω_1	ω_2	ω_3	FRF_1	FRF_2	FRF_3	
0	0	6.6	19.5	31.8	2.0	3.6	4.8	3.00
5.0	0.30	6.4	19.0	30.5	0.6	1.2	1.8	3.42
7.5	0.45	6.1	18.0	29.0	0.5	1.1	1.5	3.77
10.0	0.61	5.8	17.5	28.0	0.4	1	1.25	4.15
12.5	0.76	5.5	17.0	27.2	0.46	0.9	1.2	4.67
16.5	1	5.2	15.5	25.8	0.3	0.6	1.0	5.21
Correlation		-0.986	-0.980	-0.995	-0.814	-0.838	-0.838	

Table 5.2 Damage indices and appearance of Control Frame 1.

P,kN	P/P_{max}	DI_k	DI_{Park}	DI_{Dip}	DI_{FRF}	Appearance
0	0	0	0	0	0	Un-deformed
5.0	0.30	0.07	0.09	0.03	0.23	Un-cracked
7.5	0.45	0.15	0.18	0.06	0.36	Un-cracked
10.0	0.61	0.25	0.32	0.12	0.43	Minor cracking
12.5	0.76	0.47	0.49	0.16	0.47	Severe cracking
16.5	1	0.69	0.95	0.34	0.57	Loss of shear capacity
Correlation		0.954	0.936	0.928	0.978	

Table 5.3 Natural frequencies, FRFs and damping of Retrofitted Frame 1.

P,kN	P/P_{max}	Natural frequency of each mode, Hz			FRF magnitude of each floor, 10^{-3} g/N			Damping
		ω_1	ω_2	ω_3	FRF_1	FRF_2	FRF_3	
0	0	6.7	20.7	34.3	3.0	6.5	8.4	3.07
6.0	0.24	6.5	20.3	33.5	1.3	3.1	3.9	3.12
12.0	0.48	6.4	20.0	32.6	1.0	2.7	3.6	3.93
15.0	0.60	6.2	19.5	32.2	0.8	1.9	2.5	4.11
18.0	0.72	6.1	19.3	32.0	0.6	1.3	1.8	4.46
21.0	0.84	6.0	18.8	31.5	0.6	1.5	2.0	5.11
25.0	1	5.5	17.2	29.0	0.5	1.2	1.5	6.09
Correlation		-0.948	-0.916	-0.954	-0.886	-0.906	-0.905	

Table 5.4 Damage indices and appearance of Retrofitted Frame 1.

P,kN	P/P_{max}	DI_k	DI_{Park}	DI_{Dip}	DI_{FRF}	Appearance
0	0	0	0	0	0	Un-deformed
6.0	0.24	0.06	0.06	0.04	0.17	Un-cracked
12.0	0.48	0.29	0.14	0.08	0.29	Un-cracked
15.0	0.60	0.41	0.18	0.12	0.37	Un-cracked
18.0	0.72	0.50	0.24	0.14	0.42	Sound of fiber slip
21.0	0.84	0.58	0.32	0.17	0.44	Sound of breaking fiber
25.0	1	0.66	0.88	0.30	0.50	Loss of shear capacity
Correlation		0.989	0.823	0.943	0.986	

Table 5.5 Natural frequencies, FRFs and damping of Control Frame 2.

P,kN	P/P_{max}	Natural frequency of each mode, Hz			FRF magnitude of each floor, 10^{-3} g/N			Damping
		ω_1	ω_2	ω_3	FRF_1	FRF_2	FRF_3	
0	0	5.3	15.1	26.0	1.7	3.2	4.0	3.25
5.0	0.30	5.1	14.2	24.8	1.0	2.0	2.5	4.10
7.5	0.45	5.0	13.9	24.0	0.9	1.7	2.3	4.32
11.5	0.61	4.8	13.5	23.5	0.6	1.3	1.7	4.94
16.5	1	-	-	-	-	-	-	-
Correlation		-0.987	-0.997	-0.997	-0.924	-0.923	-0.918	

Table 5.6 Damage indices and appearance of Control Frame 2.

P,kN	P/P_{max}	DI_k	DI_{Park}	DI_{Dip}	DI_{FRF}	Appearance
0	0	0	0	0	0	Un-deformed
5.0	0.30	0.21	0.11	0.10	0.25	Un-cracked
7.5	0.45	0.40	0.18	0.14	0.37	Un-cracked
11.5	0.61	0.56	0.42	0.20	0.44	Minor cracking
16.5	1	-	-	-	-	-
Correlation		0.992	0.930	0.999	0.993	

Table 5.7 Natural frequencies, FRFs and damping of Retrofitted Frame 2.

P,kN	P/P_{max}	Natural frequency of each mode, Hz			FRF magnitude of each floor, 10^{-3} g/N			Damping
		ω_1	ω_2	ω_3	FRF_1	FRF_2	FRF_3	
0	0	6.4	18.6	33.6	4.0	8.5	10.2	3.37
6.0	0.23	6.3	18.3	33.1	2.3	4.7	6.4	3.72
9.0	0.35	5.9	17.7	32.2	1.8	3.4	4.7	4.28
15.0	0.58	5.7	17.0	31.4	1.7	3.2	4.4	4.76
18.0	0.69	5.6	16.7	30.8	1.6	3.0	4.2	5.20
21.0	0.81	5.5	16.2	30.2	1.5	2.8	3.8	5.88
26.0	1	5.2	15.8	29.4	1.4	2.7	3.7	6.81
Correlation		-0.983	-0.993	-0.994	-0.846	-0.836	-0.865	

Table 5.8 Damage indices and appearance of Retrofitted Frame 2.

P,kN	P/P_{max}	DI_k	DI_{Park}	DI_{Dip}	DI_{FRF}	Appearance
0	0	0	0	0	0	Un-deformed
6.0	0.23	0.14	0.05	0.07	0.16	Un-cracked
9.0	0.35	0.22	0.09	0.11	0.28	Un-cracked
15.0	0.58	0.43	0.19	0.17	0.34	Un-cracked
18.0	0.69	0.49	0.24	0.20	0.45	Sound of fiber slip
21.0	0.81	0.58	0.35	0.23	0.53	Sound of breaking fiber
26.0	1	0.71	0.87	0.29	0.54	Loss of shear capacity
Correlation		0.998	0.865	0.999	0.980	

Table 5.9 Natural frequencies, FRFs and damping of Control Frame 3.

P,kN	P/P_{max}	Natural frequency of each mode, Hz			FRF magnitude of each floor, 10^{-3} g/N			Damping
		ω_1	ω_2	ω_3	FRF_1	FRF_2	FRF_3	
0	0	5.6	16.8	28.3	2.5	4.0	5.0	2.34
6	0.25	5.3	16.3	27.7	2.0	3.9	4.8	2.98
9	0.38	5.2	16.0	26.6	1.5	3.2	4.2	3.27
12	0.50	5.1	15.3	26.0	1.2	2.3	3.0	3.85
15	0.63	4.9	15.0	25.2	1.2	2.2	2.9	3.98
18	0.75	4.8	14.8	24.9	0.9	1.8	2.6	4.46
21	0.88	4.6	14.2	24.3	1.0	1.5	2.0	4.65
24	1.00	4.4	13.8	23.5	0.7	1.4	2.0	5.21
Correlation		-0.995	-0.991	-0.992	-0.959	-0.966	-0.966	

Table 5.10 Damage indices and appearance of Control Frame 3.

P,kN	P/P_{max}	DI_k	DI_{Park}	DI_{Dip}	DI_{FRF}	Appearance
0	0	0	0	0	0	Un-deformed
6	0.25	0.18	0.07	0.09	0.20	Un-cracked
9	0.38	0.32	0.13	0.14	0.37	Un-cracked
12	0.50	0.40	0.21	0.17	0.42	Un-cracked
15	0.63	0.49	0.28	0.22	0.47	Minor cracking
18	0.75	0.55	0.37	0.27	0.50	Severe cracking
21	0.88	0.58	0.49	0.33	0.56	Spalling of concrete cover
24	1.00	0.68	0.96	0.38	0.59	Loss of shear capacity
Correlation		0.990	0.894	0.998	0.963	

Table 5.11 Natural frequencies, FRFs and damping of Retrofitted Frame 3.

P,kN	P/P_{max}	Natural frequency of each mode, Hz			FRF magnitude of each floor, 10^{-3} g/N			Damping
		ω_1	ω_2	ω_3	FRF_1	FRF_2	FRF_3	
0	0	6.2	18.5	33.8	6.0	12.0	16.0	2.89
10	0.23	6.0	18.2	33.0	4.0	8.0	10.0	3.55
20	0.47	5.8	18.0	32.5	3.0	5.8	8.0	3.72
25	0.58	5.7	17.3	32.0	2.4	4.6	6.4	4.31
30	0.70	5.6	17.0	31.7	2.0	4.4	6.0	5.01
35	0.81	5.5	16.8	31.5	1.5	2.8	3.8	5.97
43	1.00	5.1	16.1	30.2	1.3	2.6	3.6	7.43
Correlation		-0.971	-0.969	-0.981	-0.971	-0.966	-0.960	

Table 5.12 Damage indices and appearance of Retrofitted Frame 3.

P,kN	P/P_{max}	DI_k	DI_{Park}	DI_{Dip}	DI_{FRF}	Appearance
0	0	0	0	0	0	Un-deformed
10	0.23	0.18	0.07	0.08	0.20	Un-cracked
20	0.47	0.33	0.15	0.14	0.31	Un-cracked
25	0.58	0.38	0.21	0.17	0.35	Un-cracked
30	0.70	0.44	0.30	0.18	0.46	Sound of fiber slip
35	0.81	0.51	0.37	0.20	0.51	Severe damage
40	0.93	0.55	0.55	0.25	0.54	Sound of breaking fiber
43	1.00	0.57	0.84	0.33	0.56	Loss of shear capacity
Correlation		0.993	0.901	0.973	0.989	

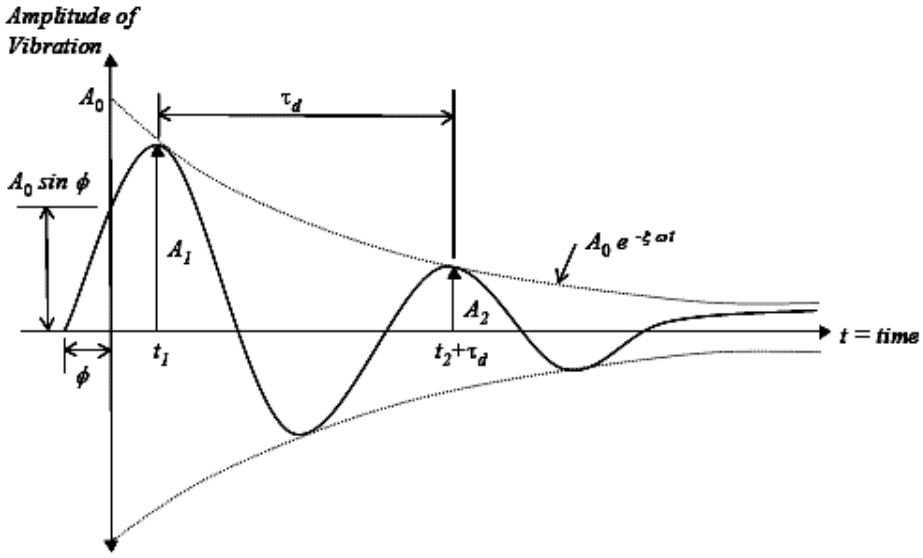

Figure 5.1 Free-vibration response of an under-damped system

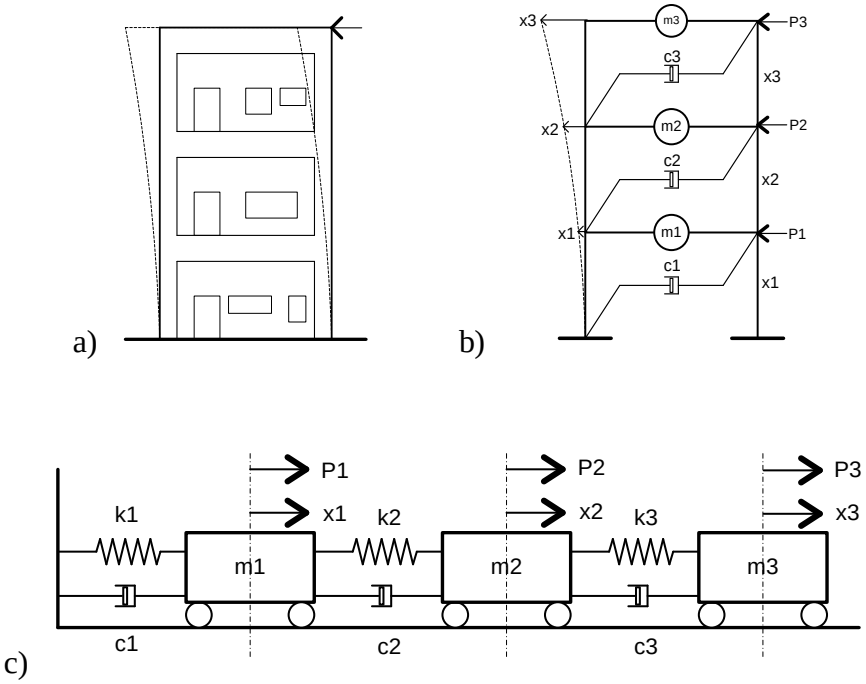

Figure 5.2 A model of a three degree of freedom system

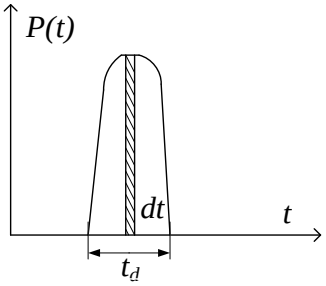

Figure 5.3 A short duration impulse excitation force

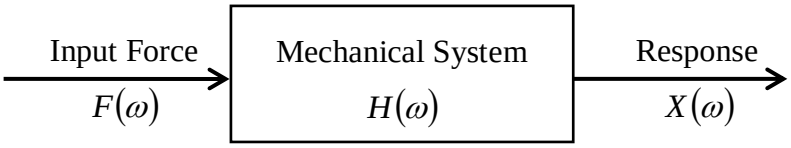

Figure 5.4 Single input and single output system (He and Fu, 2001).

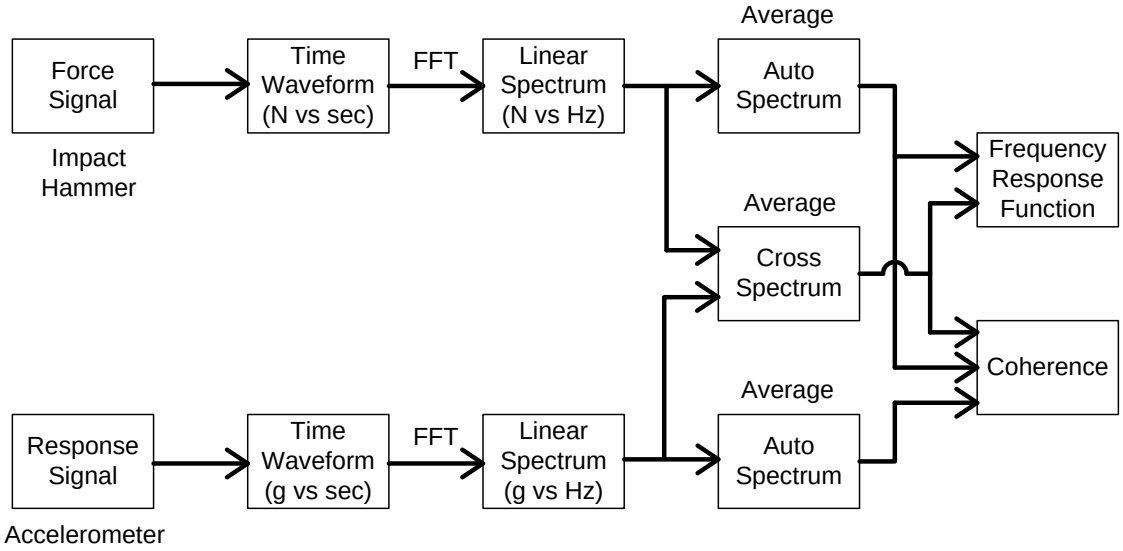

Figure 5.5 Block diagram of signal process.

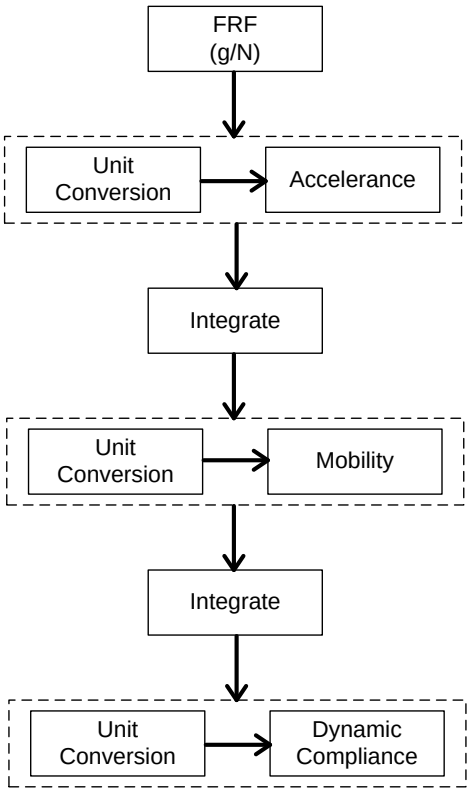

Figure 5.6 Conversion relationship between different FRFs.

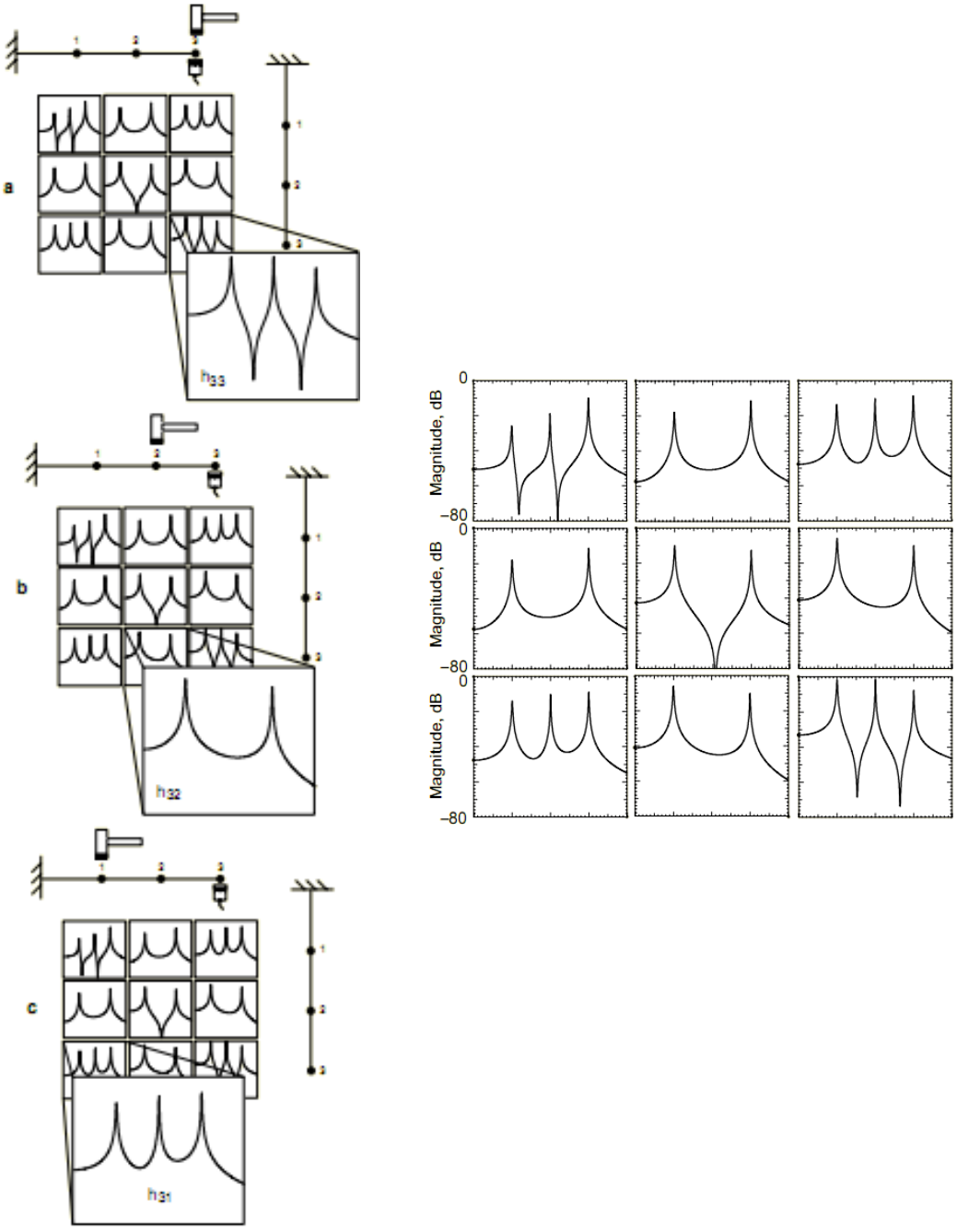

Figure 5.7 FRF response measurements of a 3 DOF model of a beam (Avitabile, 2001)

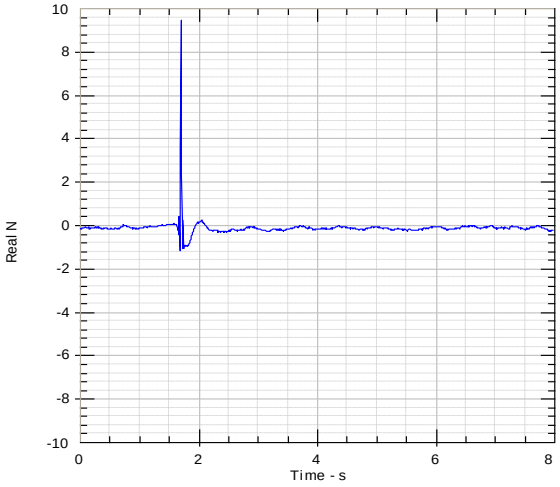

Figure 5.8 The impulse force window data

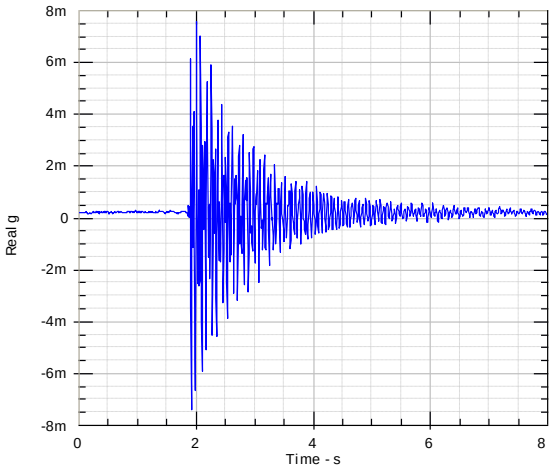

Figure 5.9 Time waveform of system response data

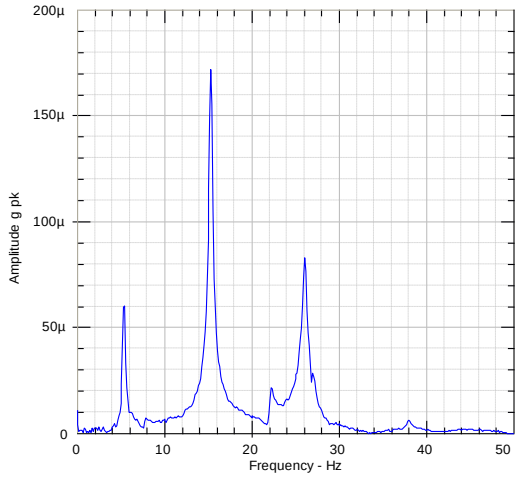

Figure 5.10 The frequency spectra of system response data

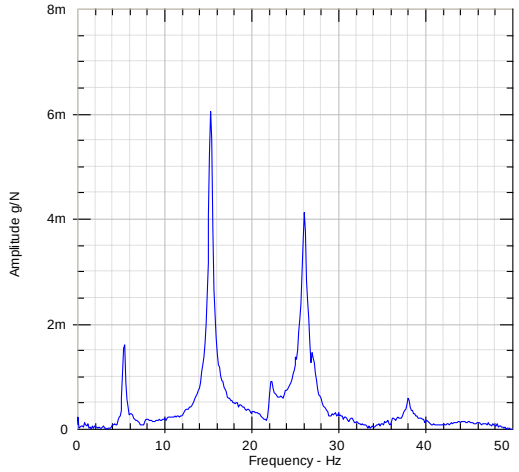

Figure 5.11 The accelerance FRF record of system data

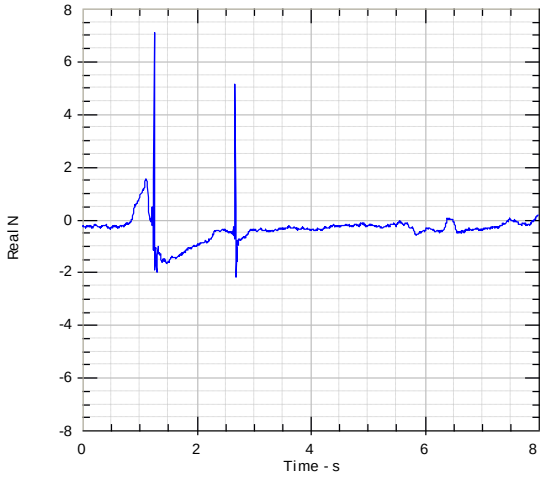

Figure 5.12 The impactor rebounds

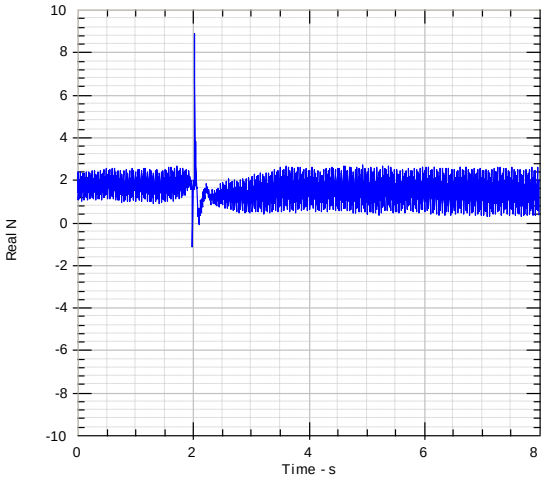

Figure 5.13 The bad input signals

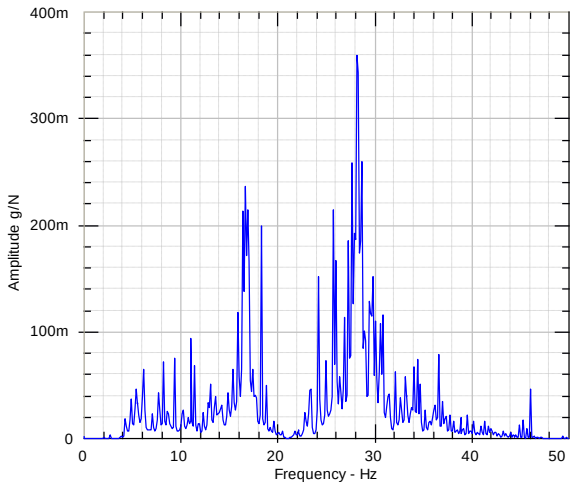

Figure 5.14 The bad frequency response function plots

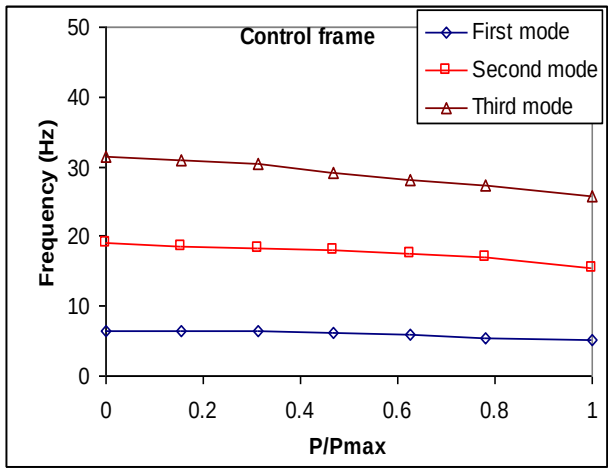

a)

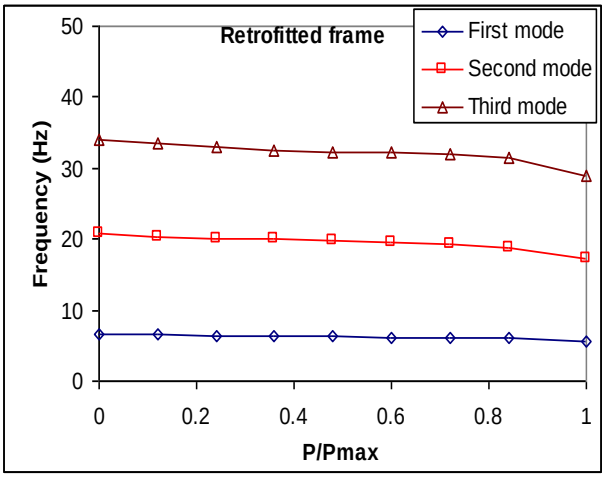

b)

Figure 5.15 Natural frequency plots: a) Control Frame 1 and b) Retrofitted Frame 1.

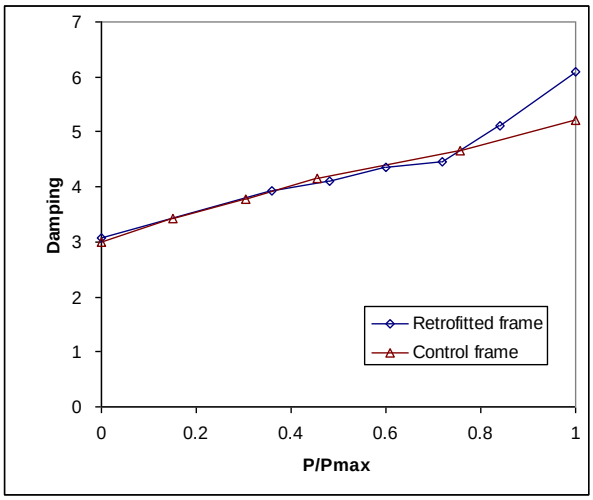

Figure 5.16 Damping coefficients of Frame 1.

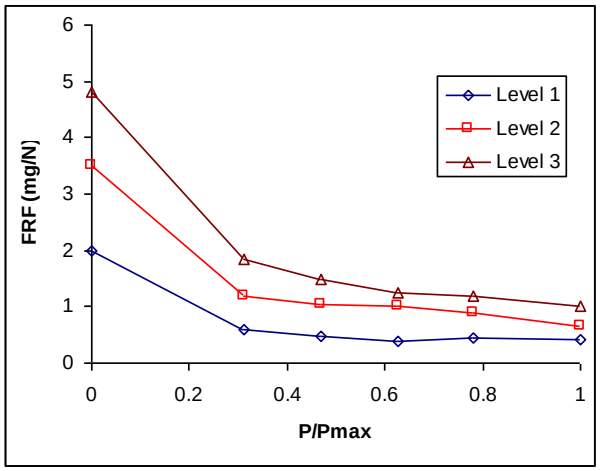

Figure 5.17 FRF magnitudes of Control Frame 1.

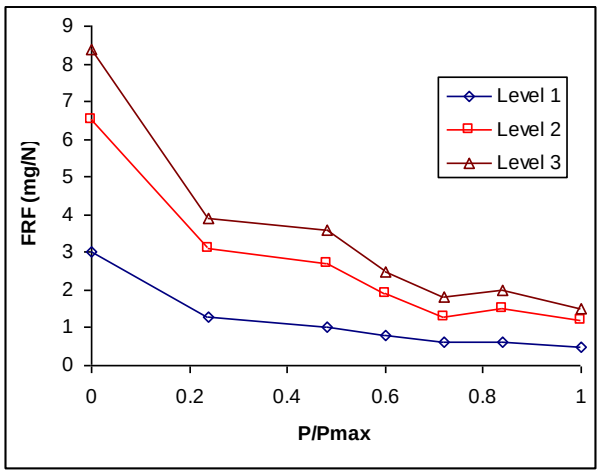

Figure 5.18 FRF magnitudes of Retrofitted Frame 1.

a)

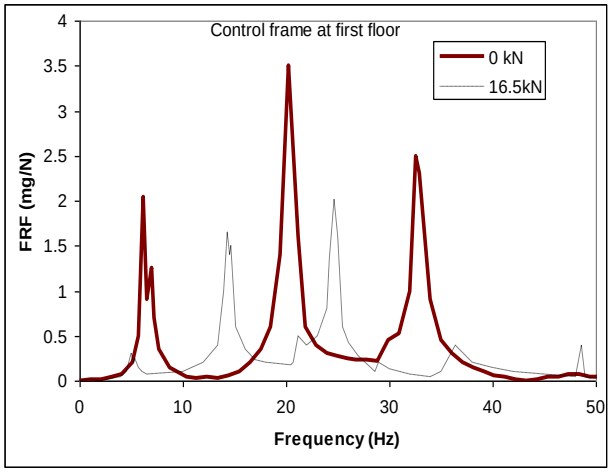

b)

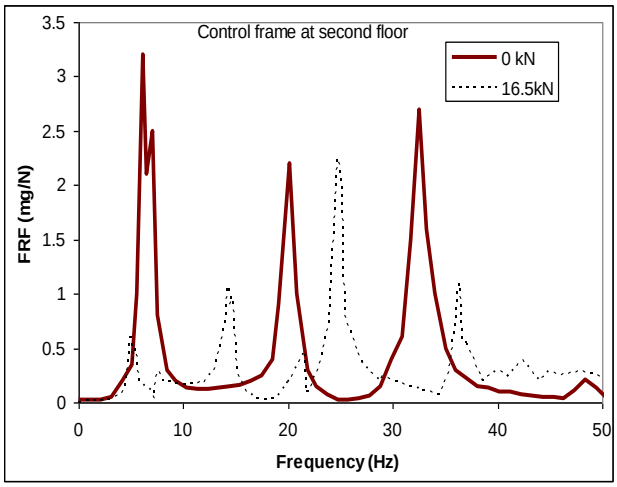

c)

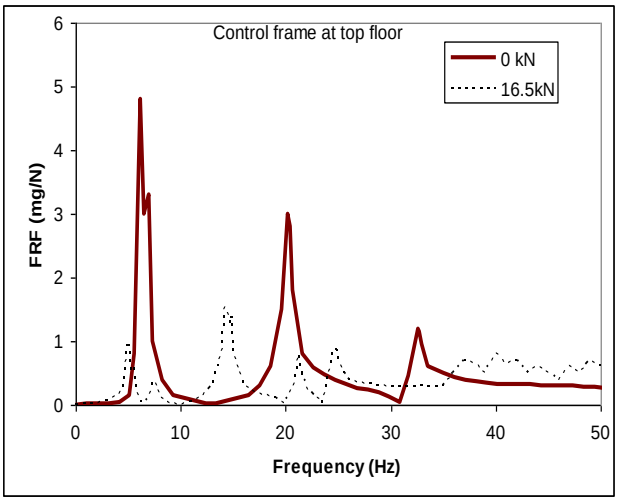

Figure 5.19 FRF plots between initial and final state of Control Frame 1: a) first floor, b) second floor and c) top floor.

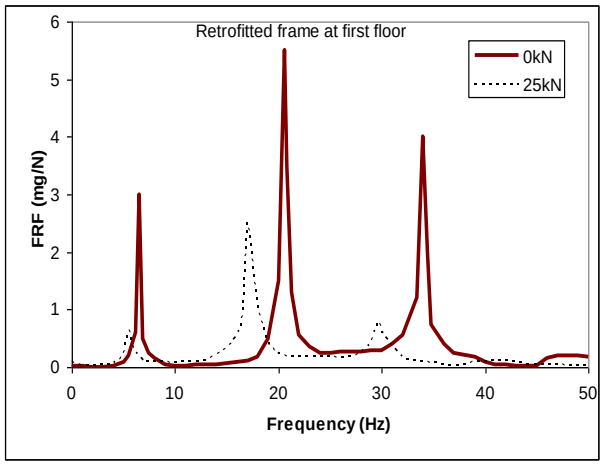

a)

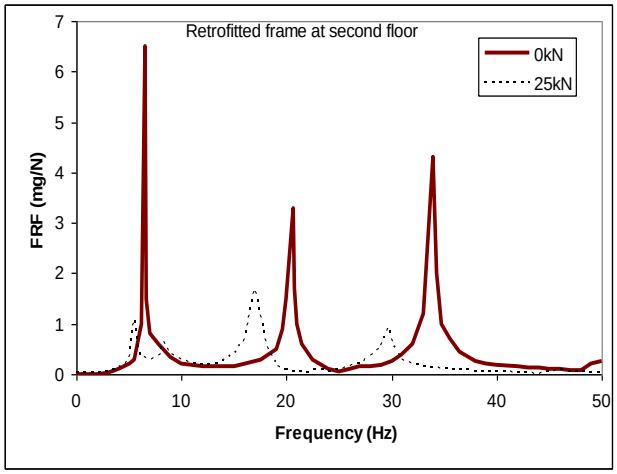

b)

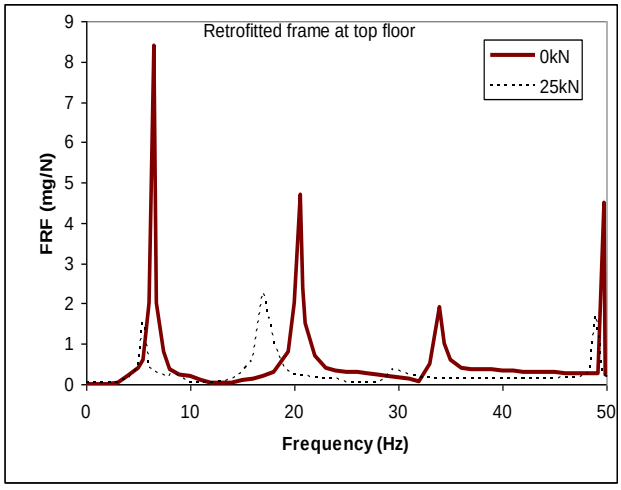

c)

Figure 5.20 FRF plots between initial and final state of Retrofitted Frame 1: a) first floor, b) second floor and c) top floor.

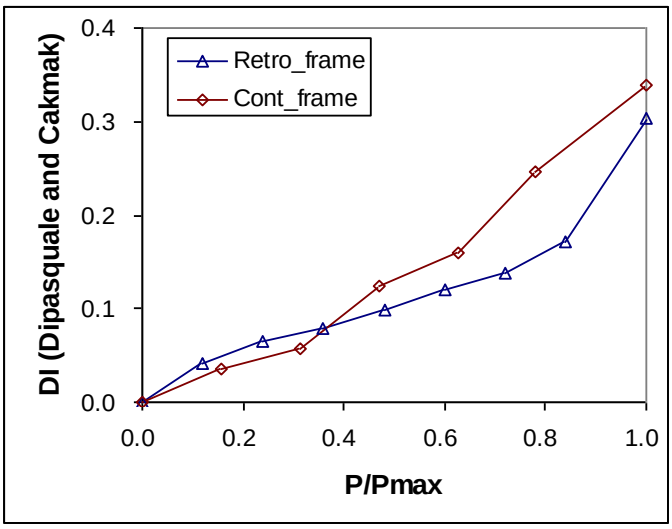

Figure 5.21 Modal plastic softening damage indices of Frame 1.

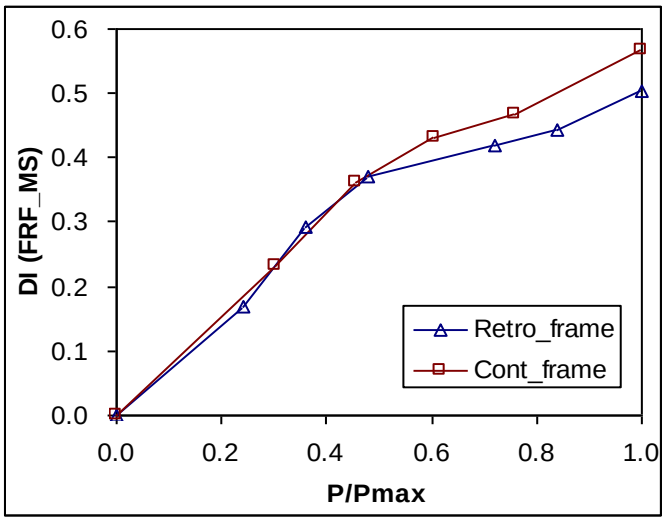

Figure 5.22 FRF based mode shape damage indices of Frame 1.

a)

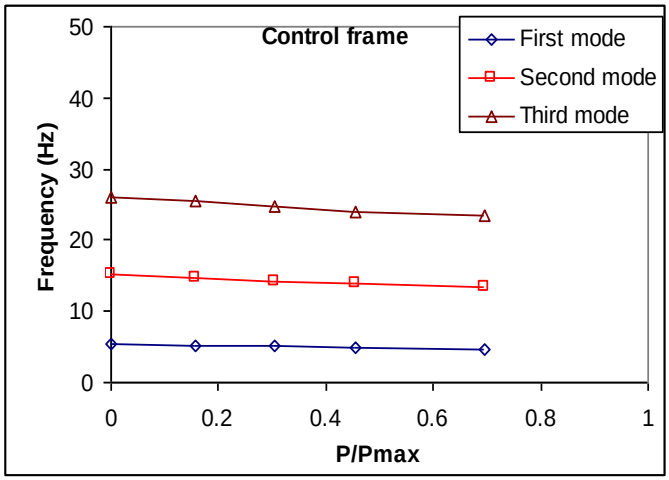

b)

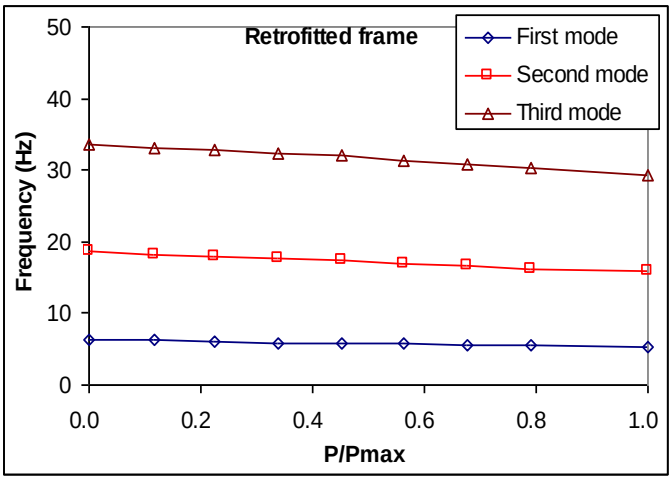

Figure 5.23 Natural frequency plots: a) Control Frame 2 and b) Retrofitted Frame 2.

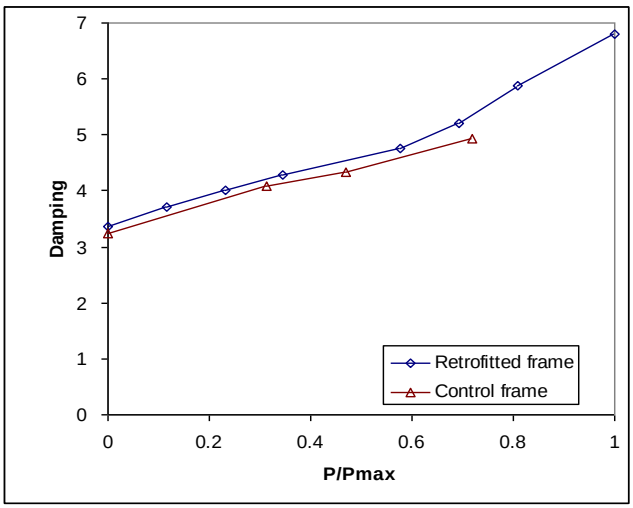

Figure 5.24 Damping coefficients of Frame 2.

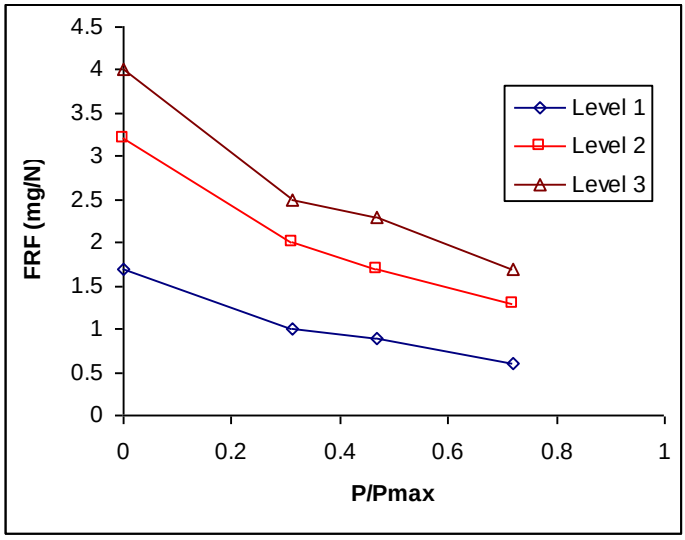

Figure 5.25 FRF magnitudes of Control Frame 2.

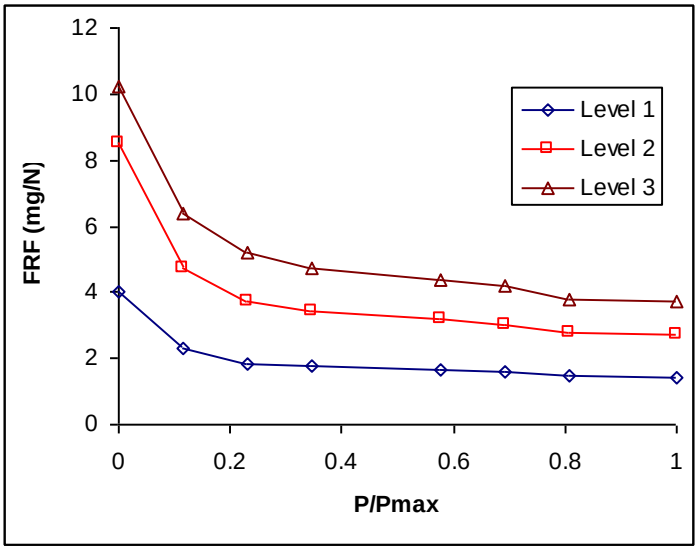

Figure 5.26 FRF magnitudes of Retrofitted Frame 2.

a)

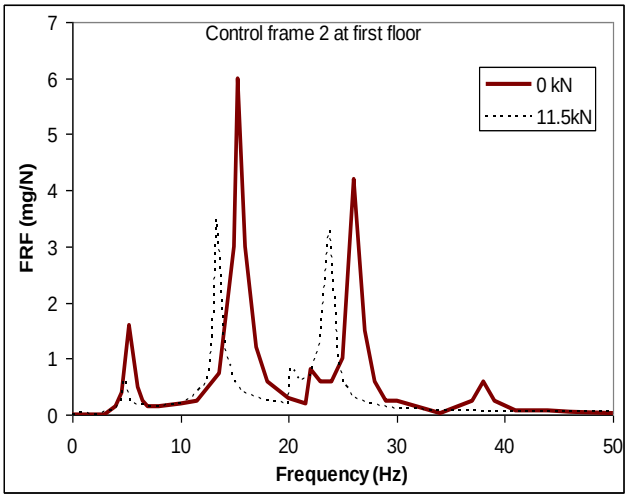

b)

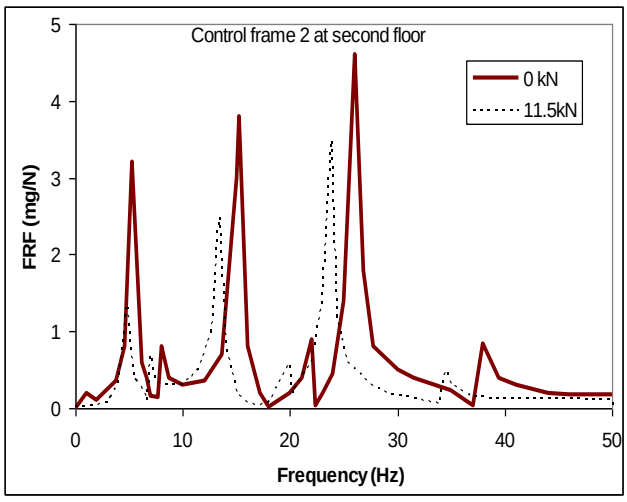

c)

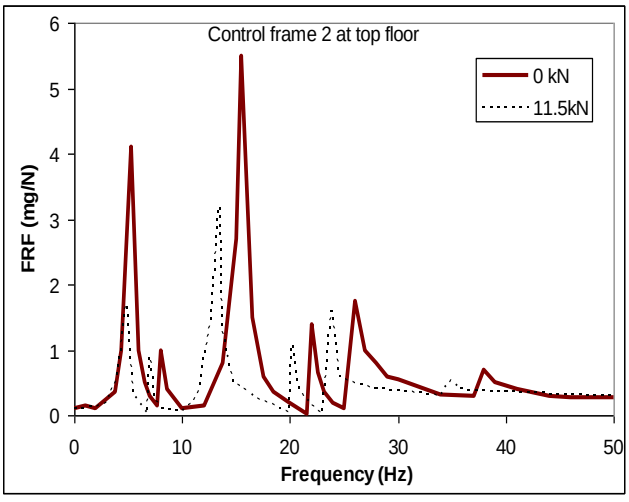

Figure 5.27 FRF plots between initial and final state of Control Frame 2: a) first floor, b) second floor and c) top floor.

a)

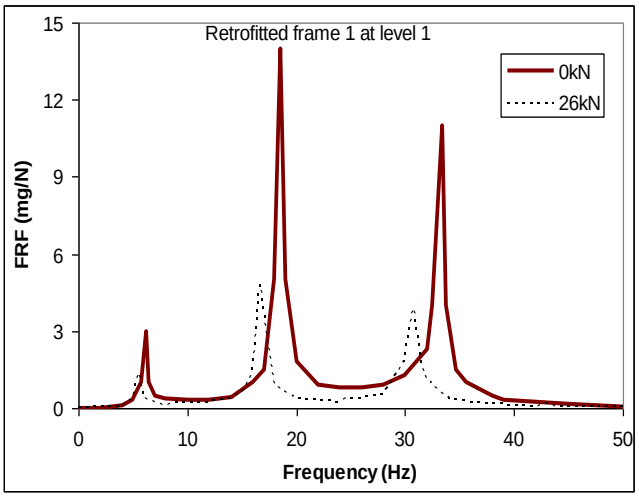

b)

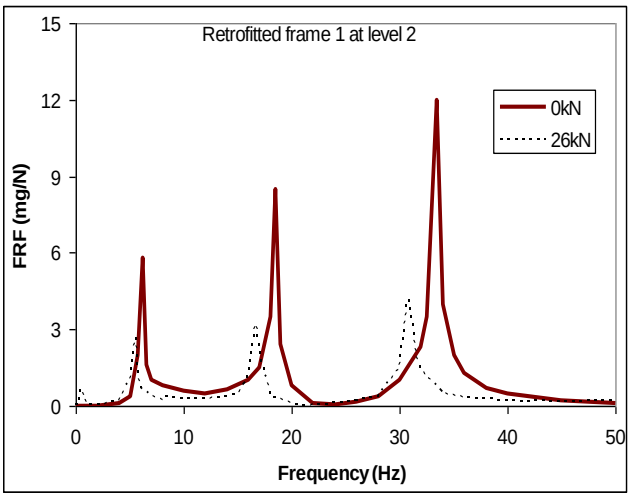

c)

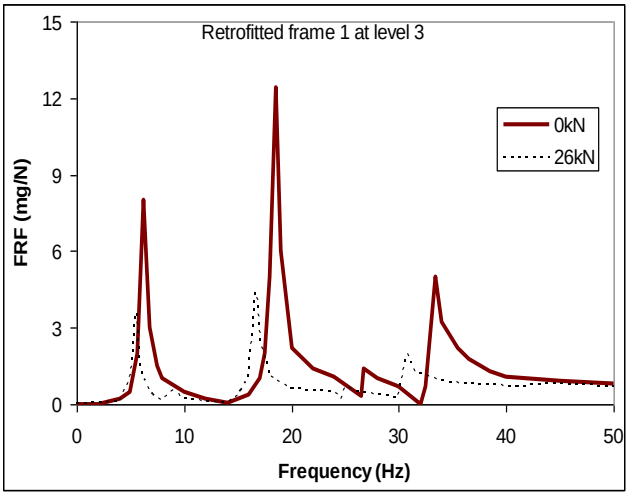

Figure 5.28 FRF plots between initial and final state of Retrofitted Frame 2: a) first floor, b) second floor and c) top floor.

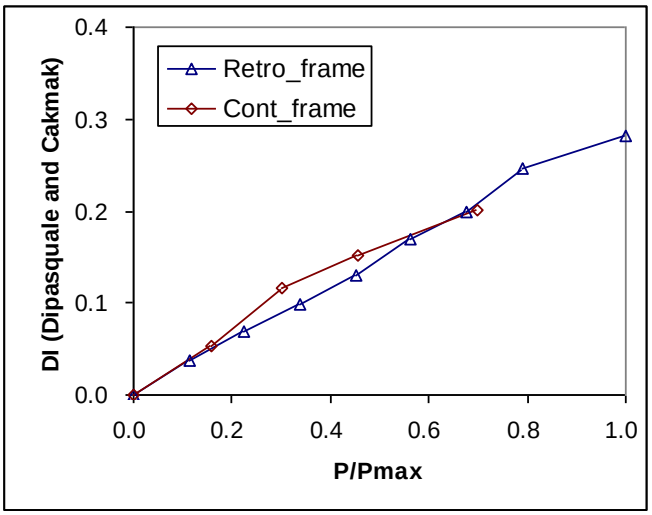

Figure 5.29 Modal plastic softening damage indices of Frame 2.

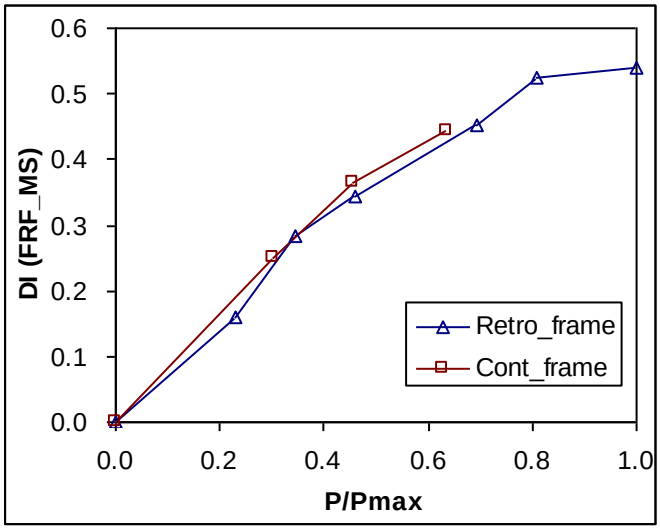

Figure 5.30 FRF based mode shape damage indices of Frame 2.

a)

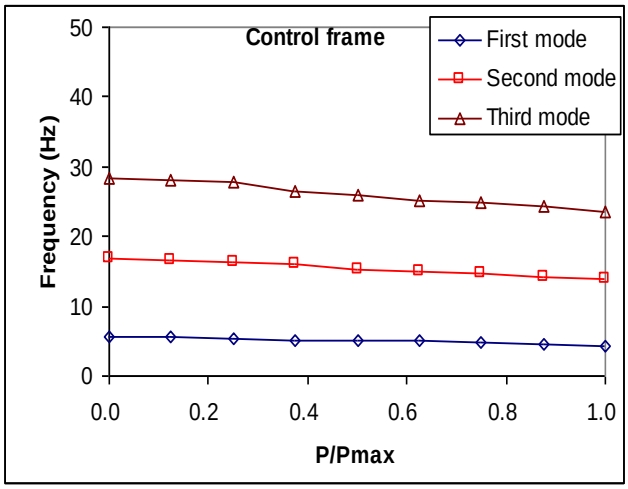

b)

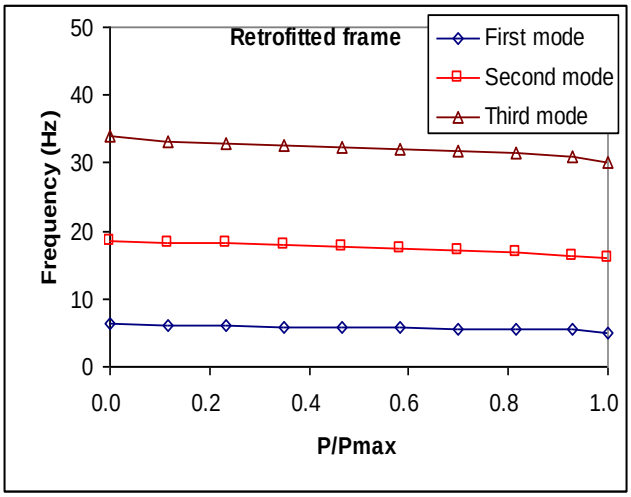

Figure 5.31 Natural frequency plots: a) Control Frame 3 and b) Retrofitted Frame 3.

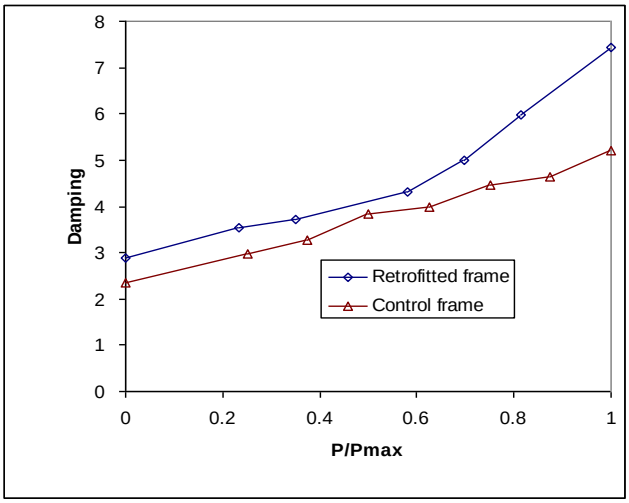

Figure 5.32 Damping coefficients of Frame 3.

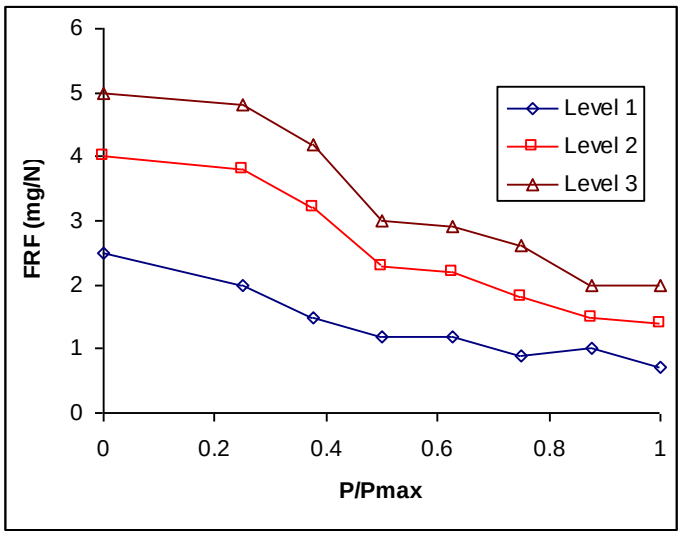

Figure 5.33 FRF magnitudes of Control Frame 3.

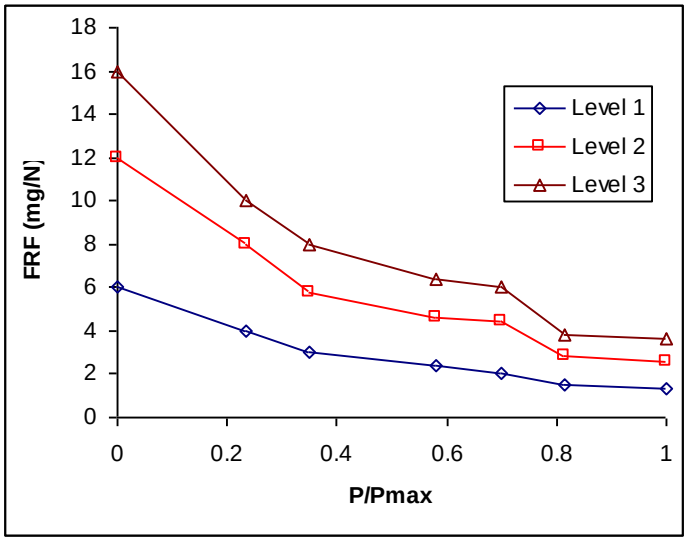

Figure 5.34 FRF magnitudes of Retrofitted Frame 3.

a)

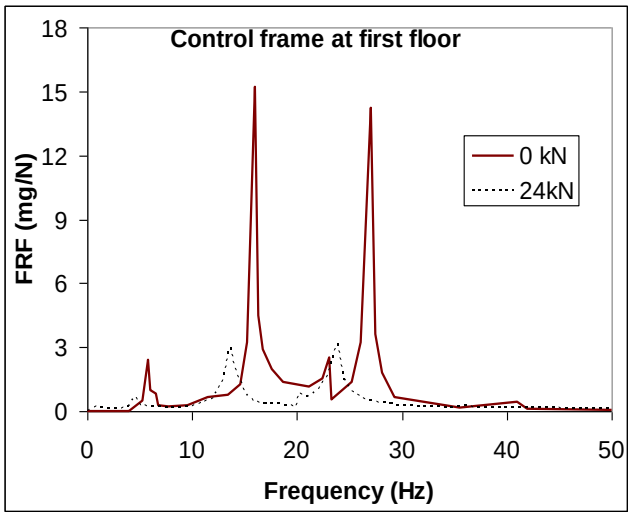

b)

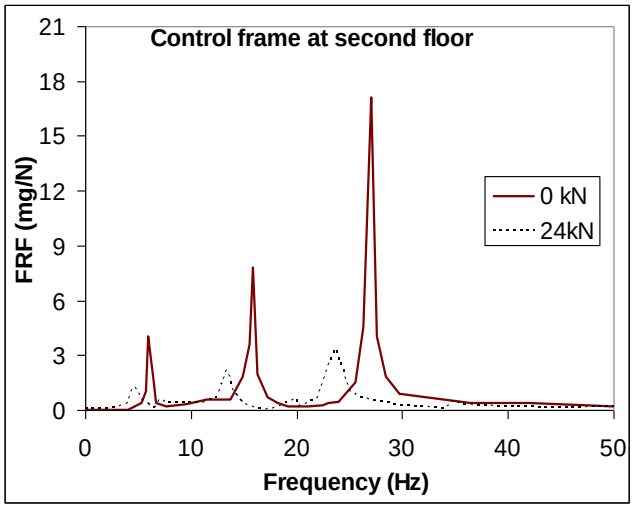

c)

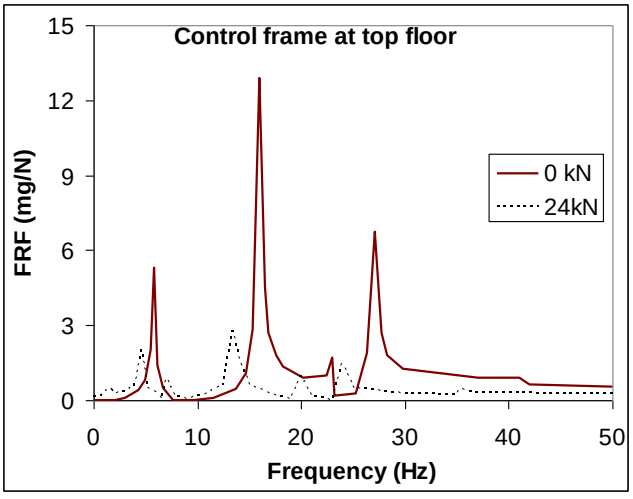

Figure 5.35 FRF plots between initial and final state of Control Frame 3: a) first floor, b) second floor and c) top floor.

a)

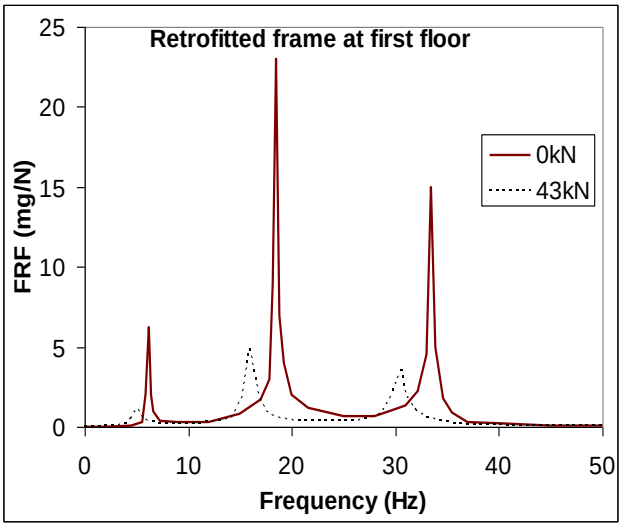

b)

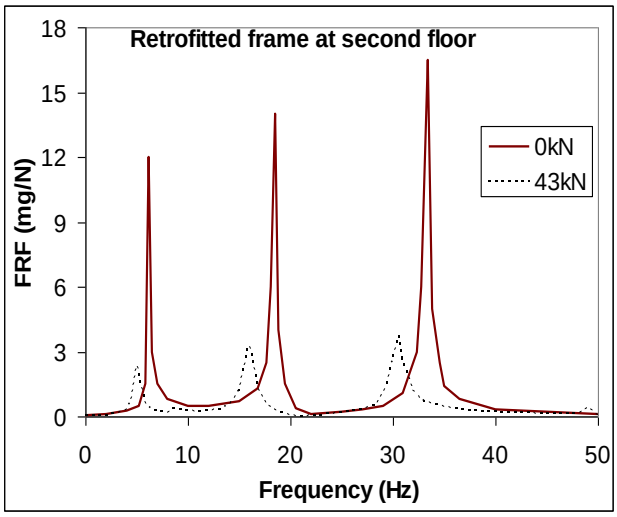

c)

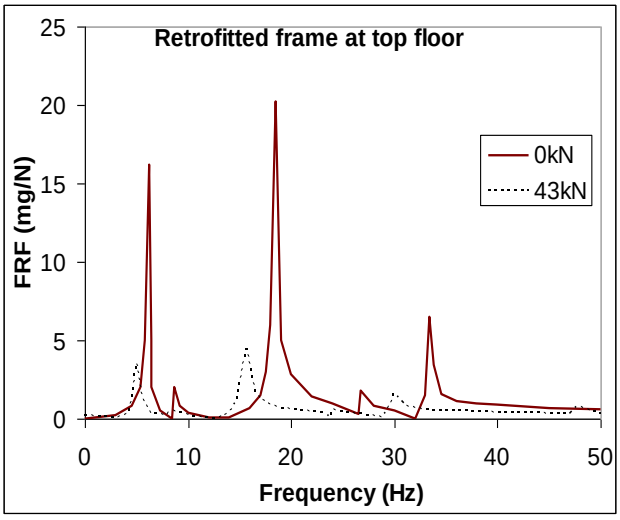

Figure 5.36 FRF plots between initial and final state of Retrofitted Frame 3: a) first floor, b) second floor and c) top floor.

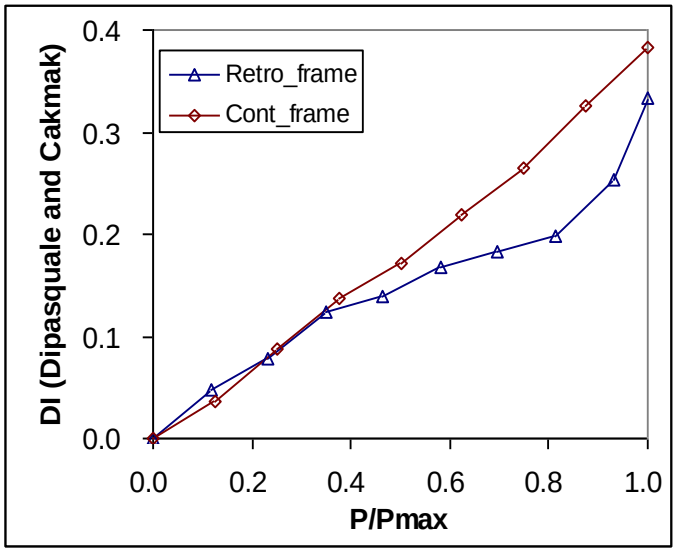

Figure 5.37 Modal plastic softening damage indices of Frame 3.

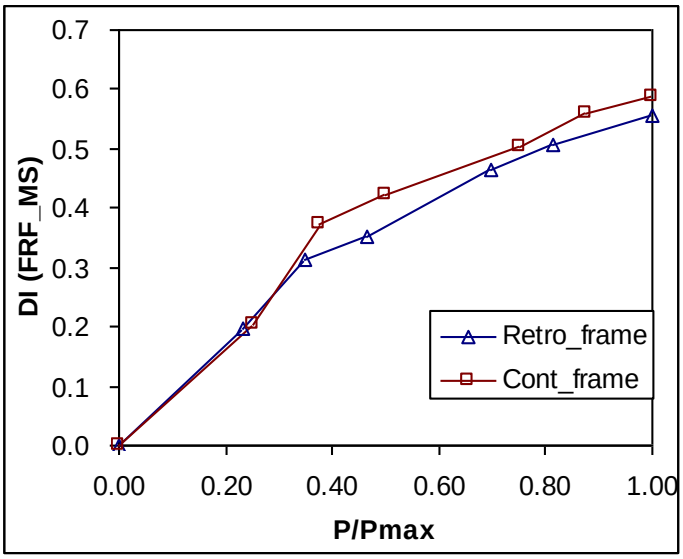

Figure 5.38 FRF based mode shape damage indices of Frame 3.

a)

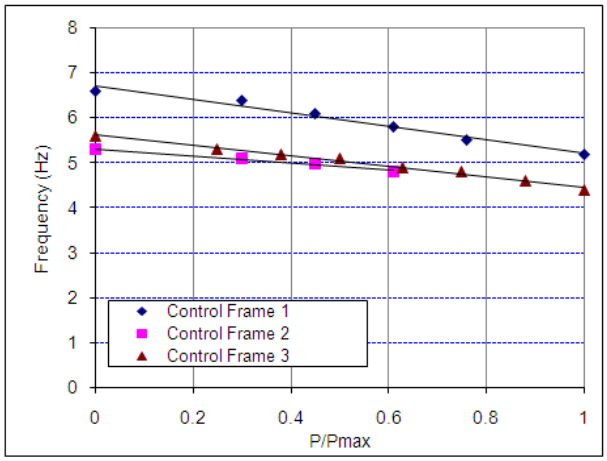

b)

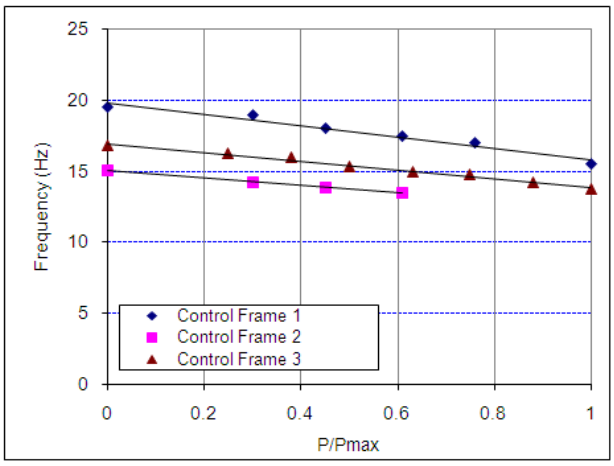

c)

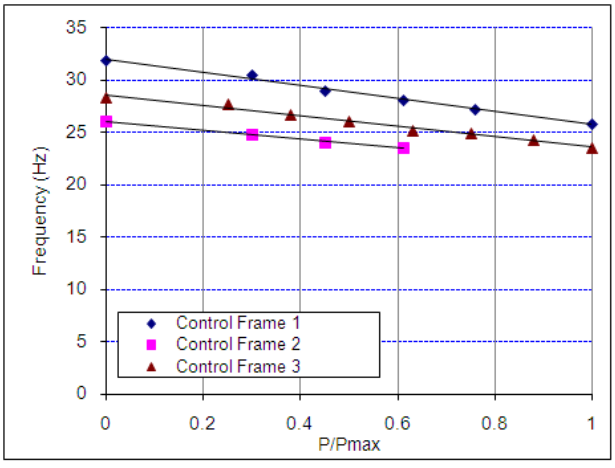

Figure 5.39 Comparison of natural frequencies between Control Frame 1, 2 and 3 : a) first mode, b) second mode, c) third mode.

a)

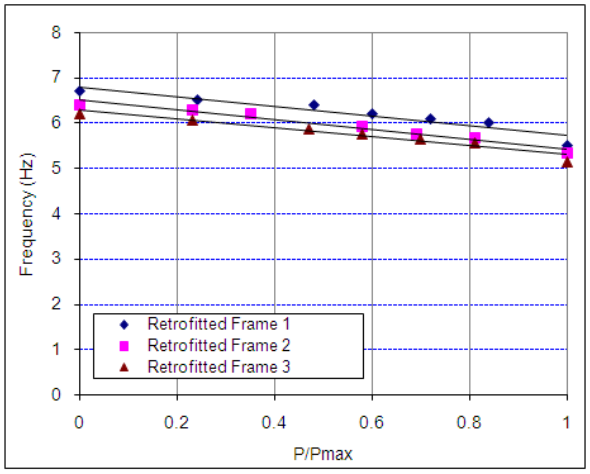

b)

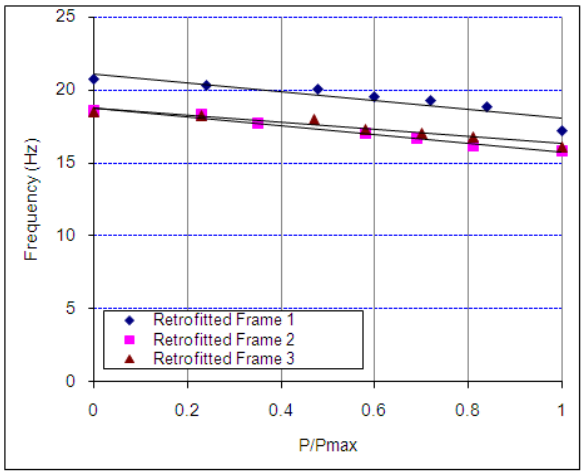

c)

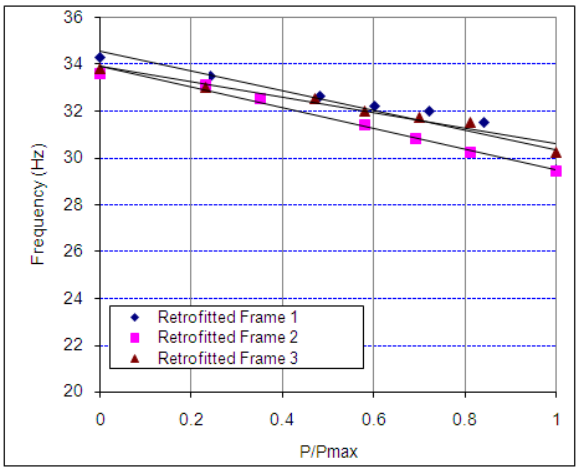

Figure 5.40 Comparison of natural frequencies between Retrofitted Frame 1, 2 and 3 : a) first mode, b) second mode, c) third mode.

a)

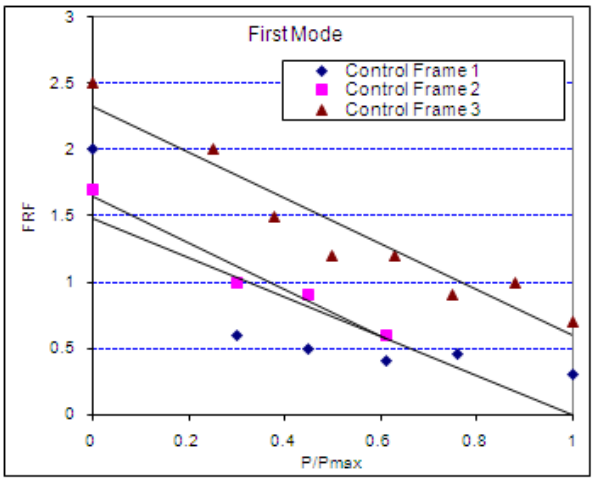

b)

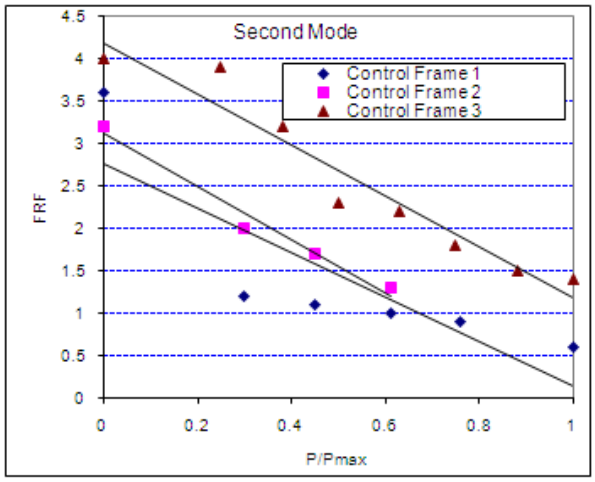

c)

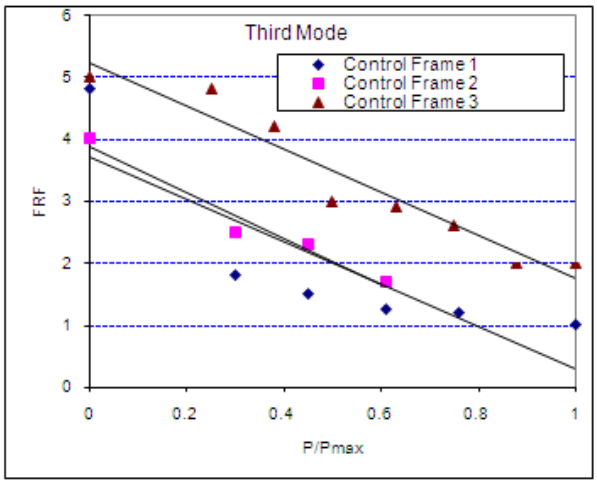

Figure 5.41 Comparison of FRFs between Control Frame 1, 2 and 3 : a) first mode, b) second mode, c) third mode.

a)

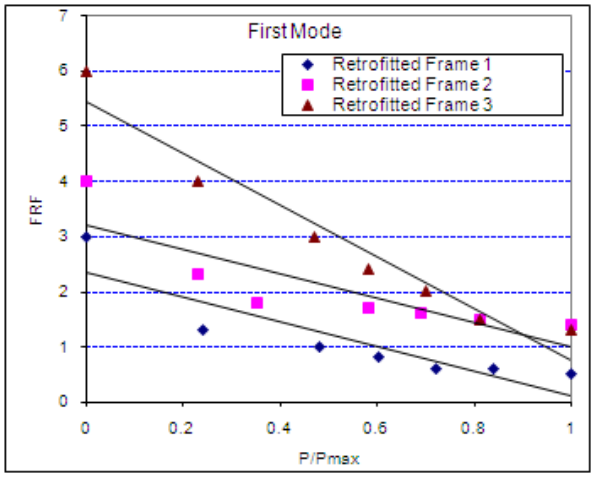

b)

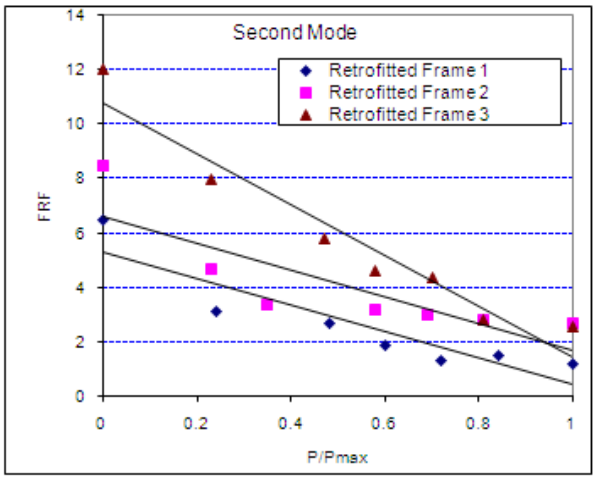

c)

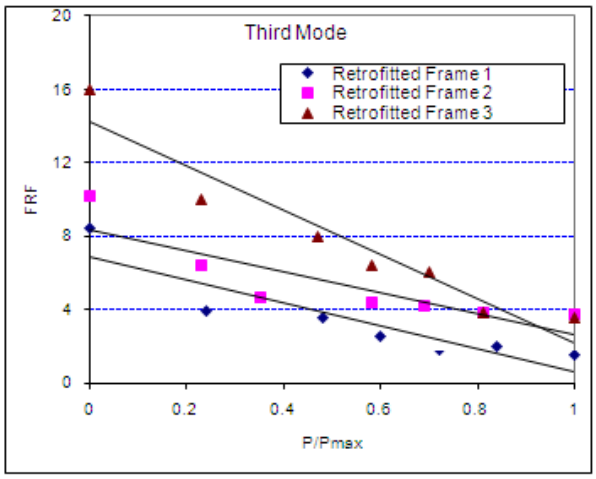

Figure 5.42 Comparison of FRFs between Retrofitted Frame 1, 2 and 3 : a) first mode, b) second mode, c) third mode.

CHAPTER 6

NONLINEAR AND DYNAMIC FINITE ELEMENT MODEL AND COMPARATIVE ANALYSIS

6.1 GENERAL

This chapter discusses the theory related to both nonlinear FE analysis and dynamic FE analysis. All the necessary steps to create the models are explained in detail. The comparative analysis between FE models and experimental results is presented. The dynamic responses of the original and FRP-strengthened frame are simulated. The modal assurance criterion and coordinate modal assurance criterion, which are derived from mode shape, are used to identify damage on structures.

6.2 NONLINEAR FINITE ELEMENT ANALYSIS

It is important to realize that the whole RC structure does not have to be analyzed using a full nonlinear formulation. However, a simplified or linear formulation can be used in many cases. It is a matter of engineering knowledge and assessment, whether the inaccuracies due to a simplified formulation are acceptable or not. FE method is a numerical technique that is used to simulate the structural behavior and the failure mechanism of structures. ATENA is FE analytical software that has versatile applications in nonlinear analysis of structure. In short, this is a useful program in the nonlinear analysis of RC members (Vimuttasoongviriya et al., 2009 and 2010; Cervenka et al., 1991, 1992, and 1995). This FE software program (ATENA-3D v4) is popular in Europe where it is applied in studies to simulate the behavior of experimental frames.

An eight-node brick element was used to model the concrete as shown in Figure 6.1. The element is capable of plastic deformation, cracking in three orthogonal directions, and crushing. A poly-line element was used to model the steel bars. Two nodes are required for this element. Each node has three degrees of freedom. The steel for the FE model was assumed to be an elastic and perfectly plastic material. A 20 node quadratic 3D brick shell element was used to model the FRP composite (ATENA Revision 2005/01, 2005). This element allows for different material layers with different

orientations. The FRP components consist of two constituents which are combined at a macroscopic level and are not soluble in each other. One constituent is the reinforcement, which is embedded in the second constituent-epoxy. The reinforcing material is in the form of anisotropic materials of glass fibers which are typically stiffer and stronger than the epoxy (Ferracuti and Savoia, 2006; Kachlakev et al., 2001). Nodes of FRP layered shell elements are connected to those of adjacent concrete solid element in order to satisfy the perfect bond assumption. Figure 6.1 shows a schematic representation of FRP composites. The material properties of epoxy and GFRP sheet are presented in Table 6.1. An eight-node brick element was used to model steel plates at the loading point at the top floor, and the supports as shown in Figure 6.2 and 6.3. A 25 mm thick steel plate was added at the supporting and loading location in order to avoid stress concentration problems. By taking advantage of the symmetry of the frame, a symmetrical half of the full frame was used for modeling. The typical FE model for half frame is shown in Figure 6.4. At a plane of symmetry, the displacement in the direction perpendicular to the plane was held at zero. The boundary conditions of supports and the symmetrical planes are shown in Figure 6.5 and 6.6. The monitoring points were measured at the middle of each floor, where the largest horizontal displacements can be expected.

6.2.1 Equivalent uniaxial law of concrete

The nonlinear behavior of concrete in the biaxial stress state is described by the relationship between effective stress σ_c^{ef} and the equivalent uniaxial strain ε^{eq}. The equivalent uniaxial strain is produced by the stress of concrete σ_{ci} with modulus E_{ci} associated with the direction *i*. Within this assumption, the nonlinearity representing a damage is caused only by the governing stress σ_{ci}. The details can be found in Chen (1982). The equivalent uniaxial strain is calculated as

$$\varepsilon^{eq} = \frac{\sigma_{ci}}{E_{ci}} \tag{6-1}$$

Unloading is a linear function close to the origin. The equivalent uniaxial stress-strain diagram for concrete and an example of the unloading point *U* are shown in Figure 6.7.

The relation between effective stress and equivalent uniaxial strain depends on a load history. The numbers of the diagram parts in Figure 6.7 are used in the results of the analysis to indicate the state of damage of concrete. A change from loading to unloading occurs when the increment of the effective strain changes sign. If subsequent reloading occurs, the linear unloading path is followed until the last loading point *U* is reached again. Then, the loading function is resumed.

6.2.2 Tension before cracking of concrete

The behavior of concrete under tension and without cracks is assumed to be linear elastic from initial state to the effective tensile strength point. The tensile strength without cracks is calculated as

$$\sigma_c^{ef} = E_o \, \varepsilon^{eq} \qquad when \quad 0 \le \sigma_c \le f_t^{'ef} \tag{6-2}$$

where E_o is the initial elastic modulus of concrete, and $f_t^{'ef}$ is the effective tensile strength derived from the biaxial failure function.

6.2.3 Tension after cracking of concrete

The exponential crack opening law is used to model the concrete crack opening as shown in Figure 6.8. This function of crack opening was derived experimentally by Hordijk (1991). The function of crack opening is calculated as

$$\frac{\sigma}{f_t^{'ef}} = \left\{ 1 + \left(c_1 \frac{w}{w_c} \right)^3 \right\} \exp\left(-c_2 \frac{w}{w_c} \right) - \frac{w}{w_c} \left(1 + c_1^3 \right) \exp\left(-c_2 \right) \tag{6-3}$$

where *w* is the crack width, w_c is the crack opening at the complete release of stress, σ is the normal stress in the crack. Values of the constants are, c_1 = 3, c_2 = 6.93, respectively. G_f is the fracture energy needed to create a unit area of stress-free crack, $f_c^{'ef}$ is the effective tensile strength derived from a failure function. The crack opening displacement *w* is derived from strains according to the crack band theory.

6.2.4 Compression before peak stress of concrete

The nonlinear behavior of compression follows the Committee Euro International du Beton Model (CEB-FIP, 1990). The formula has been adopted for the ascending branch of the concrete stress-strain law in compression as shown in Figure 6.9. This formula enables a wide range of curve forms and is appropriate for normal as well as high strength concrete.

$$\sigma_c^{ef} = f_c^{'ef} \frac{qx - x^2}{1 + (q-2)x} \tag{6-4}$$

where $f_c^{'ef}$ is concrete effective compressive strength, x is normalized strain, q is shape parameter, ε is strain, ε_c is strain at the peak stress, E_o is initial elastic modulus and E_c is secant elastic modulus at the peak stress. As a consequence of the above assumption, distributed damage which is considered before the peak stress is reached, contrary to localized damage, is considered after the peak.

6.2.5 Compression after peak stress of concrete

The fictitious compression plane model is based on the assumption that compression failure is localized in a plane normal to the direction of principal stress. All post-peak compressive displacements and energy dissipation are localized in this plane. It is assumed that this displacement is independent of the size of the structure. This hypothesis is supported by experiments conducted by Mier (1986). This assumption is analogous to the Fictitious Crack Theory for tension, where the shape of the crack-opening and the fracture energy are defined and are considered as material properties. The softening law is transformed from a fictitious failure plane, Figure 6.10, to the stress-strain relation valid for the corresponding volume of continuous material. A slope of the softening law is defined by means of the softening modulus E_d. This formulation is dependent on the size of the finite element mesh.

Fictitious compression plane model is applied to simulate compression after peak stress of concrete. The slope of softening part of stress-strain diagram is defined by two points: a peak of the diagram at the maximal stress and a limit compressive strain, ε_d,

at the zero stress. This strain is calculated from a plastic displacement, w_d, and a band size, L_d, according to the following expression:

$$\varepsilon_d = \varepsilon_c + \frac{w_d}{L_d} \tag{6-5}$$

6.2.6 Fracture process, crack width of concrete

The process of crack formation can be divided into three stages as shown in Figure 6.11. The uncracked stage is before a tensile strength is reached. The crack formation takes place in the process zone of a potential crack with decreasing tensile stress on a crack face due to a bridging effect. Finally, after a complete release of the stress, the crack opening continues without the stress (Cervenka et al., 1991, 1992, and 1995). The crack width *w* is calculated as a total crack opening displacement within the crack band.

$$w = \varepsilon_{cr} L_t^{'} \tag{6-6}$$

where ε_{cr} is the crack opening strain, which is equal to the strain normal to the crack direction in the cracked state after the complete stress release. Figure 6.11 shows that the smeared model based on the refined crack band theory can successfully describe the discrete crack propagation in plain, as well as reinforced concrete. It is also possible, that the second stress, parallel to the crack direction, exceeds the tensile strength. Then the second crack, in the direction orthogonal to the first one, is formed using the same softening model as the first crack.

6.2.7 Compressive failure of concrete

A biaxial stress failure criterion according to Kupfer et al. (1969) is used as shown in Figure 6.12. In the compression-compression stress state the failure function is

$$f_c^{'ef} = \frac{1+3.65a}{(1+a)^2} f_c^{'} \tag{6-7}$$

where σ_{c1}, σ_{c2} are the principal stresses in concrete and $f_c^{'}$ is the uniaxial cylinder strength. In the biaxial stress state, the strength of concrete is predicted under the assumption of a proportional stress path. In the tension-compression state, the failure

function continues linearly from the point $\sigma_{c1} = 0, \sigma_{c2} = f_c^{'}$ into the tension-compression region with the linearly decreasing strength:

$$f_c^{'ef} = f_c^{'} r_{ec} \tag{6-8}$$

where r_{ec} is the reduction factor of the compressive strength in the principal direction 2 due to the tensile stress in the principal direction 1.

6.2.8 Tensile failure of concrete

In the tension-tension state, the tensile strength is constant and equal to the uniaxial tensile strength, $f_t^{'}$. In the tension-compression state, the tensile strength is reduced by the relation:

$$f_t^{'ef} = f_t^{'} r_{et} \tag{6-9}$$

where r_{et} is the reduction factor of the tensile strength in the direction 1 due to the compressive stress in the direction 2.

6.2.9 Model of smeared crack

The smeared crack approach for modeling of the cracks is adopted in ATENA. Within the smeared concept two options are available for crack models: the fixed crack model and the rotated crack model. In both models the crack is formed when the principal stress exceeds the tensile strength. Although the rotated crack model is assumed that the cracks are uniformly distributed, but no shear strain occurs on the crack plane and only two normal stress components be defined (Crisfield, 1989). Therefore, this research used the fixed crack model.

In the fixed crack model (Darwin, 1974), the crack direction is given by the principal stress direction at the moment of the crack initiation. During further loading this direction is fixed and represents the orthotropic material axis. The principal stress and strain directions coincide in the uncracked concrete because of the assumption of isotropy in the concrete component. After cracking the component is introduced. The weak material axis m_1 is normal to the crack direction, the strong axis m_2 is parallel with the cracks. In a general case the principal strain axes ε_1 and ε_2 rotate and need not

to coincide with the axes of the orthotropic m_1 and m_2. This produces a shear stress on the crack face as shown in Figure 6.13. The stress components σ_{c1} and σ_{c2} denote the stresses normal and parallel to the crack plane.

6.2.10 Shear stress in cracked concrete

The shear modulus (Kolmar, 1986) is reduced with growing strain normal to the crack, as shown in Figure 6.14. This presents a reduction of the shear stiffness due to the crack opening.

$$G = r_g \, G_c \tag{6-10}$$

where r_g is the shear retention factor, G is the reduced shear modulus, G_c is the initial concrete shear modulus.

6.2.11 Compressive strength of cracked concrete

A reduction of the compressive strength after cracking in the direction parallel to the cracks in ATENA is calculated as following:

$$f_c^{'ef} = r_c \, f_c' \tag{6-11}$$

where r_c is compressive reduction factor, f_c' is compressive strength of concrete, and the constant c is 0.45, respectively. This function is based on Kolleger et al. (1988) which has the form of the Gauss's function as shown in Figure 6.15. For the zero normal strain ε_υ, there is no strength reduction, and for large strains, the strength asymptotically approaches the minimum value $f_c^{'ef} = c \, f_c^{'}$.

6.2.12 Reinforcement stress-strain law

Stress-strain law for the reinforcement steel bar is the bilinear law. In the bilinear law, elastic-perfectly plastic, is assumed as shown in Figure 6.16. The initial elastic part has the elastic modulus of steel E_s. The second line represents the plasticity of the steel with hardening and its slope is the hardening modulus E_{sh}. In case of perfect plasticity E_{sh} = 0. Limit strain ε_L represents limited ductility of steel.

6.2.13 Fiber Reinforced Polymer model

In general case of RC structure, the elemental geometric modeling of concrete has been done using 3D solid brick element with 8 up to 20 nodes in ATENA as shown in Figure 6.17. The 3D solid brick element has three degree of freedom at each node: translations in the nodal x, y and z directions. This is an iso-parametric element, capable of plastic deformation, cracking in three orthogonal directions, and crushing. The most important aspect of this element is the treatment of nonlinear material properties.

FRP modeling : The FRP modeling can be done as a 3D shell element in ATENA. The Ahmad shell element implemented in ATENA (Ahmad et al., 1970), described in ATENA theory manual. The present Ahmad element belongs to group of shell element formulation that is based on 3D elements concept. It can be used to model thin as well as thick shell or plate structures.

Geometry of the FRP : The FRP can be modeled as a shell element in ATENA. The Ahmad shell element used the 20 nodes iso-parametric brick element. This is needed, in order to be able to use the same pre and post-processors support for the shell and native 3D brick element. After the 1st step of the analysis, the input geometry will automatically change to the external geometry from Figure 6.18. As nodes 17 and 18 contain only so called bubble function, the element is post-processed in the same way as would be the iso-parametric brick element. Internally, all of the element's vectors and matrices are derived based on the internal geometry as also depicted in Figure 6.12.

Element property of the FRP : FRP is an Ahmad shell element. In the following general shell element theory concept, every node of an element has five degree of freedom, e.g. three displacements and two rotations in planes normal to mid surface of element. In order to facilitate a simple connection of this element with other true 3D elements, the five degrees of freedom are transformed into x, y, z displacement of a top node and x, y displacement of a bottom node. The two nodes are located on the normal to mid-surface, passing thru the original mid-surface element's node.

6.2.14 Equilibrium iterations

For structural analysis, Lagrangian formulation is better, and therefore attention will be restricted to this. Two forms of the Lagrangian formulation are possible. The governing

equations can either be written with respect to the undeformed original configuration at time t = 0 or with respect to the most recent deformed configuration at time t. The former case is called Total Lagrangian formulation while the latter one is called the Updated Lagrangian formulation. It is difficult to say which formulation is better because both have their advantages and drawbacks. Usually it depends on the particular structure being analyzed, and which one to use is a matter of engineering judgment. Generally, provided the constitutive equations are adequate, the results for both methods are identical. ATENA currently uses Updated Lagrangian formulation, and supports the highest, i.e. 3rd level of nonlinear behavior (ATENA Revision 2005/01, 2005). The material parameters of constitutive model in ATENA are presented in Appendix B.

6.3 NONLINEAR FINITE ELEMENT ANALYTICAL RESULTS

6.3.1 Control Frame 1 and Retrofitted Frame 1

In nonlinear FE analysis, the ATENA program uses Newton-Raphson equilibrium iterations for updating the model stiffness. The loads applied to a FE model are divided into a series of load increments called load steps. According to CEB-FIP Model Code 90 (1990), the elastic modulus of fresh concrete of Control Frame 1 was 26,810 MPa. For higher accuracy the stiffness damage index need to be scaled for damaged elements in this study. The parameters used in this index depend on the cross-section and material property of the structural element. Because the property of any FE model element is different from its actual counterpart (Kanwar et al. 2007 and Supaviriyakit et al., 2004). This index was modified on the degradation of elastic modulus and applied to the FE model. The results of the FE analysis show that ultimate state was achieved at the load of 16 kN with displacement of 49 mm. The load-displacement behavior of Control Frame 1 is shown in Figures 6.19. The energy dissipation from the FE model was observed to be 607 kN-mm. Crack pattern from the FE model is shown in Figure 6.20. It shows that cracks occurred on beam-column joints of each floor level at the ultimate state. At final state, crack pattern was diagonal shaped, indicating shear resistance capacity of this frame was weak. The substantial energy was absorbed in connections of each floor.

In case of strengthening the FE model by using FRP wrap, a 20 node quadratic 3D brick shell element was used to model the FRP composite. The frame model was strengthened by epoxy resin and FRP wrap around the damaged elements. The first part of the strengthening material was epoxy resin with a thickness of 1 mm as a 3D bilinear steel von mises. The second part was FRP sheet with a thickness of 0.34 mm. The FRP material was applied in two directions as reinforcement. First direction was along the structural element axes and the other direction was perpendicular to the first direction. From experimental results at final state of Control Frame 1, the DI_k of 0.69 was applied to calculate the damaged elasticity modulus of concrete. As a result, the elastic modulus of concrete of Retrofitted Frame 1 was 8,311 MPa. FE analysis for retrofitted frame was performed in the similar process as that for the control frame. The FE analytical results of Retrofitted Frame 1show that the ultimate load was achieved to be at a load of 26 kN and a displacement of 54.4 mm. The properties of epoxy resin and FRP sheet are presented in Table 6.1. The energy dissipation was 1,212 kN-mm. The loads versus displacement behavior at each floor are shown in Figures 6.26 along with the result of Control Frame 1. At the end of the test, there were cracks in FRP layers in connections and the heavy cracks occurred in tension zones of the FRP layer at the top floor. However, it is observed that cracks also appeared in connections of RC elements. The crack pattern at final state of Retrofitted Frame 1 is shown in Figure 6.21. FE analytical results support the use of FRP wrapped for structural strengthening. Lateral load capacity increased approximately 63%, compared to Control Frame 1.

6.3.2 Control Frame 2 and Retrofitted Frame 2

FE model of Control Frame 2 was done in same detail as Control Frame 1. The elastic modulus of fresh concrete was 24,870 MPa. The material properties used are presented in Table 6.1 along with the properties of Control Frame 1. This frame experienced each load step from initial state until the load of 11.5 kN (70% of maximum load of Control Frame 1) to simulate the medium-damage level. From FE analysis at a load of 11.5 kN, cracks started to open with displacement of 14.3 mm from initial state. The energy dissipation was observed to be 66 kN-mm. The load-displacement behavior is shown in Figures 6.22 and crack pattern is shown in Figure 6.23. Crack pattern from FE analysis shows that the first crack was observed at the column near the support in the tension zone. Another crack occurred at connections of the first, second, and top floors

respectively. These cracks are based on the assumption of perfect bond between concrete and steel reinforcing.

The first part of strengthening material of Retrofitted Frame 2 was epoxy resin with thickness of 1.5 mm. The second part was FRP wrap with thickness of 0.34 mm. FE analysis of Retrofitted Frame 2 was performed in the same manner as Retrofitted Frame 1. From this, the DI_k of 0.56 was applied leading to the elastic modulus used of concrete of Retrofitted Frame 2 is 10,943 MPa. From the FE model, ultimate state was achieved at the load of 27.2 kN and displacement of 62.6 mm. The energy dissipation was 1,098 kN-mm. The load versus displacement behavior is shown in Figures 6.22 along with the results of Control Frame 2. At the end of the test, there were no observable flexural cracks on the outside fiber layers. Crack pattern of Retrofitted Frame 2 is shown in Figure 6.24. FE analytical results support the use of FRP wrapped of medium-damage structure. Lateral load capacity increased approximately 70% and 4%, compared to Control Frame 1 and Retrofitted Frame 1, respectively.

6.3.3 Control Frame 3 and Retrofitted Frame 3

Control Frame 3 was a ductile structure, which took care of steel stirrup spacing and longitudinal steel bars hook length. The elastic modulus of fresh concrete of Control Frame 3 was 25,320 MPa. The ultimate damage state has been observed at the load of 26.7 kN and displacement of 56.9 mm. The energy dissipation has been achieved to be 961 kN-mm. The load-displacement behavior is shown in Figures 6.25. At final state, crack pattern of Control Frame 3 is shown in Figure 6.26. This figure clearly shows that there were heavy horizontal cracks in column near foundation because of the effect of bending moment. Diagonal cracks occurred in connections of each floor. Moreover, there were cracks on the middle of column at the first and the second floor. There was a gap between anchorage steel bars at middle zone of each column that caused the cracks in the model. FE analytical results approve that lateral load capacity of the ductile structure, Control Frame 3, increased approximately 67%, compared to brittle structure of Control Frame 1.

From the experimental results of Frame 3, it shows that the use of high strength adhesive epoxy injection results in proper repairing cracks in the damaged elements. Further, the elastic modulus of damaged concrete at final state of Control Frame 3 was observed to increase. Based on the results of experimental test, the elastic modulus used

in FE model of Retrofitted Frame 3 was assumed to be 25,320 MPa (fresh concrete) in this study. The first part of strengthening material was epoxy resin with thickness of 1 mm. The second part was an FRP sheet with thickness of 0.34 mm. The FE analysis for Retrofitted Frame 3 was performed in the similar process as Retrofitted Frames 1 and 2. From FE analytical results, the ultimate load of Retrofitted Frame 3 was observed at a load of 42.9 kN and displacement of 102.5 mm. The energy dissipation was measured at 2,871 kN-mm. The load versus displacement behavior at each floor is shown in Figures 6.25. The crack pattern of Retrofitted Frame 3 is shown in Figure 6.27. At the end of the analytical process, there were observable cracks on the FRP layers at beam-column joints and at tension zones of top floor columns. Horizontal and diagonal cracks were found inside each column near the foundation region. Some cracks appeared inside the middle zone of first floor columns. The deformed shape of Retrofitted Frame 3 shows that beam-column joints of each floor are stronger than column-foundation joints because there are no anchorage steel bars in columns near the foundation. Moreover, there was a gap between the FRP layer and the foundation. Thus, RC columns took loads without the help of FRP. FE analytical results support the use of FRP wrapped for structural strengthening. Lateral load capacity increased approximately 61% and 168%, compared to Control Frame 3 and Retrofitted Frame 1, respectively.

6.3.4 Nonlinear behavior comparative analysis

Developed analytical models have been validated by comparing the nonlinear behavior with experimental data. For greater accuracy the stiffness damage index needs to be scaled for each damaged element in this study. The parameters used in this index depend on the cross-section and material property of the structural element (Kanwar et al, 2007). Because the property of any FE model element is different from its actual counterpart. This index is modified on the basis of the degradation of elastic modulus and applied to the FE model. The analytical results show that the crack patterns at final state from ATENA nonlinear FE models correspond well with the observed failure mode of experimental control frames. It also shows that the crack patterns of retrofitted frames of the FE model are comparable to those that occurred during the experimental test after the strengthening layers were removed (Vimuttasoongviriya et al., 2009). The

comparisons of nonlinear behavior between the FE model and experimental result are shown in Figure 6.28 to 6.30. It shows that FE load-displacement plots in the linear range are stiffer than the experimental plots. There are several effects that may cause the higher stiffness in the model. First, micro-cracks are present in the actual elements and beam-column joints prior to loading, but the FE model does not account for these micro-cracks that reduce the stiffness of the experimental frame. Next, the assumptions of perfect bond between concrete and steel reinforcing, as well as between concrete and FRP sheet, are assumed in the FE analysis; but some slip takes place in the experiments (Chih and Hsu, 2009; Said and Nehdi, 2004; Gangadharan et al., 1991). Figure 6.28 to 6.30 also show that the ultimate load obtained from the FE model of Control Frame 1 (16 kN) was 3% less than that obtained from the experimental test (16.5 kN). The ultimate load for the FE model of Retrofitted Frame 1 was observed to be 26kN, which is higher than the ultimate load of 25 kN for the actual frame by 4%. In the case of the FE model of Retrofitted Frame 2, the ultimate load for the model of Retrofitted Frame 2 was 27.2 kN, which was 5% higher than the ultimate load of 26 kN for the experimental frame. In the case of the FE model of Control Frame 3, the ultimate load of 26.7 kN was 11% less than the ultimate load obtained from the experimental test (24 kN). The ultimate load for the model of Retrofitted Frame 3 was 42.9 kN, which was 0.14% higher than the ultimate load of 43 kN for the actual frame. This demonstrates that the analytical results are in good agreement with experimental results. However, FE models underestimate the ductile behavior of the frames because of complicated mechanisms at the crack faces, i.e. interlocking between the cracked faces, crack tips blunted by voids, and the crack branching process may slightly delay the failure at high displacement in case of the experimental frame models. These mechanisms are not considered in the FE models (Supaviriyakit et al., 2004; Kachlakev et al., 2001).

6.4 DYNAMIC FINITE ELEMENT ANALYSIS

In recent year, the implementation of the FFT based signal analyzers has provided the environmental testing laboratory with a fast and more powerful tool for acquisition and analysis of vibration data. Many researchers are actively using FE modeling techniques for structural dynamic analysis. They are beginning to use dynamic testing to complement their FE analysis activities (Ramsey, 1983). It is interaction between the

experimentalist and the analytical engineer that is so important. Both are able to communicate and reinforce one another for vibration problem solution.

In order to use FE models with confidence, it was found to be necessary to confirm the accuracy of the model by comparing the modal parameters predicted by the model with the modal parameters identified by actually testing the structures. In fact, most of the advancements in experimental modal testing came out from the demand to verify the accuracy of FE models.

Modal analysis is a useful technique for verifying and helping improve the accuracy of analytical FE models of a structure. It is a technique to solve the problem in noise, vibration and failure of structure (Ramsey, 1983). The equations of motion solved by a FE analysis are based on an idealized model and are used to predict and simulate dynamic performance of the structure. Experimental measurements on the actual hardware result in a physical check of the accuracy of the mathematical model. If the FE model predicts the same modes of vibration that are actually measured, it is reasonable to extend the use of the model for simulation (Load and Ventura, 2002).

By understanding how a structure deforms at each of its resonant frequencies, judgments can be made as the source of the disturbance or the propagation path. Modal analysis is also used to locate structural weak points. Popular FE analytical software program such as NASTRAN, ANSYS and SAP, are generally used to calculate static and dynamic response of structure. This section presents activity that consists in the numerical modeling of the original structure and FRP strengthened structure. Numerical modeling has been made by the FE program SAP 2000 (version advanced I-10.0.7) to calculate modal parameters of structure (Load and Ventura, 2002; Burgueńo et al., 2001; Kachlakev et al., 2001; Ramsey, 1983).

6.4.1 Material properties and structural model

Material properties have been defined assigning values carried out by the materials test characterization. In particular, the elastic modulus of concrete, the Poisson coefficient and yielding stress of steel has been assigned as shown in Table 6.1. After the materials definition, it has been done the definition of elements, modeled as solid model type (Barecchia, nd.). In this study, a 3D-block with 8 nodes was used to model the concrete

elements in SAP 2000 as shown in Figure 6.31. This element is an isotropic material with capable of plastic deformation, cracking and crushing.

The hypothesis of rigid floor slabs was thick shell element command. Each floor is characterized by three dynamics degree of freedom. Elements masses properties consented in master-nodes give by the mass center of each floor. For the evaluation of the mass a range criteria has been adopted. Figure 6.32 and 6.33 show the numerical model of the structure and the monitoring points, respectively. The uniaxial type was used to model the reinforcement steel bars. The steel bar for stress-strain curve was assumed to be the hysteretic type of Takeda model with Poisson's ratio of 0.3.

6.4.2 Fiber Reinforced Polymer model

A thin shell element with 4 nodes was used to model the FRP composite. This element allows for material layer with orientation. In SAP 2000 (Version 10.0.7), FRP composite consists of one constituent. The constituent is the reinforcement (Kachlakev et al., 2001; Barecchia, nd.). The reinforcing material is in the form of isotropic materials of glass fibers, which are typically stiffer and stronger than the epoxy. Nodes of FRP layered shell elements were connected to those of adjacent concrete solid element in order to satisfy the perfect bond assumption. Figure 6.31 shows a 3D-block element with 8 nodes of concrete with FRP composite.

One main difference between the test on the original and upgrade structure was in the relatively small cracking extent observed in columns for the FRP-strengthened structure (Burgueńo et al., 2001). This may be attributed to several factors. Consequently, no reduction was applied in columns gross moment of inertia.

6.5 MODAL ASSURANCE CRITERION AND COORDINATE MODAL ASSURANCE CRITERION

The measured variation of modal parameters is significant to be a good indicator of damage or repairing. The basic modal parameters such as Eigen-frequencies, modal damping ratios and mode shapes, some derived coefficients from these basic parameters can also be useful for monitoring the structures (Baghiee et al., 2009;

Maeck, 2003). The MAC and COMAC factors, which are derived from mode shape, are discussed in the following sections.

6.5.1 Modal Assurance Criterion

The Modal Assurance Criterion (MAC) is a scalar constant which is probably the most common method of establishing a correlation between experimental and analytical models (Allemang and Brown, 1982). The MAC value for two mode shape vectors ϕ_i^A and ϕ_i^B (e.g. mode shape vectors in the experimental and analytical model) is defined as:

$$MAC_{A,B} = \frac{\left|\sum_{i=1}^{n} \phi_i^A \phi_i^B\right|^2}{\sum_{i=1}^{n} \left(\phi_i^A\right)^2 \sum_{i=1}^{n} \left(\phi_i^B\right)^2} \qquad (6\text{-}14)$$

where *n* denotes the modal degree of freedom. MAC value varies from 0 to 1, which 0 for no correlation and 1 for full correlation. The deviation from 1 can be interpreted as a damage indicator in the structure (Maeck, 2003).

6.5.2 Coordinate Modal Assurance Criterion

Coordinate Modal Assurance Criterion (COMAC) is generally used to identify the mode shapes of a structure from two sets of measurements. The COMAC factor can be useful as a tool to locate damage. According to Lieven and Ewins in 1999, the COMAC value at modal coordinates *i* and *m* modes is defined as:

$$COMAC_{i,A,B} = \frac{\left|\sum_{j=1}^{m} \phi_{i,j}^A \phi_{i,j}^B\right|^2}{\sum_{i=1}^{m} \left(\phi_{i,j}^A\right)^2 \sum_{i=1}^{m} \left(\phi_{i,j}^B\right)^2} \qquad (6\text{-}15)$$

If the modal displacements in the coordinate I form two sets of measurements are identical, the COMAC factor is 1 for this coordinate.

6.6 DYNAMIC FINITE ELEMENT ANALYTICAL RESULTS

The mode shapes of FE model based on degradation of elastic modulus of concrete (Eq. 5-11) are shown in Figure 6.34 and the natural frequencies are listed in Table 6.2 to 6.7. Also shown in these tables are experimental frequencies. The natural frequencies reported in these tables show good agreement between experimental and simulated frame models. FE mode shapes at initial state are shown in Figure 6.35 to 6.40. To compare the experimental and FE mode shapes MAC values were used. Generally, the MAC values show a good correlation between experimental and numerical mode shapes. Finally, COMAC value based on experimental mode shapes was used to identify location of structural damage as shown in Figure 6.47 to 6.52. The following vibration monitoring discussions can be drawn from the results:

6.6.1 Frequency changes

Again, the relative variations of natural frequencies through load steps of experimental and FE model of all frames are shown in Table 6.2 to 6.7. In each load step, cracks were formed in frames and the natural frequencies were affected by the cracks. The frequencies of frames decreased due to a decrease in structural stiffness. For all retrofitted frames, it was expected that natural frequencies increase after strengthening because GFRP sheets must increase the stiffness. According to Table 6.2 to 6.7 the experimental modal parameters have reasonable accuracy and can be used for further applications.

In similar reinforcement detail, a relatively sharp decrease in the frequencies is observed in Control Frame 2 as compared to Control Frame 1. This phenomenon can be related to the change in mass or environmental conditions (Xia et al., 2006). The factors affecting natural frequencies include concrete aging, shrinkage, bearing and environmental conditions. In practice, these factors affect the frequencies of concrete structures in a more complicated manner.

Xia et al. (2006) showed that the frequencies decrease with an increase in temperature and humidity, but the mode shapes are insensitive to temperature and humidity changes. The variation of natural frequencies is not affected by crack location, and the damage location can not be predicted by natural frequencies (Baghiee et al., 2009; Vimuttasoongviriya et al., 2009; Kanwar et al., 2006; Doebling et al., 1998). These

studies reveal that the natural frequencies are not a useful tool for identifying damage or strengthening. In the following sections, the identification methods which employ mode shapes are discussed.

6.6.2 Variations of MAC during load steps

The experimental mode shapes of specimen frames are compared with the mode shapes of FE model by MAC values. The MAC variation as a function of load step is also shown in Table 6.8 to 6.13. A decreasing trend is observed in the MAC factors of experimental frames. In Figure 6.41 to 6.46, during the load steps the MAC values decease due to damage. This decrease is not monotonic which made the interpretation of results difficult. The non-monotonic behavior of MAC values is due to the fact that this index is sensitive to measurement (Ndambi et al., 2002). This behavior becomes more pronounced for higher modes. The measurement errors increase in higher modes and the fluctuation of MAC values is thus increased. It is worth mentioning that the damage occurred in frames seemed to be symmetrical. Other researchers have also found a decrease in MAC value for symmetrical damage pattern, although it is less than that observed for un-symmetrical damage patterns (Maeck, 2003; Ndambi et al., 2002). Due to the low sensitivity of modal assurance criterion to damage (Perera et al., 2007; Wang et al., 2007; Ndambi et al., 2002), the MAC values slightly deviate from unity during the load steps. Another factor that affects MAC values is the nature of the damage (Yeung and Smith, 2005). If the damage is distributed, such as wide spread cracking in concrete, the MAC values slightly reduce. On the other hand, the localized damage may result in larger reduction in the MAC values (Yeung and Smith, 2005).

The MAC values for Retrofitted Frames are shown in Table 6.9, 6.11 and 6.13. The same variations as described for Control Frames are observed. These observations imply that MAC values can provide information about overall stiffness change due to damage or strengthening but can not predict the location of the damage.

It has widely been accepted that MAC values greater than 0.9 well represent the correlated mode shapes when comparing the experimental and numerical mode shape (Wang et al, 2007; Farrar and Duffey 1998; Ewin, 1995). Therefore, MAC values in Table 6.8 to 6.13 show a good correlation between experimental and numerical results in primary mode shape.

6.6.3 Variations of COMAC during load steps

The COMAC values based on the measured mode shapes may indicate false damage identification (Xia et al, 2007). In calculation COMAC value, the test results of FRFs from different mode shapes corresponding to each loading step were compared with the results of initial state (Baghiee et al., 2009; Burgueno et al., 2001). The first three modes of sway were selected for calculation of COMAC factors, because these factors are sensitive to the number of mode shapes. To better interpret the results, the complement of COMAC value, i.e. 1-COMAC were used for presentation purposes. The COMAC criterion indicates consistency but not validity or orthogonality. IF there are not random or bias errors in modal vectors, the increase in 1-COMAC value relates to stiffness reduction at each degree of freedom (Baghiee et al., 2009). Figure 6.47 to 6.52 show the plots of 1-COMAC values versus degree of freedoms in different load steps. By these plots, any change in stiffness at each degree of freedom can be detected. Thus, the bar diagrams in Figure 6.47 to 6.52 show the damage progress during the load steps. The effectiveness of strengthening can also be detected using 1-COMAC values.

6.6.3.1 Control Frame 1 and Retrofitted Frame 1

In experimental test, the damage areas of Control and Retrofitted Frames were in the beam-column joint as shown in Figure 6.20 to 6.27. Bar diagrams of 1-COMAC in Figure 6.47 and 6.48 show that the damage region changes during the load steps of Control Frame 1 and Retrofitted Frame 1 respectively. From Figure 6.47, at load step of 5 kN, the 1-COMAC value of 0.3290 was in node 3, indicating damage state was in area of the top floor of the Control Frame 1. At load step of 12.5 kN, the 1-COMAC values of all nodes increase compared with initial state. At final state, the 1-COMAC value reached 0.3443 at node 1 (the first floor).

The effectiveness of strengthening in Retrofitted Frame 1 is observed in Figure 6.21. After strengthening at load step of 6 and 15 kN, the maximum values of 1-COMAC were in area of node 1. It shows that cracks occurred in the first floor. As observed in Figure 6.21 at load step of 21 and 25 kN, the 1-COMAC value of 0.5634 and 0.6807 appeared in node 2 respectively, indicating there was significant damage in the second floor of Retrofitted Frame 1 after load step of 21 kN until failure.

6.6.3.2 Control Frame 2 and Retrofitted Frame 2

The 1-COMAC values of Control and Retrofitted Frame 2 are presented in Figure 6.49 and 6.50 respectively. The maximum value of 0.3356 occurred in the area of node 3 at a load step of 5 kN, while the value of 0.5555occurred in the area of node 1 at the final state. The 1-COMAC values in Figure 6.49 of the Control Frame 2 are in agreement with the observed damage areas in experimental test at the top floor.

In Retrofitted Frame 2, the debonding of the FRP sheets extended toward the beam-column joints after load step of 18 kN. and the damage areas at beam-column joints increased as shown in bar diagrams of Figure 6.24. This observation is explained by 1-COMAC values in Figure 6.50. The maximum values of 1-COMAC at the load step of 21 kN and 26 kN were 0.2382 at node 1 and 0.4892 at node 3, respectively. These values support the huge damage occurred in area of first and top floor before fail.

6.6.3.3 Control Frame 3 and Retrofitted Frame 3

The damage areas with the damage areas observed in specimens during load steps; Control and Retrofitted Frame 3 after failure are shown in Figure 6.26 and 6.27. These results are more promising with respect to 1-COMAC factors that were calculated by experimental FRF based mode shapes. The results of 1-COMAC values are shown in Figure 6.51 and 6.52. The bar diagrams corresponding to Control Frame 3 in Figure 6.51, show the damage area and failure zone of this specimen in the area of node 3 during load steps. This bar diagram clearly shows the effectiveness of ductile reinforcement detail, following IS-13920, in Control Frame 3 when compared to specimen at initial state. It also supports that beam-column joint at the top floor was weak.

In bar diagram of Figure 6.52, it is observed that the maximum values of 1-COMAC of 0.4616 appeared at node 3 during load step of 10 kN, while the value reached 0.5565 at node 2 during load step of 30 kN. It shows that damage areas were still in the top fall at small load step, and then damage areas occurred in the second floor as the crack appeared in experimental slab. At final state, the value of 1-CMAC of 0.2745 and 0.4350 were in node 1 and node 3 respectively. It indicates that there were damage areas at the first and top floor of Retrofitted Frame 3 before failure.

6.6.4 Dynamic behavior comparative analysis

The relative variations of natural frequencies through load steps of experimental and FE model of all frames are shown in Table 6.2 to 6.7. The dynamic FE models show good agreement with the natural frequencies obtained from the experimental tests. Fundamental natural frequencies in the FE models correspond quite well with the experimental frames. However, FE models underestimate the dynamic behavior compared to actual frames (Ramsey, 1983).

Although, the MAC and COMAC values based on the measured mode shapes may indicate false damage identification but these values can be related to the presence of noise in the experimental mode shapes. These values were calculated based on measured mode shapes and the noise was not filtered out. The noisy data may affect the predicted damage region.

The failure of the experimental frames can be predicted by 1-COMAC values. However, due to the fluctuations of 1-COMAC, it becomes difficult to identify the severity of damage (Baghiee et all, 2009). When there is more than one damage region in the structural member, this criterion may not clearly show the damaged regions. This identification method allows the prediction of the damaged region that leads to the structural failure. The visual inspections of the frame specimens during the loading steps until failure are in agreement with the analysis.

Table 6.1 The detail of material properties for FE modeling

Compressive strength of concrete cutes (average)		
Element type for ATENA	3D Nonlinear Cementitious 2	
Element type for SAP 2000	3D Block Element	
Control Frame 1	Fresh concrete of 22.5 MPa Elastic modulus of 26,810 MPa*	
Retrofitted Frame 1	DI_k = 0.69 at final state of Control Frame 1 Elastic modulus of 8,311 MPa*	
Control Frame 2	Fresh concrete of 20.5 MPa Elastic modulus of 24,870MPa*	
Retrofitted Frame 2	DI_k = 0.56 at final state of Control Frame 2 Elastic modulus of 10,943 MPa*	
Control Frame 3	Fresh concrete of 23.5 MPa Elastic modulus of 25,320 MPa*	
Retrofitted Frame 3	Elastic modulus of 25,320 MPa* *(The damaged elements have been grouted with high strength adhesive epoxy injection)*	
Steel plate		
Element type for ATENA	3D Elastic Isotropic	
Element type for SAP 2000	3D Block Element	
Elastic modulus	200000 MPa	
Poisson's ratio	0.300	
Steel reinforcement bars		
Element type for ATENA	Reinforcement	
Element type for SAP 2000	Uniaxial Type	
Elastic modulus	200000 MPa	
Yield strength of steel bars	10 mm diameter bar	415 MPa
	8 mm diameter bar	415 MPa
	6 mm diameter bar	415 MPa

Table 6.1 The detail of material properties for FE modeling (continues)

Steel reinforcement bars (continues)		
Specific material weight	78.5 MN/m	
Coefficient of thermal expansion	0.000015 1/K	
Mechanical properties of FRP composite		
Element type for ATENA	Reinforcement	
Element type for SAP 2000	Thin Shell Element	
Fiber type	GFRP (G sheet EU-900)	
Thickness	0.34 mm	
Density	2.6 g/cm^3	
Strain-stress relation (from tension test in laboratory)	Strain	Stress (MPa)
	0	0
	0.0110	590.4
	0.0184	966.1
	0.0279	1594.0
Mechanical properties of epoxy		
Element type for ATENA	3D Bilinear Steel Von Mises	
Element type for SAP 2000	-	
Elastic modulus	3.05 GPa	
Compression	78 MPa	
Tension	84 MPa	
Specific weight	9.83 kN/m^3	
Poisson's ratio	0.4	

* The elastic modulus of concrete in ATENA is calculated following CEB-FIP Model 90 as mention in Appendix B.

** The elastic modulus of concrete in SAP 2000 (Version 10.0.7) is calculated following IS 456-2000.

Table 6.2 Verification of test results for Control Frame 1

Mode	frequency (Hz)						MAC	
	Initial State			Final State				
	Expermiment	FE	%	Expermiment	FE	%	Initial	Final
1	6.6	6.4	3.03	5.2	5.2	0.00	0.9979	0.9776
2	19.5	22	12.82	15.3	17.1	11.76	0.9971	0.9921
3	31.8	37.1	16.67	25.8	27	4.65	0.9817	0.9833

Table 6.3 Verification of test results for Retrofitted Frame 1

Mode	frequency (Hz)						MAC	
	Initial State			Final State				
	Expermiment	FE	%	Expermiment	FE	%	Initial	Final
1	6.7	6.7	0.00	5.5	5.2	5.45	0.9997	0.9866
2	20.7	22.9	10.63	17.2	17.1	0.58	0.9973	0.9881
3	34.3	38.7	12.83	29.5	27	8.47	0.9869	0.9785

Table 6.4 Verification of test results for Control Frame 2

Mode	frequency (Hz)						MAC	
	Initial State			Final State				
	Expermiment	FE	%	Expermiment	FE	%	Initial	Final
1	5.3	5.1	3.77	4.2	4.2	0.00	0.9993	0.9960
2	15.1	17.7	17.22	13.5	13.8	2.22	0.9917	0.9920
3	26	30.5	17.31	23.5	22.1	5.96	0.9835	0.9852

Table 6.5 Verification of test results for Retrofitted Frame 2

Mode	frequency (Hz)						MAC	
	Initial State			Final State				
	Expermiment	FE	%	Expermiment	FE	%	Initial	Final
1	5.6	5.8	3.57	4.6	5.1	10.87	0.9980	0.9897
2	16.8	19	13.10	14.2	16.4	15.49	0.9911	0.9852
3	28.3	29.7	4.95	24.3	25	2.88	0.9829	0.9879

Table 6.6 Verification of test results for Control Frame 3

Mode	frequency (Hz)						MAC	
	Initial State			Final State				
	Expermiment	FE	%	Expermiment	FE	%	Initial	Final
1	5.6	5.5	1.79	4.4	4.6	4.55	0.9971	0.9838
2	16.8	19.7	17.26	13.8	15.4	11.59	0.9995	0.9798
3	28.3	34.8	22.97	23.5	25.3	7.66	0.9851	0.9969

Table 6.7 Verification of test results for Retrofitted Frame 3

Mode	frequency (Hz)						MAC	
	Initial State			Final State				
	Expermiment	FE	%	Expermiment	FE	%	Initial	Final
1	6.2	6.1	1.61	5.2	5.1	1.92	0.9997	0.9928
2	18.5	21.3	15.14	16.1	16.8	4.35	0.9965	0.9794
3	33.8	36.3	7.40	30.2	26.9	10.93	0.9845	0.9468

Table 6.8 Verification of MAC values during load steps for Control Frame 1

P/Pmax	0	0.3	0.45	0.6	0.75	1	
Mode 1	0.9979	0.9956	0.9995	0.9962	0.9929	0.9776	MAC
Mode 2	0.9971	0.9786	0.9994	0.9806	0.9775	0.9921	MAC
Mode 3	0.9817	0.9787	0.9787	0.9921	0.9833	0.9833	MAC

Table 6.9 Verification of MAC values during load steps for Retrofitted Frame 1

P/Pmax	0	0.24	0.48	0.6	0.72	0.84	1	
Mode 1	0.9997	0.9974	0.9960	0.9932	0.9866	0.9910	0.9866	MAC
Mode 2	0.9973	0.9879	0.9879	0.9879	0.9717	0.9635	0.9881	MAC
Mode 3	0.9869	0.9802	0.9893	0.9570	0.9570	0.9651	0.9785	MAC

Table 6.10 Verification of MAC values during load steps for Control Frame 2

P/Pmax	0	0.24	0.5	0.75	
Mode 1	0.9993	0.9986	0.9951	0.9960	MAC
Mode 2	0.9917	0.9778	0.9906	0.9920	MAC
Mode 3	0.9835	0.9753	0.9864	0.9852	MAC

Table 6.11 Verification of MAC values during load steps for Retrofitted Frame 2

P/Pmax	0	0.24	0.35	0.58	0.81	1	
Mode 1	0.9980	0.9956	0.9913	0.9918	0.9891	0.9897	MAC
Mode 2	0.9911	0.9788	0.9753	0.9890	0.9898	0.9852	MAC
Mode 3	0.9829	0.9774	0.9671	0.9799	0.9662	0.9879	MAC

Table 6.12 Verification of MAC values during load steps for Control Frame 3

P/Pmax	0	0.38	0.5	0.75	0.88	1	
Mode 1	0.9971	0.9955	0.9971	0.9953	0.9819	0.9838	MAC
Mode 2	0.9995	0.9989	0.9887	0.9931	0.9887	0.9798	MAC
Mode 3	0.9851	0.9755	0.9851	0.9748	0.9833	0.9969	MAC

Table 6.13 Verification of MAC values during load steps for Retrofitted Frame 3

P/Pmax	0	0.23	0.47	0.58	0.7	0.81	1	
Mode 1	0.9997	0.9962	0.9975	0.9966	0.9997	0.9934	0.9928	MAC
Mode 2	0.9965	0.9945	0.9908	0.9862	0.9888	0.9849	0.9794	MAC
Mode 3	0.9845	0.9814	0.9869	0.9714	0.9608	0.9804	0.9468	MAC

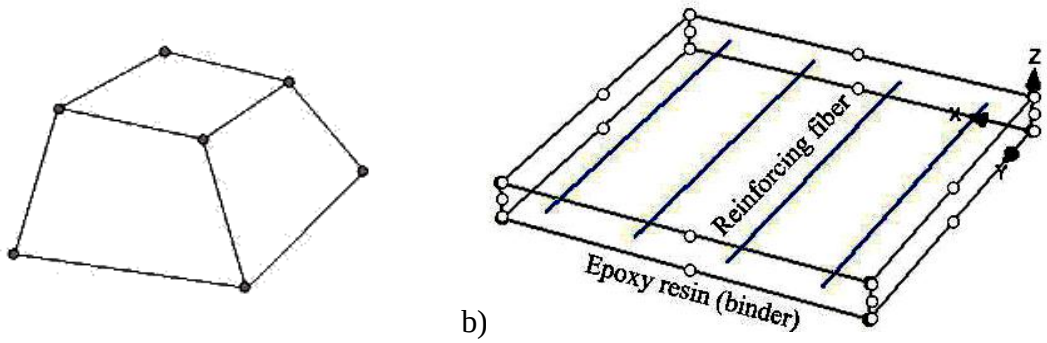

a) b)

Figure 6.1 Element types: a) 8 nodes brick element model for concrete and steel plate and b) 20 nodes shell element model for FRP composite.

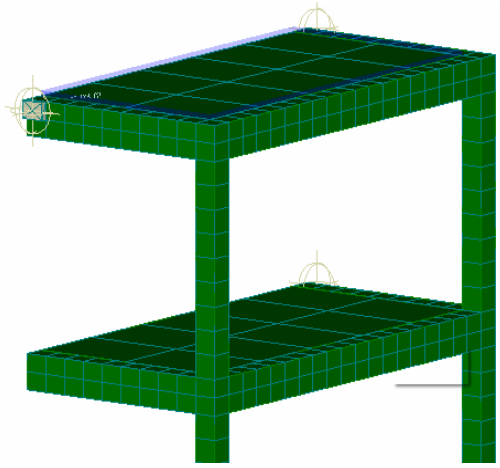

Figure 6.2 The top view of loading steel plate at middle of top floor.

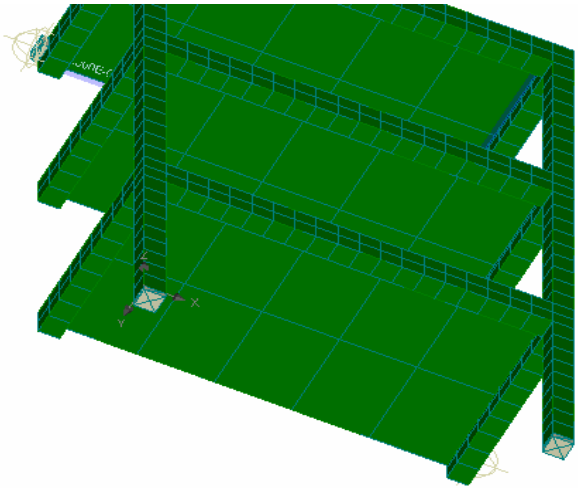

Figure 6.3 The bottom view of the frame with the steel support plates.

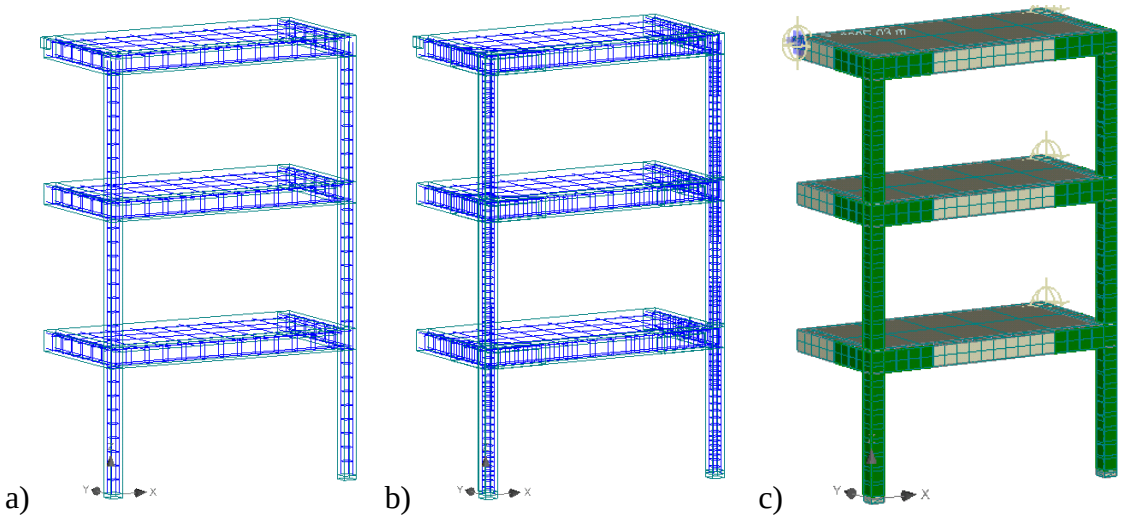

Figure 6.4 FE haft frame models: a) the reinforcement bars of Frame 1 and Frame 2, b) the reinforcement bars of Frame 3 and c) strengthened haft frame model.

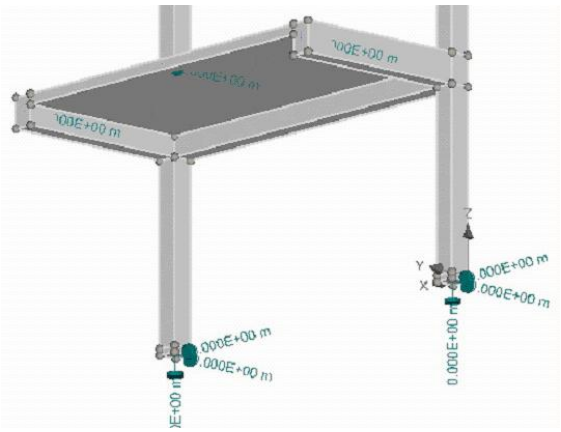

Figure 6.5 The definition of fixed support at the bottom of steel plate.

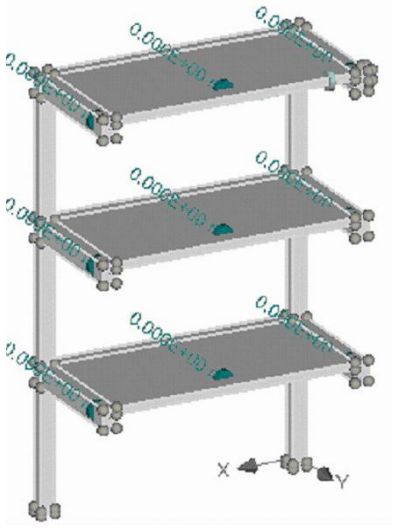

Figure 6.6 The definition of horizontal support at symmetrical plane.

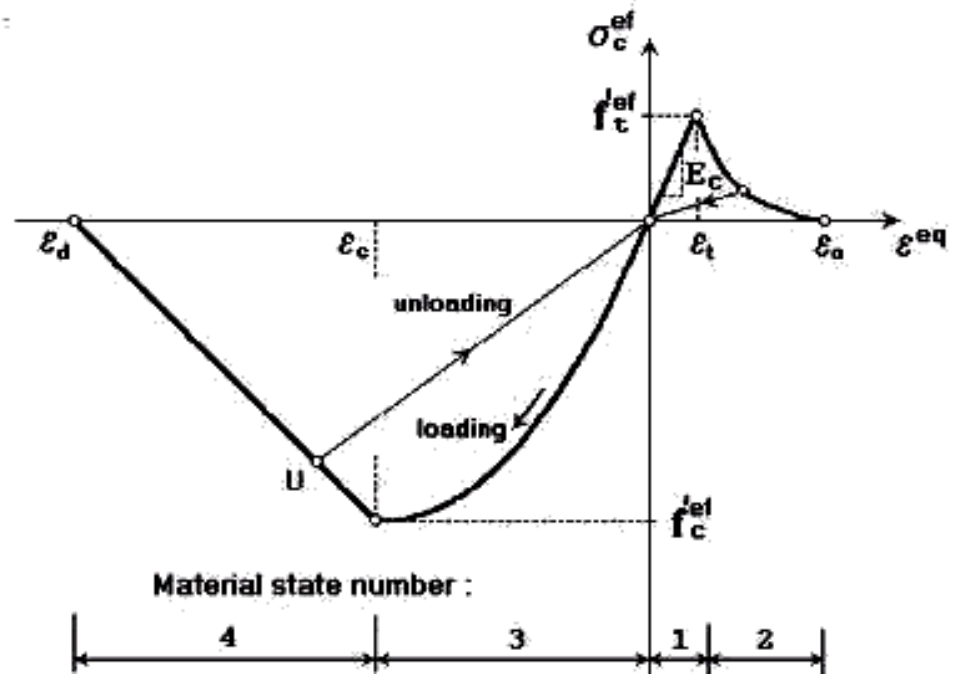

Figure 6.7 Uniaxial stress-strain relationship for concrete (Chen, 1982).

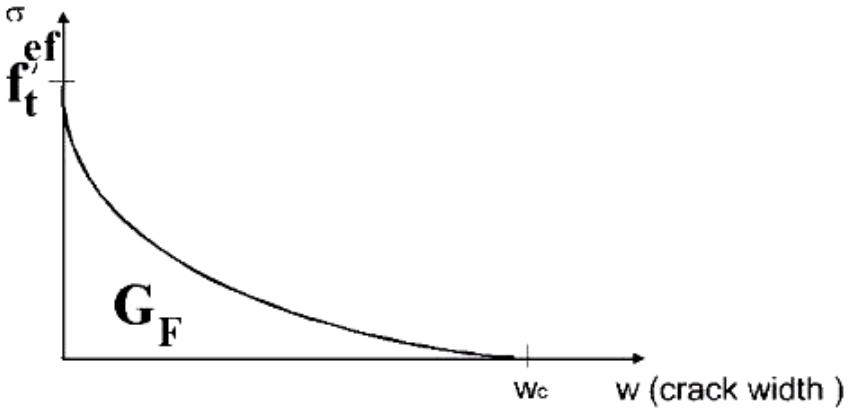

Figure 6.8 The exponential crack opening law for concrete (Hordijk, 1991).

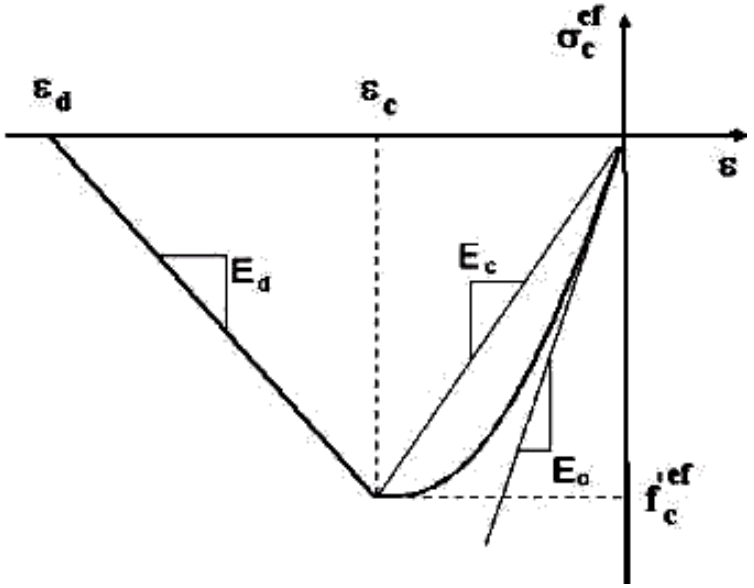

Figure 6.9 The nonlinear behavior of compression for concrete (CEB-FIP, 1990).

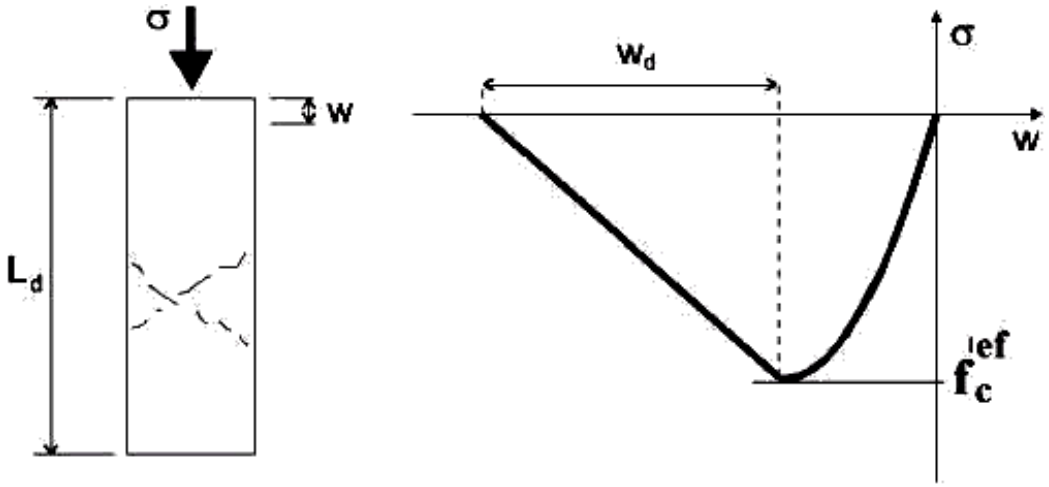

Figure 6.10 The compression behavior for concrete after peak stress (Van Mier, 1986).

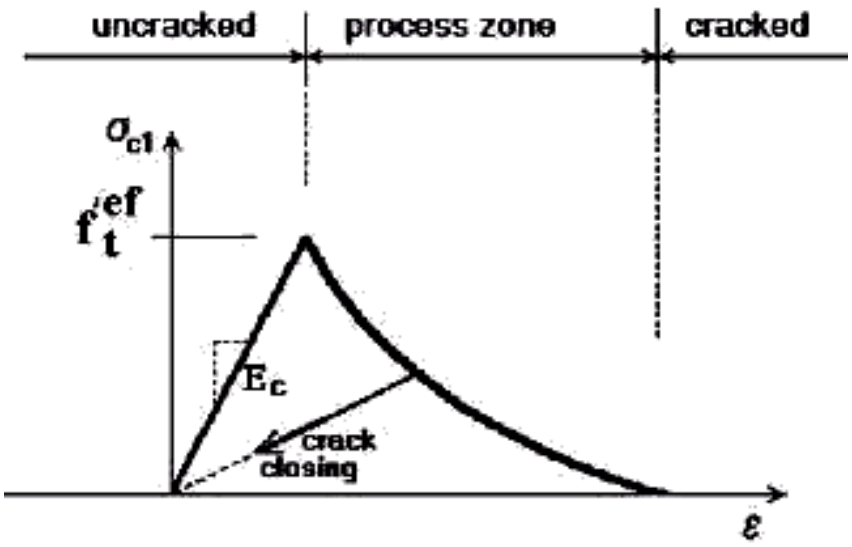

Figure 6.11 Stages of crack opening (Cervenka et al, 1991).

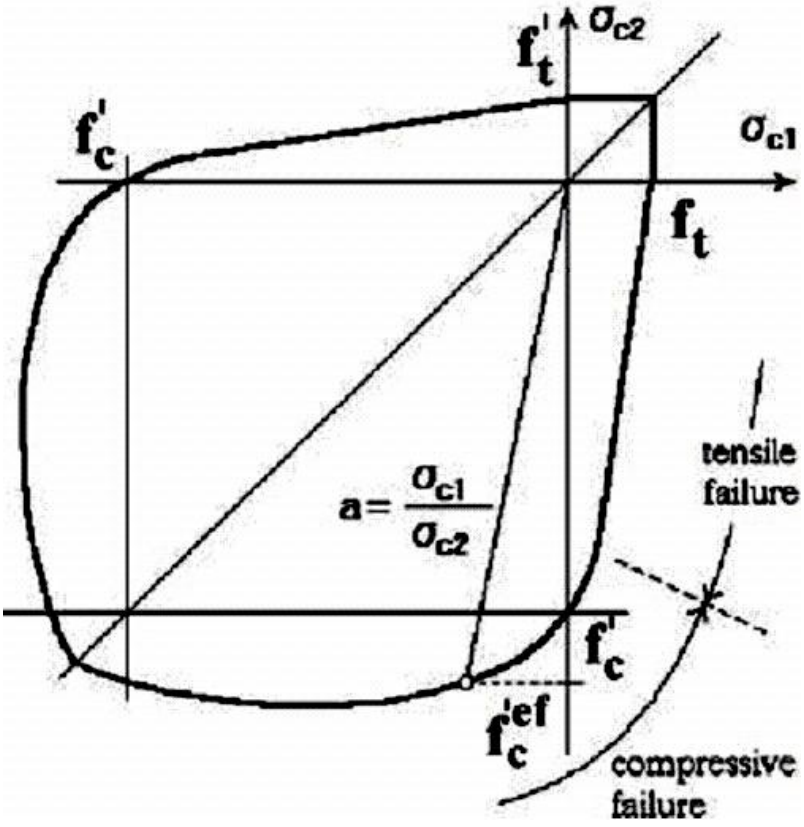

Figure 6.12 Biaxial failure function for concrete (Kupfer, 1969).

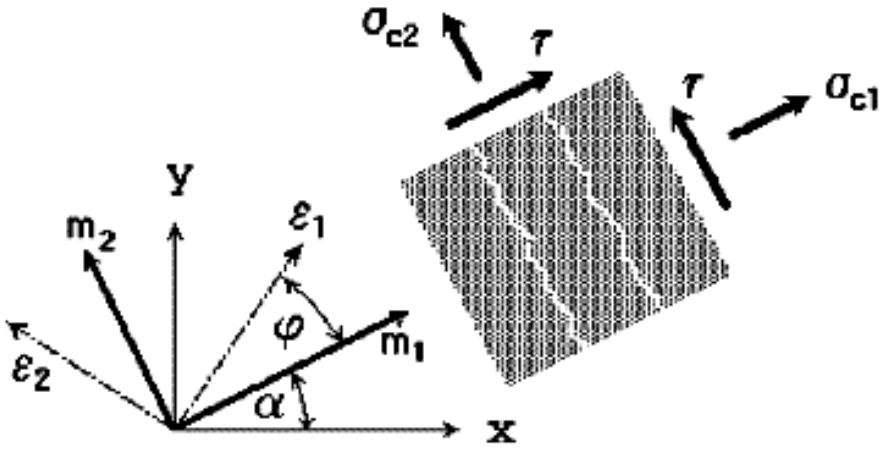

Figure 6.13 Fixed crack model of concrete (Drawin, 1974).

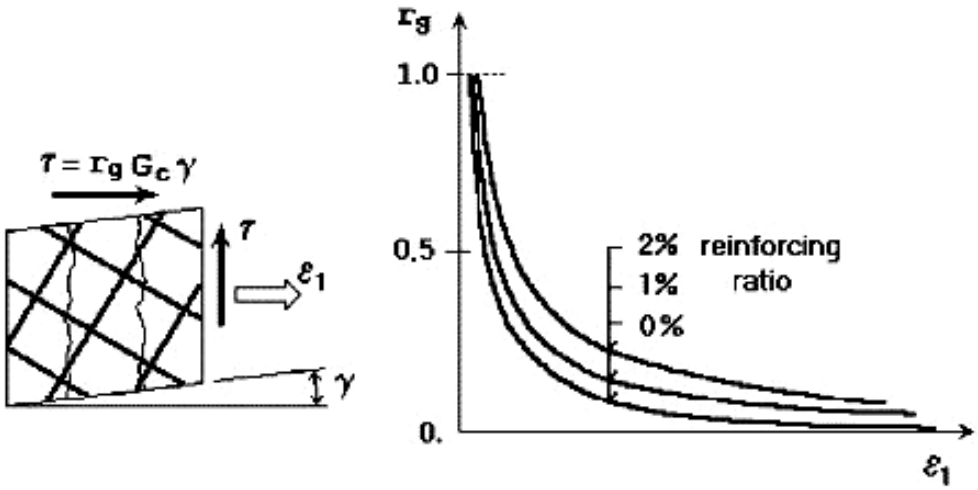

Figure 6.14 Shear retention factor of concrete (Kolmar, 1986).

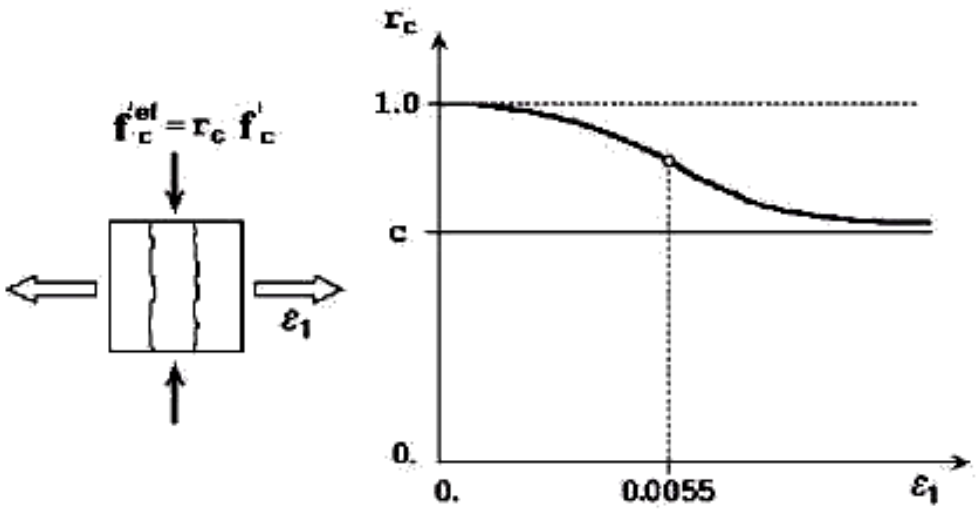

Figure 6.15 Compressive strength reduction of cracked concrete (Kolleger et al, 1988).

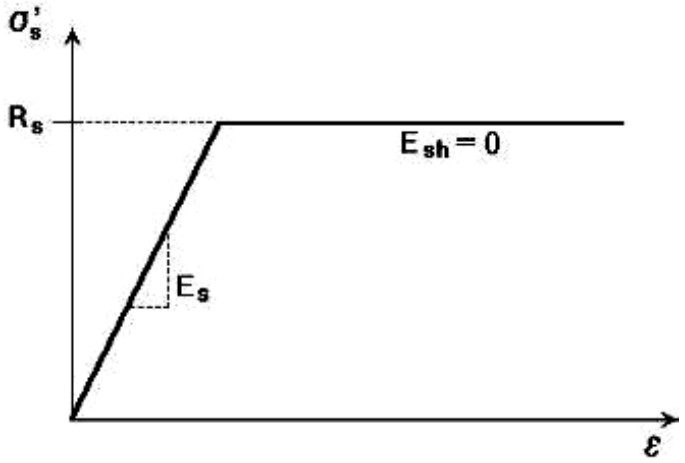

Figure 6.16 The bilinear stress-strain law for reinforcement.

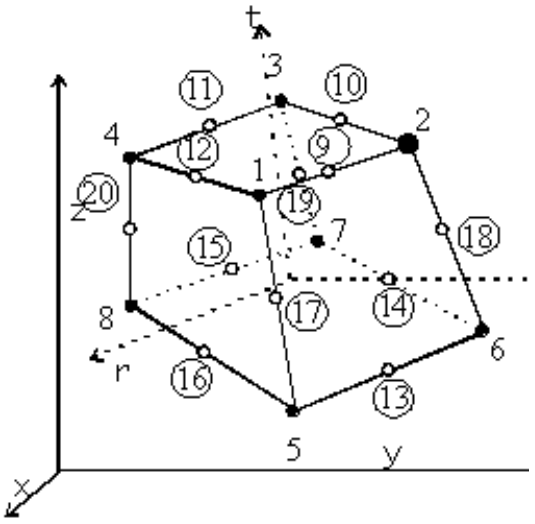

Figure 6.17 Geometry of 3D solid brick element with 8 up to 20 nodes.

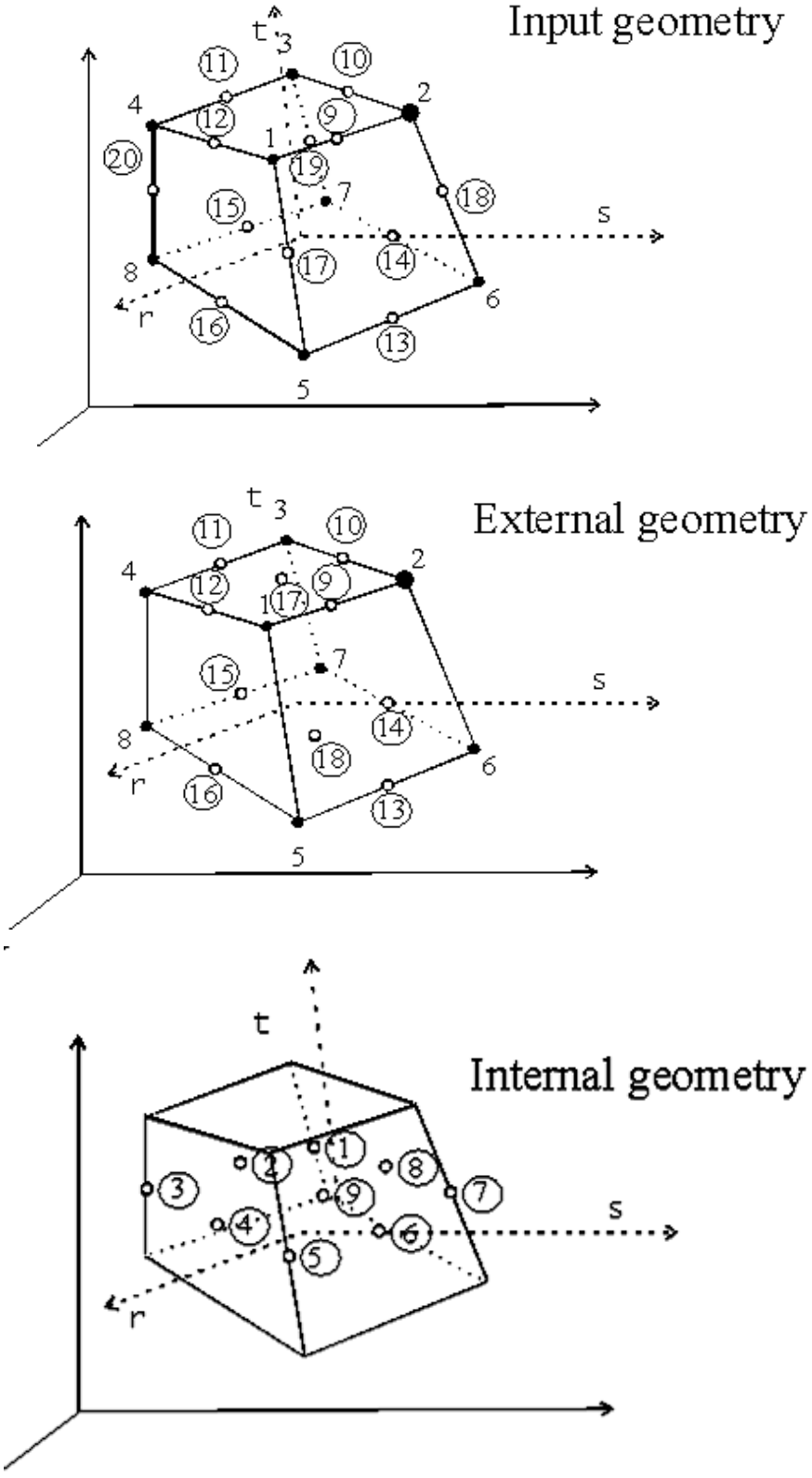

Figure 6.18 Geometry of shell element for FRP material.

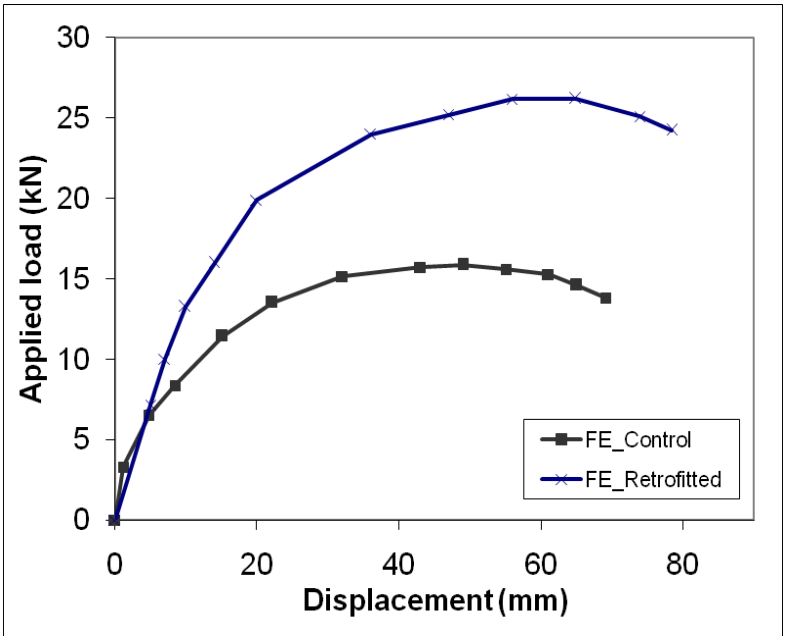

Figure 6.19 FE load-displacement plot of Frame 1

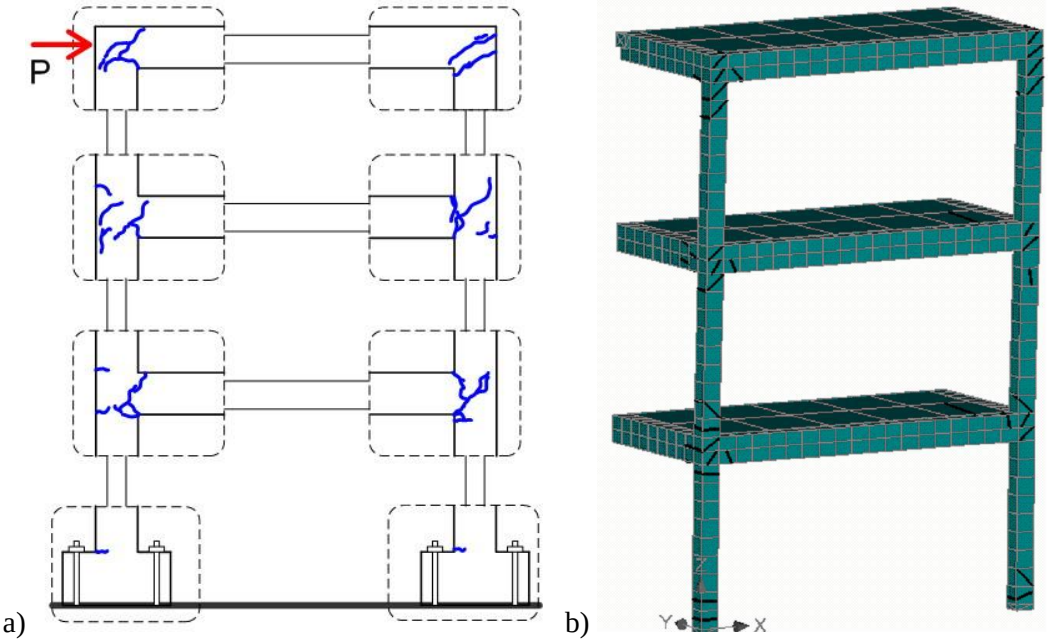

Figure 6.20 Crack patterns of Control Frame 1: a) experimental test and b) FE model.

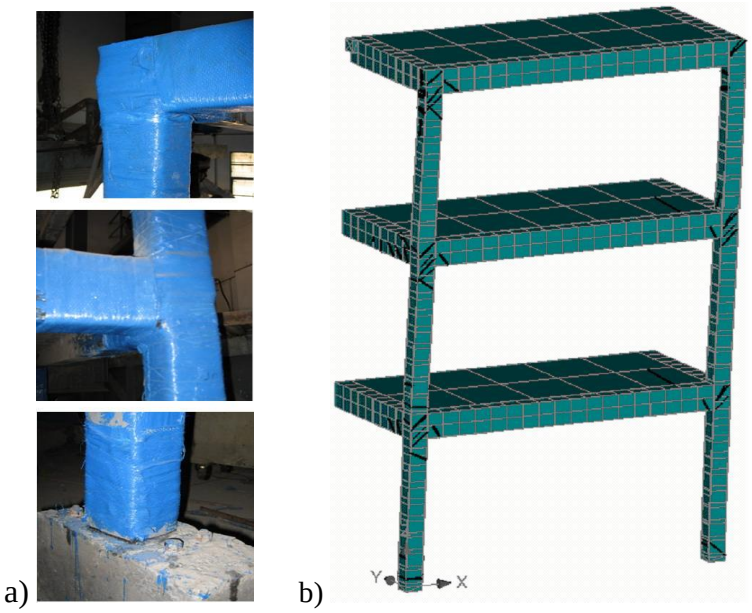

Figure 6.21 Crack patterns of Retrofitted Frame 1: a) experimental and b) FE result.

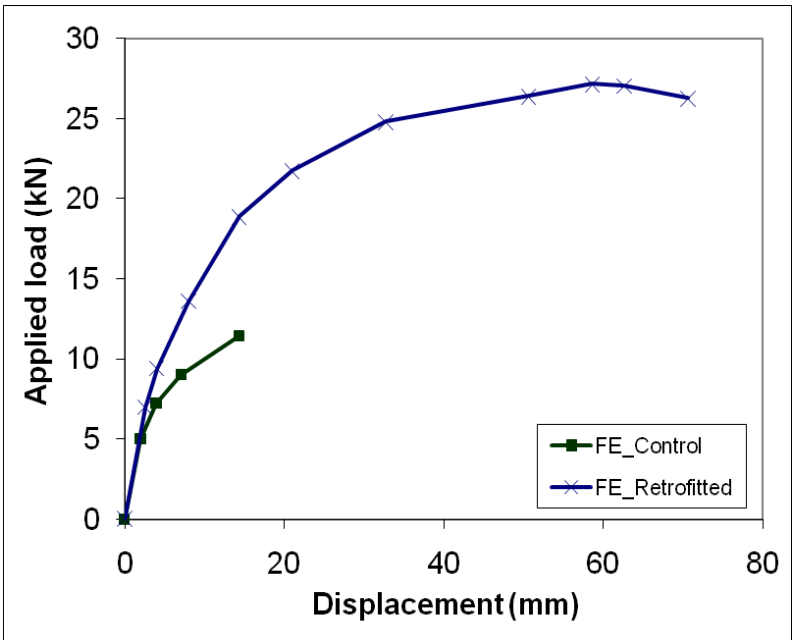

Figure 6.22 FE load-displacement plot of Frame 2

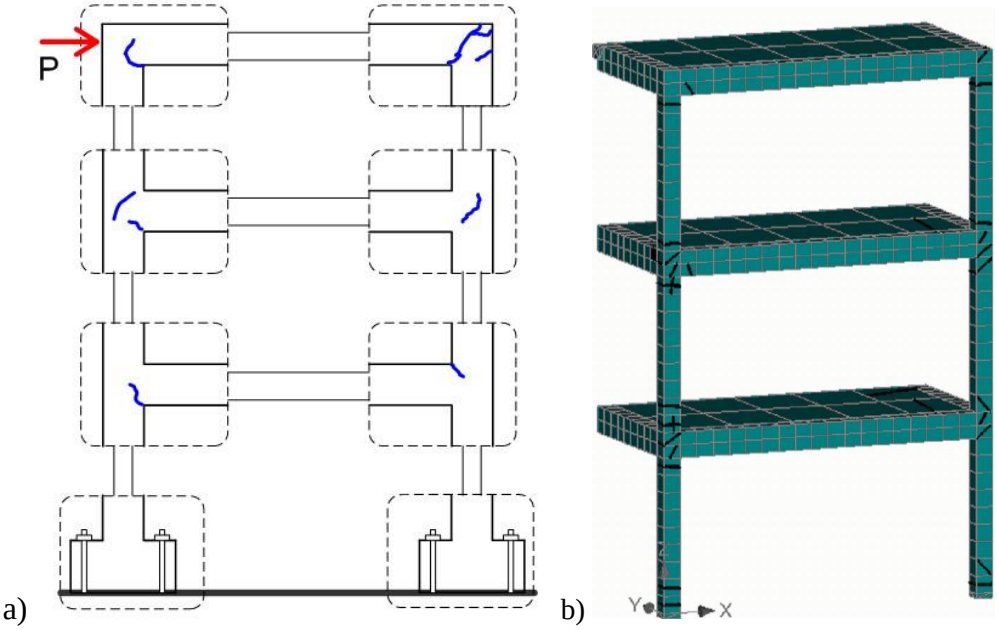

Figure 6.23 Crack patterns of Control Frame 2: a) experimental test and b) FE model.

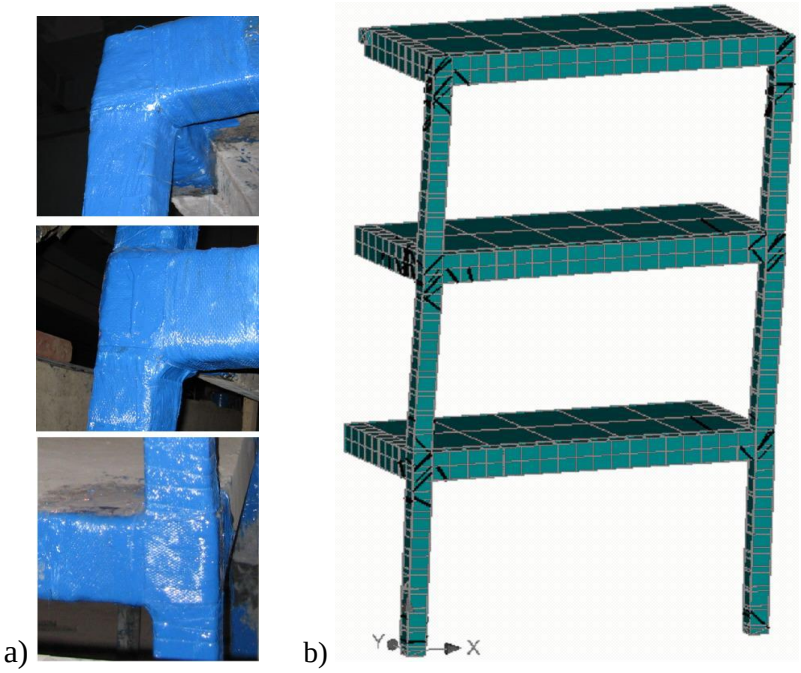

Figure 6.24 Crack patterns of Retrofitted Frame 2: a) experimental and b) FE result.

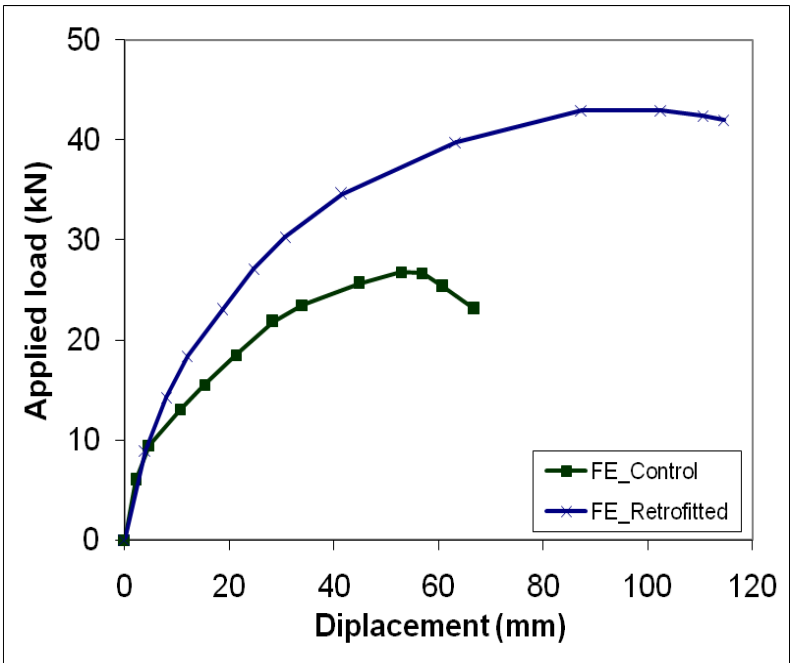

Figure 6.25 FE load-displacement plot of Frame 3

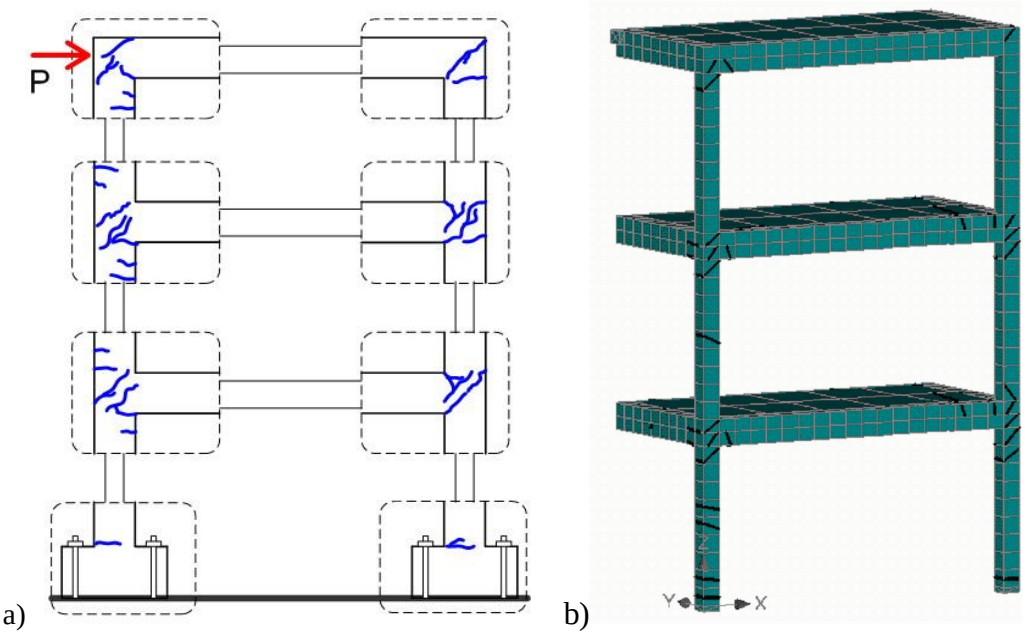

Figure 6.26 Crack patterns of Control Frame 3: a) experimental test and b) FE model.

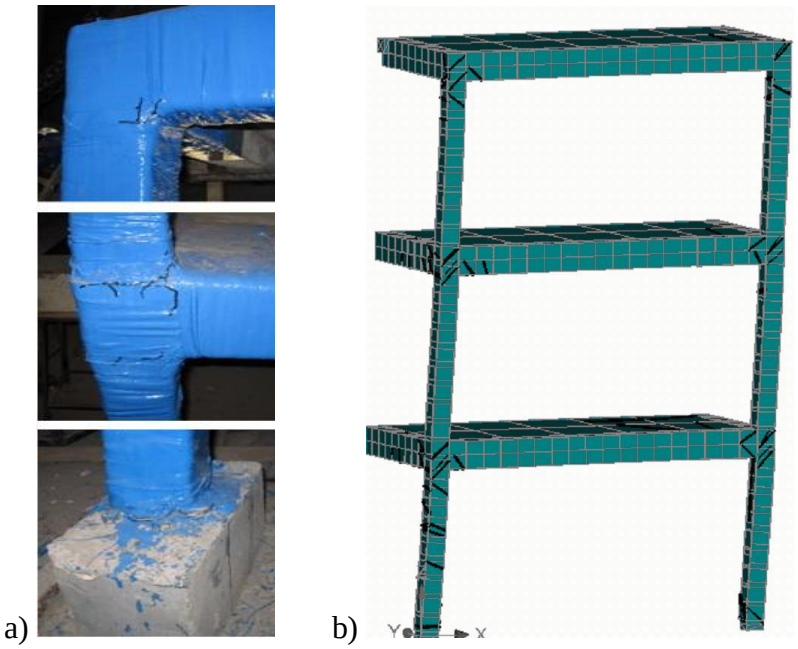

Figure 6.27 Crack patterns of Retrofitted Frame 3: a) experimental and b) FE result.

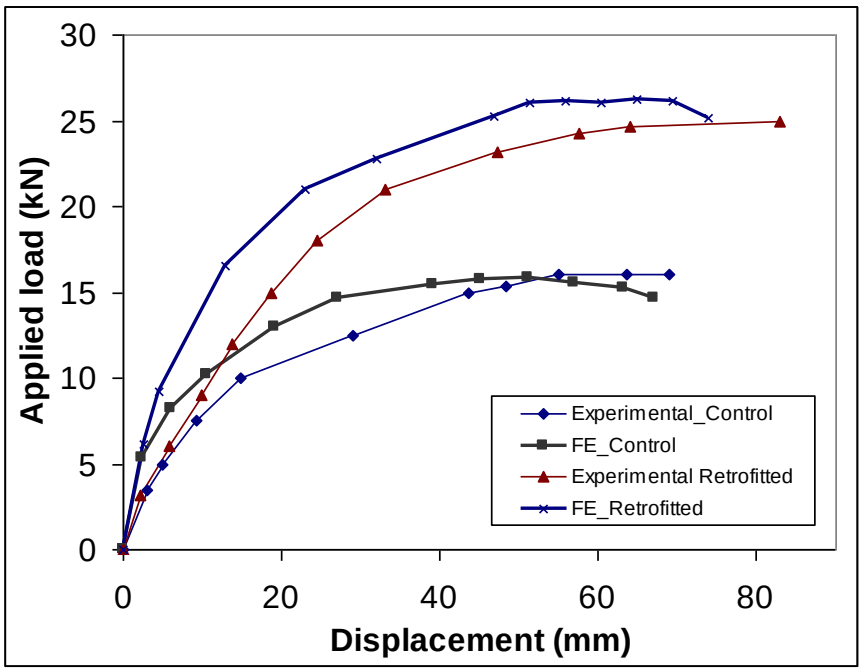

Figure 6.28 Nonlinear comparison between experimental results and FE model of Frame 1.

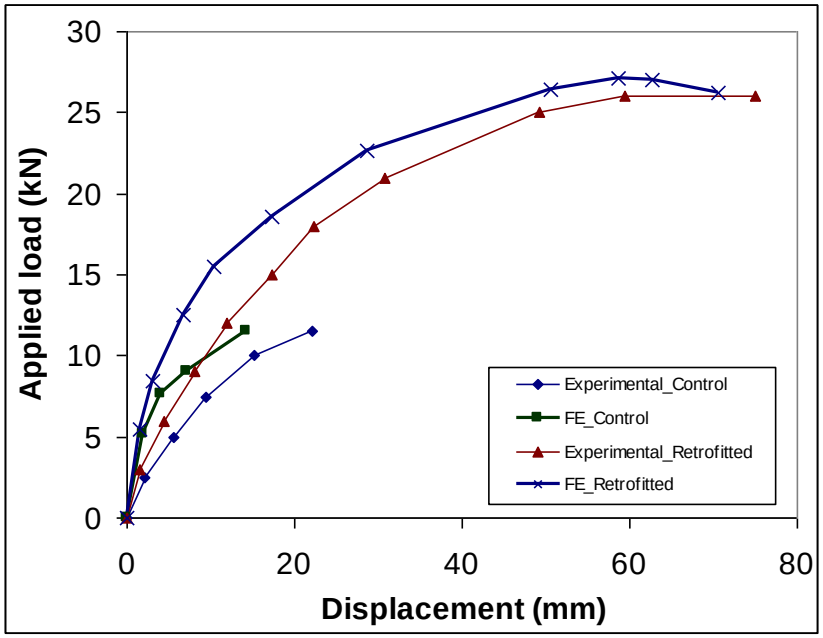

Figure 6.29 Nonlinear comparison between experimental results and FE model of Frame 2.

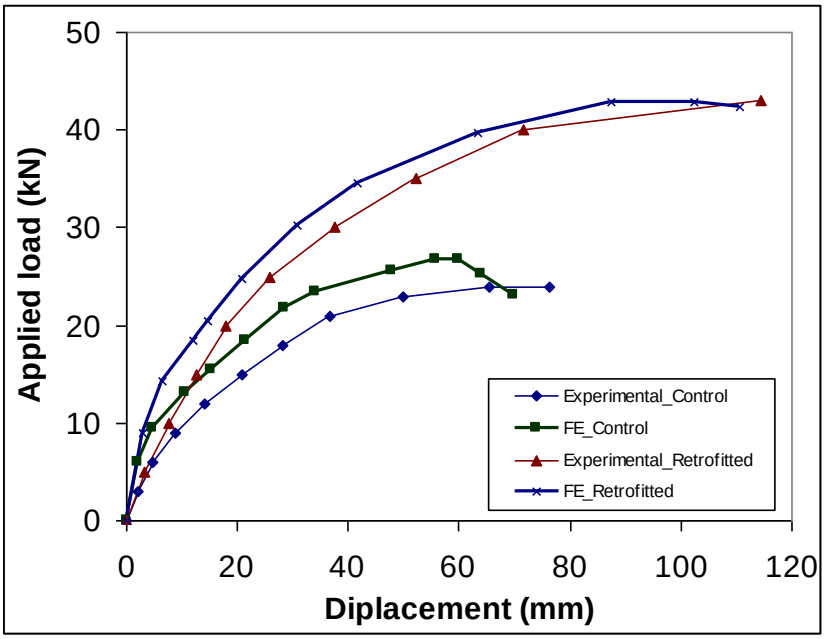

Figure 6.30 Nonlinear comparison between experimental results and FE model of Frame 3.

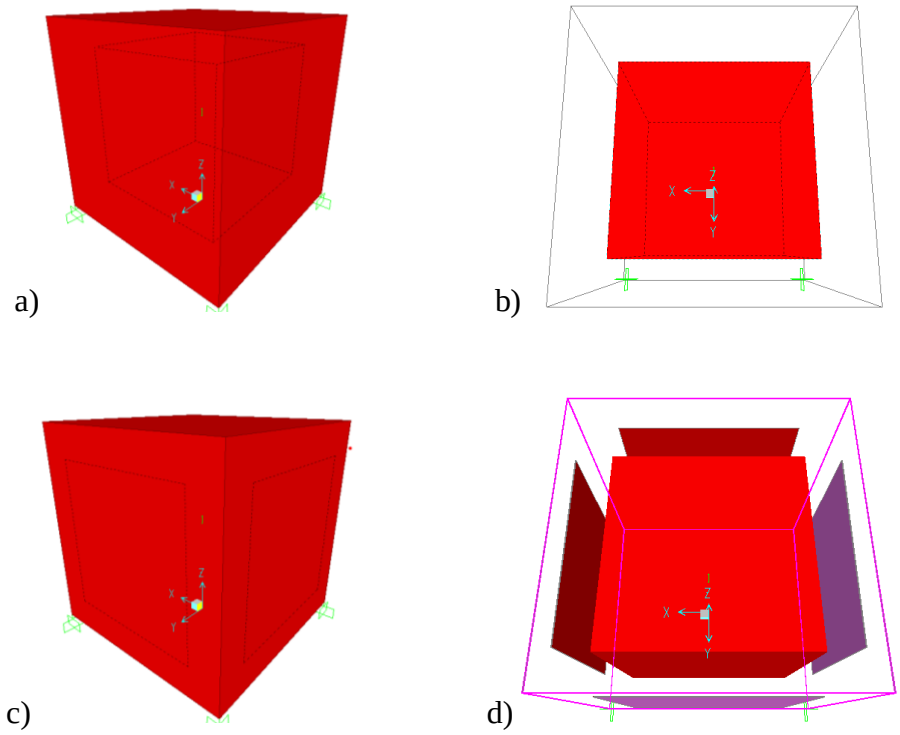

Figure 6.31 Element type of SAP 2000: a) and b) 8 nodes block element of concrete, c) and d) 8 nodes block element of concrete with FRP composite.

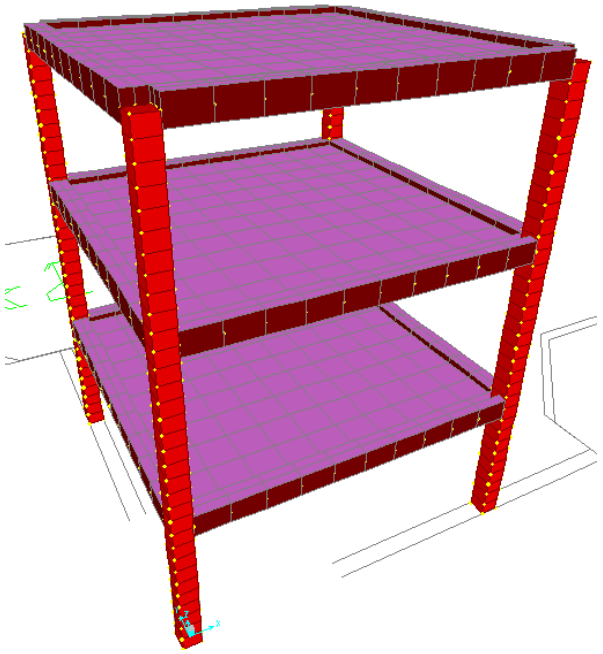

Figure 6.32 FE model of three storey RC frame.

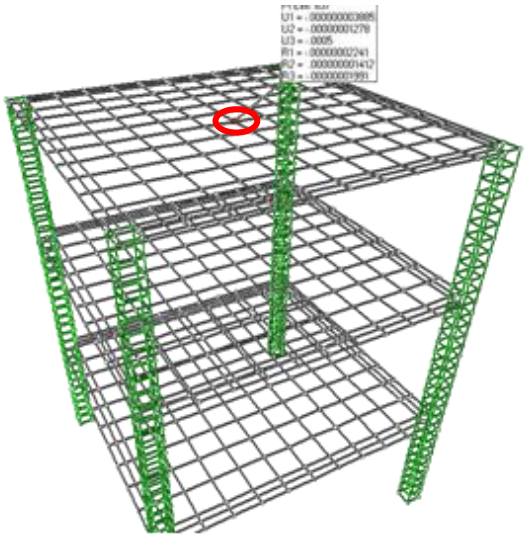

a)

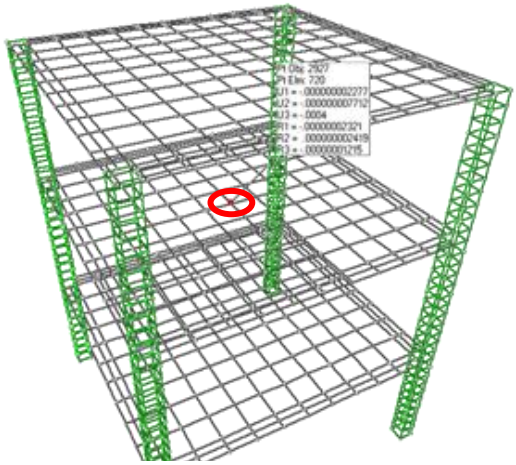

b)

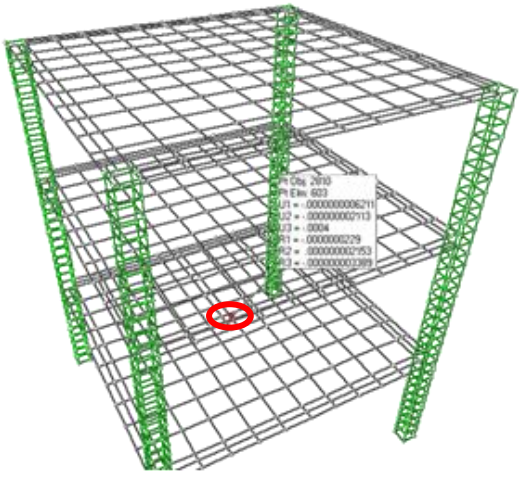

c)

Figure 6.33 The monitoring positions on FE frame model.

a)

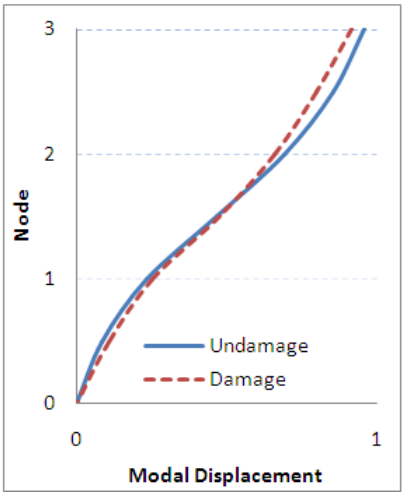

b)

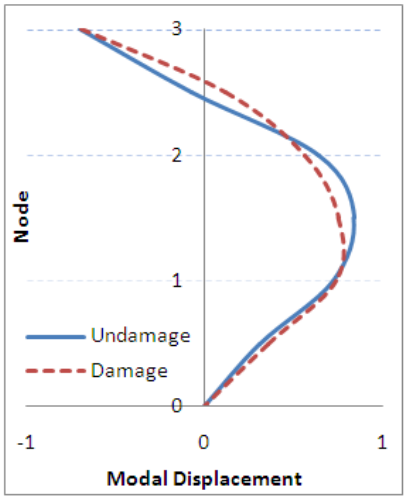

c)

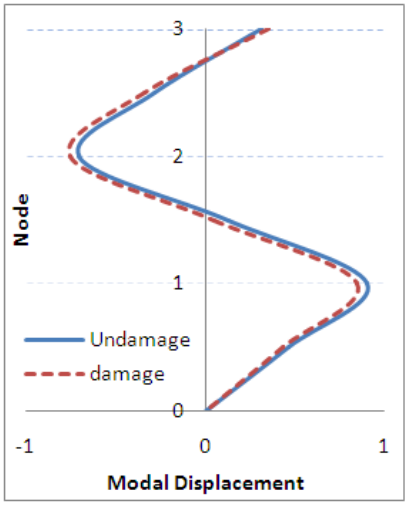

Figure 6.34 Comparison of FE mode shapes between undamaged and damaged state; a) first mode, b) second mode and c) third mode of sway

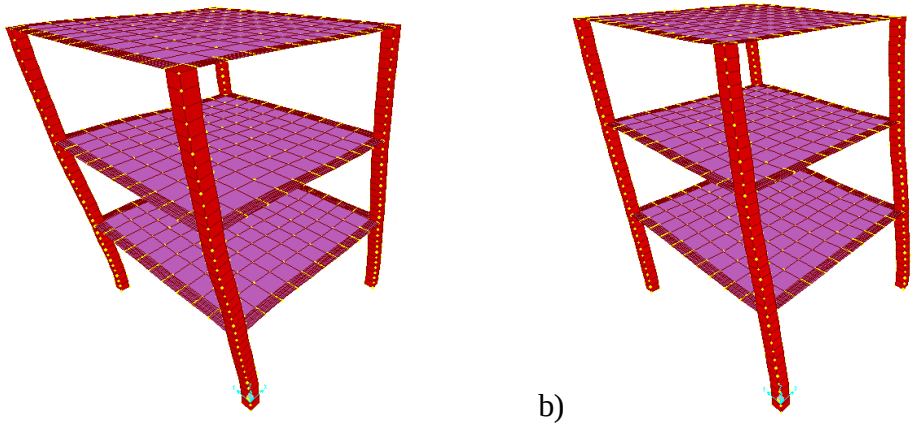

a) b)

Figure 6.35 The first and second mode: a) sway in x-axis and b) sway in y-axis

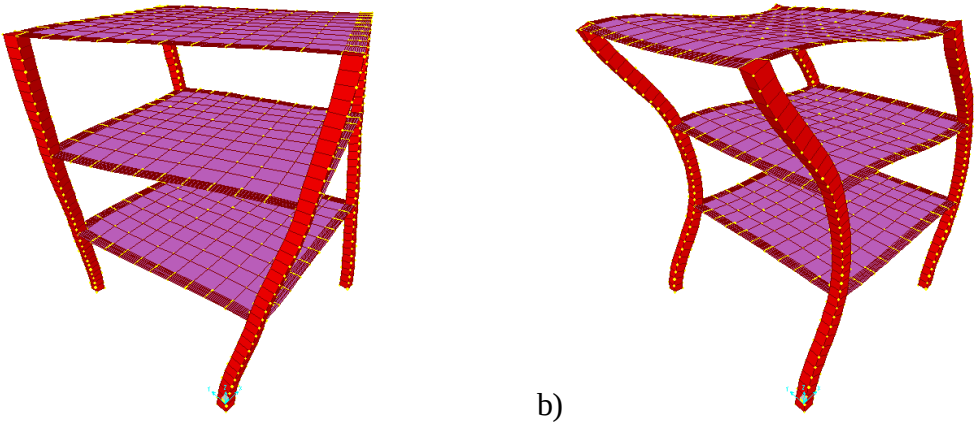

a) b)

Figure 6.36 The third and fourth mode: a) torsion and b) sway in x-axis

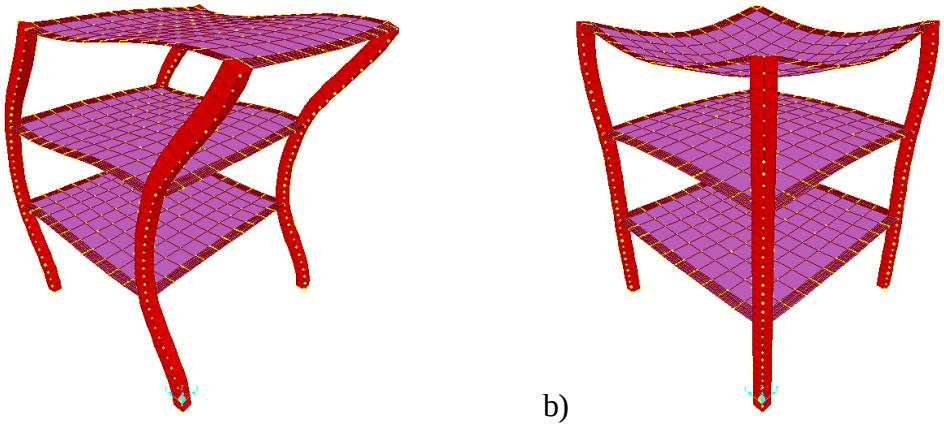

a) b)

Figure 6.37 The fifth and sixth mode: a) sway in y-axis and b) vertical mode

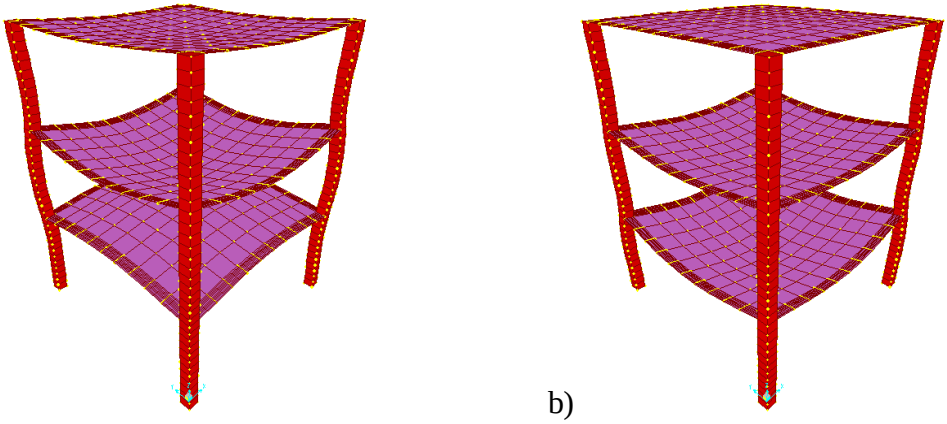

a) b)

Figure 6.38 The seventh and eighth mode: a) and b) vertical mode

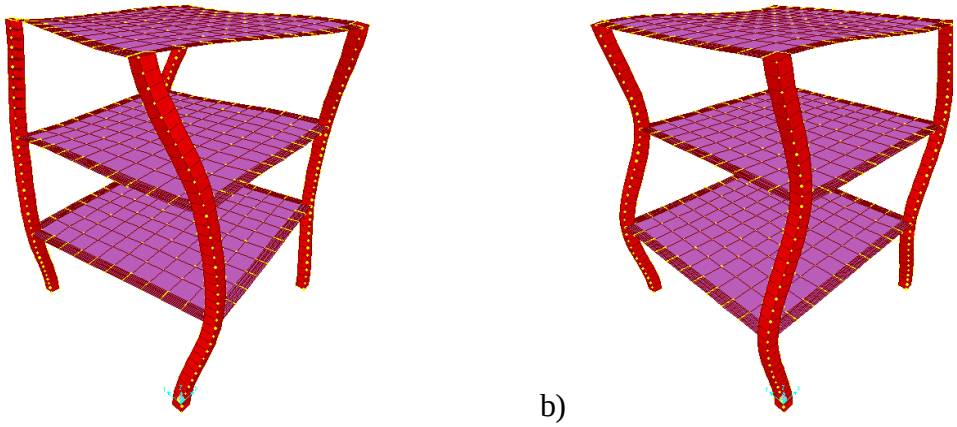

a) b)

Figure 6.39 The ninth and tenth mode: a) torsion and b) sway in x-axis

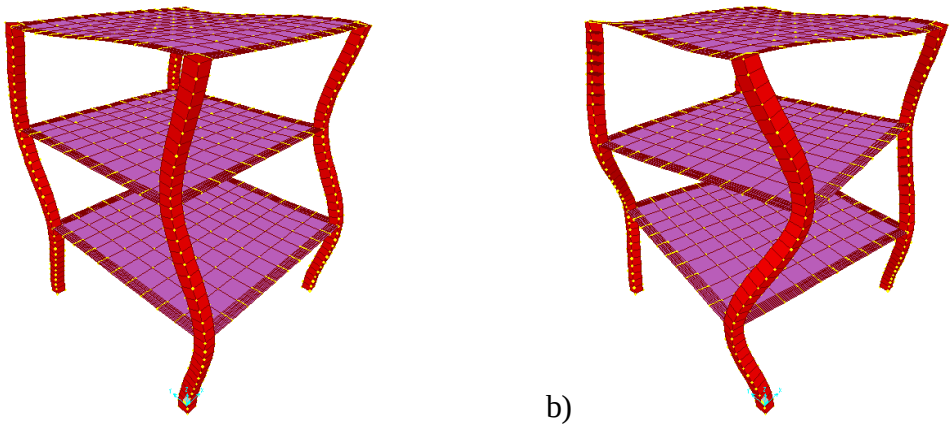

a) b)

Figure 6.40 The eleventh and twelfth mode: a) sway in y-axis and b) torsion

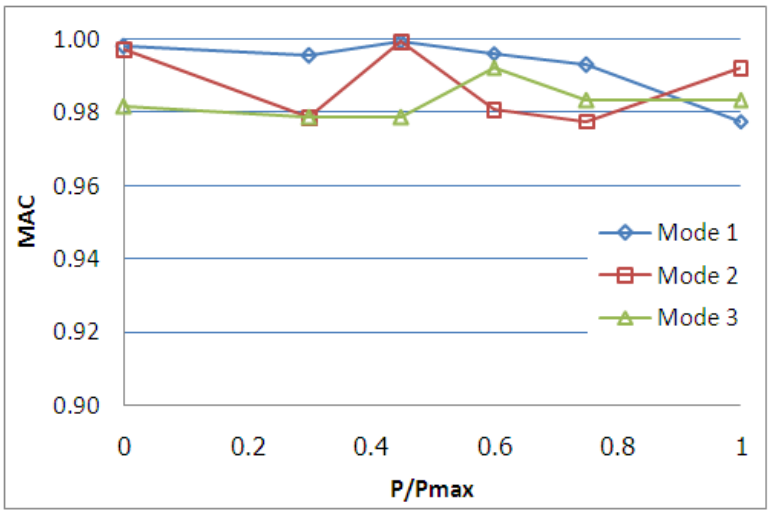

Figure 6.41 Verification of MAC values during load steps for Control Frame 1

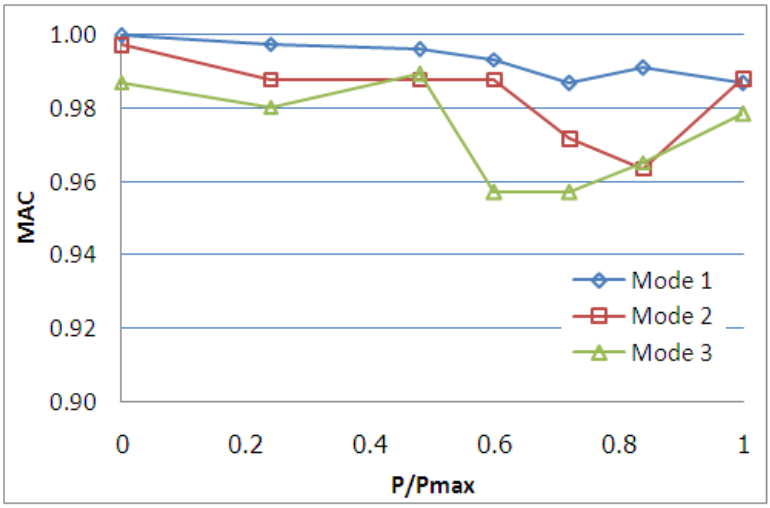

Figure 6.42 Verification of MAC values during load steps for Retrofitted Frame 1

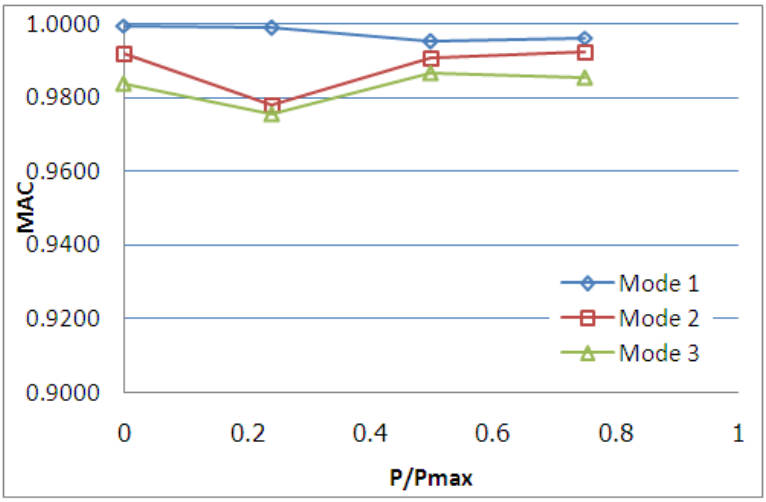

Figure 6.43 Verification of MAC values during load steps for Control Frame 2

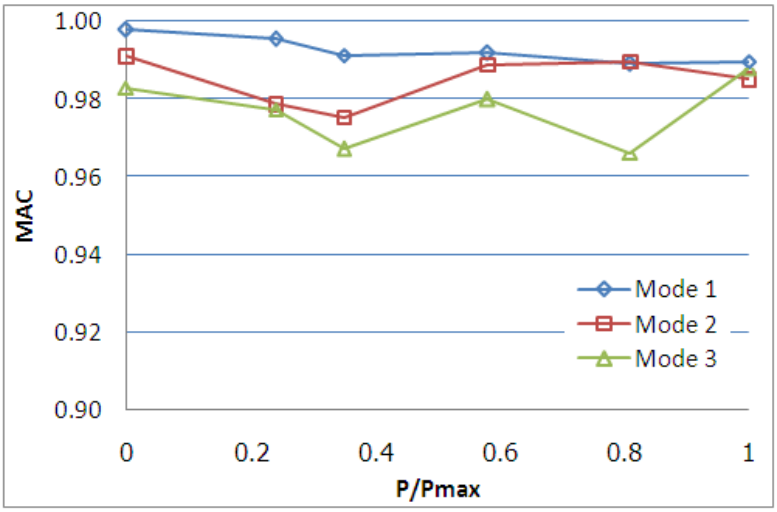

Figure 6.44 Verification of MAC values during load steps for Retrofitted Frame 2

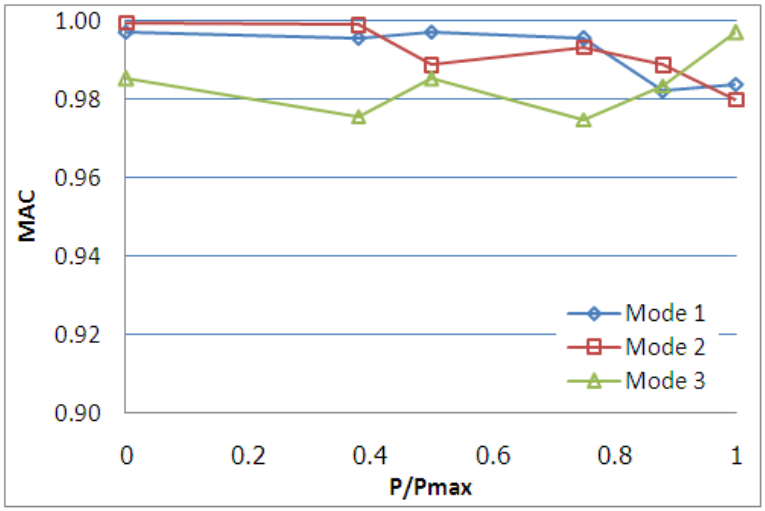

Figure 6.45 Verification of MAC values during load steps for Control Frame 3

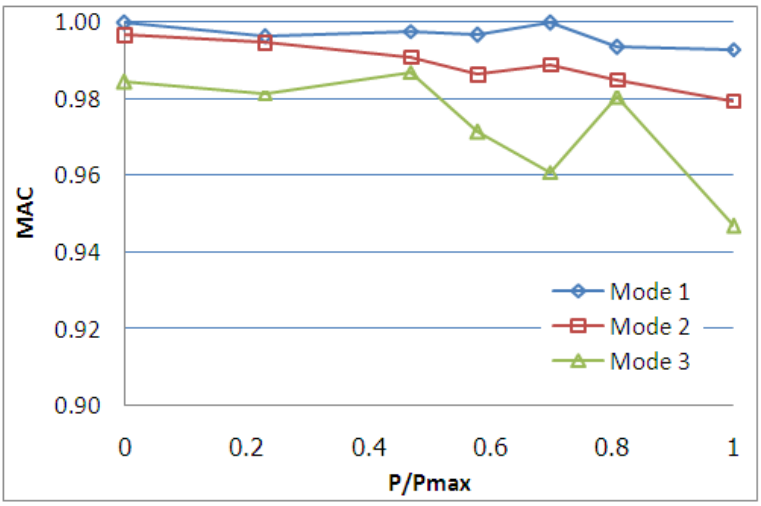

Figure 6.46 Verification of MAC values during load steps for Retrofitted Frame 3

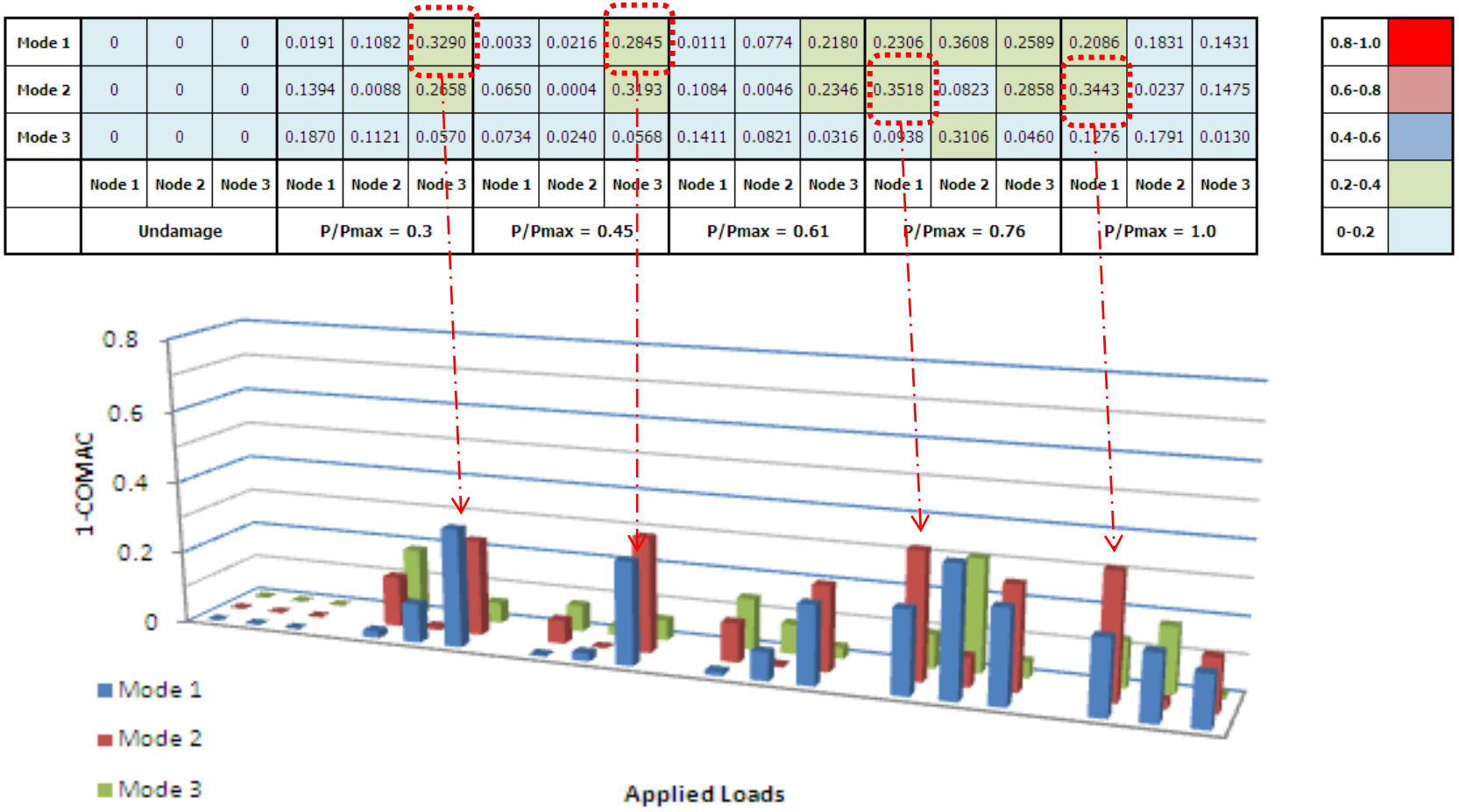

Mode 1	0	0	0	0.0191	0.1082	0.3290	0.0033	0.0216	0.2845	0.0111	0.0774	0.2180	0.2306	0.3608	0.2589	0.2086	0.1831	0.1431
Mode 2	0	0	0	0.1394	0.0088	0.2658	0.0650	0.0004	0.3193	0.1084	0.0046	0.2346	0.3518	0.0823	0.2858	0.3443	0.0237	0.1475
Mode 3	0	0	0	0.1870	0.1121	0.0570	0.0734	0.0240	0.0568	0.1411	0.0821	0.0316	0.0938	0.3106	0.0460	0.1276	0.1791	0.0130
	Node 1	Node 2	Node 3	Node 1	Node 2	Node 3	Node 1	Node 2	Node 3	Node 1	Node 2	Node 3	Node 1	Node 2	Node 3	Node 1	Node 2	Node 3
	Undamage			P/Pmax = 0.3			P/Pmax = 0.45			P/Pmax = 0.61			P/Pmax = 0.76			P/Pmax = 1.0		

0.8-1.0	
0.6-0.8	
0.4-0.6	
0.2-0.4	
0-0.2	

Figure 6.47 Change of 1-COMAC values based on experimental mode shape of Control Frame 1

Mode 1	0	0	0	0.4234	0.0376	0.5159	0.0194	0.0072	0.4171	0.1273	0.2644	0.0044	0.0551	0.4538	0.4360	0.0028	0.1585	0.3611	0.3821	0.2300	0.4386
Mode 2	0	0	0	0.6122	0.0091	0.2050	0.0404	0.0003	0.2689	0.2681	0.1248	0.0035	0.1509	0.2630	0.4558	0.0252	0.4234	0.5291	0.4874	0.4594	0.6457
Mode 3	0	0	0	0.3433	0.1705	0.0233	0.1631	0.0159	0.1791	0.4615	0.2471	0.0000	0.3141	0.2816	0.1401	0.0674	0.5634	0.1808	0.6131	0.6807	0.5071
	Node 1	Node 2	Node 3	Node 1	Node 2	Node 3	Node 1	Node 2	Node 3	Node 1	Node 2	Node 3	Node 1	Node 2	Node 3	Node 1	Node 2	Node 3	Node 1	Node 2	Node 3
	Undamage			P/Pmax = 0.24			P/Pmax = 0.48			P/Pmax = 0.60			P/Pmax = 0.72			P/Pmax = 0.84			P/Pmax = 1		

0.8-1.0	
0.6-0.8	
0.4-0.6	
0.2-0.4	
0-0.2	

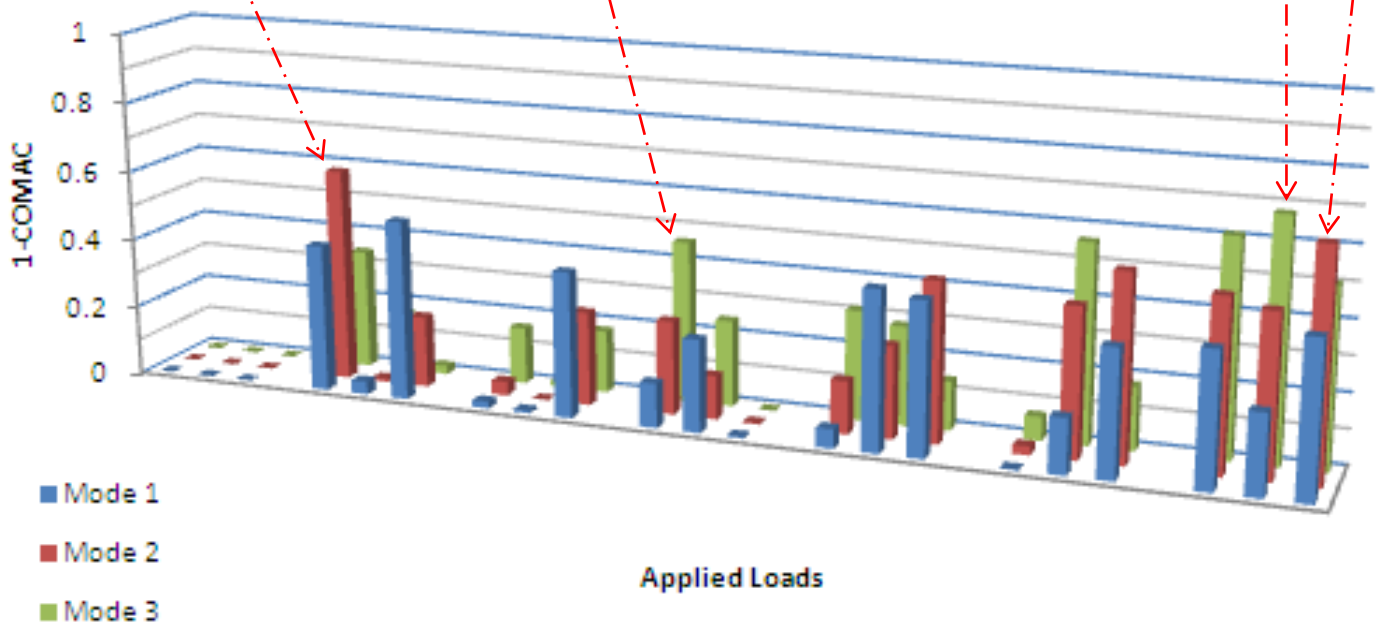

Figure 6.48 Change of 1-COMAC values based on experimental mode shape of Retrofitted Frame 1

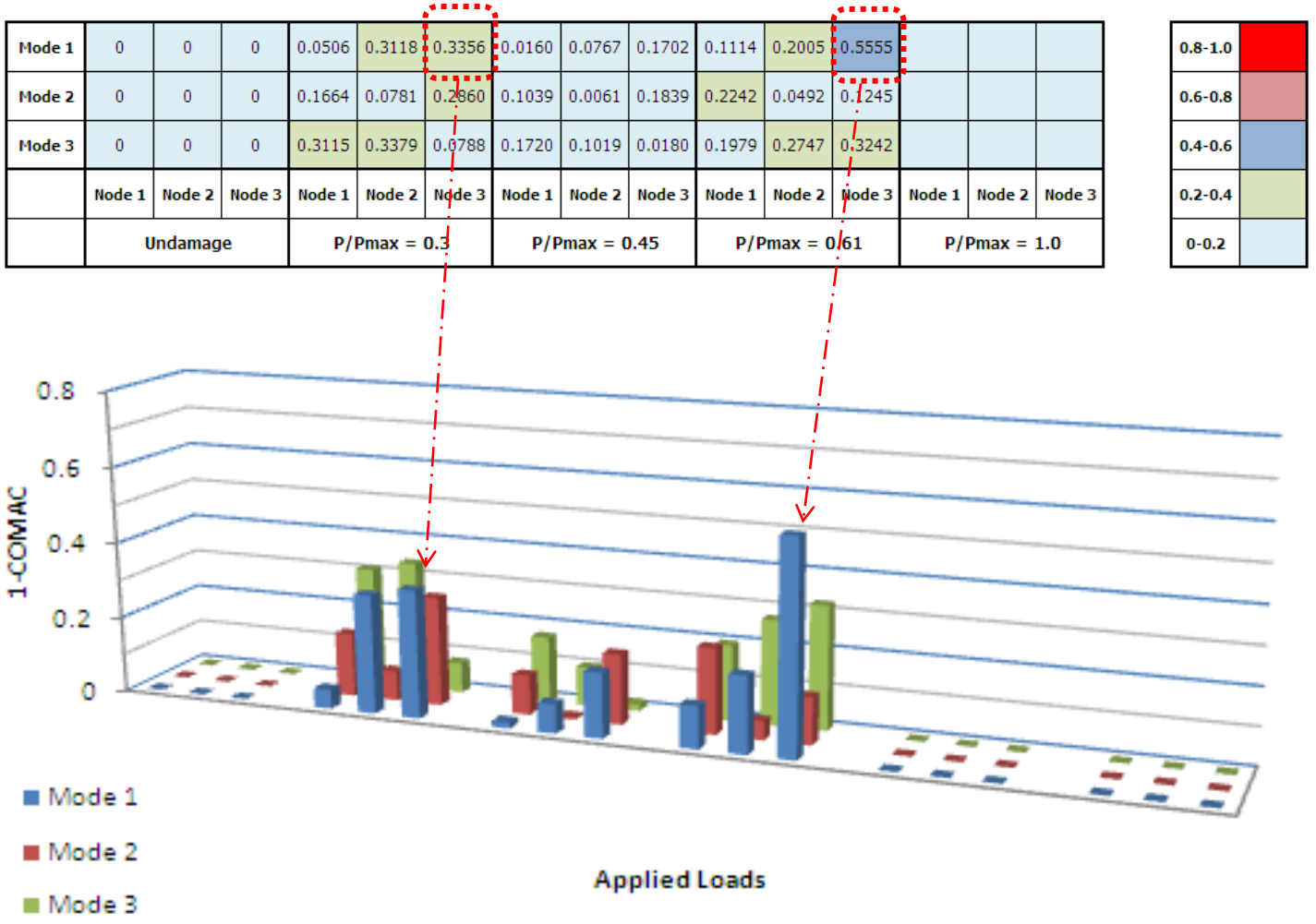

Figure 6.49 Change of 1-COMAC values based on experimental mode shape of Control Frame 2

Mode 1	0	0	0	0.0069	0.1342	0.1290	0.0015	0.4061	0.3865	0.0453	0.4796	0.1585	0.0289	0.0508	0.1435	0.0019	0.2614	0.4892
Mode 2	0	0	0	0.0052	0.0317	0.0091	0.0553	0.1570	0.1107	0.1801	0.2143	0.0171	0.2259	0.0014	0.0207	0.0601	0.0392	0.0204
Mode 3	0	0	0	0.0054	0.0845	0.0008	0.0348	0.2687	0.0469	0.1888	0.3420	0.0024	0.2382	0.0126	0.0104	0.0621	0.0978	0.1286
	Node 1	Node 2	Node 3	Node 1	Node 2	Node 3	Node 1	Node 2	Node 3	Node 1	Node 2	Node 3	Node 1	Node 2	Node 3	Node 1	Node 2	Node 3
	Undamage			P/Pmax = 0.35			P/Pmax = 0.58			P/Pmax = 0.69			P/Pmax = 0.81			P/Pmax = 1.0		

0.8-1.0	
0.6-0.8	
0.4-0.6	
0.2-0.4	
0-0.2	

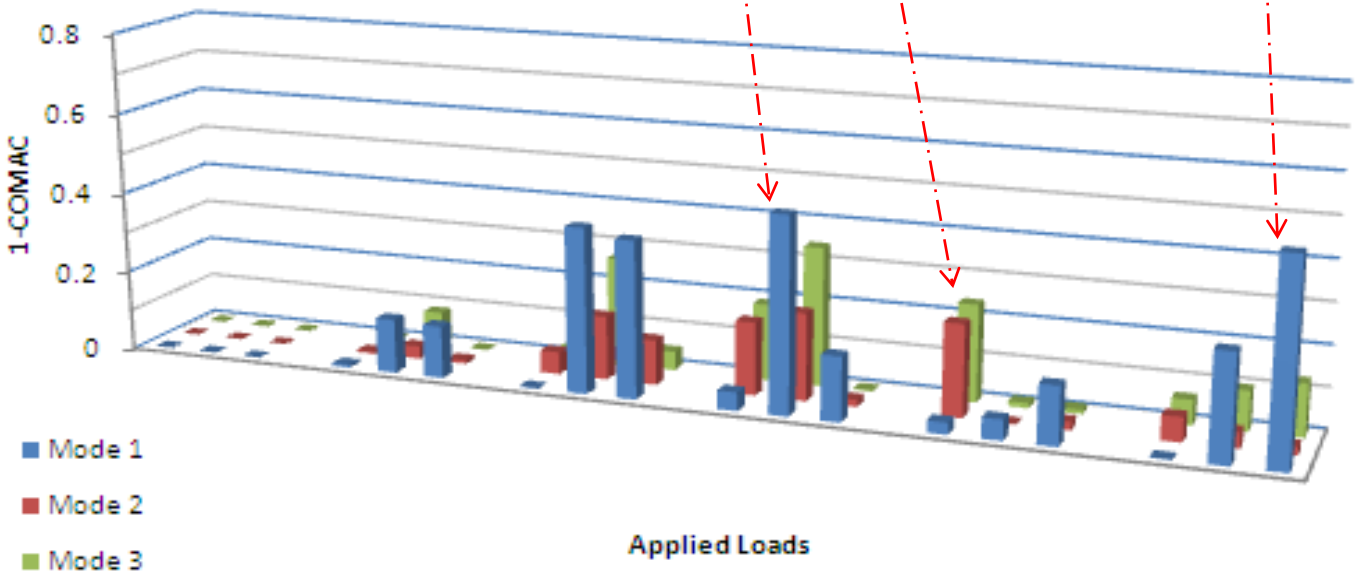

Figure 6.50 Change of 1-COMAC values based on experimental mode shape of Retrofitted Frame 2

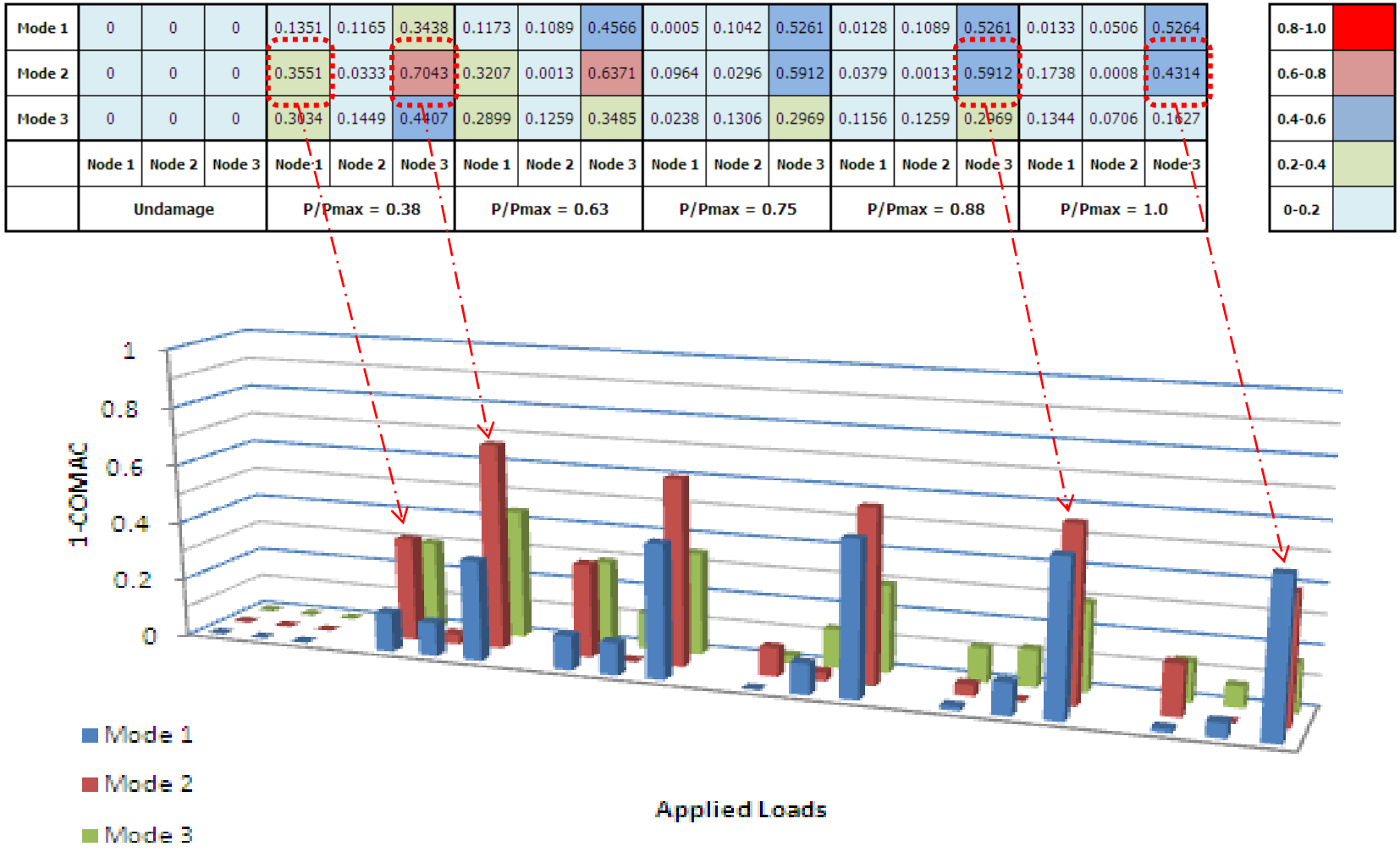

Figure 6.51 Change of 1-COMAC values based on experimental mode shape of Control Frame 3

Mode 1	0	0	0	0.0046	0.0554	0.4616	0.0037	0.1464	0.0413	0.0097	0.3625	0.0580	0.0170	0.5257	0.0336	0.0247	0.0925	0.1404	0.0140	0.0837	0.4350
Mode 2	0	0	0	0.0823	0.0021	0.4565	0.0737	0.3229	0.2315	0.1268	0.1209	0.0426	0.1698	0.5565	0.2337	0.1828	0.0059	0.1093	0.2599	0.0015	0.4373
Mode 3	0	0	0	0.0939	0.0452	0.1430	0.0837	0.2670	0.1106	0.1317	0.4138	0.0018	0.1732	0.4418	0.1143	0.2198	0.0782	0.0110	0.2745	0.0666	0.1426
	Node 1	Node 2	Node 3	Node 1	Node 2	Node 3	Node 1	Node 2	Node 3	Node 1	Node 2	Node 3	Node 1	Node 2	Node 3	Node 1	Node 2	Node 3	Node 1	Node 2	Node 3
	Undamage			P/Pmax = 0.23			P/Pmax = 0.47			P/Pmax = 0.58			P/Pmax = 0.70			P/Pmax = 0.81			P/Pmax = 1.0		

0.8-1.0	
0.6-0.8	
0.4-0.6	
0.2-0.4	
0-0.2	

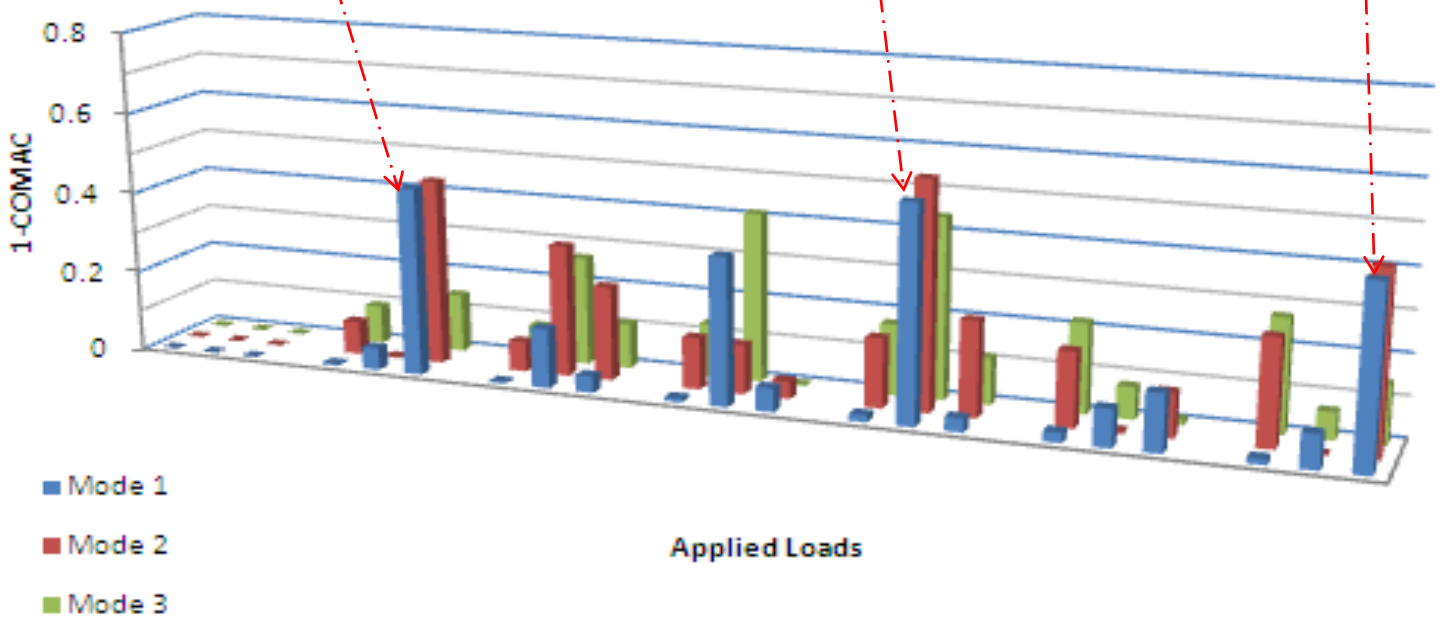

Figure 6.52 Change of 1-COMAC values based on experimental mode shape of Retrofitted Frame 3

Chapter 7

CONCLUSION

7.1 GENERAL

Vibration-based monitoring techniques have proven useful in identifying the changes of structural properties due to damage and retrofitting. The aim of present thesis was to study dynamic and nonlinear behavior of retrofitted RC frames. The damage was progressively induced by quasi-static load test. Vibration monitoring technique has been used to assess the damage of structures. Some of the significant damage index approaches have been defined in order to assess structural damage. The damaged frames were repaired using GFRP afterward. The retrofitted frames were tested in a similar way to the frames before retrofitting. Nonlinear and dynamic FE analyses were performed on the structural model. The experimental nonlinear and dynamic behaviors of each frame were compared to FE analytical results. Also, the performance of several identification method based on experimental modal data was investigated. On the basis of the present study, following conclusions are drawn.

7.2 EFFECTS OF LATERAL LOAD ON STRUCTURES

The following conclusions can be drawn from the research results of lateral loads on RC structures:

1. Experimental results confirm GFRP wraps for structural strengthening produce a significant increase in the lateral load capacity of the RC frames.

2. The ductile behavior of the retrofitted frames can be restored by GFRP sheets and external confinement can be maintained with larger lateral displacements.

3. RC frames with ductile reinforcement show a significant increase in the lateral load capacity as compared to brittle RC frames. The ductile behavior of structures is largely restored at larger lateral displacements.

4. The RC frames without ductile detailing have lesser shear resistance capacity, whereas the ductile detailed RC frames can resist both shear and bending stresses.

5. The bond mechanism between the GFRP sheets and the concrete significantly affect the crack pattern for strengthened RC frames. No significant flexural cracks were observed on the outside fiber layer along the fiber direction and no tension failure of the FRP composite sheet was observed.

6. MBrace Primer layer cannot repair huge concrete cracks, which is indicated by the slipping of the GFRP layers at beam-column joints. However, there was no slipping of GFRP sheets at smaller loads on the Retrofitted Frame 2, which indicates that MBrace Primer layer is proper for grouting the small cracks in moderate damage conditions.

7. The largest cracks in Retrofitted Frame 3 with ductile detailing were found at the edges of columns near the stub foundation. These cracks were horizontal, indicating that a plastic hinge was formed in columns of the first floor at the ultimate state. Thus, the strengthening process of damaged ductile structures should focus on the plastic hinge zone both at connection joints of the top floor and also at columns of the first floor.

8. The health of RC structures of both control and retrofitted specimens is unsafe when DI_{Park} and DI_k increase to more than 0.5 or when structural stiffness reduces to less than 50% of initial state.

9. The GFRP sheets wrapped around the structural elements were intended to provide external confinement and crushing of the concrete cover. Results show that the reduced stiffness of the repaired specimens can likely be accounted for by the fact that the FRP jacket did not bridge the crack interface.

7.3 DYNAMIC CHARACTERISTIC OF STRUCTURES

Based on vibration monitoring and correlation of damage indexes based on the change in dynamic characteristics of structure, the following main conclusions can be drawn:

1. The damage indexes of strengthened frames can be reduced, indicating better performance as compared to control frames. Damage indices based on deformation and change in stiffness show a much more acceptable accuracy correlation with dynamic damage indices in general.

2. Although the stiffness of the damaged RC structure is regained significantly by using GFRP jackets. However, they are not able to bridge the cracks fully. The failure of the strengthened specimen is due to breaking the bond between GFRP layer and concrete.

3. Based on the change in dynamic characteristics of structures in this study, the damaged structures are unsafe when DI_{Dip} increase to more than 0.2 and DI_{FRF_MS} increase to more than 0.4. Moreover, the results of damage indices show that the DI_{FRF_MS} is a more accurate method to estimate structural damage, compared to DI_{Dip}.

4. In general, damage index based on change in modal parameters works when damage reaches severe stages. However, the conducted experiment based on the impact hammer test demonstrates a useful technique to monitor health of structures when damage is hidden within the structure behind strengthening material layers.

5. The three natural frequencies of all specimens were observed to be in a frequency range of 0 to 50 Hz. The change of resonant frequency was large at primary mode as compare to higher mode. However, the effects of damaged structure on changes in natural frequency are negligible.

6. The experimental results indicate that FRF magnitudes are high in an undamaged state. They decrease after stiffness is reduced or cracks appear in the elements. Although the confinement effect influences dynamic properties such as structural stiffness, the increase of story mass has more influence.

7. In general, the structural damping increases when stiffness of structure decreases. Damped response of structure is low at initial state and increases when cracks appear in structural elements.

8. Acceleration response plot in time domain changes shape from smooth to zigzag when cracks appear in structural elements. This plot clearly shows that the GFRP jacket is not bridging the crack interface inside the repaired specimens.

7.4 THEORETICAL RESULTS AND ANALYSIS

1. Nonlinear FE load-displacement plots exhibit similar trends with those of the experimental frame model, but the plots show the FE model is slightly stiffer than the experimental model.

2. There are several conditions that may cause the higher stiffness in the nonlinear FE model. First, micro-cracks are present in the actual elements and beam-column joints prior to small loads, but these micro-cracks do not show in the FE model. Next, the assumptions of perfect bond between concrete and steel bars as well as between concrete and FRP sheets are assumed in the FE analysis, but some slippage and micro-cracks occur in the experiments.

3. The ultimate loads of the nonlinear FE models show good agreement with the data obtained from the experimental tests. Crack patterns at the final state in the FE model correspond quite well with the failure modes of the experimental frames. However, FE models underestimate the ductile behavior compared to actual frames.

4. The results of FE model were compared with the experimental dynamic test results and discussed. The comparisons between the results of dynamic FE model and the experimental results show reasonable accuracy of modal parameter identification. The results of FE model of vibrating frame specimens agree with the experimental results. In the experimental study, the reliability of modal parameter identification was investigated and a good agreement was observed between the results of tree experimental studies.

5. The modal assurance criterion is subjected to very small change by damage of retrofitting. This factor cannot determine the stiffness changes in each degree of freedom, but it can present information about overall stiffness change of the structure due to damage or retrofitting. It is concluded that coordinate modal assurance criterion

factors may detect the changes in frame damage. This index is rather able to detect, locate or quantify damage and effectiveness of retrofitting.

7.5 SCOPE FOR FUTURE WORK

1. In the present study, RC structure frames has been considered. Vibration monitoring of steel frames may also be investigated.

2. Impact hammer test was used in the present study. The dynamic effect of a shaking machine to generate harmonic excitation force needs investigation.

REFERENCES

Agarwal, P. and Shrikhande, M. (2006). Earthquake Resistant Design of Structures, Jay Print Pack Private Limited, New Delhi, India.

Ahmab, S. B. M. (1970). Analysis of Thick and Thin Shell Structures by Curved Finite Elements, *International Journal of Numerical Methods in Engineering*, **2**: 419-451.

Aktan, A. E. and Helmicki, A. (1998a). Intelligent Infrastructure: System Identification Challenges, *Proceedings of the Structural Engineers World Congress*, San Francisco, CA, USA.

Aktan, A. E., Catbas, N., Turer, A. and Zhang, Z.F. (1998b). Structural identification: Analytical aspects, *Journal of Structural Engineering*, ASCE, **124**(7): 817-829.

Aktan, A. E., Helmicki, A .J. and Hunt, V. J. (1998c). Issues in Health-Monitoring For Intelligent Infrastructure, *Journal of Smart Materials and Structures*, **7**(5): 674-692.

Al Chaar, G., Issa, M. and Sweeney, S. (2002). Behavior of Masonry-Infilled Nonductile Reinforced Concrete Frames, *Journal of Structural Enginnering*, ASCE , **128**(8), 1055-1063.

Allemang R. J. and Brown, D. L. (1982). A Correlation Coefficient for Modal Vector Analysis. *Proceedings of the1st international Modal Analysis Conference*, pp. 110-6.

Al-Sulaimani, G.J., Sharif, A., Basunbul, I.A., Baluch, M.H. and Ghaleb, B.N. (1994). Repair for reinforced concrete by fiberglass plate, *ACI structural journal*, **91**(3): 458-464.

Am brose, J. and Vergun, D. (1999). Design for Earthquakees, John & Sons, New York, NY, USA.

An, W., Saadatmanesh, H. and Ehsani, M. (1991). RC Beams Strengthened with GFRP Plates II: Analysis and Parametric Study. *Journal of Structural Engineering*, ASCE, **117**(10): 3434-3455.

Andreason, K. and Rose, J. D. (1994). Northridge, California Earthquake: Structural Performance of Buildings in San Fernando Valley, California, APA Report No. T94-5, Tacoma, Washington, DC, USA.

ATENA Revision 2005/01. *Cervenka Consulting*, Praha, Czech Republic, 2005.

Avitabile, P. (2001). Experimental Modal Analysis: A Simple Non-Mathematical Presentation, *Sound and Vibration*, January, 1-11.

Baghiee, N., Esfahani, M. R. and Moslem, K. (2009). Studies on Damage and FRP Strengthening of Reinforced Concrete Beams by Vibration Monitoring, *Engineering Structures*, **31**: 875-893.

Baker, W. A., Brown, D. H. and Tissel, J. R. (1989). Loma Prieta Earthquake, San Francisco Bay Area, APA Report No. T89-28, Tacoma, Washington, DC, USA.

Balaguru, P.N. (2003). A new concept for the computation of maximum moment capacity of reinforced concrete beams strengthened with fiber reinforced polymer. *Journal of Indian Concrete Institute*, **4**(3): 7-12.

Bansal, P., Kumar, M. and Kaushik, S. K. (nd.). Effect of Wire Mesh Orientation on Strength of Beams Retrofitted Using Ferrocement Jackets, *International Journal of Engineering*, **2**(1): 8-19.

Barbato, M. (2009). Efficient Finite Element Modeling of Reinforced Concrete Beams Retrofitted with Fibre Reinforced Polymers, *Journal of Computers and Structures*, **87**: 167-176.

Barecchia, E. and Mazzolani, F. M. (nd.). The Use of FRP Materials for the Seismic Upgrading of Existing RC Structures, Universitá degli Studi di Napoli Federico II, Facoltá di Ingegneria.

Bazant, Z. P. and Oh, B. H. (1983). Crack Band Theory for Fracture of Concrete. Materials and Structures, RILEM, **16**: 155-177.

Beards, C. F. (1996). Structural Vibration: Analysis and Damping, Arnold, London, Great Britain.

Beck, J. L. and Jennings, P. C. (1980). Structural Identification Using Linear Models and Earthquake Records, *Earthquake Engineering and Structural Dynamics*, **8**: 145-160.

Bertero, V. V. and Bresler, B. (1971). *Developing Methodologies for Evaluating the Earthquake Safety of Existing Buildings,* Report No. UCB 71-13, University of California, Berkeley, CA.

Biddah, A., Heidebrecht, A.C. and Naumoski, N. (1995), Use of push over test to evaluate damage of reinforced concrete frame structures subjected to strong

seismic ground motions, *7th Canadian Conference on Earthquake Eng.*, Montreal.

Bhutta, S. (1993). Analytical Modeling of Hybrid Composite Beams. *M.S. Thesis*, Dept. of Civil Engineering, Virginia Polytechnic Institute and State University, Blacksburg, VA.

Boroschek, R. L. and Yanez, F. V. (2000). Experimental verification of basic analytical assumptions used in the analysis of structural wall buildings, *Engineering Structures*, **22**(6): 657-669.

Bracci, J.M., Kunnath, S.K. and Reinhorn, A.M. (1997). Seismic performance and retrofit evaluation of reinforced concrete structures, *Journal of structural engineering*, ASCE, **123**(1): 3-10.

Brehm, M., Zabel, V., Bucher, C. and Ribeiro, D. (2009), An Automatic Mode Selection Strategy for Model Updating using the Modal Assurance Criterion and Modal Strain Energies, *Proceeding of 18th International Conference on the Application of Computer Seience and Mathematics in Architecture and Civil Engineering*, Weimar, Germany, 1-18.

Brown, C. B. (1987). Jaynes, Bayes and Fuzzy Identification, *Civil Engineering Systems,* **4**: 142-146.

Brownjohn, J. M. W., (1994). Estimate of damping in suspension bridges, *Proceeding, Institution of Civil Engineers*, Structures and Buildings, 104, November, pp. 401-415.

Bruneau, M., Uang, C. M. and Whittaker, A. (1998). Ductile Design of Steel Structures, McGraw-Hill, New York, NY, USA.

Buchholdt, H. A. (1997). Structural Dynamics for Engineers, Thomas Telford Services Ltd., New York, USA.

Burgueno, R., Karbhari, V. M., Seible, F. and Kolozs, R. T. (2001). Experimental Dynamic Characterization of an FRP composite Bridge Superstructure Assembly, *Composite Structures*, **54**: 427-444.

Callaghan, K. (nd.). The Correlation Coefficient, Anthology of Readings, Internet.

Camata, G., Spacone, E. and Zarnic, R. (2007). Experimental and Nonliner Finite Element Studies of RC Beams Strengthened with FRP Plates, *Journal of Composites*, **38**(B): 277-288.

Carlin, B. P., (1998). Investigation of the Strength and Ductility of Reinforced Concrete Beams Strengthened with CFRP Laminates, MS Thesis of Science in Civil Engineering, Virginia Polytechnic Institute and State University, Blacksburg, Virginia, USA.

Casas, J.R. and Aparicio, A.C. (1994). Structural damage identification from dynamic-test data, *Journal of structural engineering*, **120**(8): 2437-2450.

CEB-FIP Model Code 90 (1990). First Draft, Committee Euro-International du Beton, Bulletin d'information No. 195, 196.

Cervenka, V., Pukl, R., and Eligehausen, R. (1991). Fracture Analysis of Concrete Plane Stress Pull-out Tests, *Proceedings, Fracture Process in Brittle Disordered Materials*, Noordwijk, Holland, 19-21.

Cervenka, V. and Pukl, R. (1992). Computer Models of Concrete Structures, *Structural Engineering International*, **2**(2): 103-107.

Cervenka, V., Pukl, R., Ozbolt, J. and Eligehausen, R. (1995). Mesh Sensitivity Effects in Smeared Finite Element Analysis of Concrete Structures, *Proc. FRAMCOS 2*, 1387-1396.

Chang, S. Y., Li, Y.F. and Loh, C.H. (2004). Experimental study of seismic behaviors of as-built and carbon fiber reinforced plastics repaired reinforced concrete bridge columns, *Journal of bridge engineering*, ASCE, **9**(4): 391-402.

Chung, Y. S., Meyer, C. and Shinozuka, M. (1988). Damage Model for Reinforced Concrete, Seismic Engineering Research and Practice, *Proceedings of the 1989 ASCE Structures Congress*, San Francisco, CA, pp. 478-487.

Crisfield, M. A. and Wills, J. (1989). The Analysis of Reinforced Concrete Panels Using Different Concrete Models, Journal of Engineering Mechanic, ASCE, **115**(3): 578-597.

Darwin, D. and Pecknold, D. A. W. (1974). Inelastic Model for Cyclic Biaxial Loading of Reinforced Concrete, Civil Engineering Studies, University of Illinois, July.

Dipasquale, E. and Cakmak, A.S. (1990). Seismic Damage Assessment using Linear Models. *Soil Dynamics and Earthquake Engineering*, **4**(9): 194-215.

Doebling, S. W., Farrar, C. R. and Prime, M. B. (1998). A Summary Review of Vibration Base Damage Identification Methods, *The Shock and Vibration Digest*, **30**(2): 91-105.

Dowrick. D. J. (1988). Earthquake Resistant Design, John Willey & Sons, Singapore.

Dublois, M., Picard, A., and Beaulieu, D. (1992). Reinforcement de Putres en Beton Arme a L'Aide de Materiaux Composites: Etudes Theorique et Experimentale. *Proceeding of the First International Conference on Advanced Composite Materials in Bridges and Structures*, Sherbrooke, pp. 265-275.

Durkin, M. E. (1985). Behavior of Bukding Occupanis in Earthquake, *Earthquake Specta*, **1**(2), 271-283.

Dyngeland, T. (1989). Behavior of Reinforced concrete Panels, Dissertation, Trondheim University, Norway, BK-report 1989:1.

El-Amoury, T. and Ghobarah A. (2002). Seismic Rehabilitation of Beam-Column Joint using GFRP Sheets, *Engineering Structures*, **24**: 1397-1407.

Estekanchi, H. and Arjomandi, K. (2007). Comparison of Damage Indexes in Nonlinear Time History Analysis of Steel Moment Frames, *Asian Journal of Civil Engineering*, **8**(6): 629-646.

Ewins, D. J. (1985). *Modal Testing: Theory and Practice*, John Wiley, NY.

Fardis, M. N. and Calvi, G. M. (1995). Effects of Infills on the Global Response of Reinforced Concrete Frames, *Proceedings of the 10th European Conference on Earthquake Engineering*. A.A. Balkema, Rotterdam, Vol. 4, pp. 2893-2898.

Fardis, M. N. and Panagiotakos, T. B. (1997). Seismic Design on Response of Bare and Masony-Infilled Reinforced Concrete Buildings-Part II: Infilled Structures, *Journal of Earthquake Engineering*, **1**(3), 475-503.

Farrar, C. R., Baker, W. B., Bell, T. M., Cone, K. M., Darling, T. W., Duffey, T. A., Eklund, A. and Migliori A. (1994). *Dynamic Characterization and Damage Detection in the I-40 Bridge over the Rio Grande*, Los Alamos Report LA-12767-MS UC-906, Los Alamos, M.

Farrar, C. R. and Cone, K. M. (1995). Vibration Testing of the I-40 Bridge Before and After the Introduction of Damage, *Proceedings of the 13th International Modal Analysis Conference*, Nashville, TN. Published in cooperation with SPIE, Vol. 2460, pp. 203-209.

Farrar, C. R. and Duffey, T. A. (1998). Bridge Modal Properties using Simplified Finite Element Analysis, *Journal of Bridge Engineering*, **3**(1): 38-46.

Ferracuti, B., Savoia, M. and Mazzotti, C. (2006). A Numerical Model for FRP-Concrete Delamination. *Journal of Composites*, **37**(B): 356-364.

Finno, J. R., and Prommer, J. P. (1994). Evaluation of Inaccessible Drilled Shafts Using the Impulse Response Method, *ITI Technical Report #3*, Northwestern University, Evanston, IL.

Formenti, D. (2000). What are the Sources of Variations in Frequency Response Function Measurements, Sound and Vibration, *The Noise and Vibration Control Magazine*, **34**(1): 14-18

Gangadharan, S. N., Haftka, R. T. and Nikolaidis, E. (1991). Probabilistic System Identification of Two Flexible Joint Models, *American Institute of Aeronautics and Astronautics Journal*, **29**(8): 1319-1326

Gheorghiu, C., Rhazi, J. E. and Labossiere, P. (2005). Impact Resonance Method for Fatigue Damage Detection in Reinforced Concrete Beams with Carbon Fibre Reinforced Polymer, *Canadian Journal of Civil Engineering, NRC-CNRC*, **32**: 1093-1102.

Ghobarah, A. and Elmandoohgalal, K. (2004). Seismic Rehabilitation of Short Rectangular RC Columns, *Earthquake Engineering*, **8**(1): 45-68.

Glanville, M. J., Kwok, K. C. S. and Denoon, R. O. (1996). Full-scale damping measurements of structures in Australia, *Journal of Wind Engineering and Industrial Aerodynamics*, **59**(2-3): 349-364

Goyal, A. (2007). Structural Health Monitoring of Retrofitted RCC Beams using Vibration Measurements, ME Dissertation, Thapar University, Patiala, India.

Hajela, P. and Soeiro, F. J. (1990). Structural Damage Detection Based on Static and Modal Analysis, *American Institute of Aeronautics and Astronautics Journal*, **28**(9): 1110-1115.

Hearn, G. and Testa, R. B. (1991). Modal Analysis for Damage Detection in Structures, *Journal of Structural Engineering*, **117**(10): 3042-3036.

Hjelmstad, K. D., Banan, Mo. R. and Banan, Ma. R. (1995). Time-Domain Parameter Estimation Algorithm for Structures I: Computational Aspects, *Journal of Engineering Mechanics*, ASCE, **121**(3): 424-434.

Horbijk, D. A. (1991). Local Approach to Fatigue of Concrete, Doctor dissertation, Delft University of Technology, The Netherlands, ISBN 90/9004519-8.

Hossdorf, H. and Amerongen, C. V. (1974). Model Analysis of Structures, Van Nostrand Reinhold Company Ltd., New York, USA.

Hsu, T. T. C. (2000). Unified Theory of Reinforced Concrete, CRC Press, Boca Raton, Florida.

Huynh, D. and Tran, D. (2005). Damage Location Vector: A Non-destructive Structural Damage Detection Technique, *Journal of Computers and Structures*, **83**(2005): 2353-2367.

Ibrahim, S. R. and Mikulcik, E. C. (1977). A Method for the Direct Identification of Vibration Parameters from the Free Response, *Shock and Vibration Bulletin*, **47**(4): 183-198.

IS: 10262. (1982). Recommended Guidelines for Concrete Mix Design, *Bureau of Indian Standard*, New Delhi, India.

IS: 1489. (1976). Specifications for Portland Pozzolana Cement, *Bureau of Indian Standard*, New Delhi, India.

IS: 13920. (1993). Code of Practice for Ductile Detailing of Reinforced Concrete Structures, *Bureau of Indian Standard*, New Delhi, India.

IS: 383. (1970). Specifications for Coarse and Fine Aggregates from Natural Resources for Concrete, *Bureau of Indian Standard*, New Delhi, India.

IS: 456. (2000). Code of practice for plain and reinforced concrete. *Bureau of Indian Standards*, New Delhi, India.

IS: 8112. (1989). Specifications for High Strength Ordinary Portland Cement, *Bureau of Indian Standard*, New Delhi, India.

Jendele, L. Cervenka, J. Saouma, V. and Pukl, R. (2001). On the Choice between Discrete or Smeared Approach in Practical Structural FE Analyses of Concrete Structures, *4th International Conference on Analysis of Discontinuous Deformation in Glasgow*, Scotland, UK.

Jia, J., Boothby, T.E., Bakis, C.E. and Brown, T.L. (2005). Durability evaluation of glass fiber reinforced-polymer-concrete bonded interfaces, *Journal of composites for construction*, **9**(4): 348-359.

Jian, G., Yong, C. and Bing-nan, S. (2005). Experimental study of structural damage identification based on WPT and coupling NN, *Journal of Zhejiang University SCIENCE*, http:/www.zju.edu.ch/jzus, pp. 663-669.

Kachlakev, D., Miller, T. and Yim, S. (2001). Finite Element Modeling of Reinforced Concrete Structures Strengthened with FRP Laminates. *Final report-SPR 316*, Oregon department of transportation and Federal highway administration, Oregon, USA.

Kanwar, V., Kwatra, N., Aggarwal, P. and Gambir, ML. (2006). Vibration Monitoring of a RCC Building Model, *Proceedings of National Conference on Technology for Disaster Mitigation*, Hamirpur, India, pp. 277-285.

Kanwar, V., Kwatra, N. and Aggarwal, P. (2007). Damage Detection for Framed RCC Buildings using ANN Modelling, *Journal of Damage mechanics*, **16**(4): 457-472.

Kao, C.Y. (2003). Application of neural networks in structural health monitoring, *National Center for Research on Earthquake Engineering*, Taipei, Taiwan, www.context-gmbh.de.

Ketter, R. L., Lee, G. C. and Prawel Jr., S. P. (1979). Structural Analysis and Design, McGraw-Hill Book Company, New York, USA.

Key, D. E. (1988). Earthquake Design Practice for Building, Thomas Telford Limited, London, UK.

Khalifa, A., Gold, W.J., Nanni, A. and Aziz, A. (1998). Contribution of externally bonded FRP to shear capacity of RC flexural members, *Journal of composites for construction*, **2**(4): 195-202.

Kim, D. H. (1995). Composite Structures for Civil and Architectural Engineering, E & FN Spon, London, UK.

Ko, J.M., Sun, Z.G. and Ni, Y.Q. (2002). Multi-Stage Identification Scheme for Detecting Damage in Cable Stayed Kap Shui Mun Bridge, *Engineering Structures*, **24**: 857-868.

Kollegger, J. and Mehlhorn, G. (1988). Experimentelle und Analytische Untersuchungen zur Aufstellung eines Materialmodels fur Gerissene Stahbetonscheiben, Nr.6 Forschungsbericht, Massivbau, Gesamthochschule Kassel.

Kolousek, V. (1973). Dynamics in Engineering Structures, Butterworth, London.

Kolmar, W. (1986). Beschreibung der Kraftuebertragung uber Risse in Nichtlinearen Finite-Element-Berechnugen von Stahlbetontragwerken, Dissertation, T.H. Darmstadt.

Kupfer, H., Hilsdorf, H. K. and Rusch, H. (1969). Behavior of Concrete under Biasial Stress, *Journal ACI*, **66**(8): 656-666.

Kwon, O. and Elnashai, A. S. (2006). The effect of material and ground motion uncertainty on the seismic vulnerability curves of a RC structure, *Engineering Structures*, **28**(2): 289-303.

Lagomarsino, S. (1993). Forecast Models for Damping and Vibration Periods of Buildings, *Journal of Wind Engineering and Industrial Aerodynamics*, **48**: 221-239

Lee, D. H. and Elnashai, A. S. (2002). Inelastic Seismic Analysis of RC Bridge Piers Including Flexure-Shear-Axial Interaction, *Structural Engineering and Mechanics*, **13**(3), 241-260.

Lee, U. and Shin, J. (2002). A Frequency Response Function-Based Structural Damage Identification Method, *Computers and Structures*, **80**: 117-132.

Li, A., Assih, J. and Delmas, Y. (2001). Shear Strengthening of RC Beams with Externally Bonded CFRP Sheets, *Journal of Structural Engineering*, **127**(4): 374-380.

Li, Q. S., Fang, J. Q. and Jeary A. P. (1998). Calculation of vertical dynamic characteristics of tall buildings with viscous damping, *International journal of solids and structures*, **35**(24): 3165-3176

Lieven, N.A.J., and Ewins, D.J. (1988). Spatial correlation of mode shapes, the coordinate modal assurance criterion, *Proceedings of the 6th International Modal Analysis Conference*, pp. 690-695.

Lim, T. W. (1991). Structural Damage Detection Using Modal Test Data, *American Institute of Aeronautics and Astronautics Journal*, **29**(12): 2271-2274.

Lord, J-F., and Ventura, C. E. (2002), FE Model Calibration of a 48 Storey Building in Vancouver using Ambient Vibration Measurements, *Proceeding of 4th Conférence Spécialisée en Génie des Structures and 4th Structural Specialty Conference of the Canadian Society for Civil Engineering*, Québec, Canada, pp. 1-10.

Ludovico, M. D., Nanni, A., Prota, A. and Cosenza, E. (2005). Repair of Bridge Girders with Composites: Experimental and Analytical Validation, *ACI Structural Journal*, **102**(5): 639-648.

Lutes, L. D. and Sarkani, S. (1995). Structural damping for soil–structure interaction studies, *Structural Engineering*, **2**: 107–120.

Maeck, J. (2003). Damage assessment of Civil Engineering Structures by Vibration Monitoring, Ph.D. Thesis. Department of Civil Engineering, K. U. Leuven, Belgium.

Maia, N.M.M., Silva, J.M.M., Almas, E.A.M. and Sampaio, R.P.C. (2003). Damage Detection in Structures: from Mode Shape to Frequency Response Function Methods, *Mechanical Systems and Signal Processing*, **17**(3): 489-498.

Malvar, L. J., Warren, G.E. and Inaba, C. (1995). Rehabilitation of Navy Pier Beams with Composite Sheets. Second FRP International Symposium, Non-Metallic (FRP) Reinforced RC elements for Concrete Structures, Ghent, Belgium, pp. 533-540.

Matos, C. G. and Dodds, R. H. (2002). Probabilistic Modelling of Weld Fracture in Steel Frame Connection. Part II: Seismic Loading. *Engineering Structures*, **24**(6), 687-705.

Mazurek, D.F. and DeWolf, J.T. (1990). Experimental study of bridge monitoring techique, *Journal of structural engineering*, ASCE, **116**(9): 2532-2549.

M'Bazaa, I., Missihoun, M. and Labossiere, P. (1996). Strengthening of Reinforced Concrete Beams with CFRP Sheets", *First International Conference on Composites in Infrastructure Fibre, ICCI'96*, Tucson, AZ, pp.746-59.

McGuire, W., Gallagher, R. H. and Ziemian, R. D. (2000). Matrix Structural Analysis, John Wiley and Sons, New York, USA.

Meirovitch, L. (1986). Elements of Vibration Analysis, McGraw-Hill, Singapore.

Memon, MS. and Sheikh, S.A. (2005). Seismic Resistance of Square Concrete Columns Retrofitted with Glass-Fiber Reinforced Polymer, *ACI Structural Journal*, **102**(5): 774-783.

Mier, J. G. M. (1986). Multiaxial Strain-softening of Concrete, Part I: fracture, *Materials and Structures*, RILEM, **19**(111).

Mileti, D. S. and Nigg, J. M. (1984). Earthquakes and Human Behavior, *Earthquake Spectra*, 1(1), 89-106.

Mo, Y. L. (1994). Dynamic Behavior of Concrete Structures, Elsevier Science B.V., Amsterdam, Netherlands.

Mukherjee, A., Boothby, T.E., Bakis, C.E., Joshi, M.V. and Maitra, S.R. (2004). Mechanical behavior of fiber reinforced polymer wrapped concrete columns-complicating effects. *Journal of Composite for Construction*, **8**(2): 97-103.

Mukherjee, A. and Joshi, M. (2005). FRPC Reinforced Concrete Beam-Column Joints under Cyclic Excitation, *Composite Structures*, **70**: 185-199.

Naaman, A. And Joeng, S. (1995). Structural Ductility of Concrete Prestressed Beams with FRP Tendons. *Proceeding of the Second International RILEM Symposium – Non- Metallic (FRP) Reinforcement for Concrete Structures*, Ghent, Belgium, pp. 379-386.

Natke, H. G. and Yao, J. T. P. (1988). *Structural Safety Evaluation Based on System Identification Approaches*, Friedrick Vieweg & Son, Wiesbaden, Germany.

Ndambi, J. M., Vantomme, J. and Devisscher, J. (2000). Modal Damping as A Damage Detection Parameter in Reinforced Concrete structures, *Proceedings of the 5th international Conference on Computational Structures Technology*, Leuven, pp. 1-7.

Ndambi, J. M., Vantomme, J. and Harri, K. (2002). Damage Assessment in Reinforced Concrete Beams using Eigenfrequencies and Mode Shape Derivatives, *Journal of Structural Engineering*, **24**: 501-515.

Nelson, D. (2004). The Penguin Dictionary of Statistics, Penguin Books, England.

Newmark, N. M. and Rosenblueth, E. (1971). *Fundamentals of Earthquake Engineering*, Prentice-Hall, New Jersey, USA.

Norris, T., and Saadatmanesh, H. (1994). *Improving the Serviceability of Concrete Beams using Carbon Fiber Reinforced Polymer (CFRP) Sheets*, FHA, Grant No. DDEGRF-93-P-05.

Ooi, T. K., Engberg, R. C., Gilbert, J. A., Vaughan, R. E. and Bower, M. V. (2004). Modal Testing of A Lightweight Cementitious Structure, Experimental Techniques, November/December 2004, 37-40.

Pagnini, L. C. and Solari, G. (2001). Damping measurements of steel poles and tubular towers, *Engineering Structures*, **23**(9): 1085-1095.

Pandey, A.K., Biswas, M., and Samman, M.M. (1991). Damage detection from changes in curvature mode shapes, *Journal of Sound and Vibration*, **145**: 321-332.

Pandey, A.K. and Biswas, M. (1994). Damage Detection in Structure using Changes in Flexibility, *Journal of Sound and Vibration*, **169**(1): 3-17.

Park, Y.J. and Ang, A. H-S. (1985). Seismic Damage Analysis of RC Buildings, *Journal of Structural Engineering*, ASCE, **ST4**(111): 740-757.

Paulay, T. and Priestley, M. J. N. (1992). Seismic Design of Reinforced Concrete and Masonry Buildings, John Wiley & Sons, Toronto, Canada.

Pavese, A., Bolognini, D. and Peloso, S. (2004). FRP Seismic Retrofit of RC Square Hollow Section Bridge Piers, *Journal of Earthquake Engineering*, **8**(1): 225-250.

Paz, M. (1997). Structural Dynamics: Theory and Computation, Chapman and Hall, New York.

Penelis, G. G. and Kappos, A. J. (1997). Earthquake-resistant Concrete Structures, E & FN Spon, London, UK.

Perera, R., Recuero, A., De Diego, A. and Lopez, C. (2004). Adherence analysis of Fiber Reinforced Polymer Strengthened RC Beams, *Journal of Computers and Structures*, **82**: 1865-1873.

Perera, R., Huerta, C. and Orquin, J. M. (2007). Identification of Damage in RC Beams using Indexes based on Local Modal Stiffness, *Construction Building Material*, **22**(8): 1656-1667.

Perez, J.J., Zhao, L. and O'Riordan-Adjah, C.A. (2005). Finite Element Evaluation of The Effects of Lateral Anchorage Strips on The Behaviour of CFRP-Strengthened RC Beams, *Proceedings of the international symposium on bond behaviour of FRP in structures*, International institute for FRP in construction, pp. 303-308.

Pierce, C. E. and Dowding, C. H. (1995). Long-term Monitoring of Bridge Pier Integrity with Time Domain Reflectometry Cables, *Proceedings, Conference and Exposition of Sensors and Systems*, Sensors Magazine, pp. 399-406.

Piszczek, K. and Niziol, J. (1986). Ramdom Vibration of Mechanical Systems, PWN-Polish Scientific Publishers, Warszawa, Poland.

Powell, G.H. and Allahabadi, R. (1987). Seismic Damage Prediction by Deterministic Methods: Concept and Procedure, *Earthquake Engineering and Structural Dynamic*, **16**: 719-734.

Prion H.G.L. and Rezai M.K. (1996)**.** Damage detection by modal testing, *Proceedings of 11th World Conference on Earthquake Engineering*, Paper No. 459.

Raghavendrachar, M. and Aktan, A.E. (1992). Flexibility by Multireference Impact Testing for Bridge Diagnostics, *Journal of Structural Engineering*, ASCE, August 1992, 2186-2203.

Ramsey, K. A. (1983). Experimental Modal Analysis, Structural Modifications and FEM Analysis on a Desktop Computer, *Sound and Vibration*, February, 1-10.

Rao, J. S. (2000). Vibratory Condition Monitoring of Machines, Narosa Publishing House, New Delhi, India.

Reddy, K. R., Badami, S. B. and Balasubramanian, V. (1994). Oscillations and Waves, Universities Press Limited, Hyderguda, Hyderabad, India.

Ritchie, P., Thomas, D., Lu, W.L., and Connelly, G. (1991). External Reinforcement of Concrete Beams Using Fiber Reinforced Plastics. *ACI Structural Journal*, ACI, **88**: 490-500.

Rodriguez, R. and Barroso, L.R. (2002). Stiffness-Mass Ratios Method for Baseline Determination and Damage Assessment of a Benchmark Structure, *Proceedings of the American control conference anchorage*, AK, USA, pp. 2469-2474.

Saadatmanesh, H. and Ehsani, M.R. (1991). RC Beams Strengthened with Glass Fiber Reinforced Plastic (GFRP) Plates: Experimental Study, *Journal of Structural Engineering*, ASCE, **117**(10): 3417-3433.

Salane, H. J., Baldwin, J. W. and Duffield, R. (1981). Dynamics Approach for Monitoring Bridge Deterioration, *Transportation Research Record*, **832**: 21-28.

Salawu, O. S. and Williams, C. (1995). Bridge Assessment Using Forced-Vibration Testing, *Journal of Structural Engineering*, ASCE, **121**(2): 161 - 173.

Samali, B., Li, J., Crews, K.I. and Al-dawod, M. (2007). Load Rating of Impaired Bridges Using a Dynamic Method, *Electronic Journal of Structural Engineering*, special issue: loading on structure: 66-75.

Samtani, N. C., Wang, J. N., Pepe F. Jr. and Abrahams, M. J. (1994). Horizontal and Vertical Movements of Bridge Piers Subjected to Ship Impact, *SETTLEMENT '94, an ASCE Geotechnical Division Specialty Conference*, College Station, Texas, pp. 245-256.

Sanayei, M. and Nelson, R. B. (1986). Identification of Structural Element Stiffnesses From Incomplete Static Test Data, *Society of Automotive Engineers Technical*, SAE-861793: 7.1248 - 7.1248.

Sanayei, M. and Saletnik, M. J. (1995). Parameter Estimation of Structures from Static Strain Measurements; Part I: Formulation. *Journal of Structural Engineering*, ASCE, (In Press, July 1995).

Satake, N., Suda, K. I., Arakawa, T., Sasaki, A. and Tamura, Y. (2003). Damping Evaluation Using Full-Scale Data of Buildings in Japan, *Journal of Structural Engineering*, ASCE. 129(4): 470-477.

Sek, M. (nd.). Frequency Response Function, Victoria University, internet.

Shahawy, M., Arockiasamy, M., Beitelman, T., and Sowrirajan, R. (1995). Reinforced Concrete Rectangular Beams Strengthened with CFRP Laminates. *Composites*, **27**B: 225-233.

Stubbs, N. and Osegueda, R. (1990a). Global Non-Destructive Damage Evaluation in Solids, *International Journal of Analytical and Experimental Modal Analysis*, **5**(2): 67-79.

Stubbs, N. and Osegueda, R. (1990b). Global Damage Detection in Solids - Experimental Verification, *International Journal of Analytical and Experimental Modal Analysis*, **5**(2): 81-97.

Stubbs, N., Kim, J.T. and Tapole, K. (1992). An efficient and robust algorithm for damage localization in offshore platforms, *Proceedings of '92 ASCE 10th Structures Congress*, Texas

Stubbs, N., Kim, J. T. and Farrar, C. R. (1995). Field Verification of a Nondestructive Localization and Severity Estimation Algorithm, *Proceedings of the 13th International Modal Analysis Conference*, Nashville, TN, pp. 210 - 218.

Supaviriyakit, T., Pornpongsaroj, P. and Pinmanmas, A. (2004). Finite Element Analysis of FRP-Strengthened RC Beams, *Songklanakarin Journal of Science and Technology*, **26**(4): 497-507.

Taranath, B. S. (1998). Steel, Concrete and Composite Design of Tall Buildings, Mc Graw-Hill, New York, NY, USA.

Terro, M.J., Hamoush, S., and El-Hawary, M. (2007). Upgrading the shear strength of non-ductile reinforced concrete frame connections using FRP overlay systems. *Electronic Journal of Structural Engineering*, **7**: 8-18.

Thomson, W. (1993). Theory of Vibration with Applications: Fourth Edition, Prentice Hall, New Jersey.

Triantafillou, T.C. (1998). Shear strengthening of reinforced concrete beams using epoxy-bonded FRP composites, *ACI structural journal*, **95**(2): 107-115.

Triantafillou, T. C. and Deskovic, N. (1991). Innovative Pre-stressing with FRP Sheets: Mechanics of Short term Behavior. *Journal of Engineering Mechanics*, ASCE. **117**(7): 1652-1672.

Triantafillou, T. and Plevris, N. (1991). Post Strengthening of R/C Beams with Epoxy Bonded Fiber Composite Materials. *Proceedings of a Conference on Advanced Composite Materials in civil Engineering Structures*, ASCE, Las Vegas, USA, pp. 245-256.

URS Greiner Woodward Clyde (1999). Seismic Evaluation and Rehabilitation for Buildings, TI 809-05, US Amy Corps of Engineers, Washington-DC.

Vimuttasoongviriya, A., Kwatra, N. and Kumar, M. (2009). Effect of Lateral Quasi-Static Load on Nonlinear Behaviour and Damage Indexes of Retrofitted RC Frame Model, *Asian Journal of Civil Engineering*, **10**(5), 563-588.

Vimuttasoongviriya, A., Kwatra, N. and Kumar, M. (2010). Damage Detection of Strengthened RC Frame Model with FRP Sheets under Lateral Loads, *Proceeding of the 11th International Conference on Structures under Shock and Impact*, Tallinn, Estonia, pp. 55-67.

Vimuttasoongviriya, A., Kwatra, N. and Kumar, M. (2010). Nonlinear Behaviour and Vibration Based Damage Identifation of Retrofitted RC Frame Model, *Proceeding of the 9th International Conference for Highrise Towers ad Tall Building*, Munich, Germany, Paper No. 0958.

Vimuttasoongviriya, A., Kwatra, N. and Kumar, M. (2010). Modal Parameters Damage Method for Detecting Damage in Strengthened RC Frame Model using GFRP Laminate, *Proceeding of the 15th National Conference in Civil Engineering*, Ubonratchathani, Thiland, STR2.

Wang, J.F., Lin, C.C. and Yen, S.M. (2005). Story Damage Index of Seismically-Excited Buildings Based on Modal Parameters, *18th International Conference on Structural Mechanics in Reactor Technology*, Beijing, China, pp. 3278-389.

Wang, J.F., Lin, C.C. and Yen, S.M. (2007). A Story Damage Index of Seismically-Excited Buildings Based on Modal Frequency and Mode Shape, *Journal of Structural Engineering*, **29**(9): 2143-2157.

Wang, X., Swanson, J. A., Helmicki, A. J. and Hunt, V. J. (2007). Development of Dynamic Response-Based Objective Functions for Finite-Element Modeling of Bridges, *Journal of Bridge Engineering*, **12**(5): 552-559.

Warren, G. E., and Malvar, L. J. (1993). Structural Assessment of Reinforced Concrete Piers Using the Impact Load Method, *Proceedings of the International Conference on Nondestructive Testing of Concrete in the Infrastructure*, Dearborn, MI, pp. 378 - 390.

Wen, S. H. and Chung, D. D. L. (2000). Enhancing the Vibration Reduction Ability of Concrete by using Steel Reinforcement and Steel Surface Treatments, *Cement & Concrete Research*, **30**: 327–330.

Wolanski, A. J. (2004). Flexural Behavior of Reinforced and Prestressed Concrete Beams using Finite Element Analysis, MS Thesis of Science, Marquette University, Milwaukee, Wisconsin, USA.

Woodward, C., Minor, J., White, K. and Idriss, R. (1994). Nondestructive Evaluation of Fracture Critical Bridge, *Proceedings of the Nondestructive Testing Conference*, Structural Materials Technology, Atlantic City, NJ.

Xia, Y., Hao, H., Zanardo, G. and Deeks, A. (2006). Long Term Vibration Monitoring of an RC Slab: Temperature and Humidity Effect, *Journal of Structural Engineering*, **28**: 441-452.

Xia, Y., Hao, H., Zanardo, G. and Deeks, A. (2007). Dynamic Assessment of Shear Connectors in Slab-Girder Bridges, *Journal of Structural Engineering*, **27**(7): 1475-1486.

Yang, Z. J., Chen, J. F. and Proverbs, D. (2003). Finite Element Modeling of Concrete Cover Separation Failure in FRP Plated RC Beams, *Construction and Building Materials*, **17**: 3-13.

Yao, G.C., Chang, K.C. and Lee, G.C. (1992). Damage diagnosis of steel frames using vibrational signature analysis, *Journal of engineering mechanic*, ASCE, **118**(9), 1949-1961.

Yao, J. T. P. and Munse, W. H. (1962). *Low-Cycle Fatigue Behavior of Mild Steel*, Special Technical Publication Number 338, American Society for Testing and Materials, Philadelphia, PA.

Ye, L., Yue, Q., Zhao, S. and Li, Q. (2002). Shear Strength of Reinforced Concrete Columns Strengthened with Carbon Fiber Reinforced Plastic Sheet, *Journal of Structural Engineering*, **128**(12): 1527-1534.

Yeung W. T. and Smith J.W. (2005). Damage Detection in Bridges Using Neural Networks for Pattern Recognition of Vibration Signatures, *Journal of Structural Engineering*, **27**(5): 685-698.

APENDIX A

VIBRATION RESPONSE DATA

APPENDIX A

VIBRATION RESPONSE DATA

Control Frame 1

Initial state at a load of 0 kN

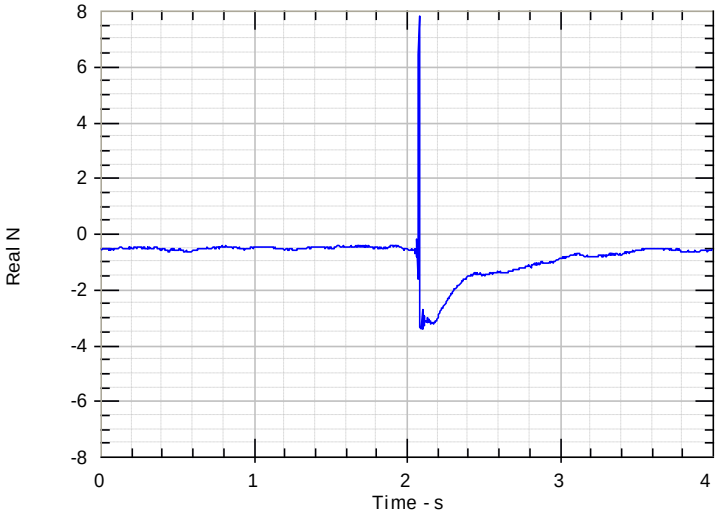

Impact force at top floor of Control Frame 1

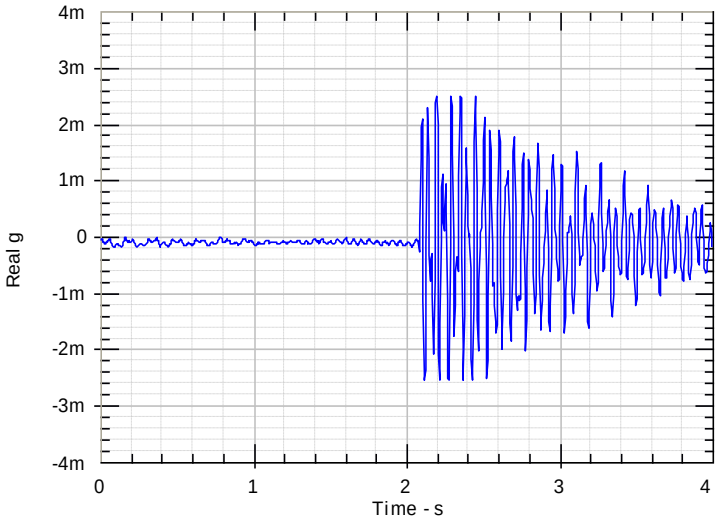

Acceleration response at first floor

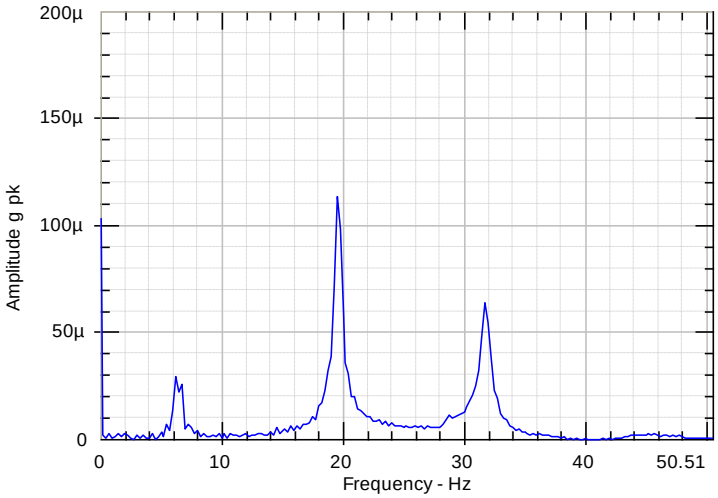

Acceleration response spectrum at first floor

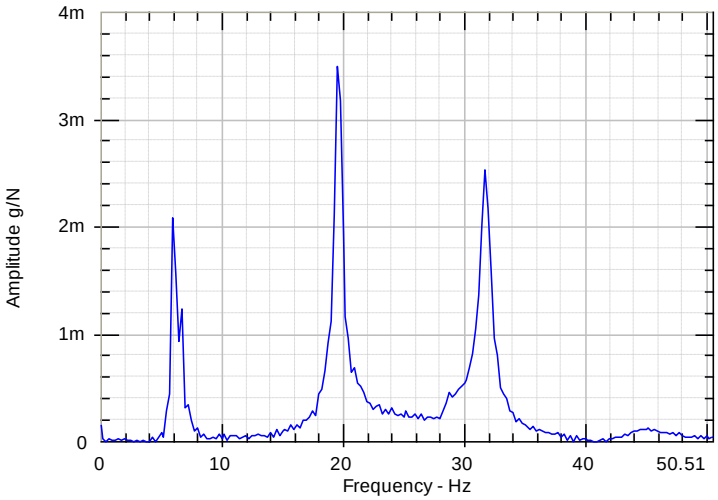

Frequency response function at first floor

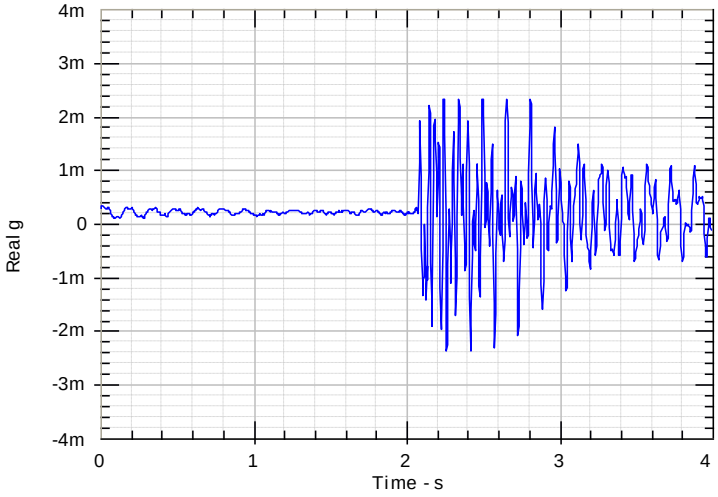

Acceleration response at second floor

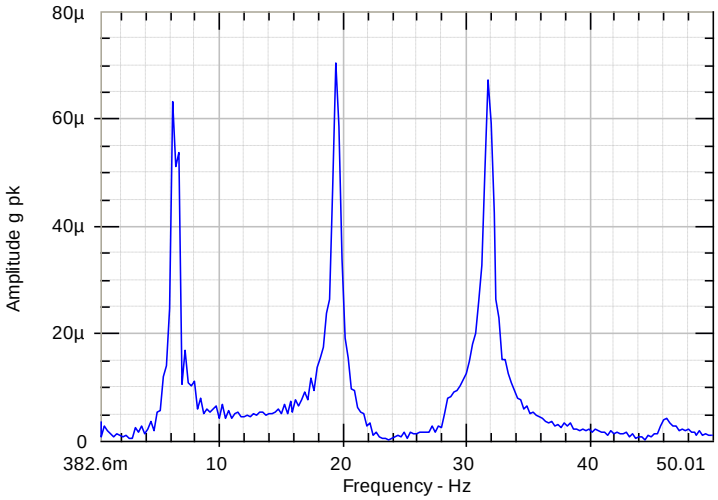

Acceleration response spectrum at second floor

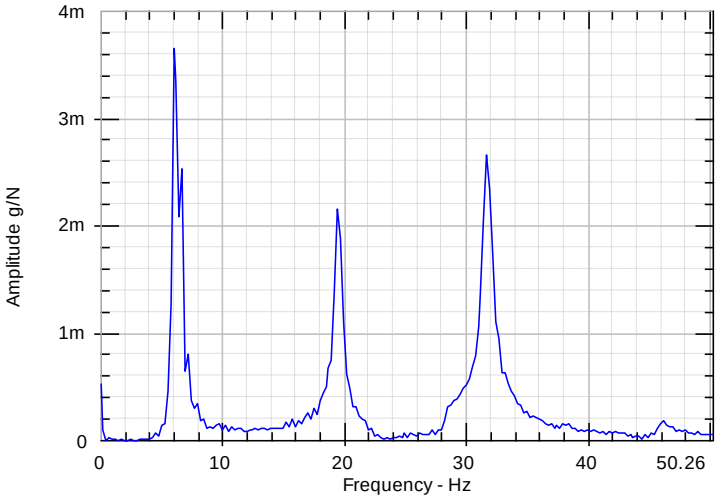

Frequency response function at second floor

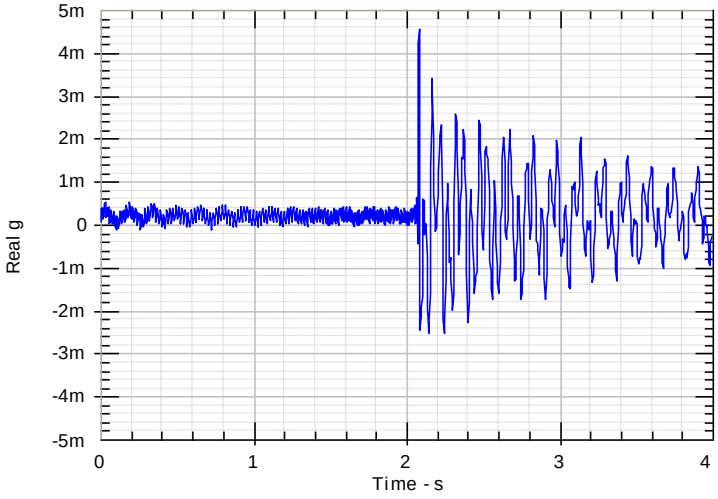

Acceleration response at top floor

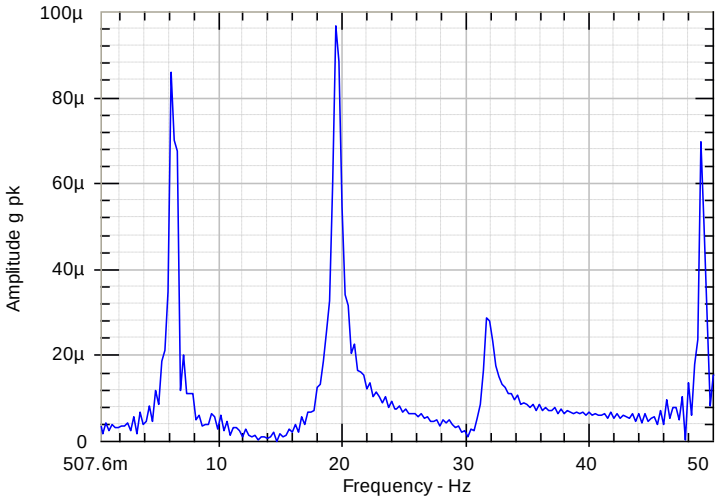

Acceleration response spectrum at third floor

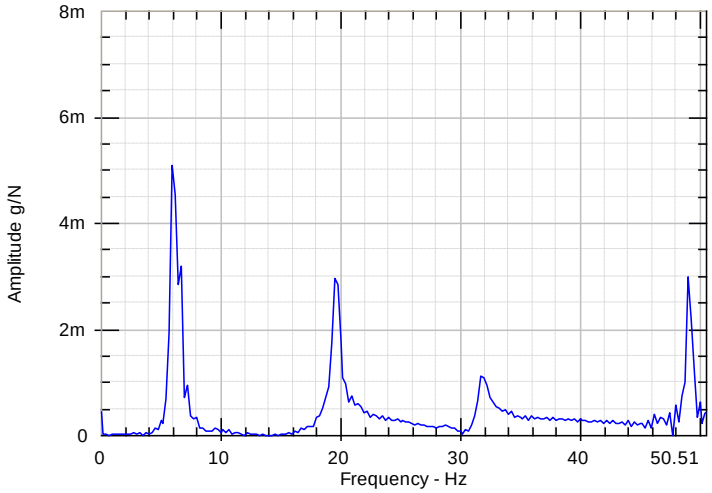

Frequency response function at top floor

Final state at a load of 16 kN

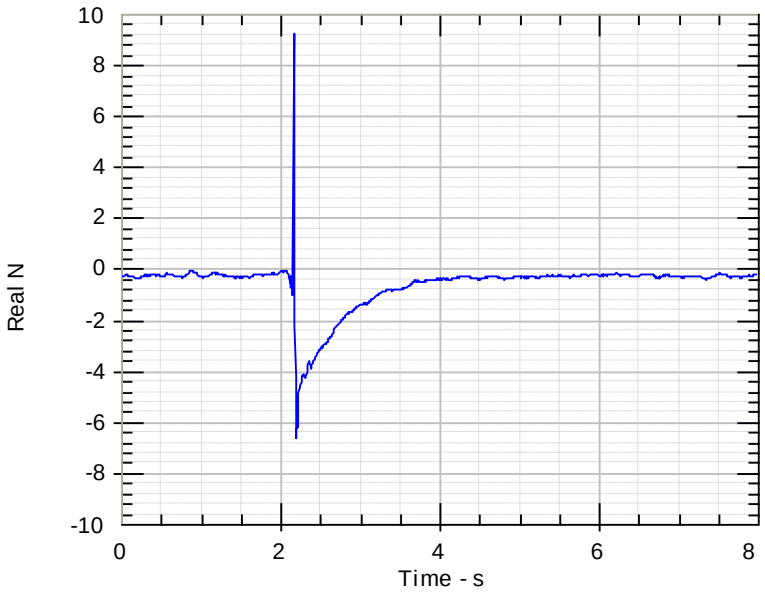

Impact force at top floor of Control Frame 1

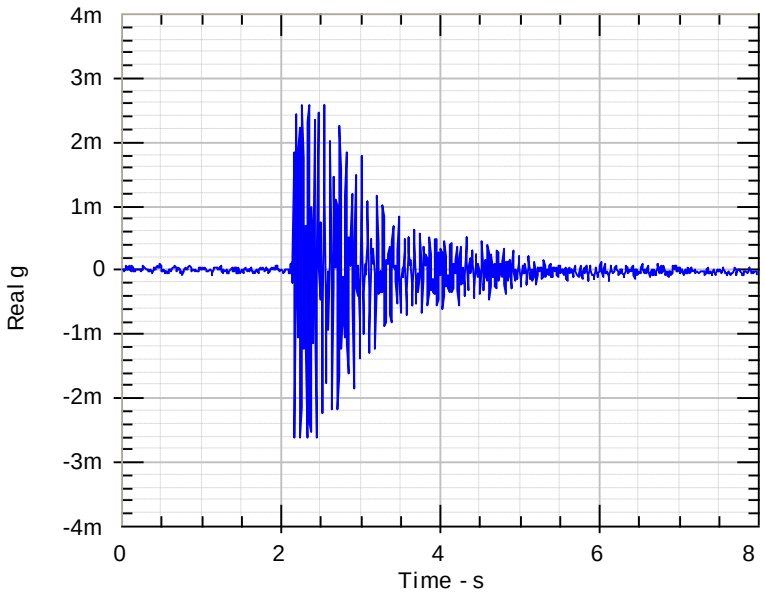

Acceleration response at first floor

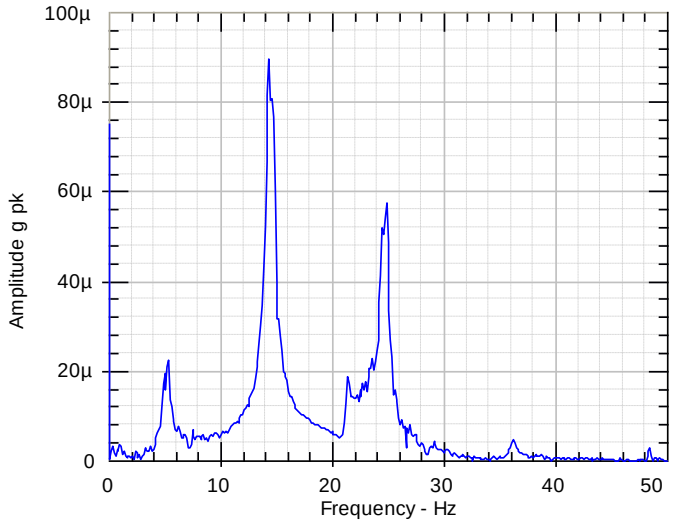

Acceleration response spectrum at first floor

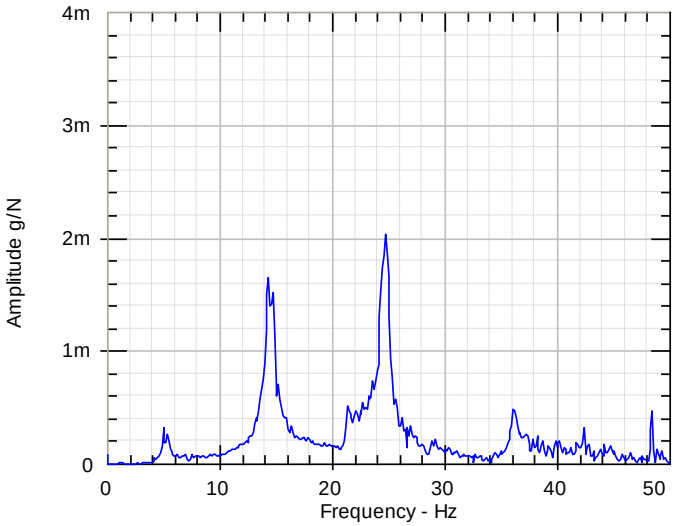

Frequency response function at first floor

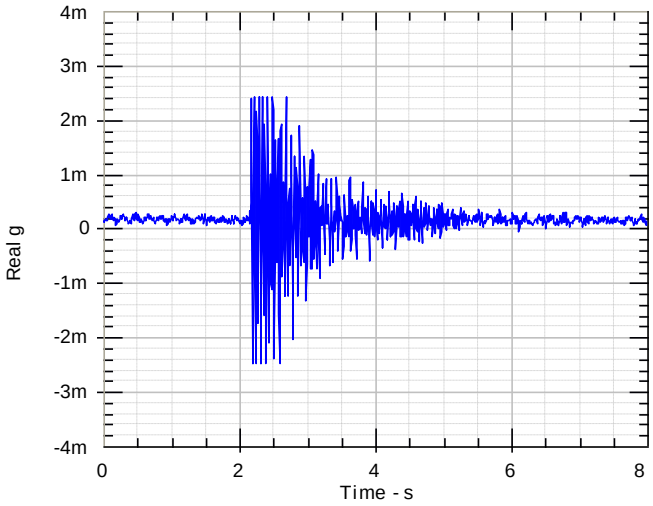

Acceleration response at second floor

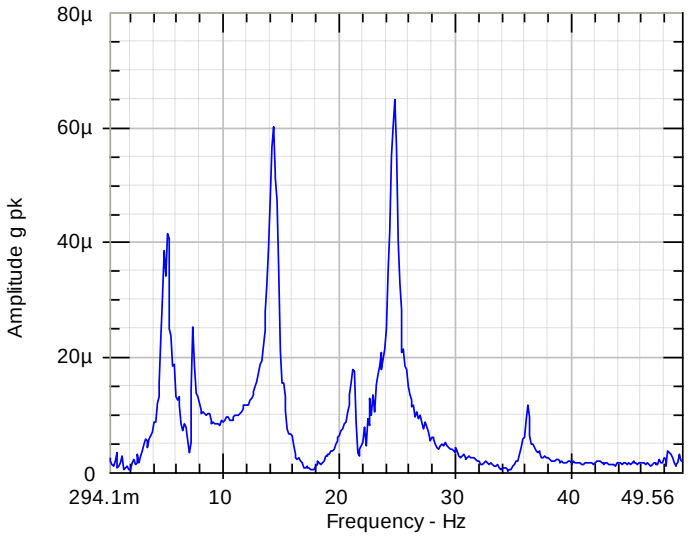

Acceleration response spectrum at second floor

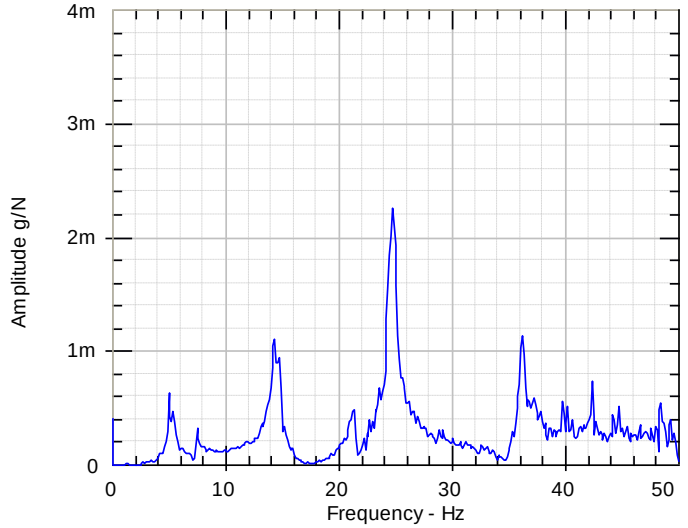

Frequency response function at second floor

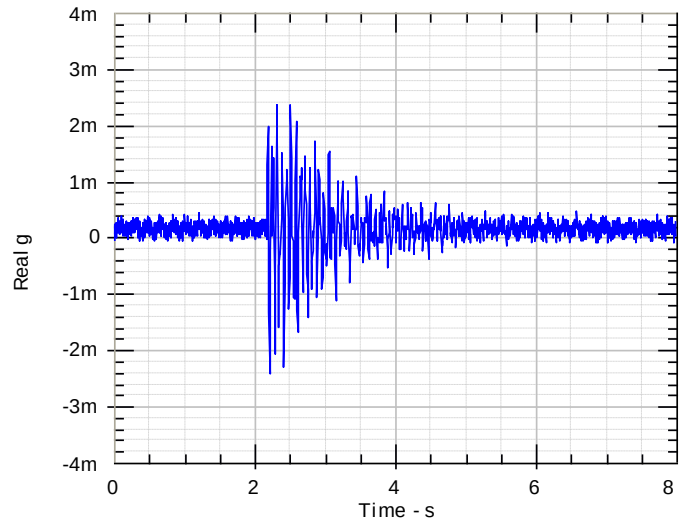

Acceleration response at top floor

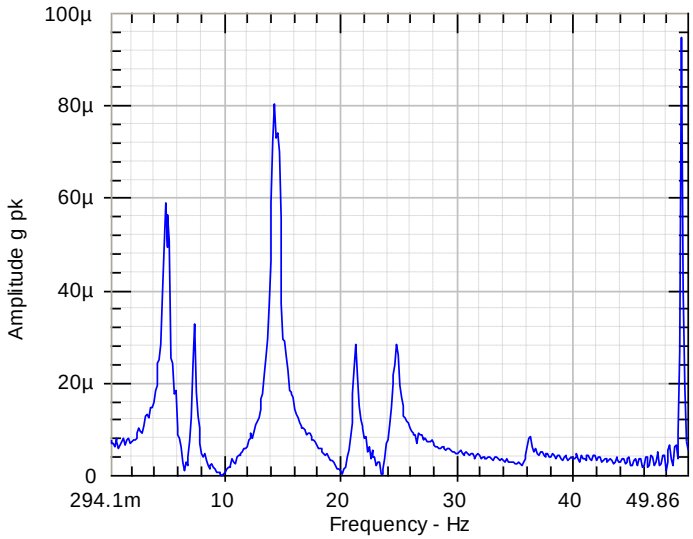

Acceleration response spectrum at top floor

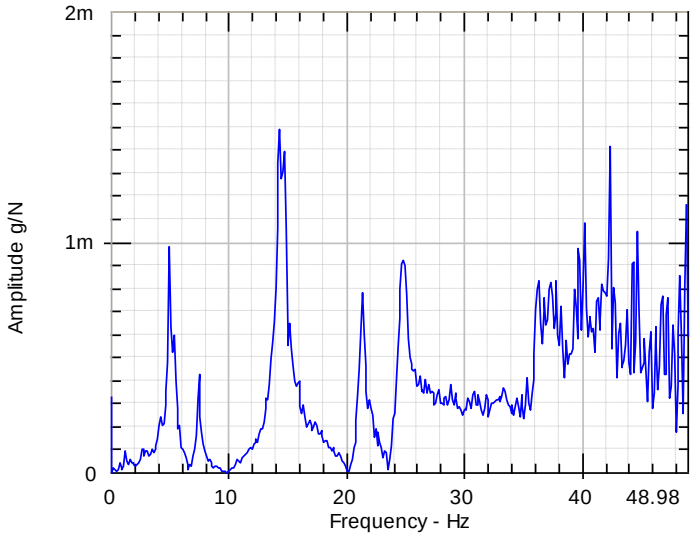

Frequency response function at top floor

Retrofitted Frame 1

Initial state at a load of 0 kN

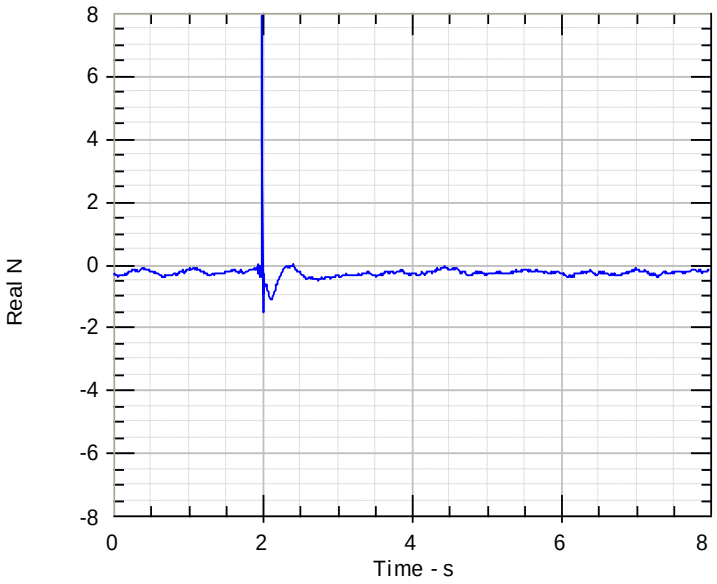

Impact force at top floor of Retrofitted Frame 1

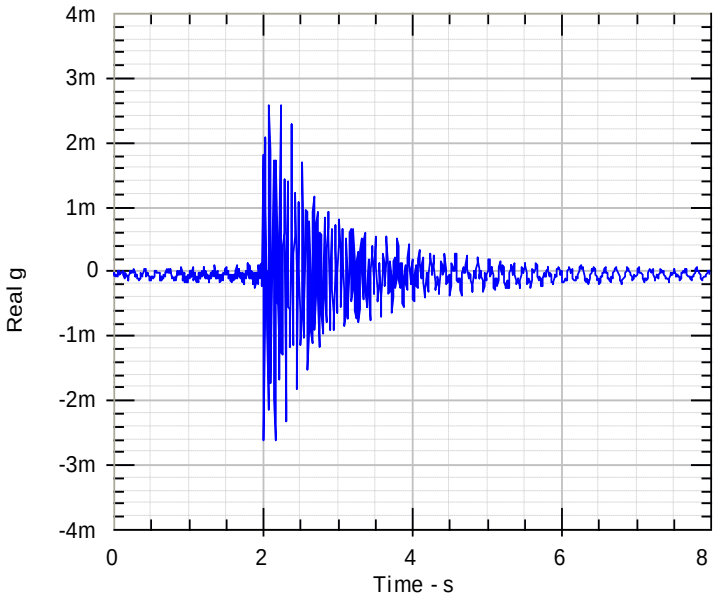

Acceleration response at first floor

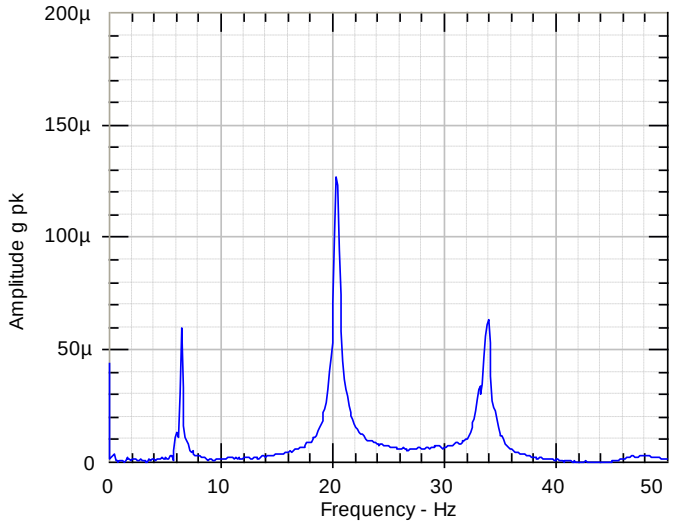

Acceleration response spectrum at first floor

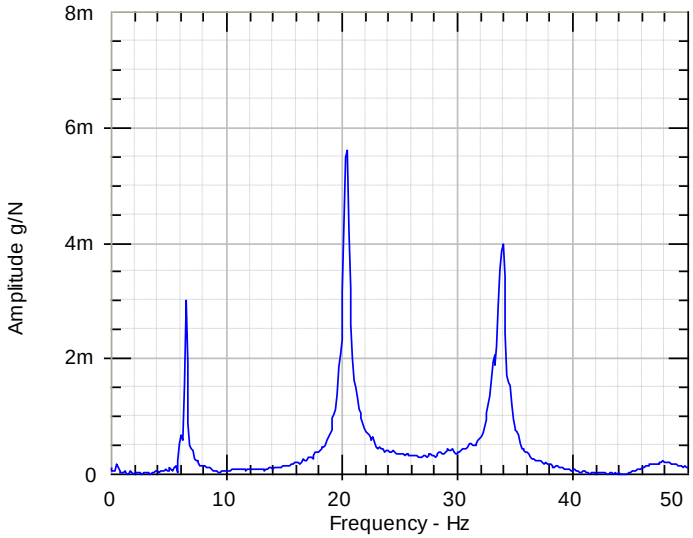

Frequency response function at first floor

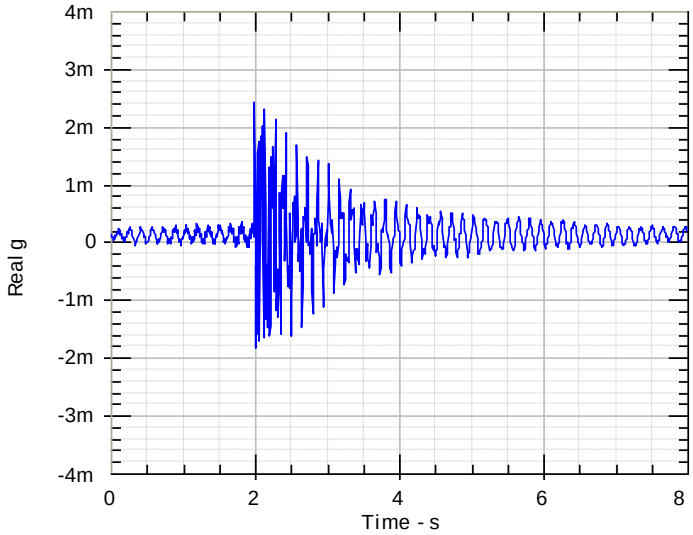

Acceleration response at second floor

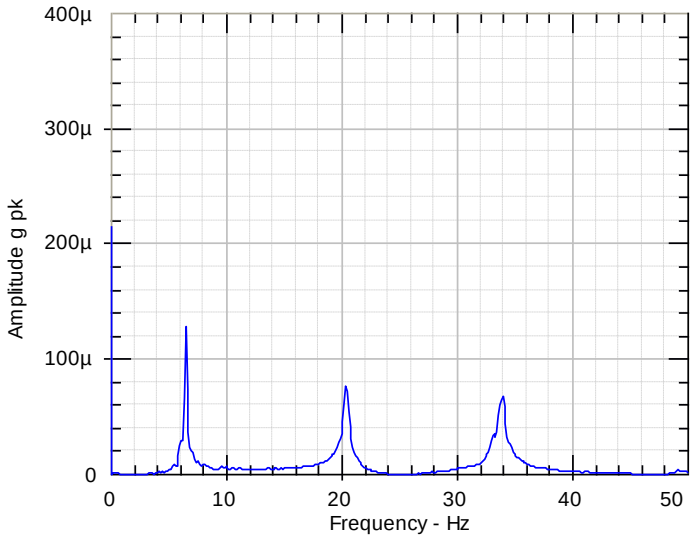

Acceleration response spectrum at second floor

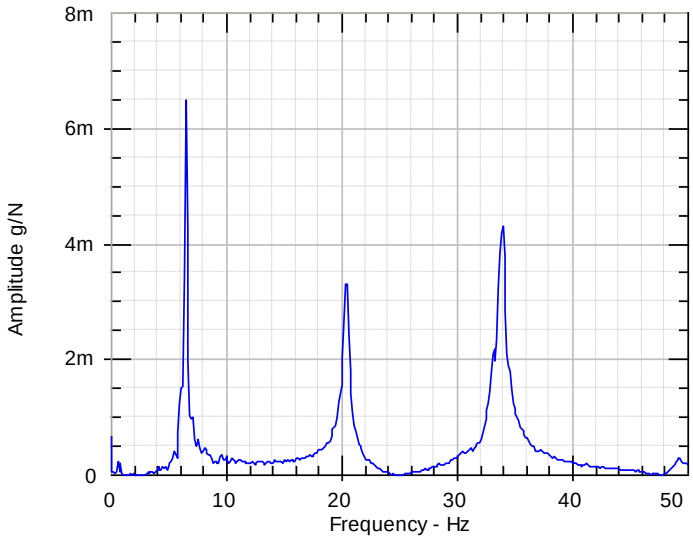

Frequency response function at second floor

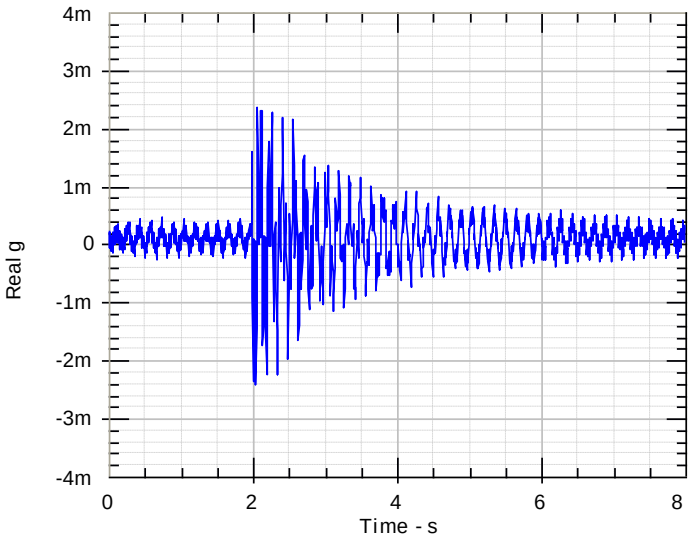

Acceleration response at top floor

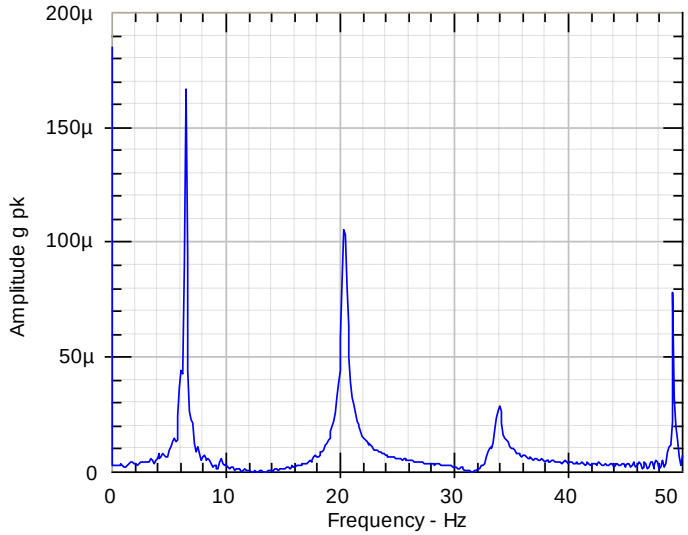

Acceleration response spectrum at top floor

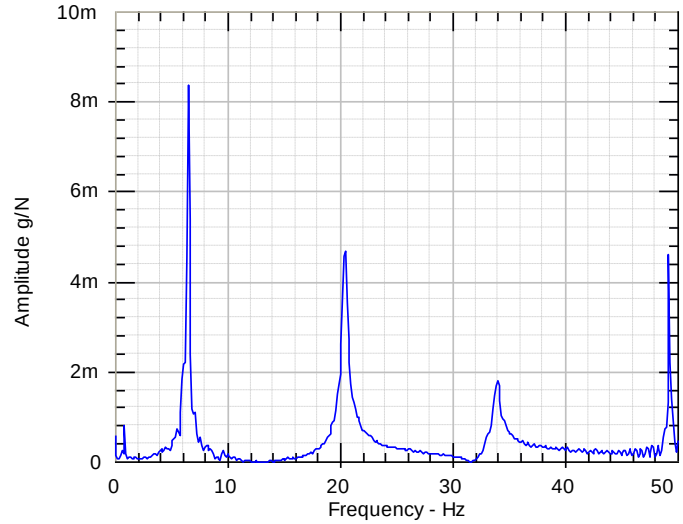

Frequency response function at top floor

Final state at a load of 25 kN

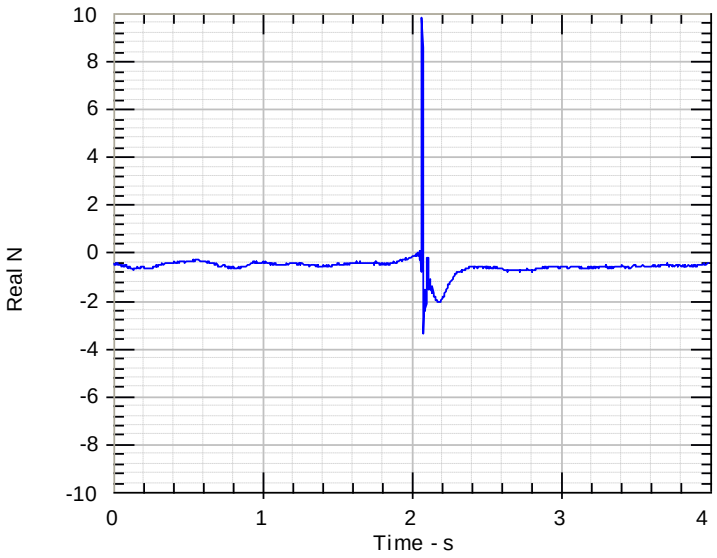

Impact force at top floor of Retrofitted Frame 1

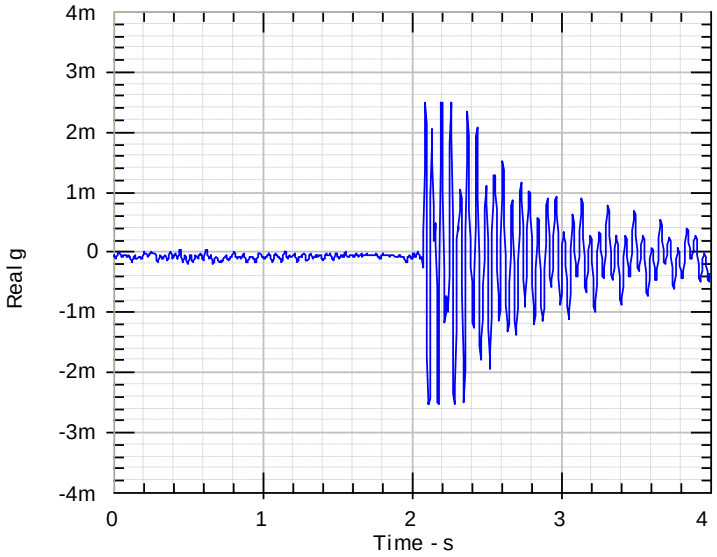

Acceleration response at first floor

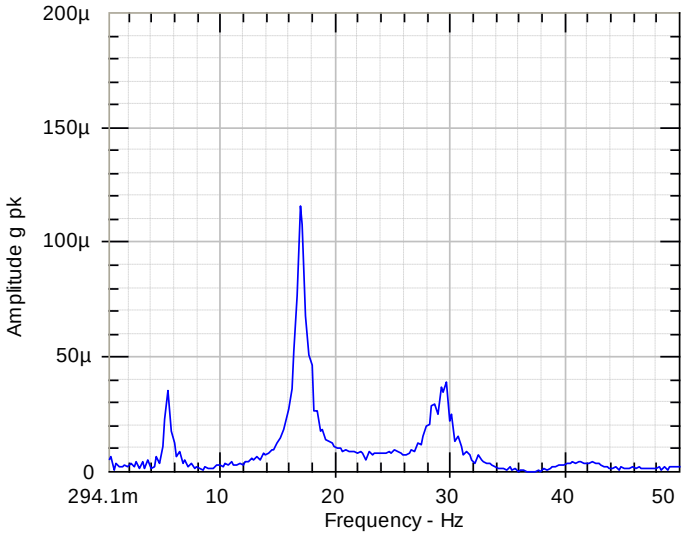

Acceleration response spectrum at first floor

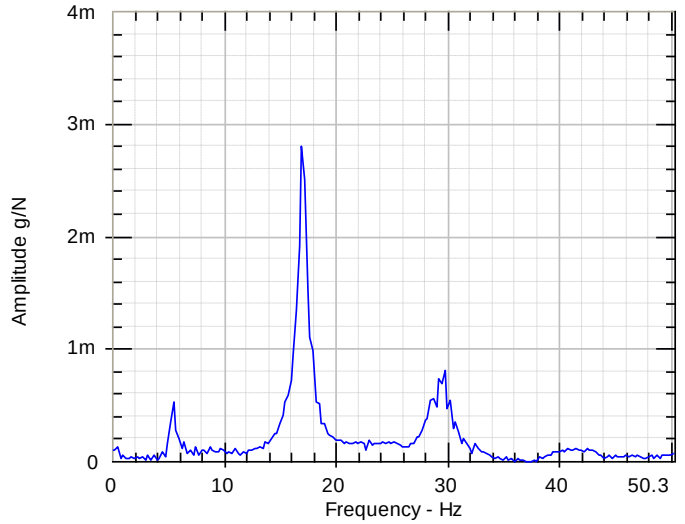

Frequency response function at first floor

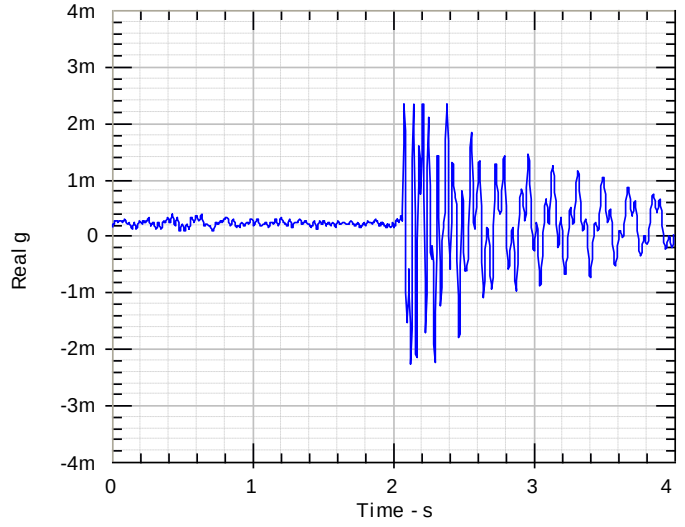

Acceleration response at second floor

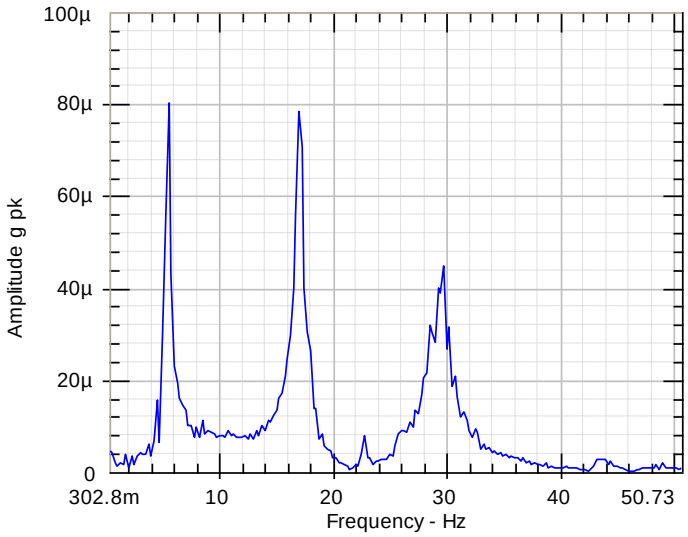

Acceleration response spectrum at second floor

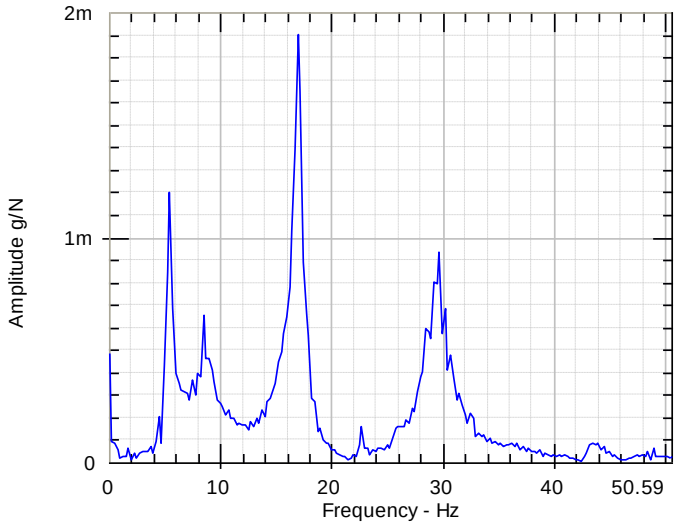

Frequency response function at second floor

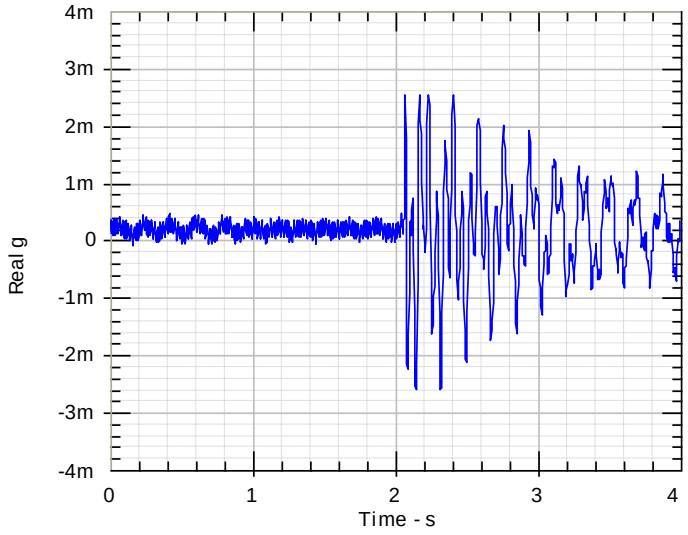

Acceleration response at top floor

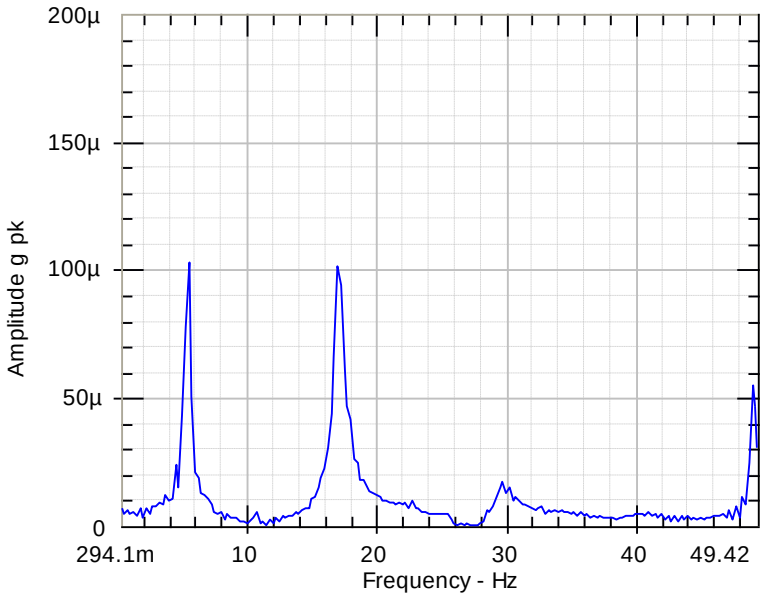

Acceleration response spectrum at top floor

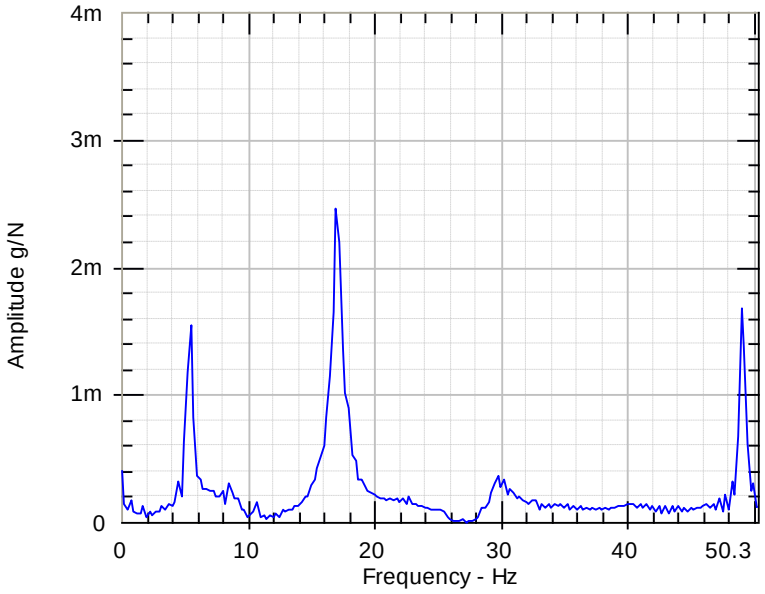

Frequency response function at top floor

Control Frame 2

Initial state at a load of 0 kN

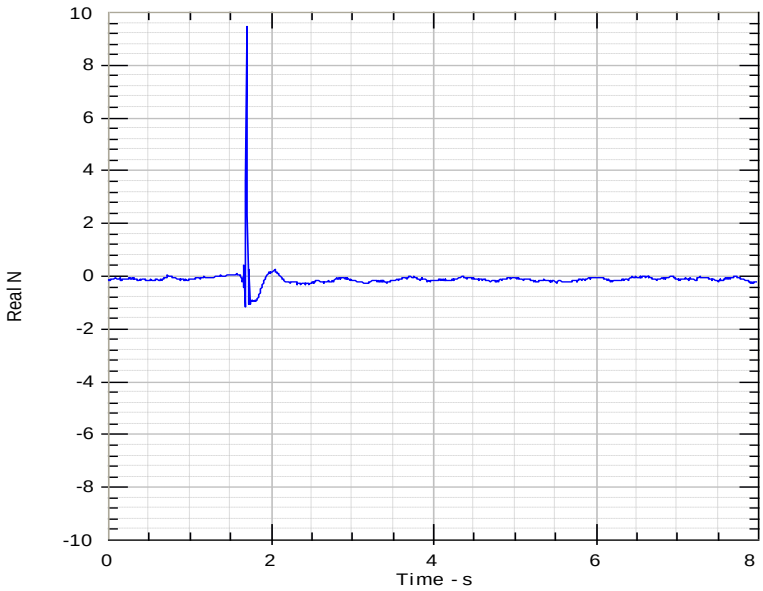

Impact force at top floor of Control Frame 2

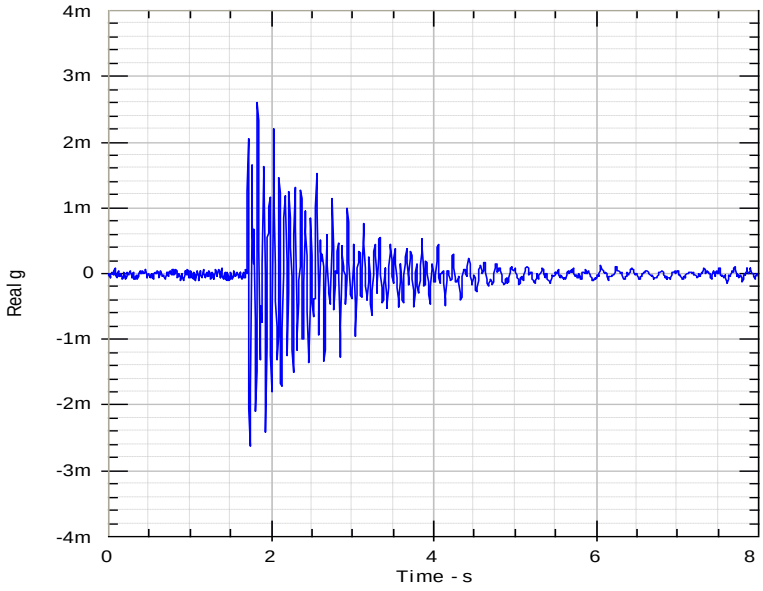

Acceleration response at first floor

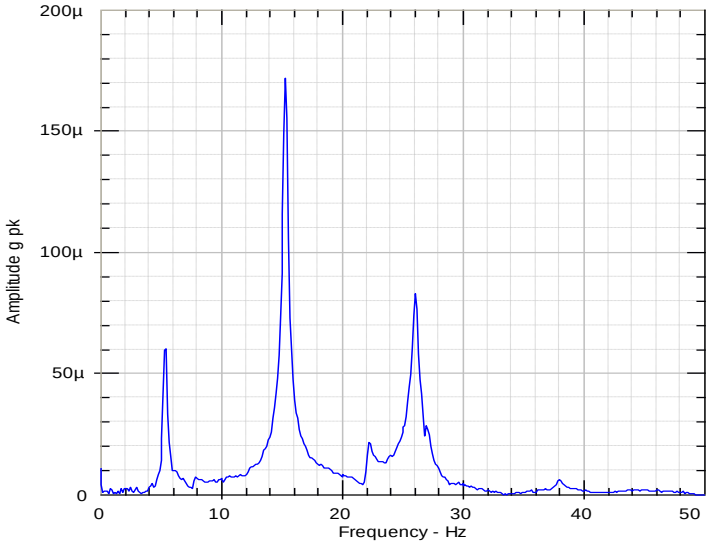

Acceleration response spectrum at first floor

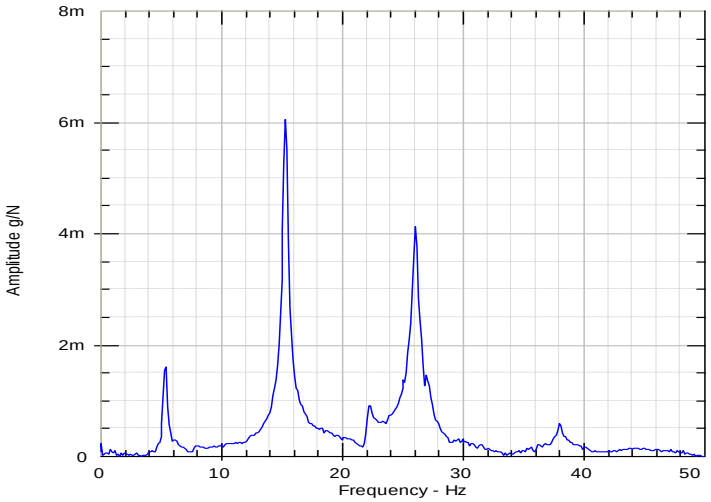

Frequency response function at first floor

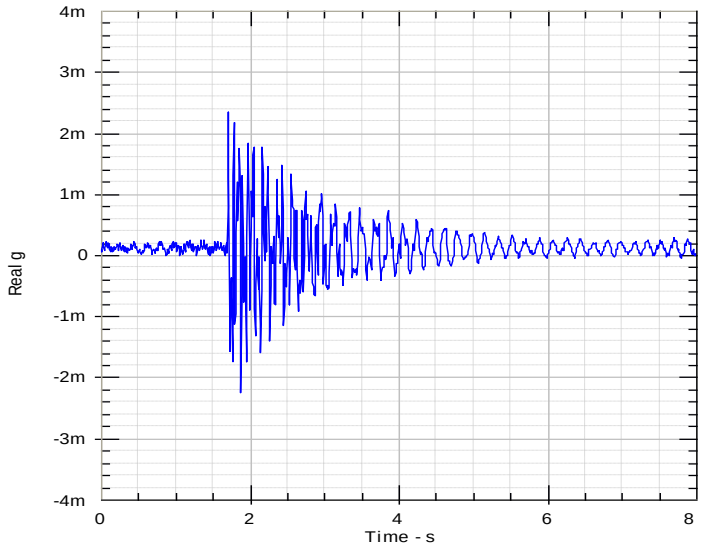

Acceleration response at second floor

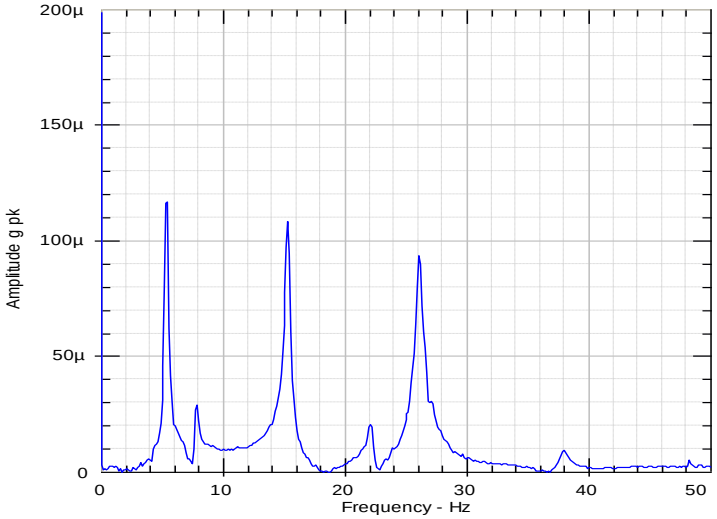

Acceleration response spectrum at second floor

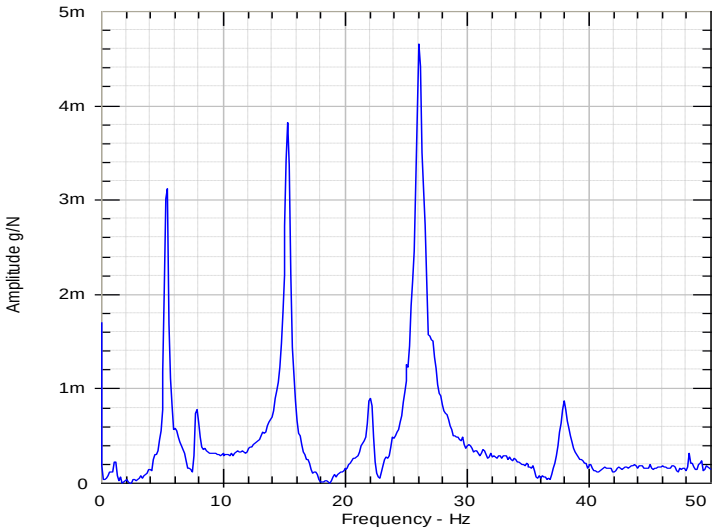

Frequency response function at second floor

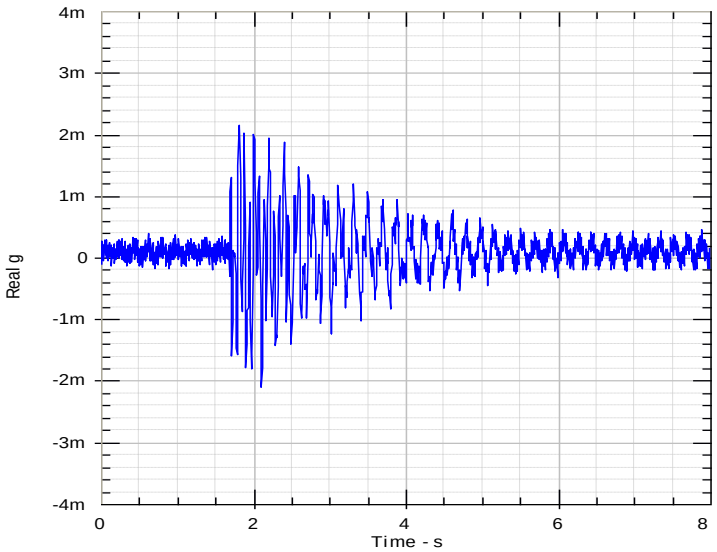

Acceleration response at top floor

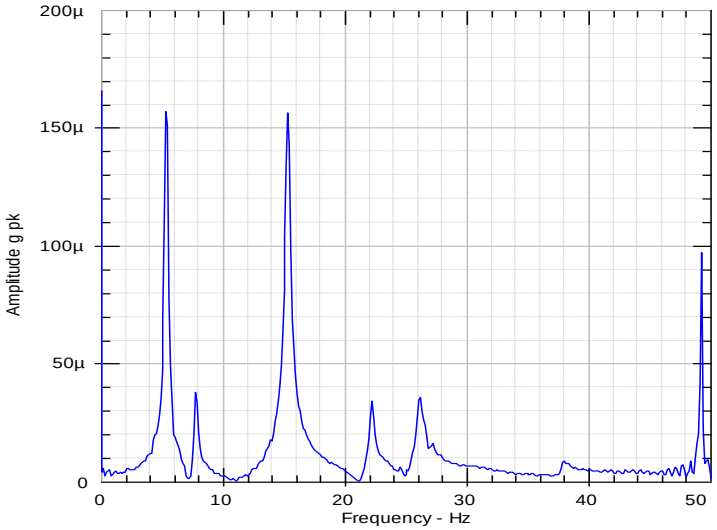

Acceleration response spectrum at top floor

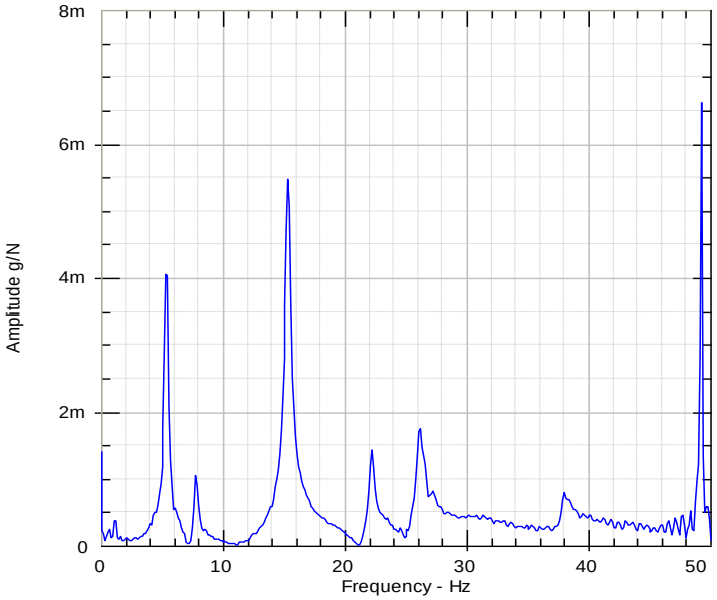

Frequency response function at top floor

Final state at a load of 11.5 kN

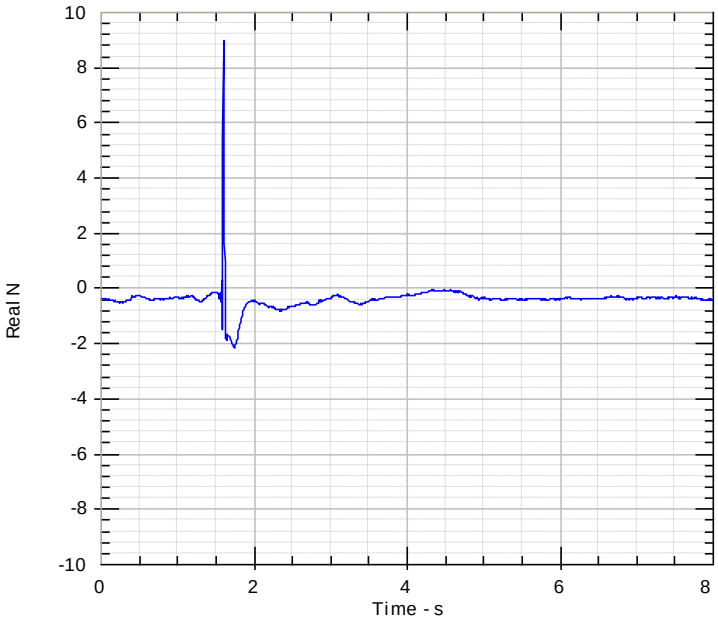

Impact force at top floor of Control Frame 2

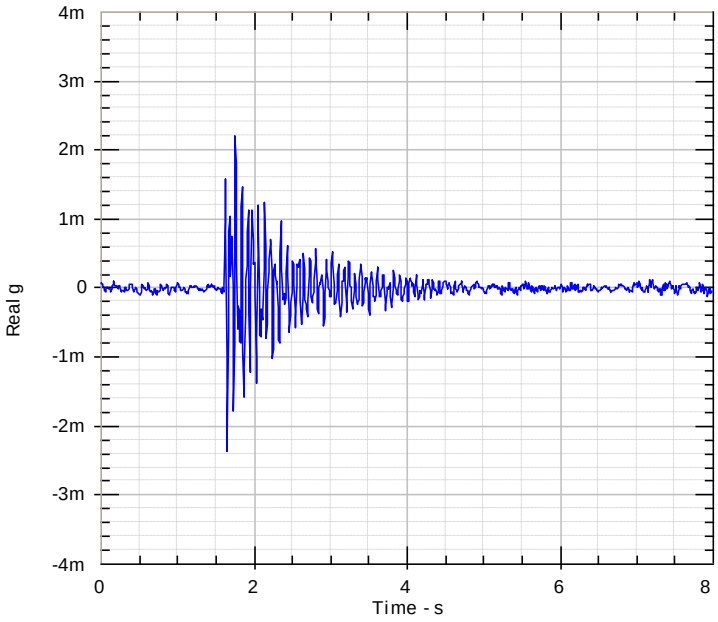

Acceleration response at first floor

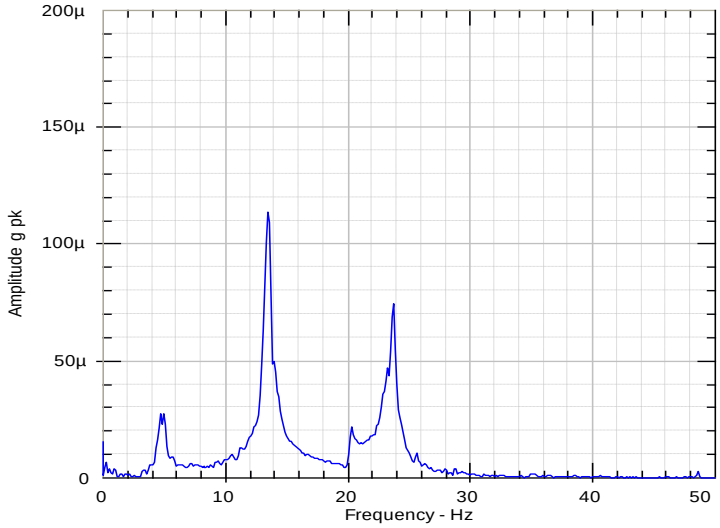

Acceleration response spectrum at first floor

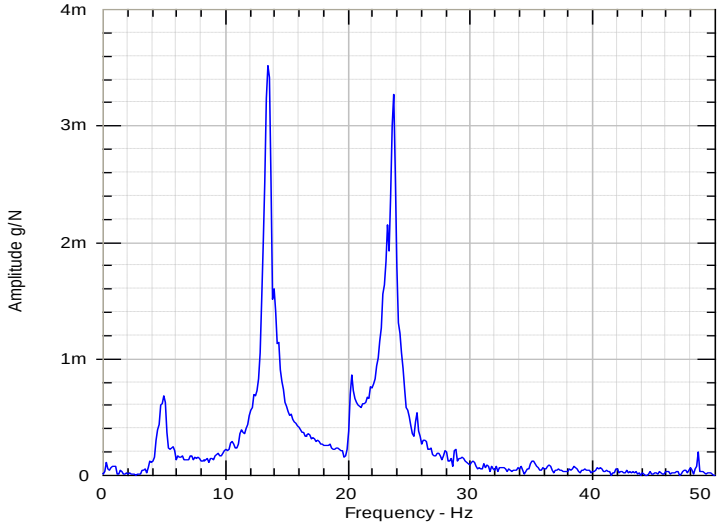

Frequency response function at first floor

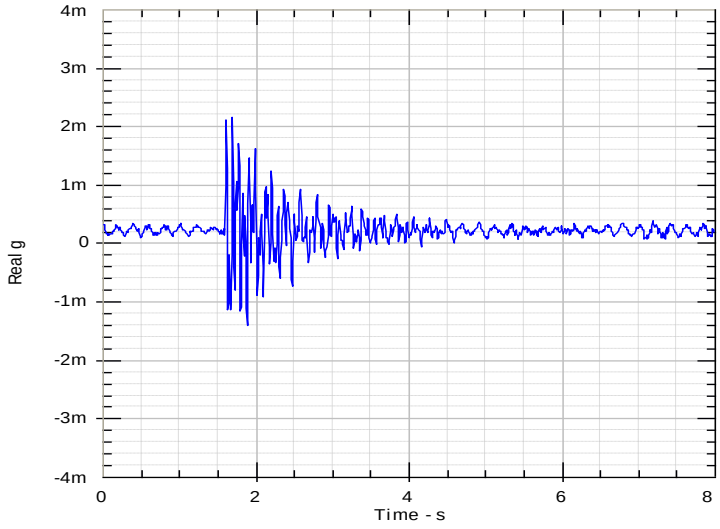

Acceleration response at second floor

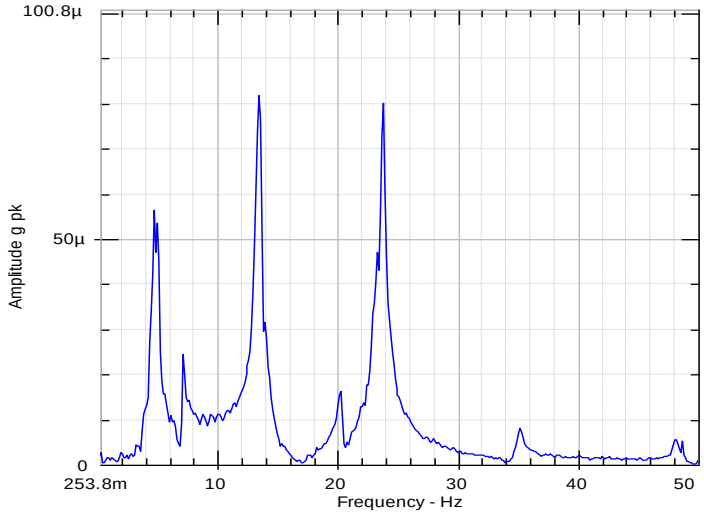

Acceleration response spectrum at second floor

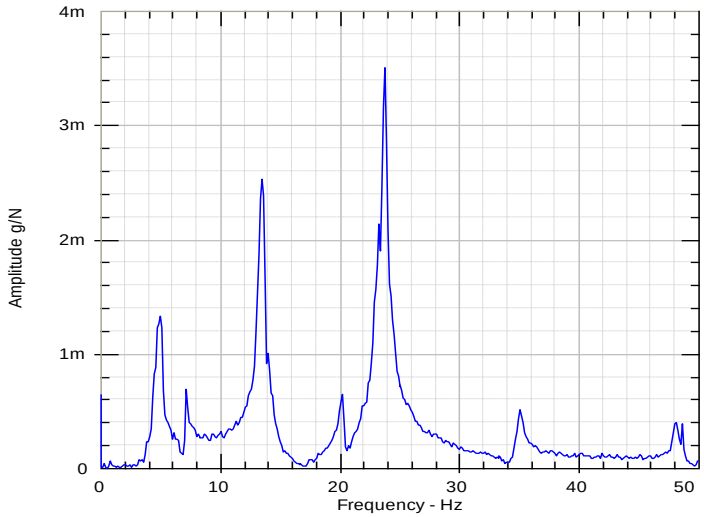

Frequency response function at second floor

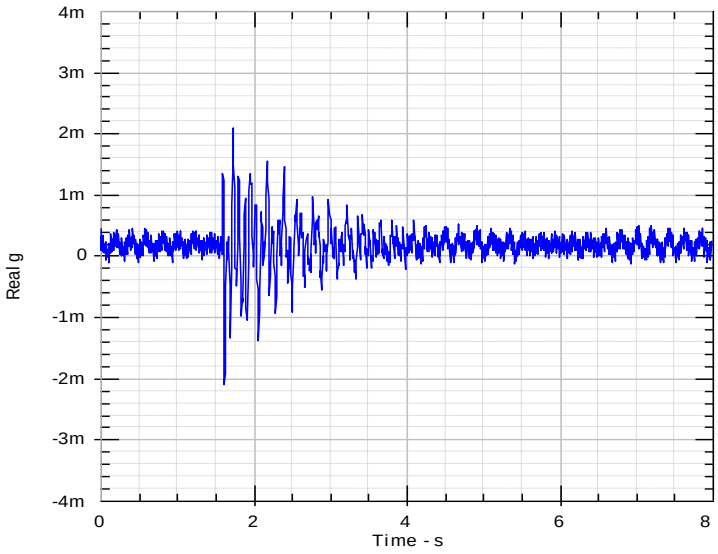

Acceleration response at top floor

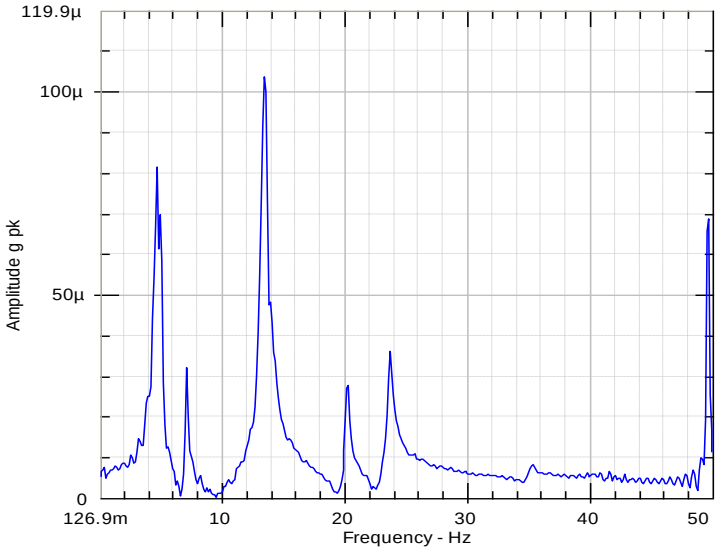

Acceleration response spectrum at top floor

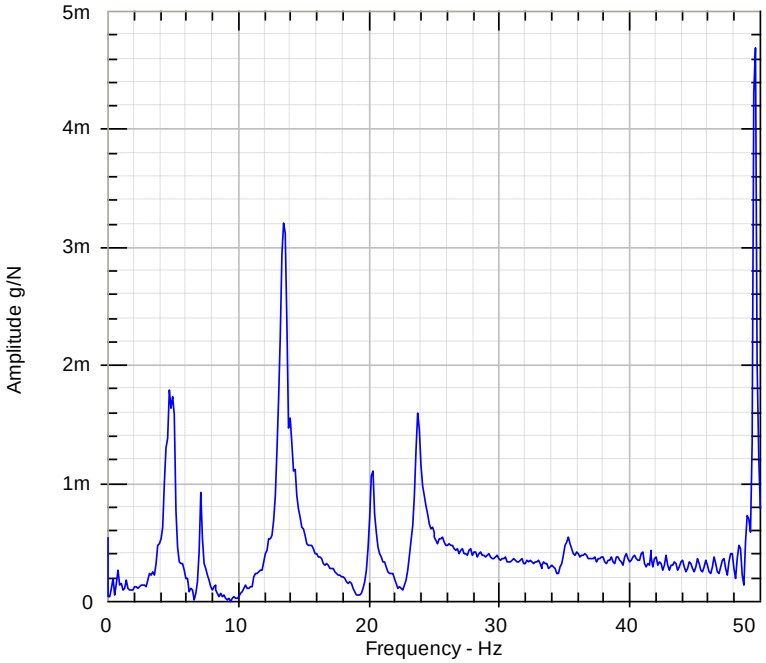

Frequency response function at top floor

Retrofitted Frame 2

Initial state at a load of 0 kN

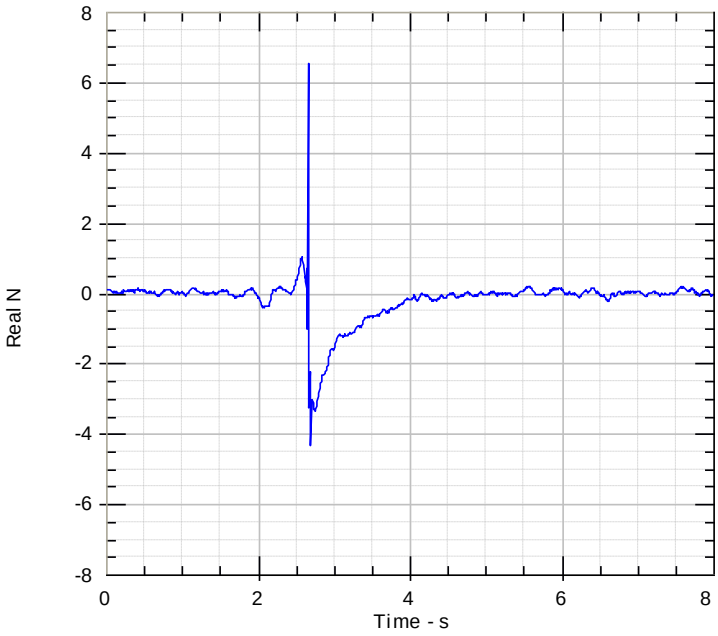

Impact force at top floor of Retrofitted Frame 2

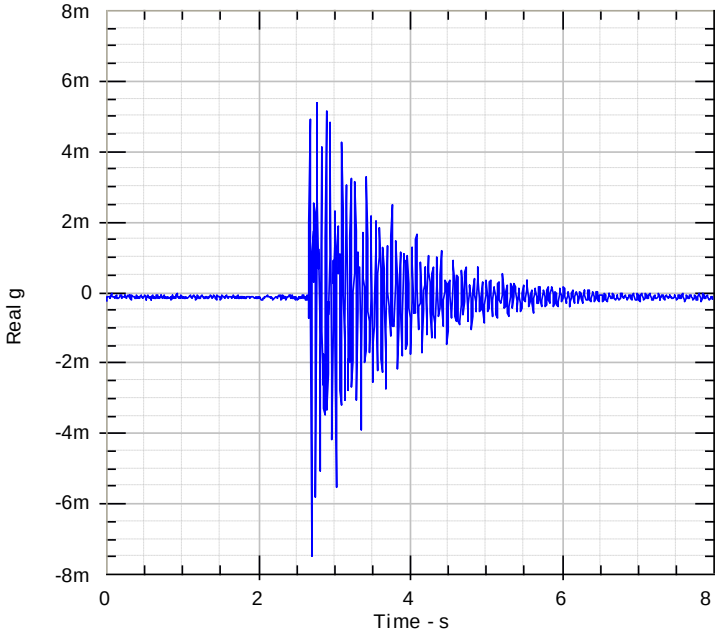

Acceleration response at first floor

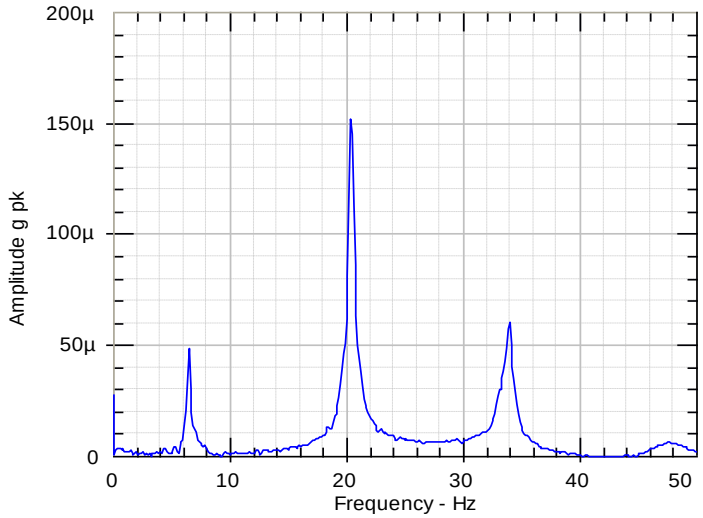

Acceleration response spectrum at first floor

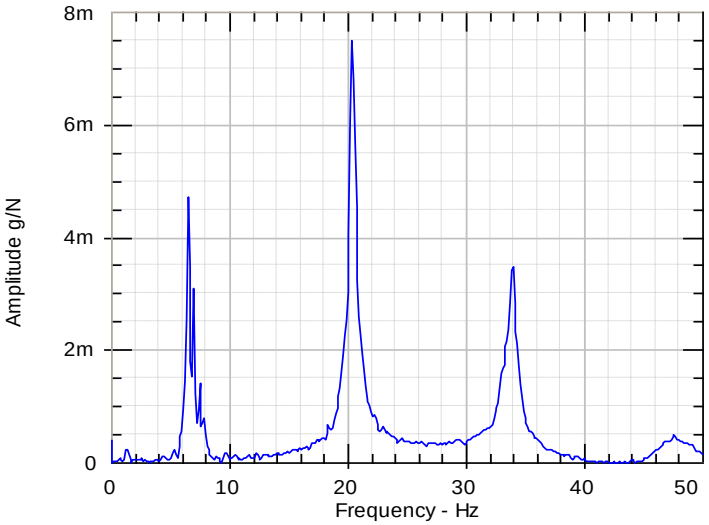

Frequency response function at first floor

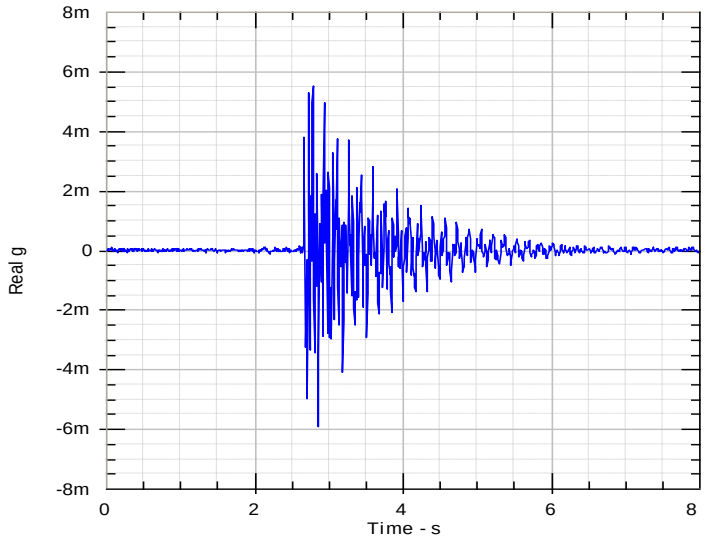

Acceleration response at second floor

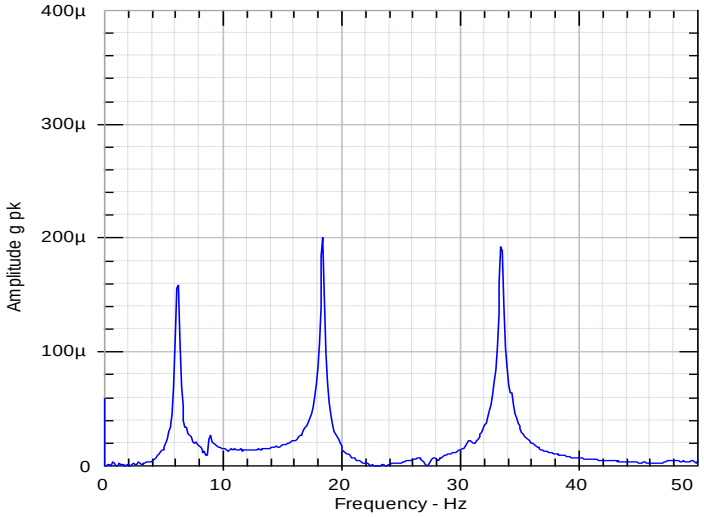

Acceleration response spectrum at second floor

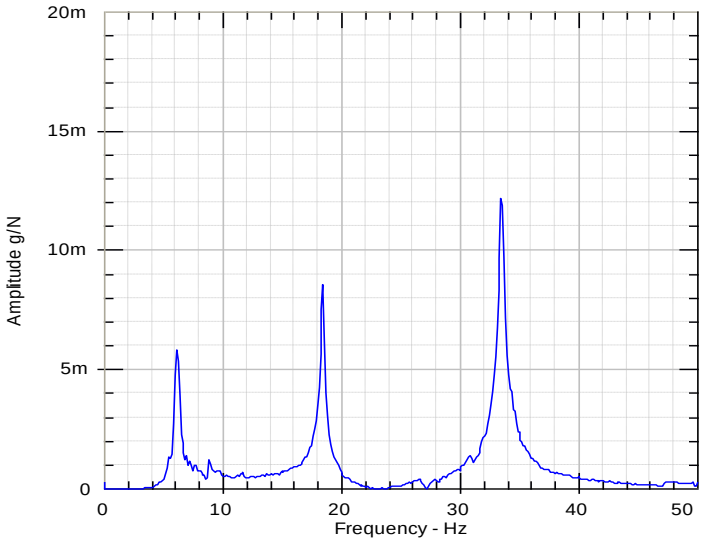

Frequency response function at second floor

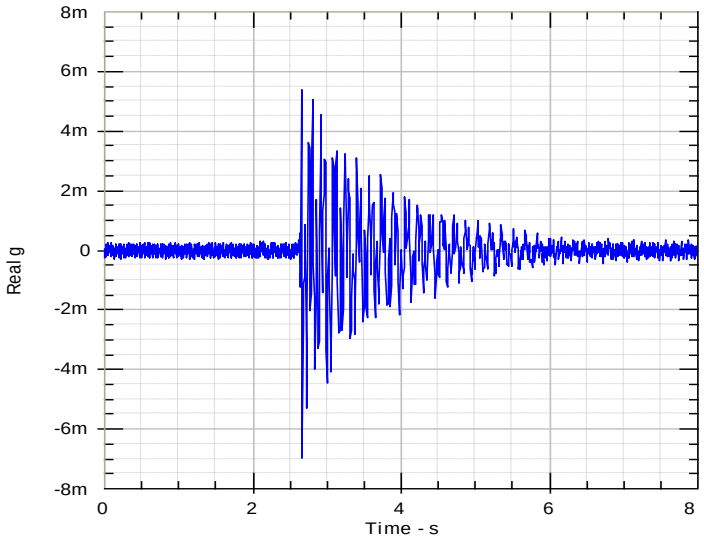

Acceleration response at top floor

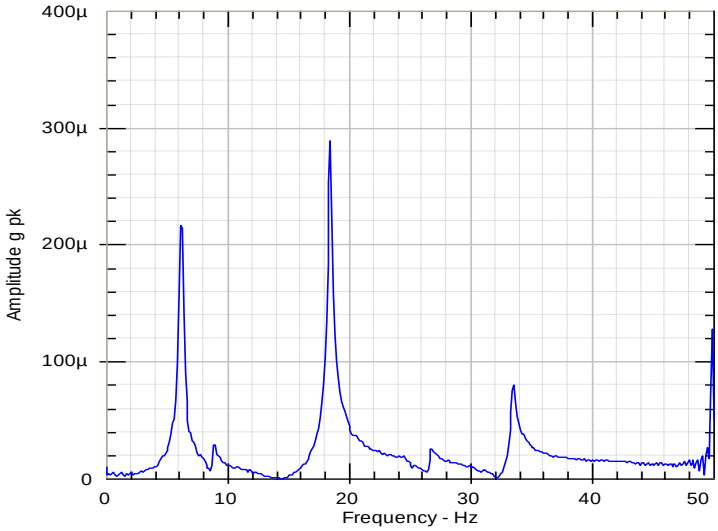

Acceleration response spectrum at top floor

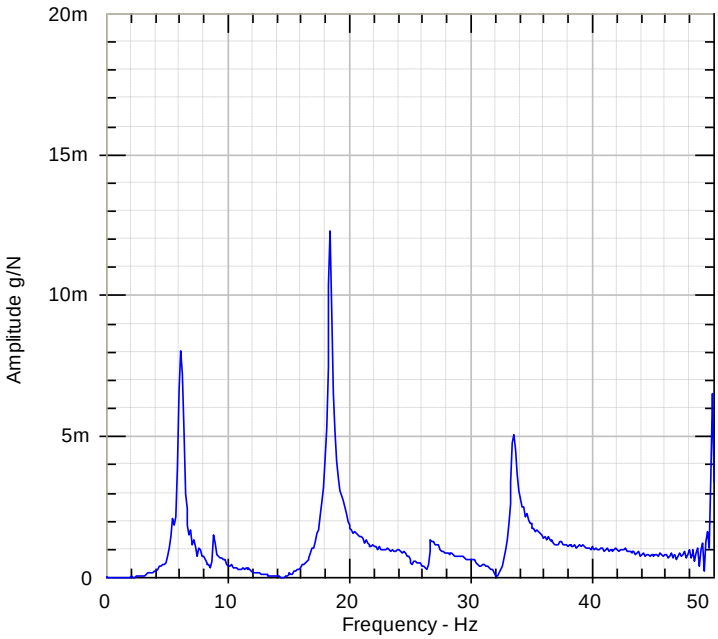

Frequency response function at top floor

Final state at a load of 26 kN

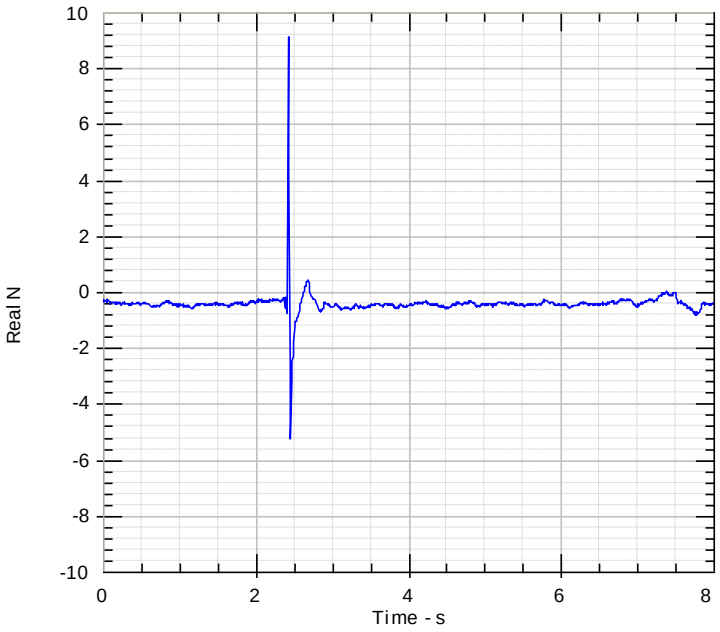

Impact force at top floor of Retrofitted Frame 2

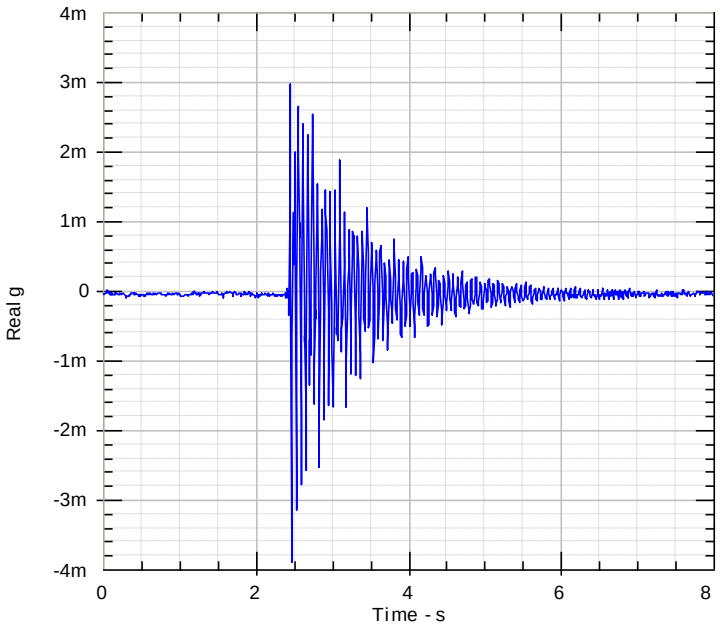

Acceleration response at first floor

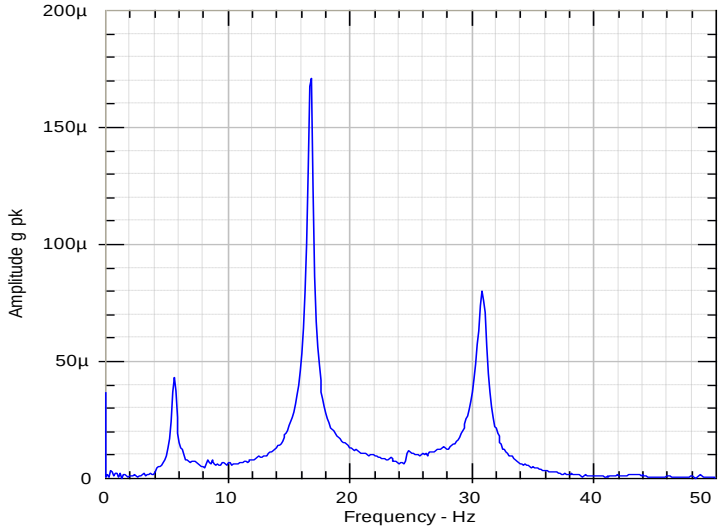

Acceleration response spectrum at first floor

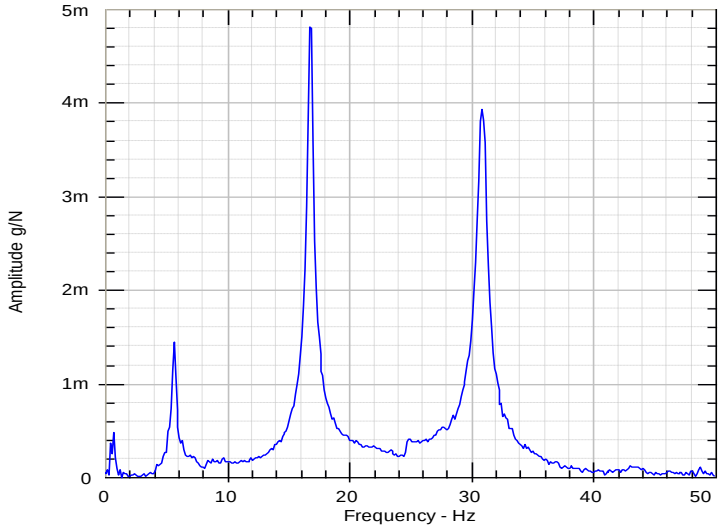

Frequency response function at first floor

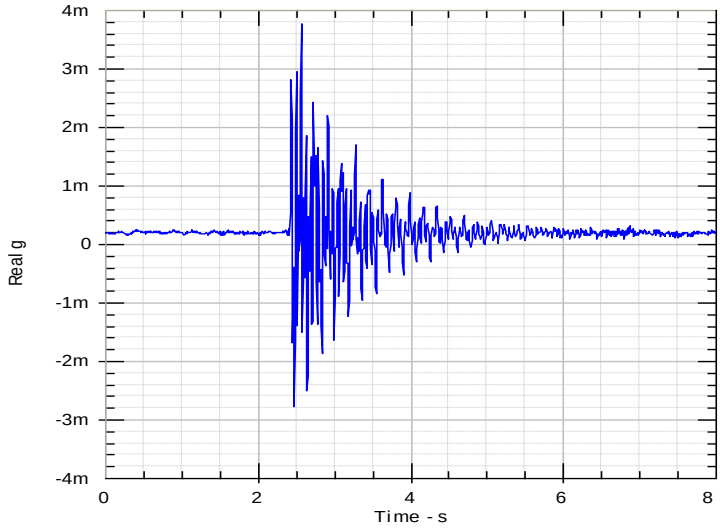

Acceleration response at second floor

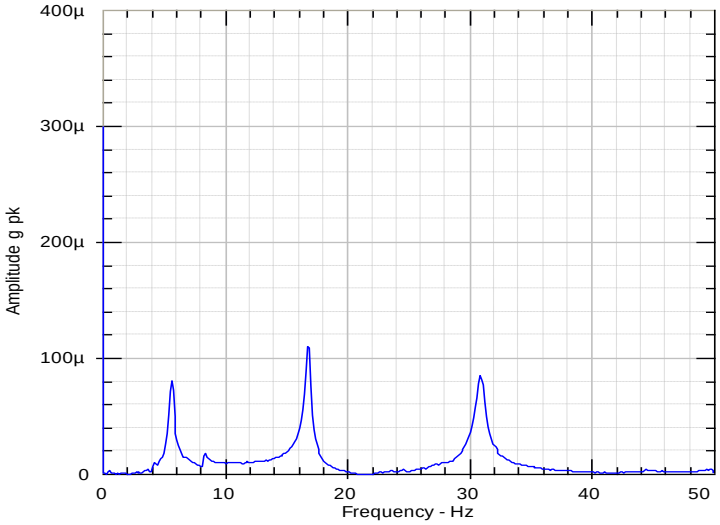

Acceleration response spectrum at second floor

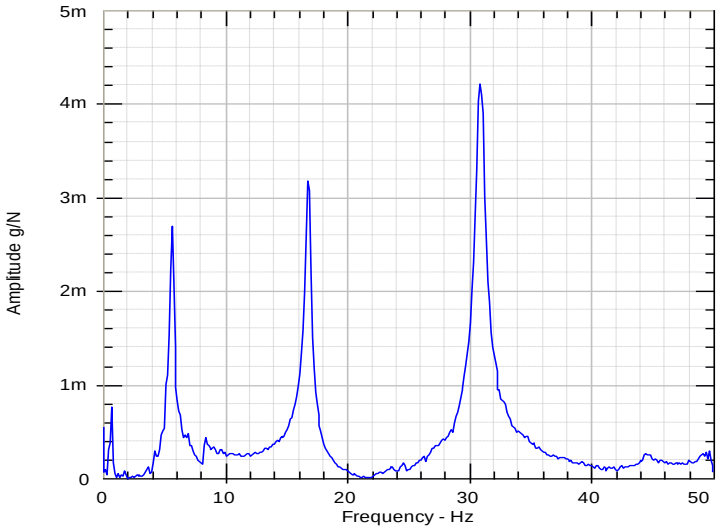

Frequency response function at second floor

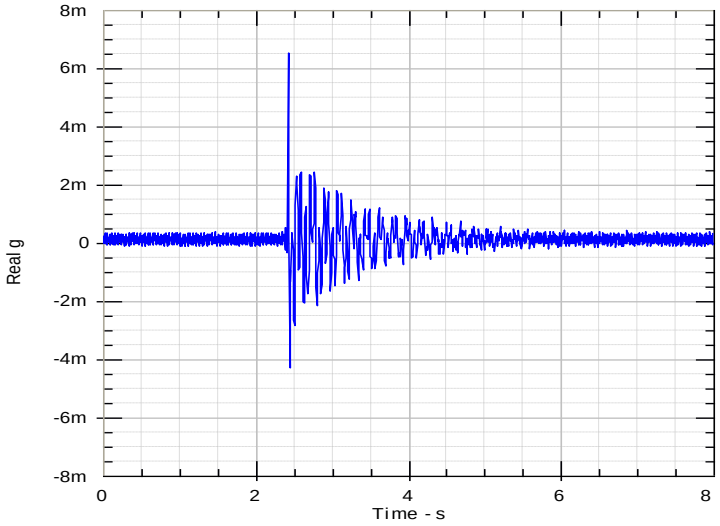

Acceleration response at top floor

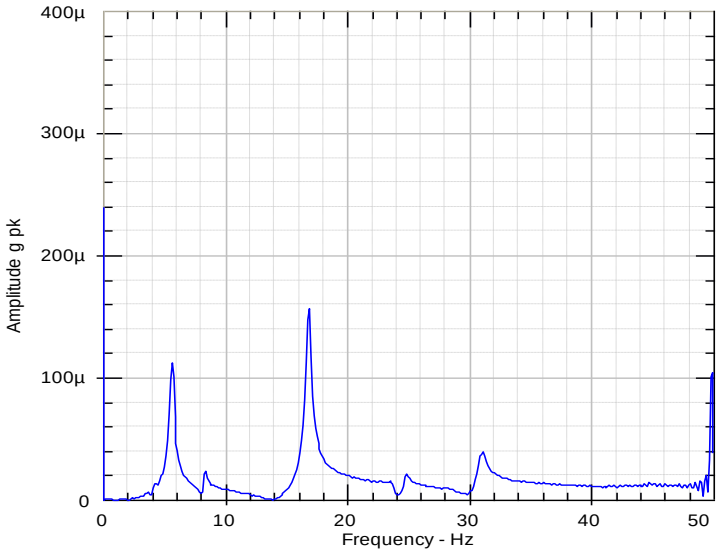

Acceleration response spectrum at top floor

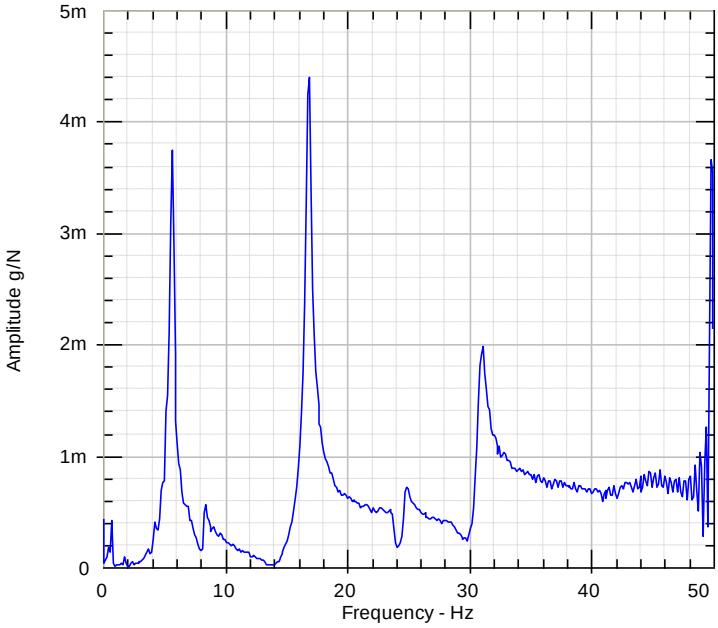

Frequency response function at top floor

Control Frame 3

Initial state at a load of 0 kN

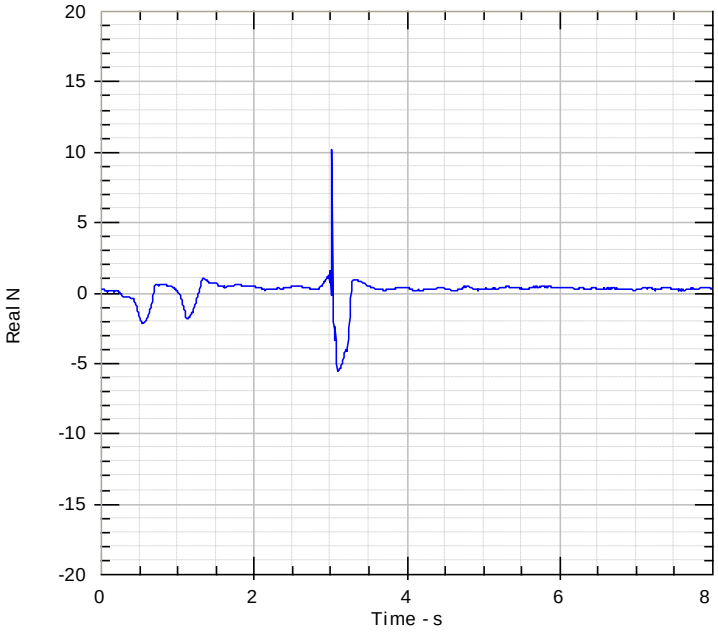

Impact force at top floor of Control Frame 3

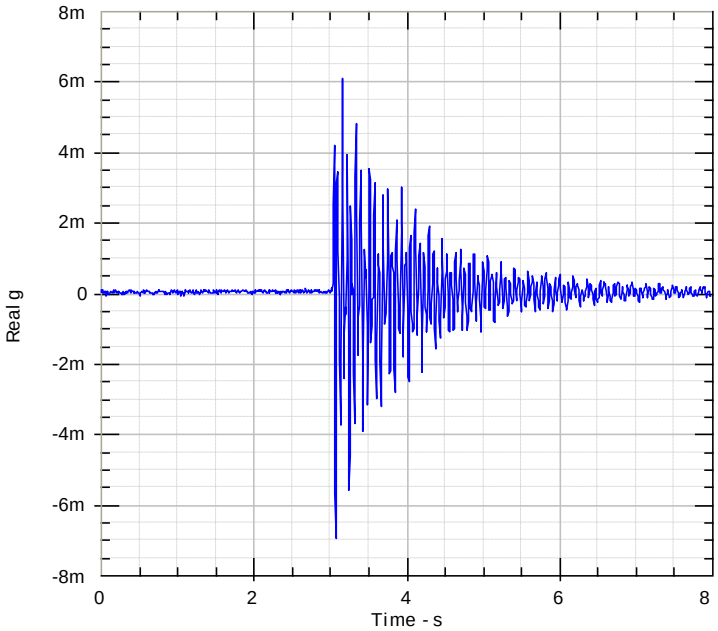

Acceleration response at first floor

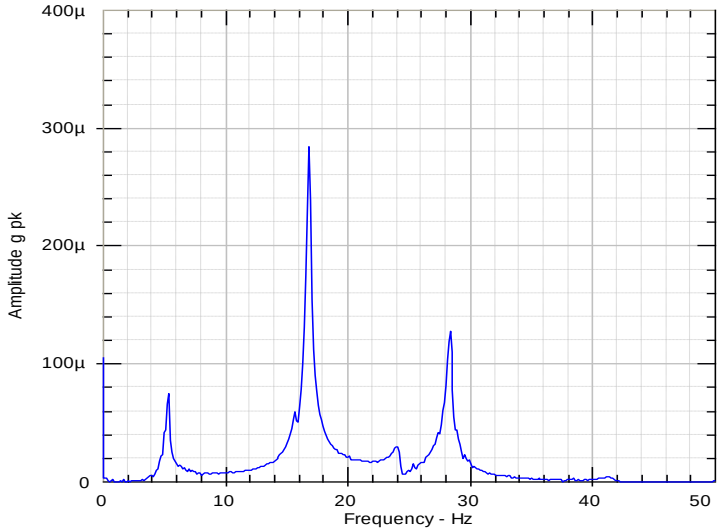

Acceleration response spectrum at first floor

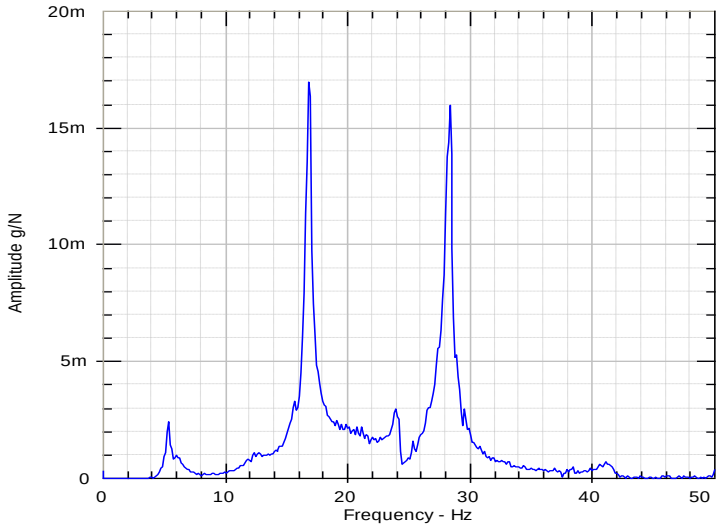

Frequency response function at first floor

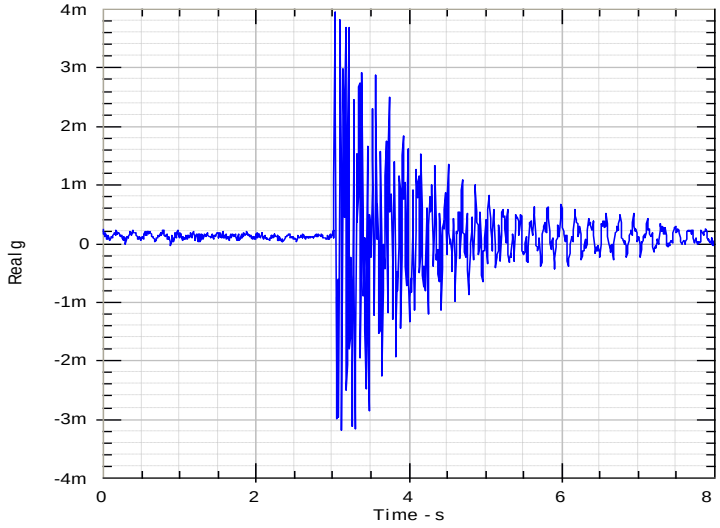

Acceleration response at second floor

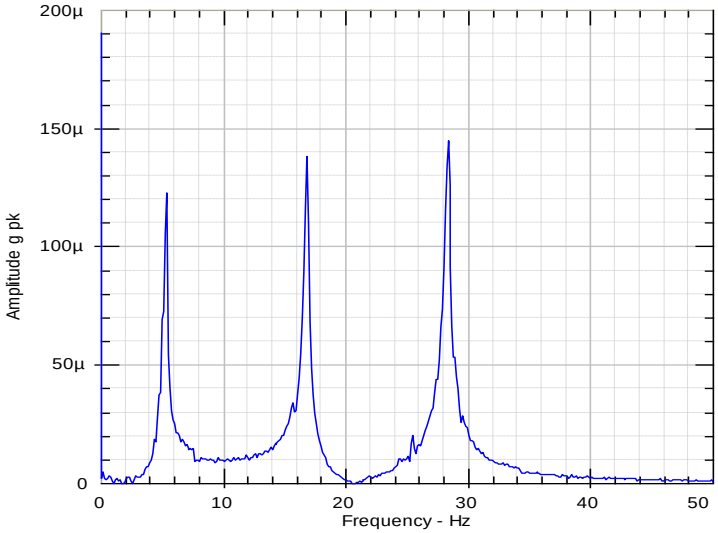

Acceleration response spectrum at second floor

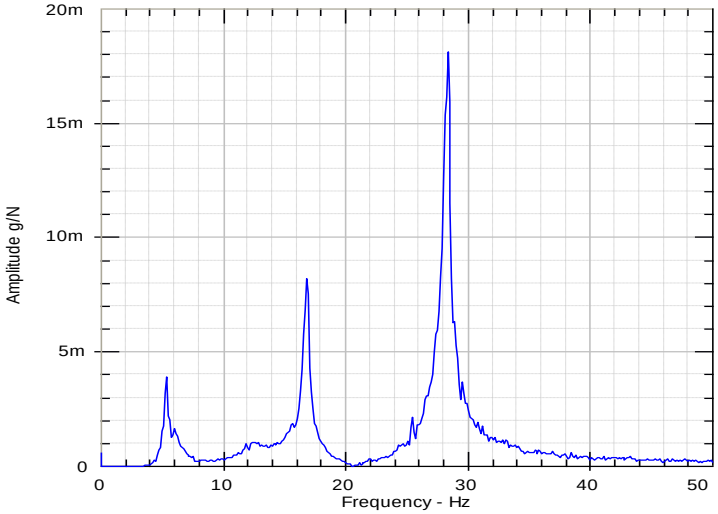

Frequency response function at second floor

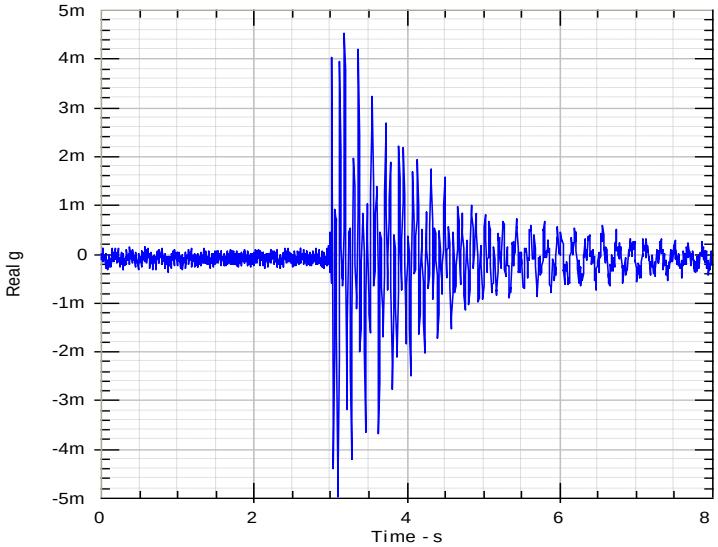

Acceleration response at top floor

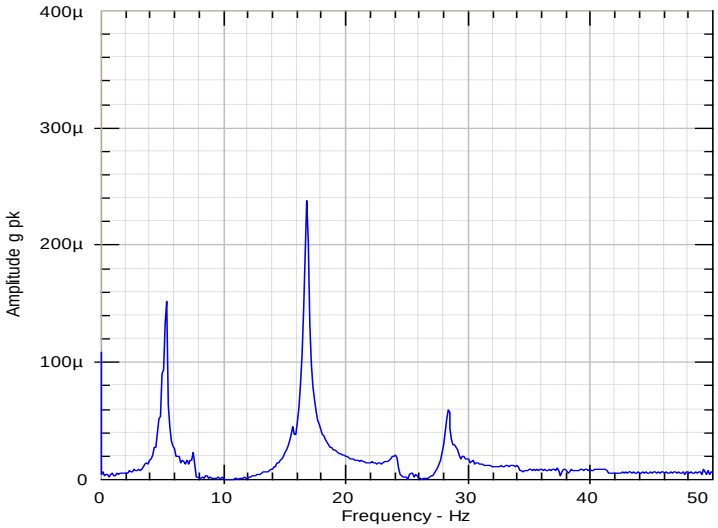

Acceleration response spectrum at top floor

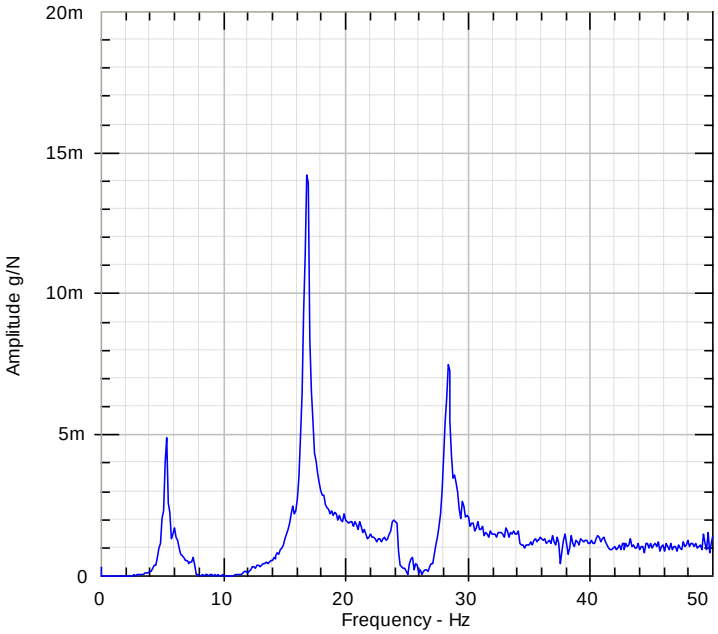

Frequency response function at top floor

Final state at a load of 24 kN

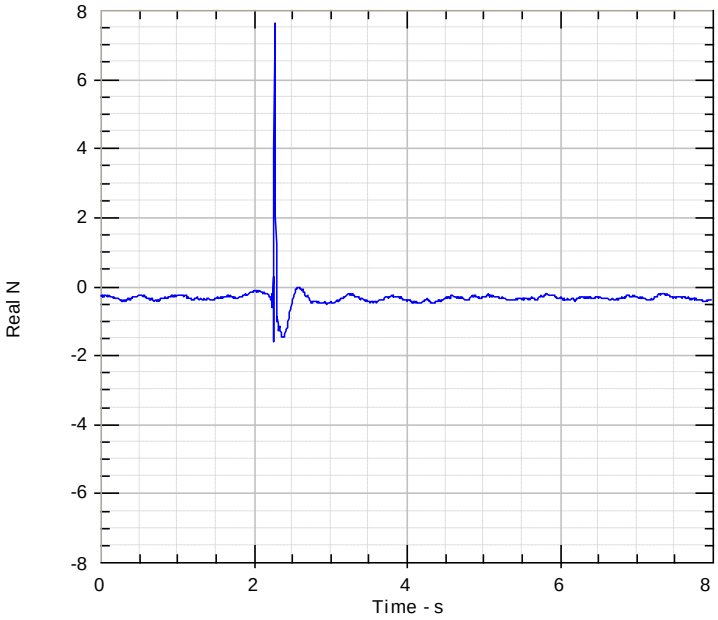

Impact force at top floor of Control Frame 3

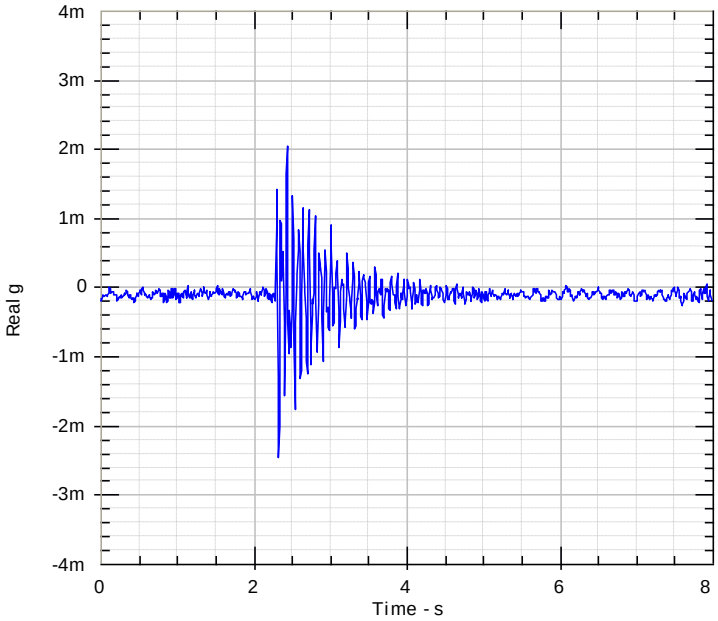

Acceleration response at first floor

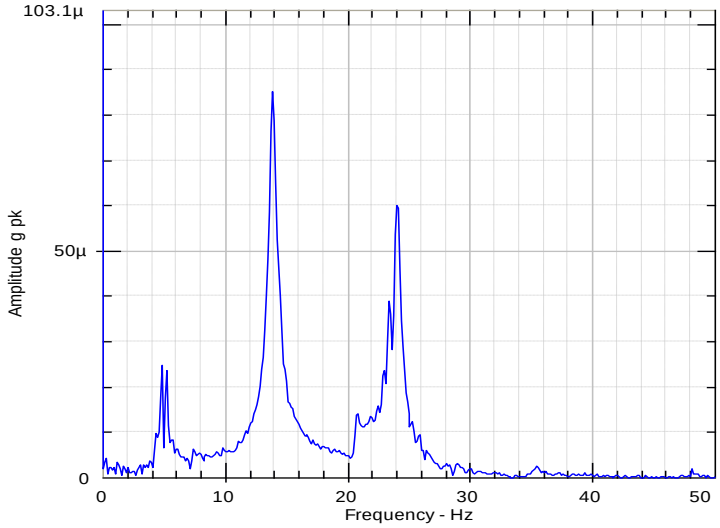

Acceleration response spectrum at first floor

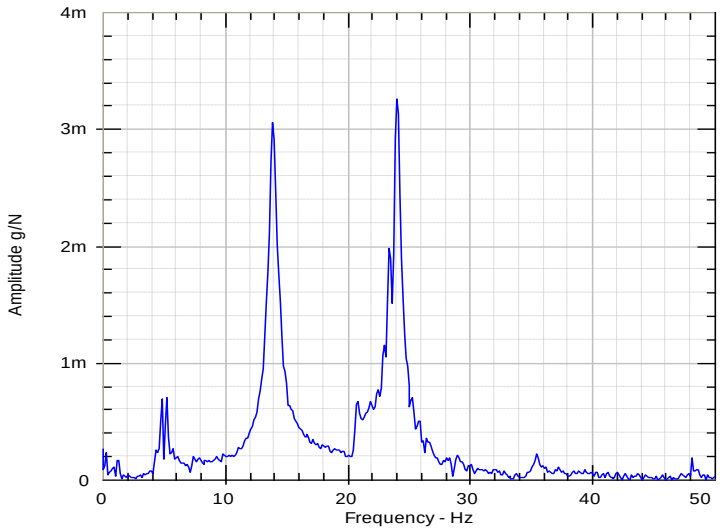

Frequency response function at first floor

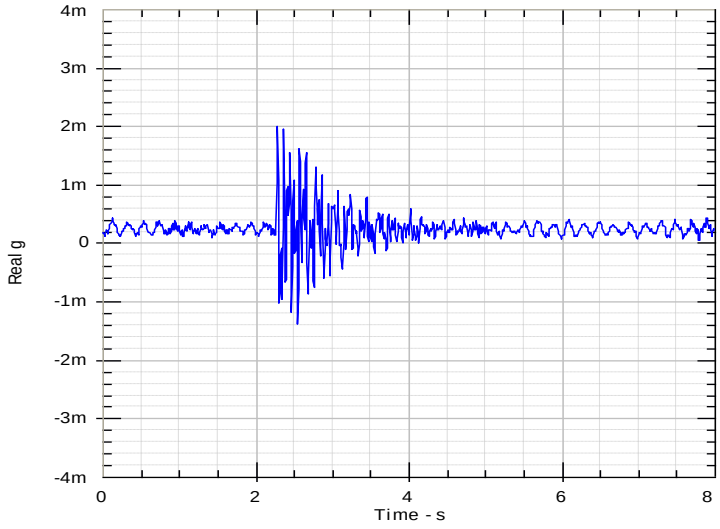

Acceleration response at second floor

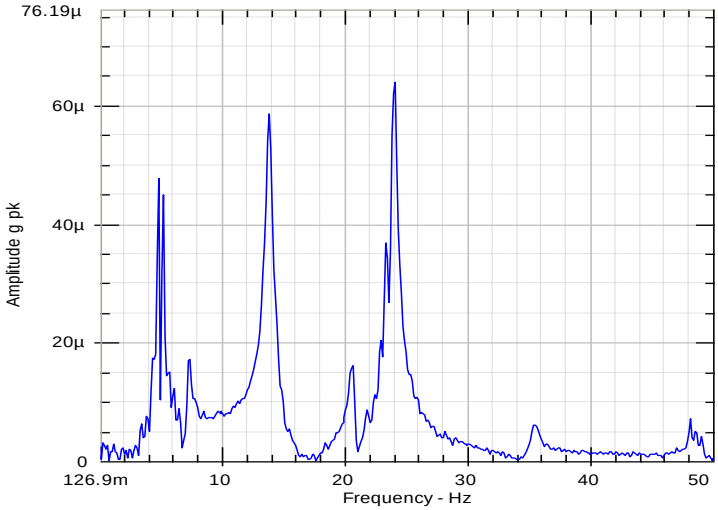

Acceleration response spectrum at second floor

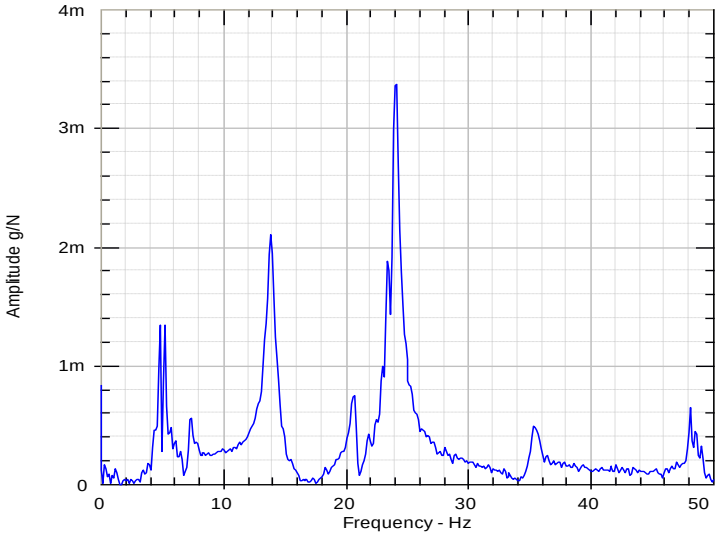

Frequency response function at second floor

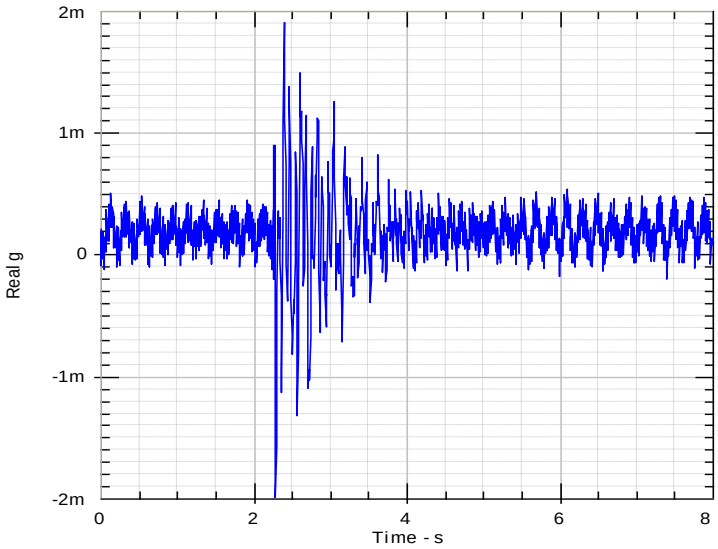

Acceleration response at top floor

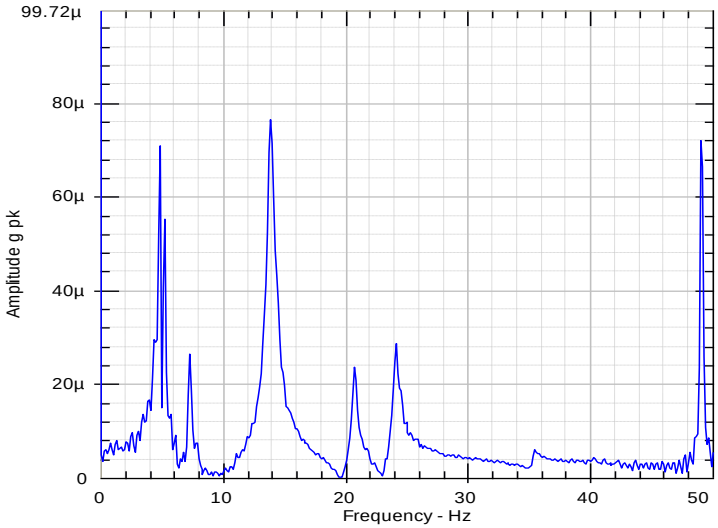

Acceleration response spectrum at top floor

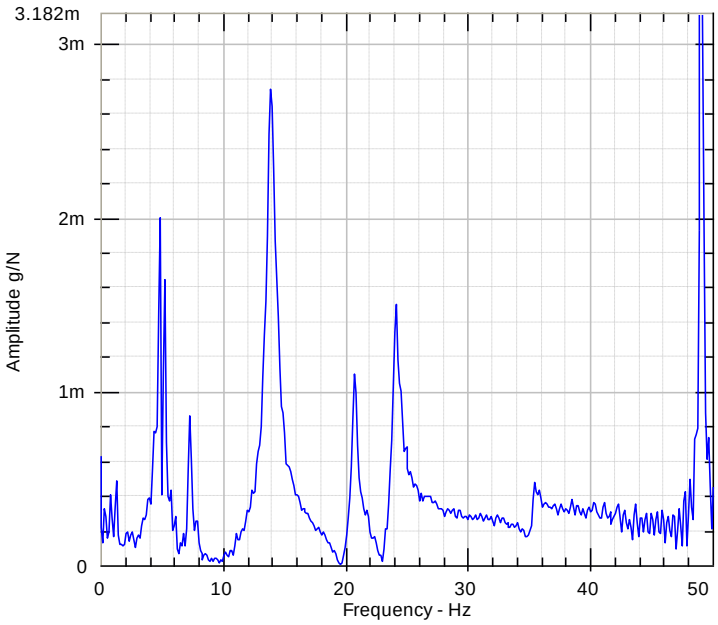

Frequency response function at top floor

Retrofitted Frame 3

Initial state at a load of 0 kN

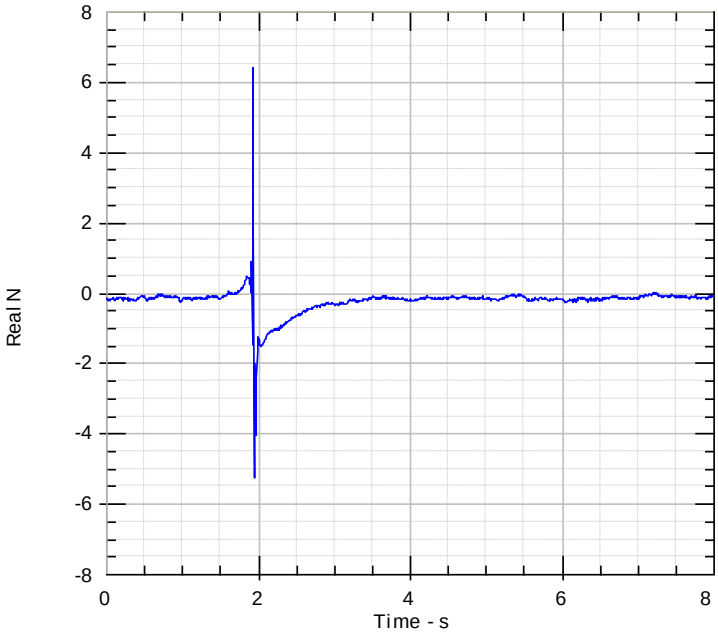

Impact force at top floor of Retrofitted Frame 3

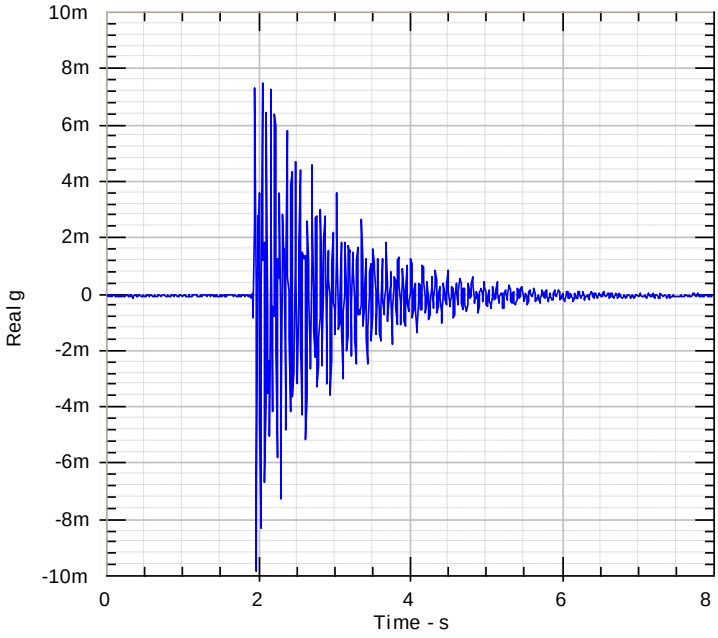

Acceleration response at first floor

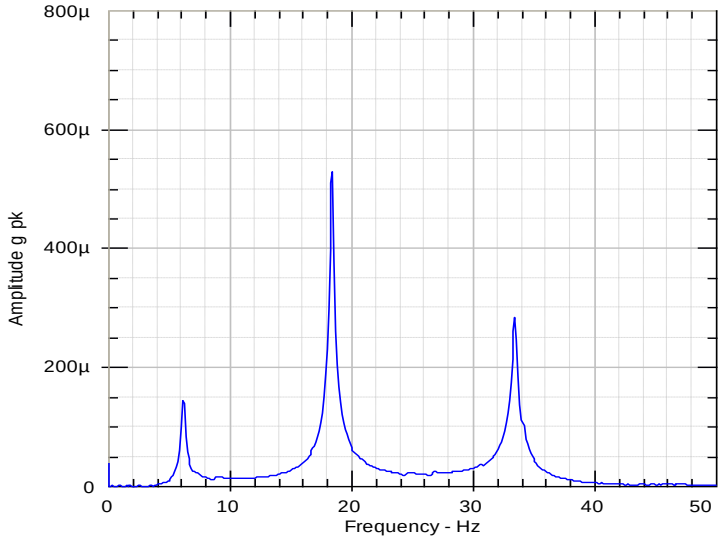

Acceleration response spectrum at first floor

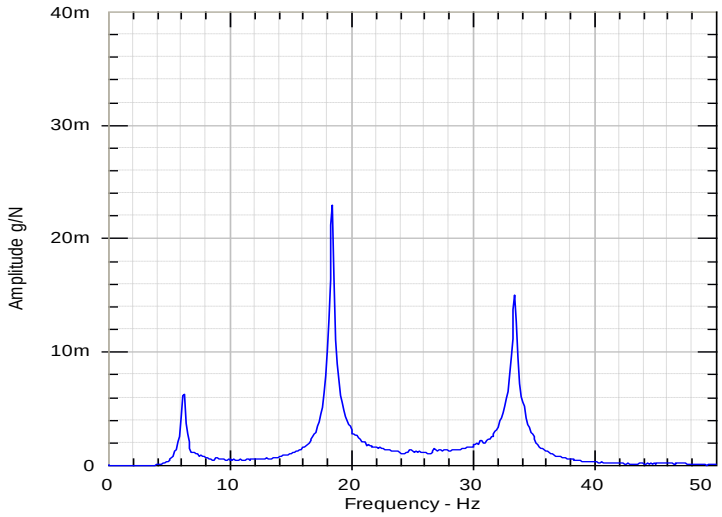

Frequency response function at first floor

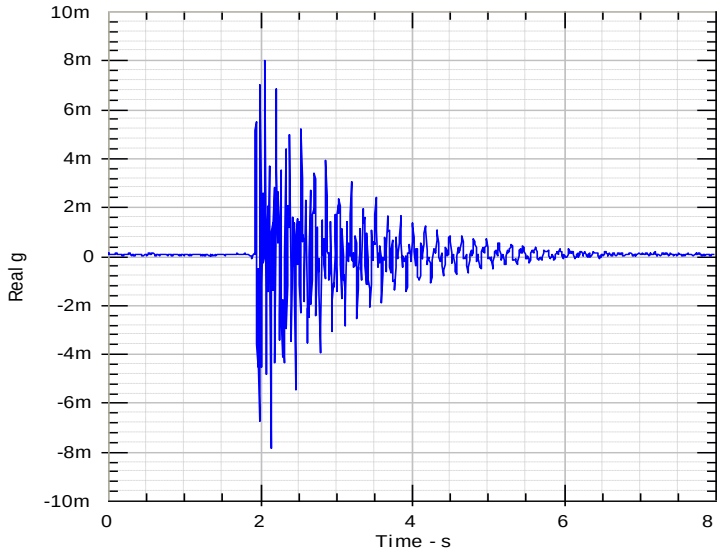

Acceleration response at second floor

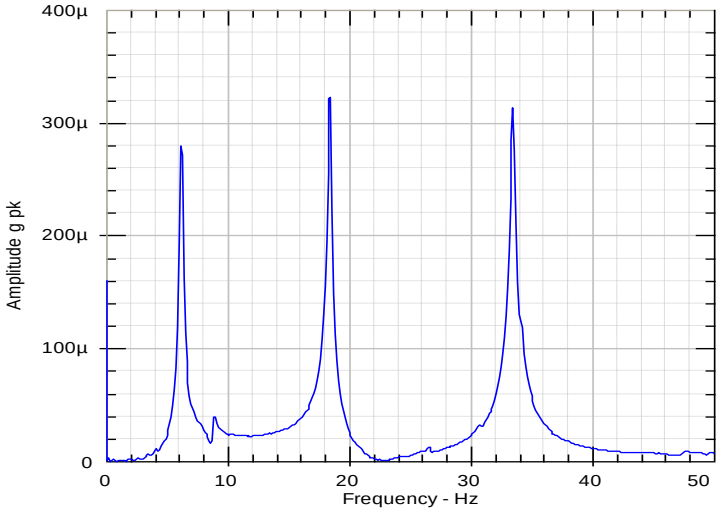

Acceleration response spectrum at second floor

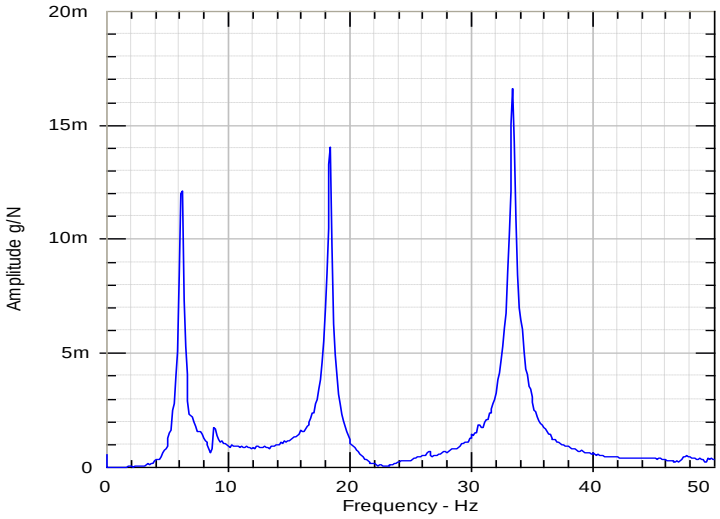

Frequency response function at second floor

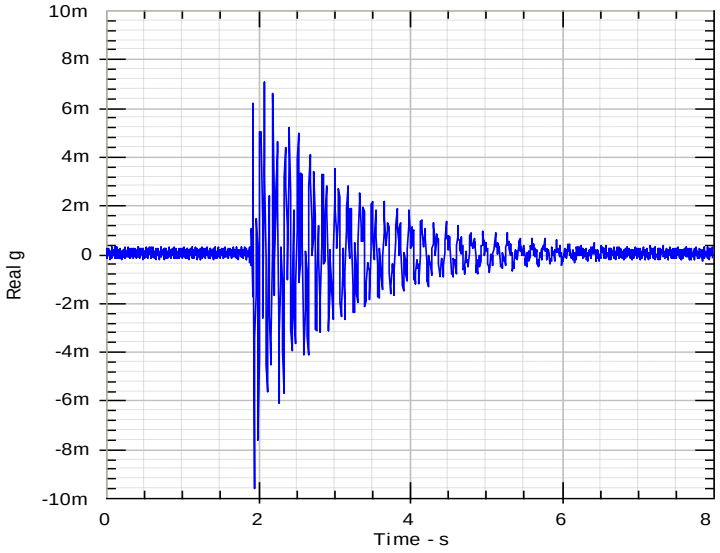

Acceleration response at top floor

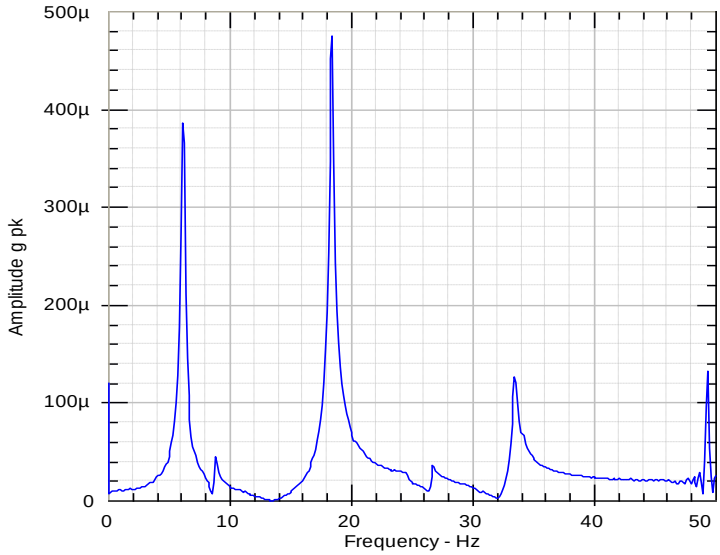

Acceleration response spectrum at top floor

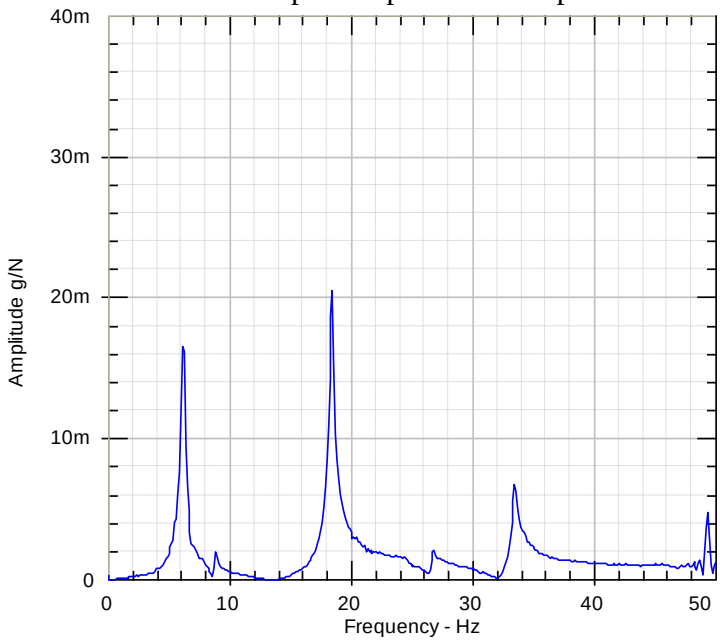

Frequency response function at top floor

Final state at a load of 43 kN

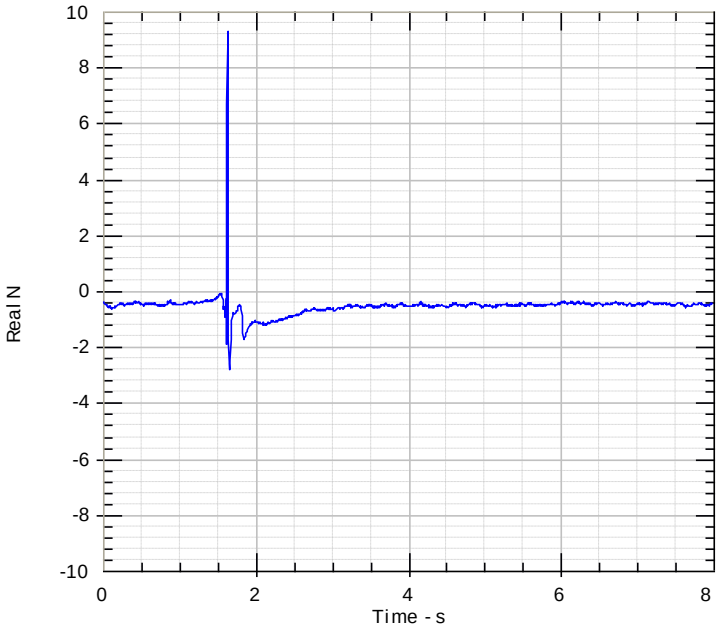

Impact force at top floor of Retrofitted Frame 3

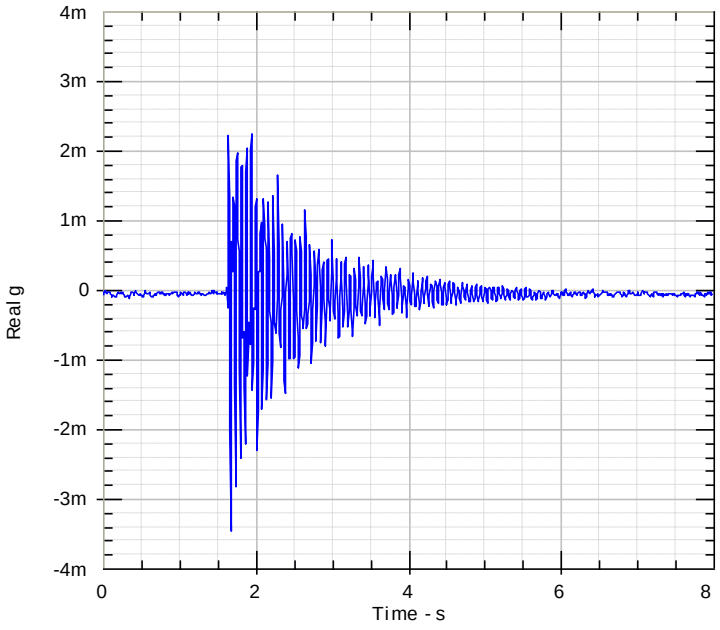

Acceleration response at first floor

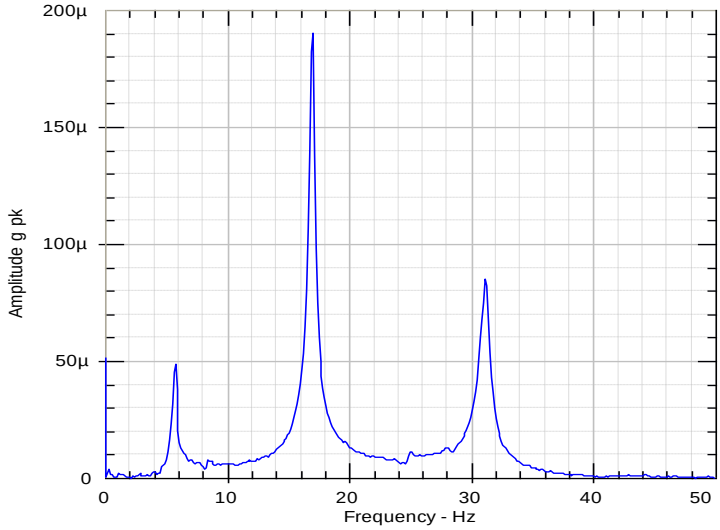

Acceleration response spectrum at first floor

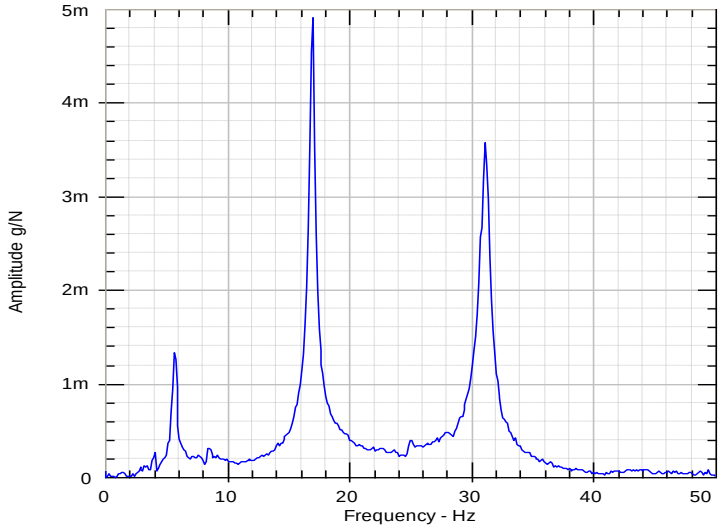

Frequency response function at first floor

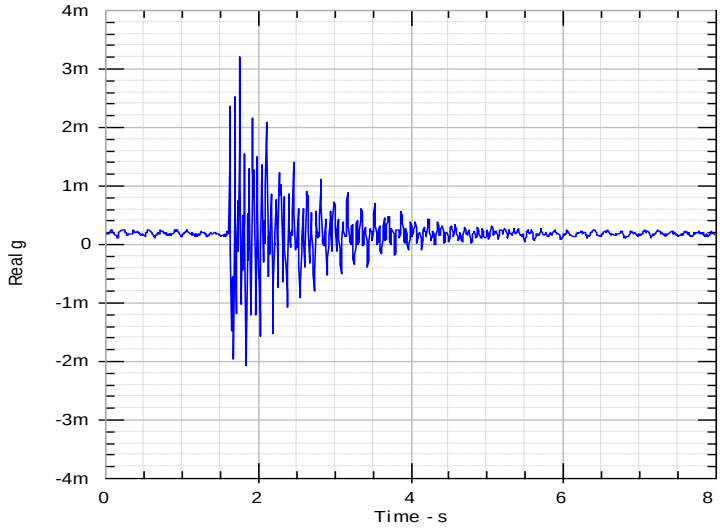

Acceleration response at second floor

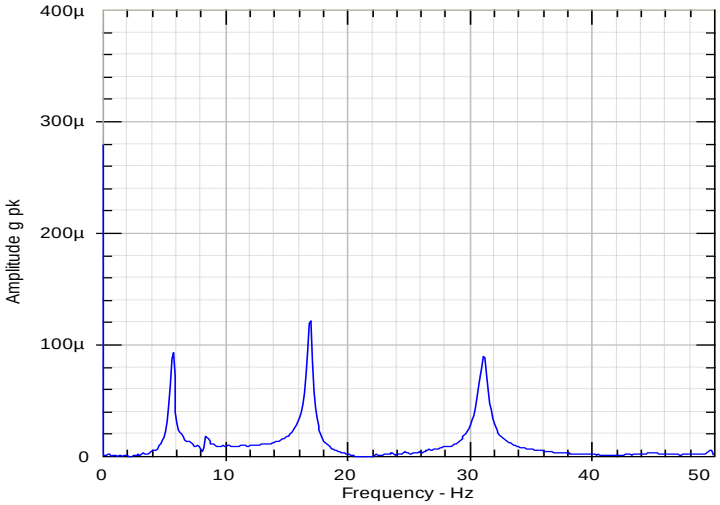

Acceleration response spectrum at second floor

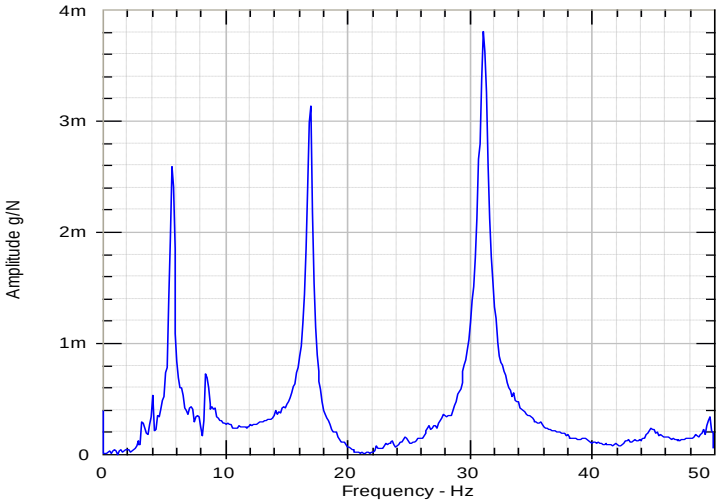

Frequency response function at second floor

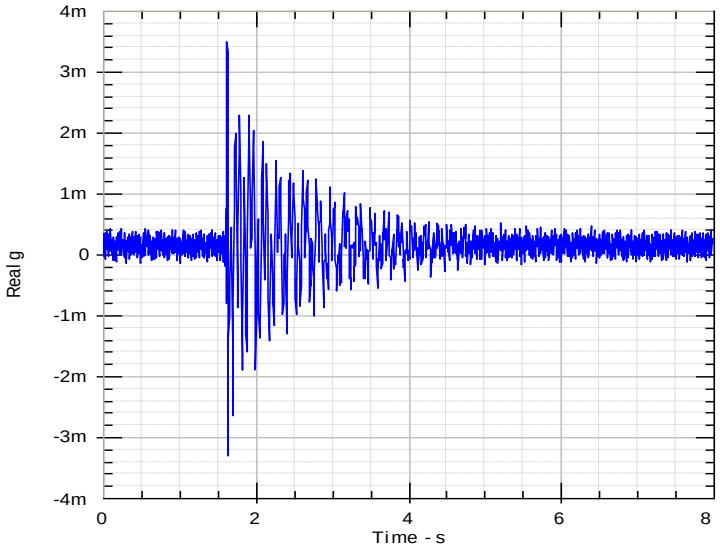

Acceleration response at top floor

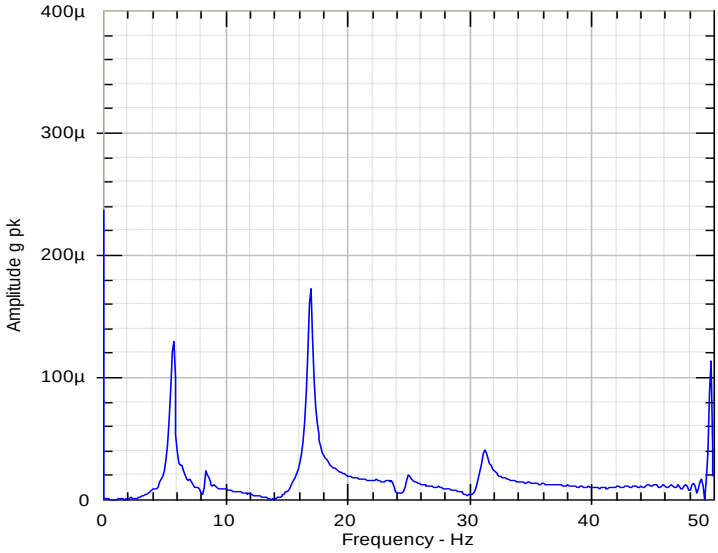

Acceleration response spectrum at top floor

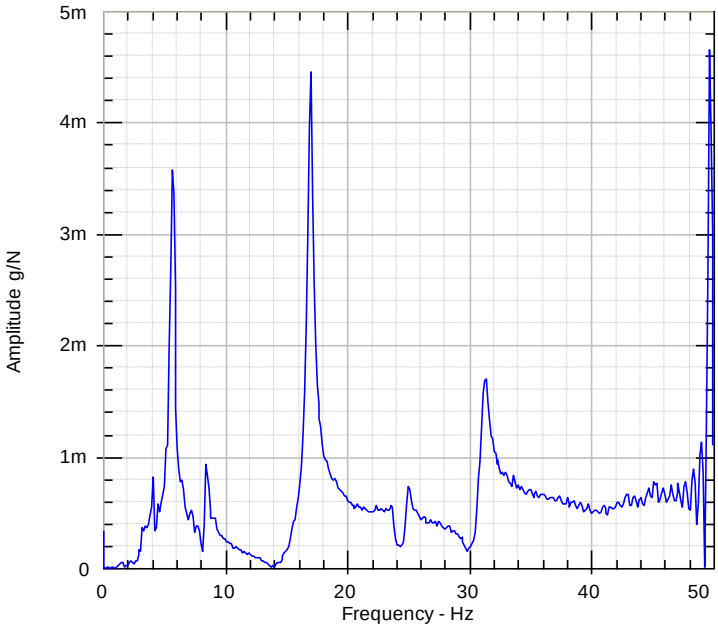

Frequency response function at top floor

APENDIX B

PARAMETER OF CONSTITUTIVE MODEL IN ATENA

APPENDIX B

PARAMETERS OF CONSTITUTIVE FE MODEL

Material parameters of constitutive model in ATENA

Parameter:	*Formula:*
Cylinder strength	$f_c^{'} = -0.85 f_{cu}^{'}$
Tensile strength	$f_t^{'} = 0.24 f_{cu}^{'\frac{2}{3}}$
Initial elastic modulus	$E_c = (6000 - 15.5 f_{cu}^{'}) \sqrt{f_{cu}^{'}}$
Poisson's ratio	$\nu = 0.2$
Softening compression	$w_d = -0.0005 mm$
Type of tension softening	1 – exponential, based on G_F
Compressive strength in cracked concrete	$c = 0.8$
Tension stiffening stress	$\sigma_{st} = 0.$
Shear retention factor	variable (Sect.2.1.7)
Tension-compression function type	linear
Fracture energy G_f according to VOS 1983	$G_F = 0.000025 f_t^{'0.7}$ *[MN/m]*
Orientation factor for strain localization	$\gamma_{max} = 1.5$ (Sect.2.1.3)

PLUBISHED ARTICLES

1. A. Vimuttasoongviriya, N. Kwatra and M. Kumar, 2009, "Effect of Lateral Quasi-Static Load on Nonlinear Behaviour and Damage Indexes of Retrofitted RC Frame Model", Asian Journal of Civil Engineering, Vol. 10, No. 5, pp. 563-587.

2. A. Vimuttasoongviriya, N. Kwatra and M. Kumar, 2010, "Non Linear behaviour and Vibration Based Damage Identification of Retrofitted RC Frame Model", Proceedings of the 9th International Conference for Highrise Towers and Tall Buildings, 14-16 April 2010, Munich, Germany, Paper No. 0958.

3. A. Vimuttasoongviriya, N. Kwatra and M. Kumar, 2010, "Modal Parameters Damage Method for Detecting Damage in Strengthened RC Frame Model using GFRP Laminate", Proceedings of the 15th National conference in Civil Engineering, 12-14 May 2010, Ubonratchathani, Thailand, Paper No. STR2.

4. A. Vimuttasoongviriya, N. Kwatra and M. Kumar, 2010, "Damage Detection of Strengthened RC Frame Model with FRP sheets under Lateral Loads", Proceeding of the 11th International Conference on Structures under Shock and Impact, 28-30 July 2010, Tallinn, Estonia, pp. 55-67.

5. A. Vimuttasoongviriya, N. Kwatra and M. Kumar, 2010, "The Effect of Lateral Quasi-Static Loading on Damage Indexes Based on Modal Parameters of Retrofitted RC Frame Model", International Conference on Noise and Vibration Engineering, 20-22 September 2010, Leuven, Belgium, pp. 1119-1133.

6. A. Vimuttasoongviriya, N. Kwatra and M. Kumar, 2011, "Vibration Monitoring of Strengthed RC Buildings using FRP Laminates", Industrial and Technology Journal, Thailand, Vol. 4, No. 1, pp. 6-17.

7. A. Vimuttasoongviriya, N. Kwatra and M. Kumar, 2011, "Nonlinear Behavior and Effect of GFRP on Strengthened RC Frame Model", Industrial and Technology Journal, Thailand, Vol. 4, No. 2, pp. 1-14.

8. A. Vimuttasoongviriya, N. Kwatra and M. Kumar, “Vibration Monitoring and Damage Assessment of a Retrofitted Frame Model”, KMITL Science and Technology Journal. This paper had 12 pages, (accepted to publish).

9. A. Vimuttasoongviriya, N. Kwatra and M. Kumar, 2011, “Damage Detection Based on Modal Assurance Criterion and Coordinate Modal Assurance Criterion”, Proceedings of the 37th Congress on Science and Technology of Thailand, 12-14 December 2011, Bangkok, Thailand, Paper No. ID 00018, (accepted to publish).